Physical Models and Statistical Methods for Understanding Electrochemical Kinetics

by

Aditya Madan Limaye

B.S. Chemical Engineering
University of California, Berkeley (2016)

Submitted to the Department of Chemical Engineering in Partial Fulfillment of the Requirements for the Degree of

Doctor of Philosophy

at the

Massachusetts Institute of Technology

May 2022

Signature of Author .....

Department of Chemical Engineering
May 13, 2022

Certified by .....

Adam P. Willard
Department of Chemistry
Thesis Supervisor

Accepted by .....

Patrick S. Doyle
Department of Chemical Engineering
Graduate Officer

Physical Models and Statistical Methods for Understanding Electrochemical Kinetics

by

Aditya Madan Limaye

Submitted to the Department of Chemical Engineering on May 13, 2022 in Partial Fulfillment of the Requirements for the Degree of Doctor of Philosophy in Chemical Engineering

ABSTRACT

Decarbonization of the global economy in order to limit rapid global surface temperature growth is a critical industrial and societal challenge for the next several decades. Yet, several sectors of the economy remain stubbornly difficult to decarbonize, such as commodity chemicals production, cement and steel manufacturing, and synthetic fertilizer synthesis, to name only a few. Emerging efforts to decarbonize these processes rely on electrochemical techniques, which use emissions-free sources of electricity to drive relevant chemical reactions. Much remains to be understood about the fundamentals of electrochemical kinetics, hampering efforts to rationally engineer decarbonized electrochemical processes. This thesis develops new physical models and applies rigorous statistical methods towards developing a more complete understanding of electrochemical kinetics.

The physical models I develop are grounded in the framework of classical statistical mechanics. In **Chapter 2**, I develop an extension to the classical Marcus kinetic theory of electron transfer that accounts for diffusive transport effects in the electrochemical double layer. In **Chapter 3**, I advance a simple physical explanation for why the reorganization energy, a key parameter in Marcus theory, exhibits marked attenuation upon approach to a constant potential electrode surface. Finally, in **Chapter 4**, I apply molecular dynamics simulations of the electrochemical double layer (EDL) to evaluate the fidelity of continuum theoretical predictions of electrostatic potential variation in the EDL.

The statistical methods I report in this thesis leverage relatively straightforward mathematical approaches to modernize classical electrochemical analyses. In **Chapter 5**, I show how applying a Bayesian analysis technique to Tafel slope analysis can correct subjective human biases in literature-reported analyses of CO_2 electroreduction data. Finally, in **Chapter 6**, I develop a new electrochemical analysis technique based on analysis of weakly nonlinear current response to a medium-amplitude oscillating voltage signal, which can serve as a complementary technique to cyclic voltammetry, a more traditional approach to electrochemical characterization.

Thesis Supervisor: Adam P. Willard
Title: Associate Professor of Chemistry

Acknowledgements

Family

To my parents, Aai and Baba. It is only through your unconditional love and constant sacrifice that I have been able to reach these heights. Thank you for building me a life in the United States, for nurturing my curiosity from a very young age, and for helping me believe that I can do anything in this world. While I cannot possibly pay back the labor of love you poured into my education, I hope to prove that it was the best investment you have ever made.

Aai, thank you for walking me to school, for all the trips to the library, for answering all my random questions as a kid. Thank you for getting me involved in scientific extracurriculars in elementary and middle school, and for teaching me to be meticulous and organized. Thank you for always listening to me and supporting me through some of my toughest times in life. I really have no idea how you managed to do all this while also having a job and running a household: you are a real life superhero.

Baba, thank you for being my first teacher, for kindling an interest in science and mathematics from a very early age. Thank you for spending your weekends at high school debate tournaments, even when those debate skills would be turned against you at the dinner table. Thank you for urging me to learn computer programming and to stay in engineering; I do always seem to come around to your point of view, even if it takes me a few years to get there. I know that me getting a degree from MIT has been a dream of yours since I was born: 27 years later, it is a reality.

Anay, it has been wonderful to grow closer as we have gotten older. I'm glad to be able to call you a close friend, and I'm excited to see what you'll be up to in your own career.

To Ravi Aaba, thank you for being a consistent positive presence in my life. Thank you for all the attention you gave me when I was a little kid visiting your house: for the chess lessons and the babushka dolls. Thank you for convincing me to stick with chemical engineering, and for staying on as a lecturer at Berkeley so that I could take two of your classes. Thank you as well for helping me sort out my life trajectory post-PhD. It's because of you that we now have two PhDs in chemical engineering in the family!

Friends

To Matt Delateur, the best college roommate I could have ever asked for. My intellectual journey to the PhD can be traced back to our many late night conversations on morality, philosophy, and science. As Ivan Karamazov said, "It's different for other people; but we in our green youth have to settle the eternal questions first of all." Thank you for teaching me the importance of tackling the eternal questions, and helping me appreciate the complexity and importance of things outside of science and engineering.

To John Cherian, there have been times during the PhD when I felt that our thoughts were inseparable. Thank you for being such a wonderful friend and intellectual companion. Although we don't share an office like we used to, I'm so happy that we still get to discuss all the things we did back in Tower 45 on a regular basis. I can't wait to congratulate you for all the great things you'll accomplish in your career.

To Matt Van Beek, thank you for being my best friend. We understand each other to an insane degree, likely because our minds were both poisoned by high school debate logic. Thanks for always being up for a conversation about anything, for challenging me intellectually throughout my time here, and for encouraging me to step out of my comfort zone socially.

To Bertrand Neyhouse and Flemming Holtorf, thanks for being amazing roommates. I've learned and laughed so much with both of you, and I'm very sad that we won't be roommates and officemates soon. Our times together in the Marney office will be some of my brightest pandemic memories.

To Amber Phillips, thank you for being an incredibly kind and supremely loyal friend. I know I can count on you to be in my corner in any situation. I'm so glad we got the chance to be friends in graduate school, and I'm even more glad that you're thriving in life post graduate school.

To Daniel Lundberg, I still remember the day we met in the first year offices in August 2018. You're a wonderful person and I feel privileged to call you my friend. Thanks for all the fun conversations and for sharing a passion for the environment and decarbonization. I can't wait to see all the wonderful things you'll do in the world.

To Kyle Lennon, one of the smartest people I've ever met. I'm so glad we got to be Plugs together in 66-252. Learning and researching alongside you has been an absolute blast. Although I won our initial paper race, I'm certain you're going to beat me on total intellectual contributions in the PhD. Thanks for challenging me intellectually and for being a wonderful friend.

To Mohammad Alkhadra (Big Mo), thanks for being an amazing person. I feel so thankful to have had the chance to be your friend — to laugh, learn, and lift alongside you. You're going to do incredible things and I can't wait to hear about them.

To Makoto Lalwani, thanks for being an amazing friend ever since college. You are one of the kindest people I've ever met, and I'm so glad you moved to the Boston area so that we can see each other more often. Thanks for supporting me during the rough times in my PhD, hearing your perspective and your own graduate school experiences was always incredibly comforting.

To Madhu Vijay, thanks for being an all-around wonderful person. I feel very lucky to call you my friend; you set such a great example of a virtuous existence. It's been incredible to "grow up" intellectually alongside you, all the way from high school policy debate to the present day.

To the ChemE ballers, past and present, thanks for being an incredible community through my whole time here at MIT. You all have inspired me to improve myself, and given me an outlet for stress relief during some of my hardest times here. I can't wait to keep balling with you all.

Colleagues

To Felipe Hernandez, I'm so lucky to have been your colleague at DESRES, and to have had the opportunity to learn math and physics from you. I wouldn't be the scientist I am today without our many discussions about math, science, and life at DESRES. Thank you for helping instill in my a sense of mathematical maturity and confidence, and also for being

an amazing friend — I always look forward to our chats.

To Zachary Schiffer, thanks for all the conversations we had in the Manthiram Lab. It's not an exaggeration to say that our chats were the most consistently positive intellectual experience of my entire PhD. I feel very fortunate to have had the chance to collaborate with you on multiple pieces of scientific work; your questions and ideas always enabled me to do better science. I'm eager to see what you make of your bright future!

To Joy Zeng, I am always inspired by your fearlessness in asking questions, your passion for learning and teaching, and your dogged perseverance. I feel very lucky to have had the chance to work with you in the Manthiram Lab; you pushed me to do better science and helped inspire me to continue improving my teaching skills. I can't wait to see what the future holds for you.

To the Willard Group, thank you for being an excellent community of theorists. I learned so much from you all during my time here, your suggestions and questions helped me do better science than I would have been able to do on my own.

To the Manthiram Lab, thank you for being an incredible community of researchers. I learned so much about experimental electrochemistry alongside you all, and despite all the circumstances, I was happy that we were able to band together even during a time of great change. Thank you for making me a better scientist, researcher, and teacher.

To the Brushett Lab, thank you for accepting me into your research community in the last six months of my time here. I'm glad to have had the chance to sit in your offices and be a part of some of your group traditions.

Mentors

To Adam Willard, thank you for being the best PhD advisor I could have ever asked for. Throughout my time at MIT, I always felt that we were on the same page scientifically. Thanks for letting me run with my ideas while also providing guidance, support, and direction when I needed it. While I thoroughly enjoyed all our conversations about science, the ones that will stand out the most in my memory are those about life and personal matters. Thanks for caring about my development as a whole person, rather than just as a researcher. I hope that we continue to stay in touch even after I leave the university.

To Karthish Manthiram, thank you for being a wonderful experimental co-advisor, and for always pushing me to do better science. I wish you the best in your academic career, and look forward to keeping up with all the scientific work that you and your group produce.

To Jim Swan, you were an absolute titan in the MIT ChemE community. I'm incredibly sad that you were taken so soon, and that I wasn't able to celebrate my thesis defense with you in attendance. You had such an enormous impact on me as a researcher and as a person ever since I entered your orbit at MIT. Thank you for being so generous with your time and your ideas, and for encouraging me to do work that mattered. I will always do my best to uphold your legacy in all my intellectual endeavors.

To Raji Pingali and Dipty Desai, my elementary and middle school science coaches, thank you for pouring many hours of effort into helping me learn science as a kid. I wouldn't be here without you.

To Chris Wolf, Bill Healy, DeeDee Sullivan, Kim Jones, and Jim Harville, thank you for helping me find my voice as a member of the Bellarmine Speech and Debate team. Every day

I find myself using the skills that you taught me — how to devise, frame, and communicate an argument convincingly and effectively.

Finally, to Clara Troyano Valls. Meeting you was the best thing to happen to me in graduate school. You're a thoroughly wonderful person, and every day you inspire me to be a better human being. You've supported me through some of the toughest emotional stretches of the PhD journey; I hope I can do the same for you in the future. I love you, and I can't wait for what the future has in store for us.

Contents

Chapter 1

Introduction

Human progress since the Industrial Revolution to the present day has coincided with the steady acceleration of greenhouse gas (GHG) emissions into the Earth's atmosphere. The same industrial technologies and energy systems that have enabled human society to flourish, as evinced by prodigious population growth and global improvement of living standards, have also summoned the looming specter of a new civilization-scale threat: anthropogenic climate change. The latest report from the Intergovernmental Panel on Climate Change suggests that in order to limit the increase in the global average surface temperature to only 2 C beyond pre-industrial levels, humanity must embark on an aggressive trajectory towards net-zero GHG emissions by the year 2050.[1] Simply imagining the collective action required to effect such a trajectory is already a staggering exercise; GHG emissions are currently part and parcel of several goods and services taken for granted in modern society: electricity to power homes, transportation to access work opportunities, concrete and steel to construct the material world, to mention only a few.

Despite the daunting nature of the challenge of broad-based GHG emissions reductions across wide swaths of industry and society ("decarbonization"), there are promising signs of progress. Electricity generation from solar and wind power in 2021 comprised 13% of US power production[2], and these GHG-free sources of power can now compete economically (on a per-energy basis) with more traditional GHG-emitting power sources. The transportation sector has been revolutionized by the advent of Li-ion battery powered electric vehicles, which comprised 4.5% of new car sales in 2021[3], and are projected to grow their share of American vehicle stock over the next several years. Yet, strong headwinds to decarbonization prevail in numerous other sectors of the economy: commodity chemical production, steel and cement manufacturing, synthetic fertilizer synthesis, maritime shipping, airborne travel, and many others. In these sectors, the "green premium" remains stubbornly large; nascent decarbonized technologies cannot yet compete economically with existing GHG-emitting modes of operation.[4]

An abundance of research interest has been directed towards developing commercializable GHG-free technologies in these high green premium applications. The modus operandi for decarbonization in these technologies is to replace traditional GHG-emitting process energy sources (oil, natural gas, or coal) with renewable electricity distributed through the power grid. Given this strategy, it is unsurprising that industrial decarbonization efforts in the research and early commercialization stage leverage electrochemical techniques, which

boast a rich scientific history. "Electrochemical technique" describes an approach that involves converting electrical energy (usually conveyed by the flow of electrons in a circuit) into chemical energy (usually stored in stable molecular bonds), or vice-versa. Fundamentally, such techniques require establishing a contact between an electrical circuit (in the simplest case, a wire) and a chemical system (in the simplest case, a beaker of electrolyte solution); the physical setting of this connection is known as the electrochemical interface. The electrochemical interface plays host to numerous electrochemical reactions, in which energy is transferred between the circuit and the solution, carried by electrons which physically transit the interface.

Studying chemical kinetics (i.e. the rates of different electrochemical reactions) at the electrochemical interface is challenging because it hosts a confluence of varied physical effects, nearly all of which play a non-trivial role in sculpting the nature of its chemical dynamics, especially under external driving. Understanding how these effects interact to produce macroscopically-observable experimental behavior is of immense practical interest for effectively engineering GHG-free approaches to tackle difficult-to-decarbonize sectors of the economy. This thesis reports on the development of new physical models and improved statistical methods for understanding electrochemical kinetics; these advances can meaningfully improve efforts to engineer the electrochemical reactions at the heart of critical decarbonized manufacturing technologies.

1.1 Physical Models

Matter at a driven electrochemical interface is subject to a number of unique physical constraints that are not present in bulk electrolyte. The interface is characterized by stark spatial anisotropy, strong electric fields, and the persistent presence of an electronic reservoir. In response to these constraints, molecules are forced to adopt typical configurations that are highly atypical in the bulk; fluctuations around these configurations are also highly constrained. Ultimately, all of these physical effects manifest themselves in the macroscopically observable characteristics of electrochemical interfaces, which can be probed quantitatively with powerful experimental tools. Although experimental approaches can provide a wealth of information about the nature of chemical dynamics at an interface, they often convolve the numerous physical effects at play in an electrochemical setting. Physical models are the scalpels with which we can begin to cut apart these effects; when applied judiciously, in conjunction with experimental data, they can sort out the relative importance of different microscopic physical phenomena. This thesis advances three major thrusts of fundamental physical modeling, each concerning the impact of molecular fluctuations on the rates of interfacial electrochemical reactions.

In **Chapter 2**, we extend the classical Marcus kinetic model for an electron transfer reaction carried out in bulk electrolyte to account for the effects of diffusive species transport in the electrochemical double layer, a universal feature of electrochemical interfaces. We formulate this model in a coordinate system that separately resolves both the transport of redox species in the direction perpendicular to the electrode surface and the thermal fluctuations of the solvent environment that drive electron transfer. This formulation enables us to explore how the observable characteristics of electrochemical systems are influenced by

spatial variations in the electric fields and electronic couplings that are inherent to the double-layer, especially under conditions of low ionic strength, where screening lengths are larger. We apply this model to highlight the fundamental interplay between two physical attributes of interfacial electrochemistry: electrode coupling and electrostatic driving. Using a simple model system designed to isolate this interplay we demonstrate how variations in the location of electron transfer can lead to systematic changes to the electrochemical transfer coefficient. We also illustrate that for certain redox reactions, differences in electrostatic driving between products and reactants can lead to non-monotonic current voltage behavior.

Chapter 3 focuses on developing a simple physical understanding for the suppression of the Marcus reorganization energy upon approaching an interface held at a constant potential by means of an external circuit. We propose that this phenomenon, which has been reported in experimental and simulation studies which utilize varied approaches, arises from the physically universal impact of image charges that arise at a constant potential interface. By plumbing the effects of image charges into a simple statistical field theory model, we demonstrate that the suppression of reorganization energies upon approach to the interface is a direct consequence of the polarization response of a constant potential electrode. We contextualize these results by discussing their implications for the rates of Marcus-like "outer–sphere" electron transfer reactions.

Finally, **Chapter 4** examines the structure of electrostatic potential profiles in the electrochemical double layer. These potential profiles are usually understood and contextualized by macroscopic models of continuum electrostatics, which assume that the solvent can be faithfully represented by a homogeneous dielectric medium, and often discount the effects of ions of finite size. We interrogate the accuracy of these models by examining the results of molecular dynamics simulations of aqueous electrolytes sandwiched between two metal electrodes held at a constant potential difference. While some of the essential features of the continuum electrostatics theories are reproduced, our results demonstrate that the molecular nature of the dielectric solvent molecules and the ions comprising the electrolyte has a marked effect on the observed electrostatic potential profiles. These results motivate the development of improved electrostatics models that properly account for these small length scale effects.

1.2 Statistical Methods

Modern techniques in statistics and data science can help accurately quantify the uncertainty associated with a reported experimental result. Despite finding more use across science and engineering in recent years, rigorous statistical techniques are still woefully underemployed in the analysis of electrochemical data. Experimental electrochemical techniques of various stripes are often hampered by outmoded approaches to data handling: for example, linear fitting techniques for analysis of results reign supreme, and uncertainties in analysis results are often incompletely quantified and reported, if at all. Since the results of such analyses are often used to impute fundamental knowledge about a chemical mechanism or physical phenomenon at work, it behooves electrochemical researchers to employ more sophisticated statistical tools when analyzing and reporting results. Application of statistical prescriptions to classical electrochemical analysis may sometimes involve relatively straightforward

changes to post-experimental data analysis; in other contexts, a fundamental overhaul of the experimental procedure may be preferable. This thesis advances two major thrusts along these lines, proposing the use of rigorous statistical techniques when collecting and analyzing current-voltage measurements on electrochemical systems.

In **Chapter 5**, we develop a Bayesian data analysis approach to estimate the Tafel slope (a key parameter often quoted the characterize the efficacy of an electrochemical catalyst) from experimentally-measured current-voltage data. Our approach obviates the human intervention required by current literature practice for Tafel estimation, and provides robust, distributional uncertainty estimates. Using synthetic data, we illustrate how data insufficiency can unknowingly influence current fitting approaches, and how our approach allays these concerns. We apply our approach to conduct a comprehensive re-analysis of data from the CO_2 reduction literature. This analysis reveals no systematic preference for Tafel slopes to cluster around certain "cardinal values" (e.g. 60 or 120 mV/decade). We hypothesize several plausible physical explanations for this observation, and discuss the implications of our finding for mechanistic analysis in electrochemical kinetic investigations.

Chapter 6 focuses on developing an electrochemical characterization technique that hinges on analyzing the nonlinear current response of an electrochemical system to a small amplitude oscillating voltage signal. Using a mathematical framework based on Fourier analysis and time-dependent perturbation theory, we derive expressions that link the output current signal to the input voltage signal and the underlying microscopic parameters of the electrochemical system. We confirm the validity of our mathematical formalism by comparison to time-domain numerical simulations of an interfacial reaction-diffusion model. Employing standard regression tools, we analyze the results of oscillating voltage experiments on the model ferrocyanide/ferricyanide redox couple to extract the values of the electron transfer rate constant, electrochemical transfer coefficient, and equilibrium potential. Our technique is a complementary tool to traditional cyclic voltammetry approaches to characterization, and may be better suited for high-throughput experimentation applications.

1.3 References

[1] H.-O. Pörtner, D.C. Roberts, M. Tignor, E.S. Poloczanska, K. Mintenbeck, A. Alegría, M. Craig, S. Langsdorf, S. Löschke, V. Möller, A. Okem, and B. Rama. Climate change 2022: Impacts, adaptation, and vulnerability. contribution of working group ii to the sixth assessment report of the intergovernmental panel on climate change. 2022. URL `https://report.ipcc.ch/ar6wg3/pdf/IPCC_AR6_WGIII_SummaryForPolicymakers.pdf`.

[2] Tyler Hodge. New renewable power plants are reducing u.s. electricity generation from natural gas, 2022. URL `https://www.eia.gov/todayinenergy/detail.php?id=50918`.

[3] Sean Tucker. Electric vehicle sales surging as overall new car sales fall, 2022. URL `https://www.kbb.com/car-news/electric-vehicle-sales-surging-as-overall-new-car-sales-fall/`.

[4] Bill Gates. *How to Avoid a Climate Disaster: The Solutions We Have and the Break-*

throughs We Need. Knopf Doubleday Publishing Group, 2021. ISBN 9780385546140. URL https://books.google.com/books?id=pHK0DwAAQBAJ.

Chapter 2

Expanding Marcus Theory to Account for Transport Phenomena in the Electrochemical Double Layer

2.1 Introduction

Electron transfer (ET) reactions at electrode-electrolyte interfaces take place within the electrical double layer (EDL), a region in which many of the physical properties that influence ET are sharply varying. [1] Traditional models of interfacial ET reactions omit these variations by using approximations that effectively "flatten" the EDL so that it is localized to the electrode surface. In this work, we develop a model that explicitly resolves the spatial variations in the EDL and the dynamics of species within it, enabling a detailed microscopic investigation of EDL effects on interfacial ET. Our model illustrates a ubiquitous physical effect that emerges due to an interplay between electrostatic driving forces within the EDL and the spatially-dependent electronic coupling that drives interfacial ET reactions. We demonstrate that this interplay establishes an optimal location for ET, resulting in experimentally verifiable modifications to the electrochemical transfer coefficient/Tafel slope. Furthermore, we highlight that our simple model contains the physical effects necessary to capture and contextualize the enigmatic non-monotonic current voltage behavior in peroxodisulfate electroreduction experiments, as first observed by Frumkin[1,2]. Our model is sufficiently general and easy to interpret, leaving it well-poised to offer fresh mechanistic insight into a number of additional electrochemical phenomena.

A characteristic feature of all solid-electrolyte interfaces, the EDL forms due to the preferential affinity of a specific charged species to the solid surface[3]. This preferential affinity leads to a buildup of excess charge in a region of finite width, typically 1–5 nm, that decays away from the solid surface. Across this narrow space-charge region, both the electrical potential and the electronic coupling between the reactive species and the electrode can change

[1]The material in this chapter is reproduced in part with permission from: Limaye, A. M.; Willard, A. P., Modeling Interfacial Electron Transfer in the Double Layer: The Interplay between Electrode Coupling and Electrostatic Driving. *J. Phys. Chem. C* **2020**, 124, 2, 1352–1361. Copyright © 2019 American Chemical Society, `https://doi.org/10.1021/acs.jpcc.9b08438`.

dramatically. Recent experimental studies have suggested that variations inside the EDL can exert significant influence on interfacial ET reactions.[4] These studies have led to numerous hypotheses about the role of EDL structure in interfacial ET reactions, however, evaluating these hypotheses requires the development of models that properly account for EDL effects.

Macroscopic transport models of electrochemical systems often assume the EDL is infinitesimally thin. Under this assumption, interfacial ET processes can be modeled using Marcus theory[5–7], encoded as a boundary condition by the Butler-Volmer equation[8], or more sophisticated analogs[9]. This approach is sufficient to model some systems, but deviations from experimental behavior in others have inspired a number of empirical corrections that re-introduce EDL effects[10–13]. Continuum models with empirical EDL corrections are indispensable for engineering electrochemical devices, and will continue to find use in the quantitative interpretation of experimental results. However, reliance on *post hoc* EDL corrections hampers the ability of these models to make mechanistic remarks on the nature of ET reactions.

Electronic structure simulations, on the other hand, provide a great deal of information about the energetics of small molecular clusters near electrode interfaces. Modern density functionals can accurately predict species adsorption energies on metallic surfaces, and shed light on the preferred molecular conformations of reactive species[14]. These methods are regularly used for characterizing the thermodynamics of ET reactions, and are a useful tool for catalyst design[15]. However, electronic structure simulations typically struggle to access the characteristic length and time scales of the EDL. These scales are essential for developing a complete kinetic picture of interfacial ET processes that involve collective solvent rearrangement (e.g. with rates determined by Marcus theory)[16].

Our model operates at the intermediate length and time scales relevant to the EDL, and provides a useful complement to the previously discussed techniques. It is inspired by previous work applying reaction-diffusion equations to study the Anderson-Holstein ET model in a quasi-classical limit[17,18]. We extend these efforts by incorporating an additional reaction coordinate tracking the position of a reactive species inside the EDL. Inclusion of this electrode approach coordinate allows us to directly investigate the interplay between electrostatic and electrochemical potentials variations within the EDL. While our model does not resolve any molecular detail or macroscopic transport phenomena, it represents the essential physics of EDL effects on interfacial ET in a natural, understandable manner. Under appropriate parametrization, our model reproduces experimental results, and recovers the correct limiting behavior when EDL effects are unimportant.

In this chapter, we start by sketching a qualitative description of the physical components of our model, followed by a presentation of its mathematical formalism. We apply this model in two different contexts. First, we study the spatial localization of ET events in the electroreduction of a neutral reactant at a cathode, and examine its impact on the electrochemical transfer coefficient. Second, we study how spatial localization of ET events depends on the applied potential in a model for peroxodisulfate electroreduction. Our results offer a compelling microscopic explanation for the non-monotonic current-voltage behavior observed in this system that is entirely consistent with contemporary macroscopic models.

2.2 Smoluchowski Master Equation Model

Reaction Coordinates

Our model resolves fluctuations along two distinct coordinates relevant to electron transfer in the EDL. The first is a Marcus coordinate, x, which tracks the collective polarization of the local dielectric solvent environment on a reactive species. In the Marcus picture[5–7,19], the initial and final states of an ET reaction are characterized by very distinct preferred configurations of the surrounding solvent polarization field. ET events can occur when a fluctuation along a solvent polarization coordinate renders the two states roughly isoenergetic[16,20,21]. Marcus' key insight was the assumption that fluctuations along the solvent coordinate obey Gaussian statistics. The validity of Gaussian statistics (equivalently, the presence of a quadratic free energy well) in this context has been verified by numerous simulation studies, and represents a spectacular success of linear response theory[16,22,23]. In our model, x is a unitless coordinate which will house a parabolic confining free energy representing the collective preference for a species-specific solvent polarization state.

The second is an approach coordinate, z, tracking the distance of a reactive species from the electrode surface. Electrode approach is a relevant coordinate when studying interfacial ET because numerous physical quantities affecting ET vary drastically with distance from the interface. For example, screening phenomena cause the electrostatic potential to approach its bulk value as one moves away from a constant potential interface. Additionally, the quantum mechanical electronic coupling between the reactive species and the band orbitals of the electrode changes significantly with z, serving to facilitate ET near an electrode surface. A recent study incorporated an approach coordinate to examine the interaction between interfacial ET and *macroscopic* transport processes in electrochemical devices[24]. In contrast, our model allows us to understand the influence of *microscopic* property variations and diffusive transport on interfacial ET. Hence, the approach coordinate in this model is resolved within a length scale L representing the spatial extent of the EDL, most closely associated with the Debye screening length of the electrolyte.

Free Energy Surfaces

The thermodynamics of our model are encoded into the free energy profiles of each reactive species. Specifically, we express the free energy for species i on the coordinate product space (x, z) as,

$$F_i(x,z) = \frac{k_{\text{reorg}}}{2}\left[x - \bar{x}_i\right]^2 + q_i\left[\phi(z) - \phi(0)\right] + E_{\text{int},i}. \tag{2.1}$$

The first term represents the (Marcus) free energy cost of deforming the solvent coordinate away from its minimum $\bar{x}_i$, where k_{reorg} specifies the width of the parabola (proportional, up to an order-one constant, to the reorganization energy). The second term represents the electrostatic energy of a point charge of magnitude q_i in an externally-applied potential $\phi(z)$. The third term is an intrinsic energy offset associated with species i. This could be due to, for example, an energetic cost for intramolecular rearrangement that accompanies an ET event.

Equation (2.1) requires specification of an electrostatic potential profile, $\phi(z)$, describing the manner in which screening attenuates the applied potential. A litany of models employing

different assumptions about screening physics describe the functional dependence of potential decay in the EDL[8,25,26]. The conclusions we draw from our model are insensitive to the details of the potential profile, as long as it decays to its bulk value when $z = L$. With simplicity in mind, we select a linear decay function to describe the potential drop across the entire EDL,

$$\phi(z) = V\left[1 - \frac{z}{L}\right], \tag{2.2}$$

where V is the applied (electrode) potential. In our model, electrostatic interactions between charged species and the potential are "one-way": species motions are influenced by the potential, but do not distort the potential profile. Physically, this corresponds to a situation in which a reactive species is dilute in an inert supporting electrolyte, a common setup for practical electrochemical measurements.

Dynamics

An ensemble of independent walkers initialized on the free energy surface of Eq. (2.1) and connected to a thermal bath at inverse temperature β will evolve according to Langevin dynamics. Instead of tracking the trajectories of the independent walkers, we can examine the dynamics of the entire probability distribution $P_i(x, z, t)$ as it evolves from its initial condition. In the overdamped (Brownian) limit, the distribution is propagated in time by the Smoluchowski diffusion operator[27]

$$\hat{\mathcal{L}}_i P_i \equiv \mathcal{D}\nabla \cdot \left[e^{-\beta F_i}\nabla\left(e^{\beta F_i} P_i\right)\right], \tag{2.3}$$

where $\mathcal{D}$ is a (scalar) diffusion constant. In the form written in Eq. (2.3), the Smoluchowski operator implicitly obeys the fluctuation-dissipation theorem. In terms familiar to electrochemical literature, Eq. (2.3) takes advantage of the Nernst-Einstein relation to parameterize electromigrative drift and diffusion rates by a *single* diffusion constant[8]. The fluctuation-dissipation theorem is valid for systems at or near equilibrium; non-equilibrium generalizations have been developed for electrochemical systems, but are beyond the scope of this work[28].

In addition to diffusing on its own free energy surface, a member of species i can also undergo an outer-sphere ET event to transform into a different species j. This type of ET phenomenon is inherently quantum mechanical, and involves a switch between two Born-Oppenheimer surfaces near a diabatic crossing point. A full quantum dynamical description of the diabatic intersection is outside the scope of this study. However, we can extract information about the resultant occupation statistics on the two diabatic surfaces using surface hopping (SH) dynamics. Under the SH picture, a walker can "hop" between surfaces at a rate proportional to the electronic coupling. In terms of distributional evolution, SH dynamics can be modeled with a master equation approach which includes continuous balanced sink/source rates that transform one species to another, effectively connecting free energy surfaces. This approach has been used heuristically[29–31] and also developed rigorously[17,18,32] in prior work on interfacial ET.

The sink and source rates must be set such that the stationary distribution of the dynamics respects the proper equilibrium (Boltzmann) distribution. There is, in principle, no

unique way to define these rates, but a simple expression for the sink/source rate between surfaces i and j in accordance with prior work[17,33] is,

$$\zeta_{i\to j}(x,z) = \frac{\Gamma_{ij}(z)}{\hbar} f\left[F_j(x,z) - F_i(x,z)\right], \tag{2.4}$$

where $f[\cdot]$ is the Fermi distribution of the electrode. The coupling profile, $\Gamma_{ij}(z)$, changes upon electrode approach, primarily because of increasing overlap between the molecular orbitals of the redox species and the band orbitals of the electrode[34]. Previous studies on ET[29,34–38] and self-assembled monolayers[39,40] have used the exponential form,

$$\Gamma_{ij}(z) = \bar{\Gamma}_{ij} \exp\left[-z/z_{\mathrm{dec},ij}\right], \tag{2.5}$$

for this decay, consistent with detailed quantum mechanical calculations[41–43]. Prior studies report a wide range of values for $\bar{\Gamma}_{ij}$ and $z_{\mathrm{dec},ij}$, suggesting that they are dependent on the chemical details of the system. Hence, the coupling magnitude and decay rate are important physical parameters in our model, and we thoroughly examine the effects of varying them within reasonable values. We note that Eq. (2.5) neglects any dependence of the coupling on the applied electrode potential, though this effect may play an important role at high electrode surface charge density[36].

Conservation of probability mass yields the following set of coupled partial differential equations describing the dynamics of the species population distributions,

$$\frac{\partial P_i}{\partial t} = \hat{\mathcal{L}}_i P_i + \sum_{j\neq i} \left[\zeta_{j\to i} P_j - \zeta_{i\to j} P_i\right]. \tag{2.6}$$

For numerical and analytical convenience, we will non-dimensionalize Eq. (2.6) utilizing the EDL length scale L and the diffusive timescale $\tau \equiv L^2/\mathcal{D}$. The scaled spatial coordinate, time, hopping rate, and propagator are given by $\tilde{z} = z/L$, $\tilde{t} \equiv t/\tau$, $\tilde{\zeta}_{i\to j} \equiv \tau \cdot \zeta_{i\to j}$, and $\hat{\tilde{\mathcal{L}}} \equiv \tau \cdot \hat{\mathcal{L}}$, respectively. Full details on the non-dimensionalization procedure are described in Section 7.1. From here on, we will drop all tildes, and work exclusively with the non-dimensional variables. Taken together, these equations comprise a Smoluchowski master equation (SME) that describes the distributional evolution of our reactive ensemble.

Boundary Conditions

Finally, we need to specify appropriate boundary conditions on Eq. (2.6). We would like to use the SME to determine the amount of current passed from the electrode in a non-equilibrium steady state (NESS) defined by a particular applied voltage V. The NESS is created by maintaining a constant probability density (equivalently, a concentration) of reactant species and a vanishing probability density of product species at the EDL boundary ($z = 1$). Both probability densities are equilibrated with respect to the Marcus coordinate x at the EDL boundary. In a real system, these concentrations could be maintained by fast convective mass transport mechanisms (vigorous stirring, a rotating-disk electrode, etc.). It is worth noting that many electrochemical phenomena of interest (cyclic voltammetry peaks[44], Sand's time[45], etc.) are the result of slow external mass transport processes influencing

interfacial ET rates. Assessing the effects of external mass transfer limitations is outside the scope of this work, but it is easy to imagine a multi-scale scheme that couples the SME dynamics described here to a macroscopic transport model[46].

We consider the electrode surface at $z = 0$ to be ideally blocking; it does not admit species adsorption or intercalation, implying a no-flux boundary condition for all species. Because of the strongly confining Marcus potential in the x coordinate, with sufficiently large domains, it is largely immaterial whether we specify a zero-concentration or a no-flux boundary condition at the x-boundaries. For computational convenience, we choose to specify no-flux boundary conditions. The boundary conditions uniquely specify a steady-state solution to Eq. (2.6), which we compute numerically. Various properties of the NESS (current, preferred position of ET, etc.) can be computed using the numerical steady-state solution. Computational details on our solution scheme can be found in Section 7.1.

2.3 Spatial Localization of Electron Transfer

The electrode approach coordinate z mediates a physical tradeoff that is germane to nearly all interfacial electrochemistry. Due to the decay of the potential $\phi(z)$ (as modeled by Eq. (2.2)), the driving force for ET is greatest further from the electrode. At the same time, the electronic coupling that facilitates ET decays with z (as modeled by Eq. (2.5)), achieving its greatest value at the electrode surface. The competition between these two effects leads to an optimal/modal position for ET, with experimentally-measurable consequences. Here, we evaluate these consequences with a simple model.

Model Specification

The simplest possible model system exhibiting this behavior is the case of a netural species (species 0) being reduced in a single-electron outer-sphere reaction to produce a negatively charged species (species 1). Due to its simplicity, this model is excellent for gaining an intuitive understanding of the SME, and also showcases the effects of changing the $\bar{\Gamma}_{01}$ and $z_{\mathrm{dec},01}$ parameters of the coupling profile. We select parameters that are in line with typical electrochemical reactions, choosing $E_{\mathrm{int},0} = 0$ eV, $E_{\mathrm{int},1} = 0.20$ eV, $k_{\mathrm{reorg}} = 1$ eV, and $T = 300$ K. We study the current-voltage behavior of this system by varying the applied voltage V across a broad range of tunings of the parameters $\bar{\Gamma}_{01}$ and $z_{\mathrm{dec},01}$. All conclusions derived from this model are relatively insensitive to properly-correlated changes in the selected parameters.

Figure 2.1 shows free energy profiles for both species when the electrode is held at $V = -0.25\,\mathrm{V}$. Because species 0 carries no charge, its free energy has no electrostatic contribution, and is independent of the approach coordinate. The free energy for species 1, however, exhibits a strong dependence on the approach coordinate. At $z = 1.00$, the reduced state is favored energetically by 50 meV, a driving which vanishes entirely at $z = 0.80$ due to decay of the electrical potential in the EDL. Our model is equivalent to a traditional Marcus theory description at the $z = 1$ spatial slice, where changing the applied potential by an amount δV shifts the driving force felt by the reactive species by exactly δV. For $z < 1$, a region not considered in traditional Marcus theory, screening causes the driving force to shift by an

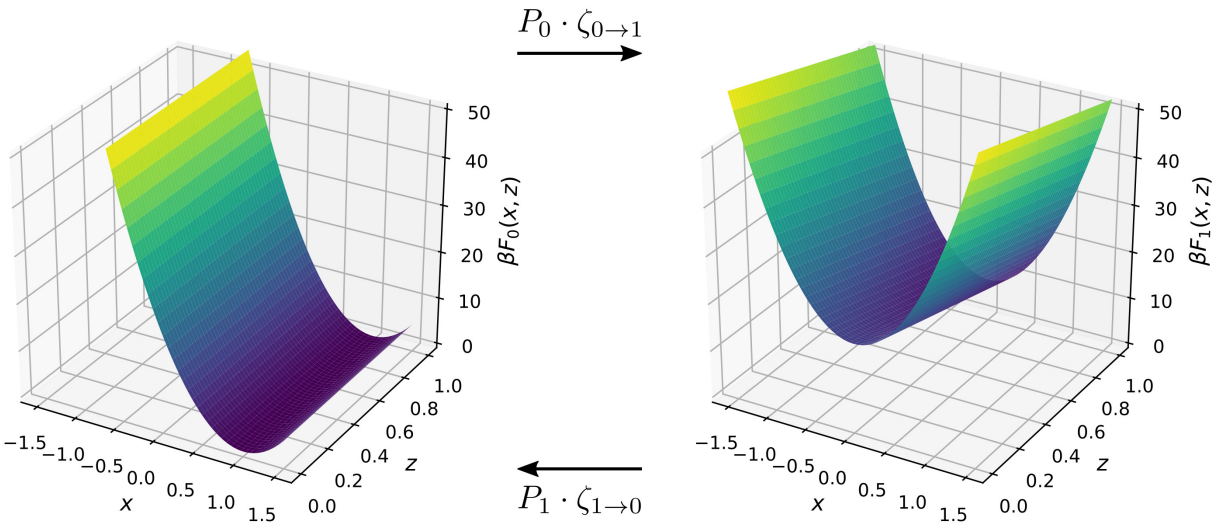

Figure 2.1: Free energy profiles computed from Eq. (2.1) for a simple two-species model. The $z = 0$ and $z = 1$ boundaries correspond to the electrode surface and the edge of the EDL, respectively.

amount *strictly less* than δV.

Mapping ET Location

Our model resolves where ET events occur along the electrode approach coordinate. In the NESS, there will be a net current between states, which can be quantified as a function of the Marcus coordinate and the approach coordinate by the following observable:

$$\Delta(x,z) \equiv \frac{\zeta_{0\to1}P_0 - \zeta_{1\to0}P_1}{\int\int \mathrm{d}x\mathrm{d}z\,[\zeta_{0\to1}P_0 - \zeta_{1\to0}P_1]}. \tag{2.7}$$

This observable essentially describes the flux of population between the two states occurring at a specific point in coordinate space. In the case of traditional Marcus theory, the reaction occurs only at the EDL boundary, implying $\Delta(x,z) = \delta[x - x^*] \cdot \delta[z - 1]$, where $\delta[\cdot]$ denotes a Dirac delta function, and x^* denotes the value of x where the parabolas cross. The SME model improves on traditional Marcus theory by resolving the electrode approach coordinate. In order to isolate the z-dependence, we marginalize over the Marcus coordinate:

$$\bar{\Delta}(z) \equiv \int \mathrm{d}x\ \Delta(x,z). \tag{2.8}$$

Since the EDL thickness L sets the length scale of our model, changes in the electrostatic screening length or the decay length of the coupling profile are equivalently described by varying the $z_{\mathrm{dec},01}$ parameter.

Figure 2.2 depicts the effects of changing $z_{\mathrm{dec},01}$ on $\Delta(x,z)$ when $\bar{\Gamma}_{01} = 6$ eV. Figure 2.2A illustrates that when the coupling profile decays quickly, electron transfer only occurs within a short distance of the electrode surface. Here, the driving force is much smaller than

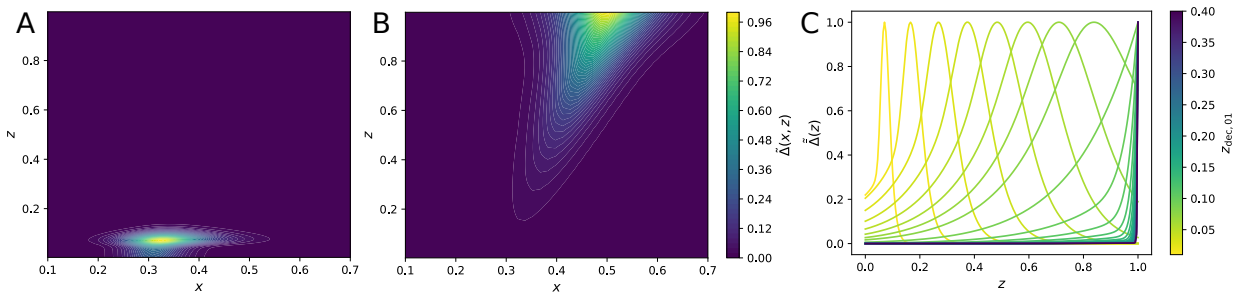

Figure 2.2: Mapping the spatial localization of electron transfer. (A, B) Spatial maps of $\Delta(x, z)$ for $z_{\text{dec},01} = 0.01$ and $z_{\text{dec},01} = 0.10$, respectively. (C) Traces of the normalized marginal current $\bar{\Delta}(z)$ for values of $z_{\text{dec},01} \in [0.01, 0.40]$.

the applied voltage. Figure 2.2B illustrates that when the coupling profile decays gradually, the electron transfer peaks at z-values further away from the electrode. Here, the driving force is higher, approaching the applied voltage. Figure 2.2C depicts profiles of $\bar{\Delta}(z)$ as a function of the coupling decay parameter $z_{\text{dec},01}$, each independently normalized. We observe that the width of the profiles increases as $z_{\text{dec},01}$ increases, indicating that ET is occuring over a broader region of space. At extremely high values of $z_{\text{dec},01}$, the SME model collapses to traditional Marcus theory, since all ET events are localized to $z = 1$. Physically, this corresponds to a situation where the electrolyte screening length is considerably smaller than a typical electronic tunneling distance. This matches expectation – traditional Marcus theory is known to work well for pure outer-sphere interfacial electrochemistry, where electrons tunnel from electrode to species through the entire EDL[10].

Transfer Coefficients

Variation in the location of ET within the EDL can precipitate measurable changes in the transfer coefficient α. The transfer coefficient is defined by the empirical Butler-Volmer current-voltage relationship for a cathodic reaction[8],

$$i = i_0 \exp\left\{\alpha \cdot \beta \left[-eV - \Delta E_{\text{int}}\right]\right\}, \tag{2.9}$$

where i is the measured current density, i_0 is the zero-potential (exchange) current density, e is the fundamental charge unit, and $\Delta E_{\text{int}} \equiv E_{\text{int},1} - E_{\text{int},0}$. The underpinnings of Marcus kinetics[16] imply the Arrhenius relationship,

$$i = i_0 \exp\left[-\beta E_a\right],$$

where E_a is the activation energy. Hence, the transfer coefficient α must obey the relationship,

$$\alpha = -\left[\frac{\partial E_a}{\partial (eV)}\right]. \tag{2.10}$$

In plain terms, α quantifies the amount that an externally-applied voltage V changes the activation energy, and hence the observed current. Up to appropriate unit scalings, the transfer

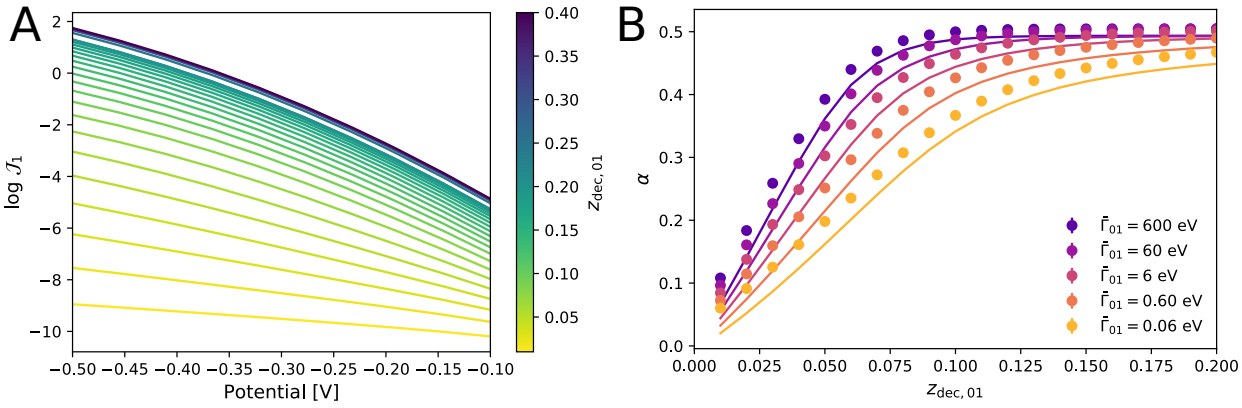

Figure 2.3: Current-voltage curves and transfer coefficient predictions from the two-surface model. (A) Several current-voltage curves measured for different values of the coupling localization parameter $z_{\mathrm{dec},01}$ (expressed non-dimensionally as a fraction of L), with $\bar{\Gamma}_{01} = 6$ eV. (B) Transfer coefficients determined by linear fitting for a number of different coupling strengths are shown as colored dots. The solid lines are predictions from the simple model/approximation developed in Eq. (2.14).

coefficient is the inverse of the Tafel slope, another quantity often resolved in electrochemical measurements. Traditional Marcus theory offers the following prediction for the dependence of α on the applied potential (see Section 7.1 for a detailed derivation):

$$\alpha_{\mathrm{Marcus}} = \left[\frac{1}{2} + \frac{\Delta E_{\mathrm{int}} + eV}{k_{\mathrm{reorg}}}\right]. \tag{2.11}$$

Equation (2.11) implies that at the equilibrium potential $V_{\mathrm{eq}} = -\Delta E_{\mathrm{int}}/e$, the transfer coefficient should be exactly 1/2, then decrease with more cathodic applied potentials, eventually becoming negative at potentials below $-\left(k_{\mathrm{reorg}} + 2\Delta E_{\mathrm{int}}\right)/2e$, corresponding to the Marcus inverted regime. Thus, the expectation for typical outer-sphere electrochemical reactions is that the transfer coefficient decreases from $\alpha = 1/2$ as the potential is tuned from V_{eq} to more negative values.

Figure 2.3 shows current-voltage measurements for several different values of the coupling localization parameter $z_{\mathrm{dec},01}$, holding $\bar{\Gamma}_{01} = 6$ eV. Transfer coefficients are determined by simple linear regression to the initial region of the curves, and are plotted as solid circles in Fig. 2.3B. Counter to expectation, at low values of $z_{\mathrm{dec},01}$, the equilibrium potential transfer coefficients predicted by the model are significantly smaller than the Marcus theory prediction of 1/2. The attenuated transfer coefficients are a direct consequence of the driving force/coupling strength tradeoff in the z-coordinate. For small $z_{\mathrm{dec},01}$ values, ET can only occur within a short distance from the electrode surface, where the potential deviates very little from the electrode potential (and hence the electrostatic driving force is very low). Due to this "pinning" effect, increasing the applied potential has less of an effect on the activation energy of the reaction compared to the case where the reaction occurs at the EDL boundary $z = 1$ (see Section 7.1 for schematic illustration).

We can devise a simple approximation for the functional dependence of the transfer coefficient α on $z_{\mathrm{dec},01}$ by leveraging information contained in the net current profile $\Delta(x, z)$.

Given that ET occurs at any value of z, the activation energy is now a function of the approach coordinate, with a profile denoted as $E_a(z)$. The average activation energy $\langle E_a \rangle$ can be determined by integrating $E_a(z)$ against the empirical marginal of the net current,

$$\langle E_a \rangle = \frac{\int \mathrm{d}z \ \bar{\Delta}(z) E_a(z)}{\int \mathrm{d}z \ \bar{\Delta}(z)}. \tag{2.12}$$

Equations (2.1) and (2.2) yield the following expression (see Section 7.1 for complete derivation) for the activation energy profile,

$$E_a(z) = \frac{k_{\mathrm{reorg}}}{2} \left[\frac{1}{2} + \frac{\Delta E_{\mathrm{int}} + eVz}{k_{\mathrm{reorg}}} \right]^2 . \tag{2.13}$$

Assuming that the net current profile is roughly independent of the applied potential, applying the Leibniz rule yields,

$$\alpha = - \int \mathrm{d}z \ \tilde{\bar{\Delta}}(z) \cdot \left[\frac{\mathrm{d}E_a}{\mathrm{d}(eV)} \right] \ , \tag{2.14}$$

where $\tilde{\bar{\Delta}}(z)$ denotes $\bar{\Delta}(z)$ normalized by its own integral. The solid lines in Fig. 2.3B are constructed from numerical evaluation of Eq. (2.14), and match the qualitative behavior of the measured α quite well. However, Eq. (2.14) assumes a limit of small coupling, resulting in systematic underestimation of the measured α values. The non-adiabatic hopping expression used in the SME model enables transitions away from the parabola crossing, thus increasing the measured α value. When this smearing effect is reduced by increasing k_{reorg}, the predictions from Eq. (2.14) achieve quantitative agreement with the measured α values from the SME model (see Section 7.1).

Implications

The variation of the preferred electron transfer position in z with changes in the $z_{\mathrm{dec},01}$ parameter has implications for the analysis of current-voltage behavior for outer-sphere ET reactions. Current-voltage curves are typically fit to Eq. (2.9), which predicts an exponential dependence between the the observed current and the *applied* potential. This relationship can only hold if all ET events occur at $z = 1$, and should fail spectacularly for ET events that are localized much closer to the interface, where the reaction potential is much lower in magnitude than the applied potential.

A correction to the Butler-Volmer equation developed by Frumkin accounts for this effect by adjusting the driving force to the mean potential at the most likely transition state (TS) position (termed "psi-prime" in the original literature)[47,48]. Frumkin originally set the psi-prime potential to the potential at the outer Helmholtz plane (OHP). Disagreements with experimental results inspired a number of studies that expanded on Frumkin's formalism, but they all preserve the assumption that the most likely reaction site is at the OHP[49–52]. We note that there is no *a priori* basis to assume that the most likely position for the ET event is exactly at the OHP. We demonstrate that this position can be fuzzy, and intricately dependent on molecular details of the redox species (coupling profile with an electrode), as well as on electrolyte characteristics (screening length).

If the typical position of ET is within the region of potential decay in the EDL, then there are additional implications for the measured transfer coefficient. In particular, we show that transfer coefficients can be significantly lower than the traditional Marcus prediction of 1/2 for reactions that occur inside the EDL. Previous studies[53–57] have speculated about the effects of changing reaction site position on the transfer coefficient; the SME model presented here confirms this speculation in a quantitative manner. This phenomenon provides a plausible explanation for the unusually high Tafel slopes observed for certain outer-sphere reactions such as ammonia oxidation[58]. Even when the typical position of ET is outside the EDL, as is common for high ionic strength electrolytes with small screening lengths, L, experiments performed at a series of decreasing ionic strengths can provide additional information about the system. At a particular ionic strength, the transfer coefficient suppression described here will arise; since the variation of L with ionic strength is well-known[27], one can use this "onset length" to infer the spatial extent of the electronic coupling profile for the original system, a quantity which is difficult to access in any other manner.

2.4 Potential-Dependent Spatial Localization of Electron Transfer

The model discussed in the previous section involves the reduction of a neutral species, which is completely unresponsive to electrostatic forces in the EDL. In this case, we find empirically that the optimal position for ET is roughly independent of the applied potential. However, it is often the case that both the oxidized and reduced species are ionic, and thus both responsive to electrostatic forces in the EDL. Since these forces depend on the applied potential, changes in the potential can change the modal position of ET, yielding consequences which could be measured experimentally.

Background

The effects of electrostatic repulsion from an electrode on current-voltage behavior are often treated using Frumkin's correction to the Butler-Volmer equation. In textbook form[8], the correction reads,

$$i_{0,\mathrm{obs}} = \exp\left[\beta\left(e\alpha - q_{\mathrm{ion}}\right)\phi(z_{\mathrm{rxn}})\right] \cdot i_{0,\mathrm{true}}, \tag{2.15}$$

where q_{ion} is the charge carried by the ionic reactant species, z_{rxn} is the most likely position of the reaction, and $\phi(z_{\mathrm{rxn}})$ is the electrostatic potential at this position. Equation (2.15) packages the driving force correction mentioned previously with another correction describing the attenuation (magnification) of the species concentration due to electrostatic repulsion (attraction). To understand the implications of this equation, consider the electroreduction of an anionic species at a cathodic applied potential. If z_{rxn} is far from the electrode (near the EDL boundary), the Frumkin correction will be small, because $\phi(z_{\mathrm{rxn}})$ should be nearly zero (the bulk potential), leading to roughly unperturbed Butler-Volmer current-voltage behavior. On the other hand, if z_{rxn} is very close to the electrode, the Frumkin correction shuts off all current at cathodic voltages, because electrostatic repulsion of the anion depletes its concentration at z_{rxn}. In all cases, if z_{rxn} is assumed constant over a linear voltage sweep,

Eq. (2.15) predicts monotonic current-voltage behavior – depending on the value of q_{ion}, the current could either uniformly increase or decrease over the sweep.

Frumkin and others did a number of experiments[2,47,59] on the electroreduction of the peroxodisulfate anion in the following cathodic half-reaction:

$$\mathrm{S_2O_8}^{2-} + 2\,\mathrm{e}^- \longrightarrow 2\,\mathrm{SO_4}^{2-}. \tag{2.16}$$

Unexpectedly, experiments consistently observe non-monotonic "S"-shaped current-voltage behavior. When tuning from low to high cathodic voltages, the current increases and goes through a maximum, at which point it begins to descend steeply and then goes through a minimum, and then continues to increase for the rest of the scan range (see Figure 1 of Frumkin et al.[2]). This unusual behavior is only observed in a handful of systems that feature the reduction of a large anionic species carrying a high charge[1]. The prevailing physical explanation for this phenomenon relies on electrostatic forces in the EDL[2]. The initial increasing current branch occurs at cathodic potentials below the potential of zero charge (pzc) of the electrode. In this voltage regime, the electrode carries a slightly positive surface charge, which interacts favorably with the anionic reactive species; the current increases with voltage according to Eq. (2.9). The subsequent current decrease occurs upon crossing the pzc, when the negatively charged surface generates electrostatic repulsion that attenuates the current in the manner described by Eq. (2.15). The current minimum and following increase at even more cathodic potentials has proven difficult to rationalize experimentally[52].

Much of the literature on peroxodisulfate electroreduction focuses on explaining the dependence of specific features in the "S"-shaped current-voltage curves on the concentrations of different spectator ions[60–62]. Our model resolves the "S"-shape without invoking molecular detail, suggesting that distance-dependent electrostatic driving and coupling alone are sufficient to explain this anomalous behavior.

Model Specification

The peroxodisulfate electroreduction reaction maps naturally to a two-surface model that includes an anionic species (species 0) carrying charge $q_0 = -1$ and another anionic species (species 1) carrying charge $q_1 = -2$. For convenience, we assign parameter values $E_{\text{int},0} = 0$ eV, $E_{\text{int},1} = 0.05$ eV, $k_{\text{reorg}} = 1$ eV, and $T = 300$ K. For these fixed parameter values, we study current-voltage behavior over a range of $z_{\text{dec},01}$ values.

Changing $z_{\text{dec},01}$ could correspond to altering the electrostatic screening length in the solution or modifying the species/surface chemistry, altering the spatial localization of the electronic coupling. Our model does not resolve the presence of specific ions in the EDL other than the redox-active species, implying that the "pzc" in our model coincides with the point of zero applied potential, $V = 0$. Figure 2.4 depicts the species free energy profiles when the electrode is held at $V = -0.25\,\mathrm{V}$. Both species carry a charge, and hence both free energy surfaces depend on the approach coordinate.

Understanding S-Shaped Current-Voltage Behavior

Figure 2.5A depicts current-voltage curves over a range of values of $z_{\text{dec},01}$. Our model recovers "S"-shaped current-voltage behavior as observed by Frumkin for a limited range of

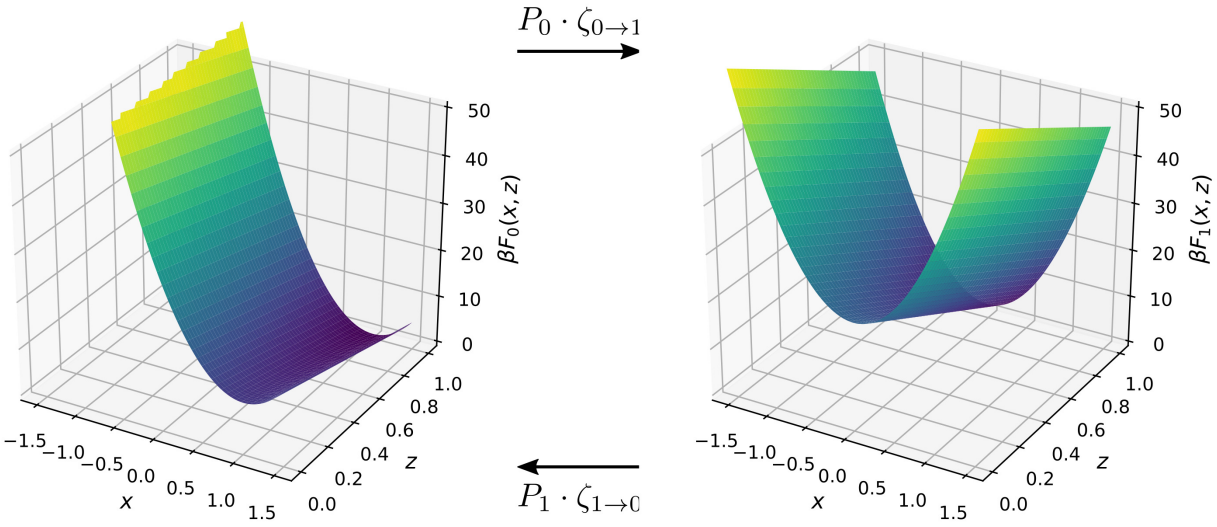

Figure 2.4: Free energy profiles computed from Eq. (2.1) for a model mapping to the peroxodisulfate reduction system in Eq. (2.16)

values of $z_{\text{dec},01} \in [0.06, 0.09]$. On either side of this region, we see very different asymptotic behavior. For $z_{\text{dec},01} > 0.09$, electrostatic repulsion effects contribute only a small kink in the current-voltage behavior. Figure 2.5B confirms that in this case, the current continues to increase exponentially at more cathodic potentials, flattening only due to the effects of the avoided inverted region in Marcus kinetics at an electrode. For $z_{\text{dec},01} < 0.06$, on the other hand, electrostatic repulsion effects strongly influence the current-voltage behavior, leading to negative transfer coefficients that eventually approach zero at far more cathodic potentials.

This behavior can be rationalized in the context of Eq. (2.15) by assuming that z_{rxn} depends on the applied potential. This dependence is not considered in the original Frumkin treatment, and is a unique consequence of the interplay between electrostatic repulsion and distance dependent driving/coupling. Since the SME model gives us direct access to spatial map of ET events, we can define

$$\langle z \rangle_{\text{rxn}} \equiv \int \mathrm{d}z \cdot z \cdot \tilde{\tilde{\Delta}}(z), \tag{2.17}$$

where $\langle z \rangle_{\text{rxn}}$ denotes the *mean* position for ET. Unlike in the case of the neutral reactant species, Fig. 2.5C demonstrates that $\langle z \rangle_{\text{rxn}}$ is indeed a function of the applied potential. Cathodic of the pzc, $\langle z \rangle_{\text{rxn}}$ increases with applied voltage for all values of $z_{\text{dec},01}$, since the reactant is repelled from the negatively-charged electrode surface. However, due to distance-dependent coupling, the rate of increase depends strongly on the value of $z_{\text{dec},01}$. At high $z_{\text{dec},01}$, the ET reaction is facile even far away from the electrode, so $\langle z \rangle_{\text{rxn}}$ quickly reaches the EDL boundary, where electrostatic repulsion is minimized and driving force is maximized. For low $z_{\text{dec},01}$, the ET reaction is very sluggish at large z, so $\langle z \rangle_{\text{rxn}}$ creeps away from the electrode surface slowly. The effects of changing $\langle z \rangle_{\text{rxn}}$ as a function of applied potential are observed clearly in Fig. 2.5D, which tracks $\phi\left(\langle z \rangle_{\text{rxn}}\right)$ as a function of the applied potential.

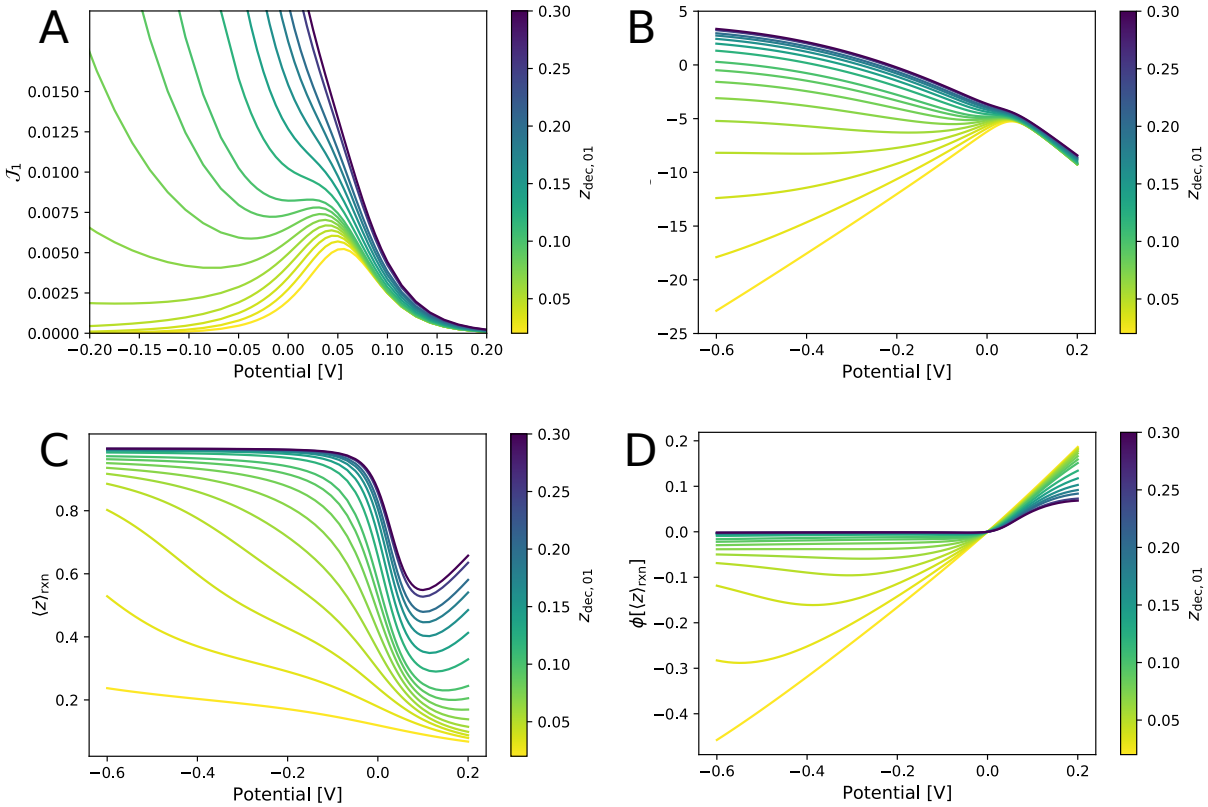

Figure 2.5: Results from model mapped to peroxodisulfate reduction. (A) Current-voltage curves computed for a family of models with different $z_{\mathrm{dec},01}$ values. (B) Same data as in top left, but the current is plotted on a logarithmic scale, enabling the simple identification of regions with positive and negative Tafel slopes. (C) Traces of the most likely site for electron transfer, determined from the mean value of $\Delta(x, z)$, defined in Eq. (2.7) as a function of the applied potential, for various values of $z_{\mathrm{dec},01}$. (D) Traces of the electrostatic potential at the most likely site for electron transfer, a value that plays an operative role in the Frumkin correction in Eq. (2.15).

Non-monotonic current-voltage behavior occurs when $\phi\left(\langle z \rangle_{\text{rxn}}\right)$ goes through a minimum, demarcating a switch between an increasing and decreasing Frumkin correction.

Implications

Results from the SME model suggest that the striking "S"-shaped behavior observed in the peroxodisulfate electroreduction experiments is best contextualized on a continuum parameterized by $z_{\text{dec},01}$, a dimensionless quantity relating the length scales for electronic tunneling and electrostatic screening. When the tunneling length scale is much larger than the screening length scale, the Frumkin correction is negligible, consistent with experimental results for reactions involving electron tunneling through the entire EDL[10,63]. When the tunneling length scale is much smaller than the screening length scale, electrostatic repulsion dominates and shuts off ET, since the reactant cannot approach close enough to couple to the band orbitals of the electrode. When the two scales are delicately balanced, electrostatic repulsion effects initially reduce the current, until the potential driving force is large enough to drive ET entirely at the EDL boundary. The microscopic insight provided by the SME model is consistent with modern work on peroxodisulfate reduction, which has argued that the current increase at highly cathodic potentials is due to broadening of the "reaction zone" over which ET may occur[52]. In fact, prior studies have speculated that the most likely transition state position for peroxodisulfate reduction can deviate from the OHP position as a function of applied potential[10,63–65]. Our model lends rigorous theoretical support toward this hypothesis.

Admittedly, the model developed here omits many pieces of physics that are known to operate on the length and time scales associated with the EDL. Certain physical effects are genuinely outside the scope of our model. Reactions that proceed through specifically adsorbed intermediates, or result in intercalation of a reactant species into the electrode generally do not proceed through electron tunneling, and hence are poorly described by our outer-sphere formalism. When such physics is dominant, numerous other models[35,66–68] are more appropriate for interpreting experimental results. Other effects can be naturally incorporated into our formalism, given a sufficient avenue (e.g. interface-sensitive experiments or high-level quantum mechanical calculations) towards accurate parameterization. For example, ion approach toward an interface often requires shedding its solvation shell(s), which can carry a heavy free energy penalty.[68–70] On the other hand, image-charge effects at conducting interfaces are known to stabilize ionic species at an electrode surface[23,71], and also renormalize the characteristic price for fluctuations along the Marcus coordinate[71,72]. Both of these effects are highly sensitive to the chemical details of the system, yet can be included by appropriately parameterized modifications to Eq. (2.1). While we choose to isolate and intuitively understand the more universal competition between electrostatic driving and electronic coupling in this work, the aforementioned modifications are fertile ground for future work.

2.5 References

[1] AN Frumkin and NV Nikolajeva. On the electroreduction of anions. *The Journal of Chemical Physics*, 26(6):1552–1553, 1957.

[2] AN Frumkin, NV Nikolaeva-Fedorovich, NP Berezina, and Kh E Keis. The electroreduction of the s2o82- anion. *Journal of Electroanalytical Chemistry and Interfacial Electrochemistry*, 58(1):189–201, 1975.

[3] John O'M Bockris and Amulya KN Reddy. *Modern electrochemistry 2B: electrodics in chemistry, engineering, biology and environmental science*, volume 2. Springer Science & Business Media, 2000.

[4] Leanne D. Chen, Makoto Urushihara, Karen Chan, and Jens K. Nørskov. Electric Field Effects in Electrochemical CO2 Reduction. *ACS Catalysis*, 6(10):7133–7139, oct 2016. ISSN 2155-5435. doi: 10.1021/acscatal.6b02299. URL `http://pubs.acs.org/doi/10.1021/acscatal.6b02299`.

[5] Rudolph A Marcus. On the theory of oxidation-reduction reactions involving electron transfer. i. *The Journal of Chemical Physics*, 24(5):966–978, 1956.

[6] Rudolph A Marcus. Theory of oxidation-reduction reactions involving electron transfer. 4. a statistical-mechanical basis for treating contributions from solvent, ligands, and inert salt. *Discussions of the Faraday Society*, (29):21–31, 1960.

[7] Rudolph A Marcus. Chemical and electrochemical electron-transfer theory. *Annual review of physical chemistry*, 15(1):155–196, 1964.

[8] Allen J Bard, Larry R Faulkner, Johna Leddy, and Cynthia G Zoski. *Electrochemical methods: fundamentals and applications*, volume 2. Wiley New York, 1980.

[9] C. E. D. Chidsey. Free Energy and Temperature Dependence of Electron Transfer at the Metal-Electrolyte Interface. *Science*, 251(4996):919–922, 1991. ISSN 0036-8075. doi: 10.1126/science.251.4996.919. URL `http://www.sciencemag.org/cgi/doi/10.1126/science.251.4996.919`.

[10] David J. Gavaghan and Stephen W. Feldberg. Extended electron transfer and the frumkin correction. *Journal of Electroanalytical Chemistry*, 491(1):103 – 110, 2000. ISSN 1572-6657. doi: https://doi.org/10.1016/S0022-0728(00)00210-2. URL `http://www.sciencedirect.com/science/article/pii/S0022072800002102`.

[11] Mustafa Sabri Kilic, Martin Z. Bazant, and Armand Ajdari. Steric effects in the dynamics of electrolytes at large applied voltages. II. Modified Poisson-Nernst-Planck equations. *Physical Review E*, 75(2):021503, feb 2007. ISSN 1539-3755. doi: 10.1103/PhysRevE.75.021503. URL `https://link.aps.org/doi/10.1103/PhysRevE.75.021503`.

[12] Mustafa Sabri Kilic, Martin Z. Bazant, and Armand Ajdari. Steric effects in the dynamics of electrolytes at large applied voltages. I. Double-layer charging. *Physical Review E*, 75(2):021502, feb 2007. ISSN 1539-3755. doi: 10.1103/PhysRevE.75.021502. URL https://link.aps.org/doi/10.1103/PhysRevE.75.021502.

[13] Martin Z. Bazant, Kevin T. Chu, and B. J. Bayly. Current-Voltage Relations for Electrochemical Thin Films. *SIAM Journal on Applied Mathematics*, 65(5):1463–1484, jan 2005. ISSN 0036-1399. doi: 10.1137/040609938. URL http://epubs.siam.org/doi/10.1137/040609938.

[14] Jens K. Nørskov, Frank Abild-Pedersen, Felix Studt, and Thomas Bligaard. Density functional theory in surface chemistry and catalysis. *Proceedings of the National Academy of Sciences*, 108(3):937–943, 2011. ISSN 0027-8424. doi: 10.1073/pnas.1006652108. URL https://www.pnas.org/content/108/3/937.

[15] Zhi Wei Seh, Jakob Kibsgaard, Colin F. Dickens, Ib Chorkendorff, Jens K. Nørskov, and Thomas F. Jaramillo. Combining theory and experiment in electrocatalysis: Insights into materials design. *Science*, 355(6321), 2017. ISSN 0036-8075. doi: 10.1126/science.aad4998. URL https://science.sciencemag.org/content/355/6321/eaad4998.

[16] David Chandler. Electron transfer in water and other polar environments, how it happens. In *Classical and Quantum Dynamics in Condensed Phase Simulations*, pages 25–49. WORLD SCIENTIFIC, jun 2010. ISBN 978-981-02-3498-0. doi: 10.1142/9789812839664_0002. URL http://www.worldscientific.com/doi/abs/10.1142/9789812839664{_}0002.

[17] Wenjie Dou, Abraham Nitzan, and Joseph E. Subotnik. Surface hopping with a manifold of electronic states. II. Application to the many-body Anderson-Holstein model. *Journal of Chemical Physics*, 142(8), 2015. ISSN 00219606. doi: 10.1063/1.4908034.

[18] Wenjie Dou, Abraham Nitzan, and Joseph E. Subotnik. Surface hopping with a manifold of electronic states. III. Transients, broadening, and the Marcus picture. *The Journal of Chemical Physics*, 142(23):234106, 2015. ISSN 0021-9606. doi: 10.1063/1.4922513. URL http://aip.scitation.org/doi/10.1063/1.4922513.

[19] R. A. Marcus. Exchange reactions and electron transfer reactions including isotopic exchange. theory of oxidation-reduction reactions involving electron transfer. part 4.—a statistical-mechanical basis for treating contributions from solvent, ligands, and inert salt. *Discuss. Faraday Soc.*, 29:21–31, 1960. doi: 10.1039/DF9602900021. URL http://dx.doi.org/10.1039/DF9602900021.

[20] Arieh Warshel. Dynamics of reactions in polar solvents. semiclassical trajectory studies of electron-transfer and proton-transfer reactions. *The Journal of Physical Chemistry*, 86(12):2218–2224, 1982.

[21] Jenn Kang Hwang and Arieh Warshel. Microscopic examination of free-energy relationships for electron transfer in polar solvents. *Journal of the American Chemical Society*, 109(3):715–720, 1987.

[22] J Blumberger and M Sprik. Redox free energies from vertical energy gaps: Ab initio molecular dynamics implementation. In *Computer Simulations in Condensed Matter Systems: From Materials to Chemical Biology Volume 2*, pages 481–506. Springer, 2006.

[23] Adam P. Willard, Stewart K. Reed, Paul A. Madden, and David Chandler. Water at an electrochemical interface—a simulation study. *Faraday Discuss.*, 141:423–441, 2009. doi: 10.1039/B805544K. URL http://dx.doi.org/10.1039/B805544K.

[24] Alec J. Coffman, Aparna Karippara Harshan, Sharon Hammes-Schiffer, and Joseph E. Subotnik. Modeling electron transfer in diffusive multidimensional electrochemical systems. *The Journal of Physical Chemistry C*, 123(21):13304–13317, 2019. doi: 10.1021/acs.jpcc.9b02068. URL https://doi.org/10.1021/acs.jpcc.9b02068.

[25] David Leonard Chapman. Li. a contribution to the theory of electrocapillarity. *The London, Edinburgh, and Dublin Philosophical Magazine and Journal of Science*, 25(148): 475–481, 1913.

[26] Zbigniew Stojek. *The Electrical Double Layer and Its Structure*, pages 3–9. Springer Berlin Heidelberg, Berlin, Heidelberg, 2010. ISBN 978-3-642-02915-8. doi: 10.1007/978-3-642-02915-8_1. URL https://doi.org/10.1007/978-3-642-02915-8_1.

[27] Abraham Nitzan. *Chemical Dynamics in Condensed Phases: Relaxation, Transfer and Reactions in Condensed Molecular Systems*. Oxford university press, 2006.

[28] N. Tankovsky and E. Syrakov. A modified einstein–nernst relation between mobility and diffusion of charges to evaluate the non-equilibrium, transient processes of ions in electrolytes. *Ionics*, 15(5):589, Dec 2008. ISSN 1862-0760. doi: 10.1007/s11581-008-0305-1. URL https://doi.org/10.1007/s11581-008-0305-1.

[29] John D. Morgan and Peter G. Wolynes. Adiabaticity of electron transfer at an electrode. *The Journal of Physical Chemistry*, 91(4):874–883, 1987. doi: 10.1021/j100288a023. URL https://doi.org/10.1021/j100288a023.

[30] Nalini Chakravarti and KL Sebastian. Electrochemical electron transfer: a diffusion-reaction equation approach. *Chemical Physics Letters*, 193(6):456–460, 1992.

[31] Peter J Mahon, Jan C Myland, and Keith B Oldham. A fresh approach to voltammetric modelling. *Journal of Electroanalytical Chemistry*, 537(1-2):1–5, 2002.

[32] Wenjun Ouyang, Jeffery G Saven, and Joseph E Subotnik. A surface hopping view of electrochemistry: Non-equilibrium electronic transport through an ionic solution with a classical master equation. *The Journal of Physical Chemistry C*, 119(36):20833–20844, 2015.

[33] Wenjun Ouyang and Joseph E Subotnik. The dynamics of charge transfer with and without a barrier: A very simplified model of cyclic voltammetry. *The Journal of Chemical Physics*, 146(17):174103, 2017.

[34] Joshua Jortner. Temperature dependent activation energy for electron transfer between biological molecules. *The Journal of Chemical Physics*, 64(12):4860–4867, 1976.

[35] Wolfgang Schmickler. A unified model for electrochemical electron and ion transfer reactions. *Chemical Physics Letters*, 237(1-2):152–160, 1995.

[36] AA Kornyshev, AM Kuznetsov, and J Ulstrup. Effect of overpotential on the electronic tunnel factor in diabatic electrochemical processes. *The Journal of Physical Chemistry*, 98(14):3832–3837, 1994.

[37] Norman Sutin. Theory of electron transfer reactions: insights and hindsights. *Progress in Inorganic Chemistry: An Appreciation of Henry Taube*, pages 441–498, 1983.

[38] JJ Hopfield. Electron transfer between biological molecules by thermally activated tunneling. *Proceedings of the National Academy of Sciences*, 71(9):3640–3644, 1974.

[39] Fu-Ren F Fan, Jiping Yang, Lintao Cai, David W Price Jr, Shawn M Dirk, Dmitry V Kosynkin, Yuxing Yao, Adam M Rawlett, James M Tour, and Allen J Bard. Charge transport through self-assembled monolayers of compounds of interest in molecular electronics. *Journal of the American Chemical Society*, 124(19):5550–5560, 2002.

[40] R Erik Holmlin, Rainer Haag, Michael L Chabinyc, Rustem F Ismagilov, Adam E Cohen, Andreas Terfort, Maria Anita Rampi, and George M Whitesides. Electron transport through thin organic films in metal- insulator- metal junctions based on self-assembled monolayers. *Journal of the American Chemical Society*, 123(21):5075–5085, 2001.

[41] Marshall D Newton. Quantum chemical probes of electron-transfer kinetics: the nature of donor-acceptor interactions. *Chemical Reviews*, 91(5):767–792, 1991.

[42] J Seitz-Beywl, M Poxleitner, MM Probst, and K Heinzinger. On the interaction of ions with a platinum metal surface. *International Journal of Quantum Chemistry*, 42(5): 1141–1147, 1992.

[43] Joseph L Katz, Stuart A Rice, Sang-il Choi, and Joshua Jortner. On the excess electron and hole band structures and carrier mobility in naphthalene, anthracene, and several polyphenyls. *The Journal of Chemical Physics*, 39(7):1683–1697, 1963.

[44] Noémie Elgrishi, Kelley J. Rountree, Brian D. McCarthy, Eric S. Rountree, Thomas T. Eisenhart, and Jillian L. Dempsey. A practical beginner's guide to cyclic voltammetry. *Journal of Chemical Education*, 95(2):197–206, 2018. doi: 10.1021/acs.jchemed.7b00361. URL `https://doi.org/10.1021/acs.jchemed.7b00361`.

[45] W.M. Deen. *Analysis of Transport Phenomena*. Topics in chemical engineering. Oxford University Press, 2012. ISBN 9780199740284. URL `https://books.google.com/books?id=60YsAwEACAAJ`.

[46] Alejandro A. Franco. Multiscale modelling and numerical simulation of rechargeable lithium ion batteries: concepts, methods and challenges. *RSC Advances*, 3(32):13027, jul 2013. ISSN 2046-2069. doi: 10.1039/c3ra23502e. URL `http://xlink.rsc.org/?DOI=c3ra23502e`.

[47] AN Frumkin, OA Petry, and NV Nikolaeva-Fedorovich. On the determination of the value of the charge of the reacting particle and of the constant α from the dependence of the rate of electro-reduction on the potential and concentration of the solution. *Electrochimica Acta*, 8(4):177–192, 1963.

[48] Oleg A. Petrii, Renat R. Nazmutdinov, Michael D. Bronshtein, and Galina A. Tsirlina. Life of the tafel equation: Current understanding and prospects for the second century. *Electrochimica Acta*, 52(11):3493 – 3504, 2007. ISSN 0013-4686. doi: https://doi.org/10.1016/j.electacta.2006.10.014. URL `http://www.sciencedirect.com/science/article/pii/S0013468606011017`.

[49] GA Tsirlina, OA Petrii, RR Nazmutdinov, and DV Glukhov. Frumkin correction: microscopic view. *Russian Journal of Electrochemistry*, 38(2):132–140, 2002.

[50] Pavel A Zagrebin, Galina A Tsirlina, Renat R Nazmutdinov, Oleg A Petrii, and Michael Probst. Corrected marcus plots. *Journal of Solid State Electrochemistry*, 10(3):157–167, 2006.

[51] Maria Yu. Rusanova, Galina A. Tsirlina, Renat R. Nazmutdinov, and W. Ronald Fawcett. Role of charge distribution in the reactant and product in double layer effects: Construction of corrected tafel plots. *The Journal of Physical Chemistry A*, 109(7):1348–1356, 2005. doi: 10.1021/jp046917s. URL `https://doi.org/10.1021/jp046917s`. PMID: 16833451.

[52] Renat R Nazmutdinov, Dmitrii V Glukhov, Oleg A Petrii, Galina A Tsirlina, and Galina N Botukhova. Contemporary understanding of the peroxodisulfate reduction at a mercury electrode. *Journal of Electroanalytical Chemistry*, 552:261–278, 2003.

[53] Michael J Weaver and Thomas L Satterberg. The position of the reaction site and the relative reactivities of simple outer-and inner-sphere electrode reactions. the reduction of some chromium (iii) amine complexes at mercury electrodes. *The Journal of Physical Chemistry*, 81(18):1772–1783, 1977.

[54] R Parsons. The transfer coefficient in electrode reactions. *Croatica Chemica Acta*, 42 (2):281–291, 1970.

[55] WR Fawcett. The location of the reaction site and discreteness-of-charge effects in electrode kinetics. *Canadian Journal of Chemistry*, 59(13):1844–1853, 1981.

[56] Joã Carlos R Reis. Thermodynamic analysis of the symmetry factor and the transfer coefficient in electrode kinetics. *Journal of The Electrochemical Society*, 144(7):2404–2409, 1997.

[57] W Ronald Fawcett, Grace J Chavis, and Magdalena Hromadová. Charge distribution effects in polyatomic reactants involved in simple electron transfer reactions. *Electrochimica Acta*, 53(23):6787–6792, 2008.

[58] Zachary J. Schiffer, Nikifar Lazouski, Nathan Corbin, and Karthish Manthiram. Nature of the first electron transfer in electrochemical ammonia activation in a nonaqueous medium. *The Journal of Physical Chemistry C*, 123(15):9713–9720, 2019. doi: 10.1021/acs.jpcc.9b00669. URL https://doi.org/10.1021/acs.jpcc.9b00669.

[59] WR Fawcett and MD Mackey. The electroreduction of peroxydisulphate anion in formamide. *Journal of Electroanalytical Chemistry and Interfacial Electrochemistry*, 27(2): 219–231, 1970.

[60] W Smit and JG Hoogland. The mechanism of the anodic formation of the peroxodisulphate ion on platinum—iv. influence of alkali-metal cations. *Electrochimica Acta*, 16(7): 981–993, 1971.

[61] E Lust, R Truu, and K Lust. Electroreduction of peroxodisulfate anion at bi (111) single-crystal plane electrode. *Russian Journal of Electrochemistry*, 36(11):1195–1202, 2000.

[62] RR Nazmutdinov, DV Glukhov, GA Tsirlina, and OA Petrii. Molecular description of the persulfate ion reduction on a mercury electrode. *Russian journal of electrochemistry*, 38(7):720–731, 2002.

[63] Edmund J.F. Dickinson and Richard G. Compton. Influence of the diffuse double layer on steady-state voltammetry. *Journal of Electroanalytical Chemistry*, 661(1):198 – 212, 2011. ISSN 1572-6657. doi: https://doi.org/10.1016/j.jelechem.2011.08.002. URL http://www.sciencedirect.com/science/article/pii/S1572665711003973.

[64] WR Fawcett. The effect of ionic size in the double layer on the kinetics of electrode reactions. *Journal of Electroanalytical Chemistry and Interfacial Electrochemistry*, 22 (1):19–28, 1969.

[65] Chuhong Lin and Richard G. Compton. Understanding mass transport influenced electrocatalysis at the nanoscale via numerical simulation. *Current Opinion in Electrochemistry*, 2018. ISSN 2451-9103. doi: https://doi.org/10.1016/j.coelec.2018.08.001. URL http://www.sciencedirect.com/science/article/pii/S2451910318301261.

[66] W. Schmickler and J. Mohr. The rate of electrochemical electron-transfer reactions. *The Journal of Chemical Physics*, 117(6):2867–2872, 2002. doi: 10.1063/1.1490925. URL https://doi.org/10.1063/1.1490925.

[67] Wolfgang Schmickler. A theory of adiabatic electron-transfer reactions. *Journal of Electroanalytical Chemistry and Interfacial Electrochemistry*, 204(1):31 – 43, 1986. ISSN 0022-0728. doi: https://doi.org/10.1016/0022-0728(86)80505-8. URL http://www.sciencedirect.com/science/article/pii/0022072886805058.

[68] Wolfgang Schmickler and Elizabeth Santos. *Interfacial electrochemistry*. Springer Science & Business Media, 2010.

[69] Kang Xu, Yiufai Lam, Sheng S. Zhang, T. Richard Jow, and Timothy B. Curtis. Solvation sheath of li+ in nonaqueous electrolytes and its implication of graphite/electrolyte interface chemistry. *The Journal of Physical Chemistry C*, 111(20):7411–7421, 2007. doi: 10.1021/jp068691u. URL https://doi.org/10.1021/jp068691u.

[70] W. Schmickler. Electron and ion transfer reactions on metal electrodes. *Electrochimica Acta*, 41(14):2329 – 2338, 1996. ISSN 0013-4686. doi: https://doi.org/10.1016/0013-4686(96)00063-1. URL http://www.sciencedirect.com/science/article/pii/0013468696000631. Double Layer Modeling.

[71] Michael A. Pounds, Mathieu Salanne, and Paul A. Madden. Molecular aspects of the eu3+/eu2+ redox reaction at the interface between a molten salt and a metallic electrode. *Molecular Physics*, 113(17-18):2451–2462, 2015. doi: 10.1080/00268976.2015.1046526. URL https://doi.org/10.1080/00268976.2015.1046526.

[72] Soumya Ghosh, Samantha Horvath, Alexander V Soudackov, and Sharon Hammes-Schiffer. Electrochemical solvent reorganization energies in the framework of the polarizable continuum model. *Journal of chemical theory and computation*, 10(5):2091–2102, 2014.

Chapter 3

Understanding Attenuated Marcus Reorganization Energies in the Electrochemical Double Layer

3.1 Introduction

Electrodes facilitate outer-sphere electrochemical reactions by providing a tunable source of thermodynamic bias and by shaping the microscopic electric field fluctuations that mediate electron transfer (ET) kinetics.[1] The electrode's contribution to these fluctuations quite literally reflects that of the adjacent electrolyte solution, due to image charge effects. In this manuscript, we investigate the general role of image charges in modifying the electrostatic potential distributions experienced by species in the vicinity of an electrode-electrolyte interface. We use molecular dynamics (MD) simulations with constant potential boundary conditions to demonstrate the simultaneous narrowing of Marcus parabola widths and lowering of reorganization energies as reactive species approach the electrode within the electrolyte screening length. We construct a Gaussian field theory to show that these simultaneous effects are consequences of the constant potential boundary imposed by the electrode, and that they can be intuitively framed in terms of image charge effects. These results thus provide a physical basis for understanding the position dependent Marcus rates that have been previously observed in simulation studies,[1–3] and a theoretical prescription for including these general effects in the parameters of microkinetic models.

When an interfacial electrochemical reaction involves the tunneling of an electron between the electrode and a weakly coupled reactant, its rate can depend on the thermal fluctuations of the electrolyte solution. Hush and Chidsey formalized this dependence by extending Marcus' theory for homogeneous ET[4–6] to an interfacial setting, which includes the contribution of the continuum electronic states of the electrodes.[7–11] Like Marcus theory, Marcus-Hush-Chidsey theory formulates the rate of outer-sphere electron transfer as a function of the solvent reorganization energy, λ, which represents the free energy penalty of

[1]The material in this chapter is reproduced in part with permission from: Limaye, A. M.; Ding, W.; Willard, A. P., Understanding attenuated solvent reorganization energies near electrode interfaces. *J. Chem. Phys.* **2020**, 152, 114706. https://doi.org/10.1063/5.0003428.

a "vertical" ET event that preserves the nuclear configuration of the reactive species and its solvent environment. Larger values of λ are typically associated with larger activation barriers and thus lower ET rates.

Physical and electrostatic constraints imposed by an electrode can cause λ to vary as a function of redox species position relative to the electrode surface. This position dependence can be studied by analyzing the results of all-atom MD simulations of model electrode-electrolyte systems. For instance, λ can be computed by sampling the equilibrium statistics of the vertical energy gap coordinate, ΔE, for redox species that reside at specific distances from the electrode surface.[12–17] The distributions that govern these statistics are related to free energy surfaces of the oxidized or reduced diabatic states, and take the form of Marcus parabolas when the statistics of ΔE are Gaussian.

For a given redox reaction, the value of λ is primarily determined by fluctuations of the surrounding molecular environment, however, it can be significantly modified by the polarization response of a nearby electrode. For a perfectly conducting planar electrode, this polarization response can be conveniently represented with image charges, whereby every charge in the electrolyte is reflected with opposite sign across a mirror plane along the electrode surface. One implication of the image charge picture is that the electrostatic fluctuations that originate from the electrode inherit their statistics from the electrolyte solution. However, the image plane imposes a constraint on these fluctuations, *i.e.*, that they are equal and opposite, resulting in general and predictable physical consequences near the electrode.

Previous simulation and experimental studies of simple redox ions in the vicinity of an electrolyte-electrolyte interface have found λ to decrease monotonically as ions approach the electrode surface.[2,3,13,18] This decrease has been attributed to the influence of image charge interactions,[13] however, the specific physical details of this influence have yet to be fully formalized. With simulation data alone it is challenging to disentangle the interplay between the direct interaction of a redox ion with its own image charge and the indirect interactions of a redox ion with the image charge of other electrolyte species. Here, we combine MD simulation with theoretical modeling to generate new physical insight into the role of electrode polarization in mediating interfacial ET rates.

In the following section, we present the results of MD simulations in which we have computed the dependence of λ on the distance of the redox species from the electrode. We decompose this dependence into separate position dependent components and discuss their physical implications. Then, in Sec. 3.3, we present a statistical field theory that captures the effect of the electrode in constraining the potential fluctuations at the electrochemical interface.

3.2 Electrode-Electrolyte Molecular Dynamics Simulations

3.2.1 Background

Marcus theory provides an intuitive theoretical framework for describing the influence of thermal environmental fluctuations on outer-sphere interfacial ET rates. It describes ET

as a transition between two weakly coupled diabatic states: one in which a target redox species is in an oxidized state, and the other in which it is in a reduced state. The reaction coordinate for this redox transition is typically chosen to be the vertical energy gap,

$$\Delta E(\{\mathbf{r}^N\}) = E_{\text{red}}(\{\mathbf{r}^N\}) - E_{\text{ox}}(\{\mathbf{r}^N\}), \tag{3.1}$$

where $\{\mathbf{r}^N\}$ denotes the configuration of all nuclei in the system, and $E_{\text{red}}(\{\mathbf{r}^N\})$ and $E_{\text{ox}}(\{\mathbf{r}^N\})$ are the potential energies of the reduced and oxidized states, respectively (in identical nuclear configurations). Thermal fluctuations lead to variations in ΔE, with thermodynamic consequences that can be quantified in terms of free energy surfaces – often referred to as Marcus parabolas – as illustrated in Fig. 3.1A.

If the electronic coupling, H_{redox}, between the states is small, then the rate of ET is given by the standard Marcus formula,

$$k_{\text{ET}} = \frac{2\pi}{\hbar}|H_{\text{redox}}|^2 \frac{1}{\sqrt{4\pi k_{\text{B}} T \lambda}} e^{-\beta \Delta A^{\ddagger}}, \tag{3.2}$$

where $k_{\text{B}}T$ is the Boltzmann constant multiplied by temperature, $\beta = (k_{\text{B}}T)^{-1}$, and $\hbar$ is the reduced Planck constant. If the statistics of ΔE are Gaussian, then $\Delta A^{\ddagger}$, the activation energy, is given by,

$$\Delta A^{\ddagger} = \frac{(\lambda + \Delta A^0)^2}{4\lambda}, \tag{3.3}$$

where ΔA^0 is the reaction free energy (see Fig. 3.1A). In this expression, the reorganization energy, λ, is related to the width of the Marcus parabolas through the linear response relationship,

$$\lambda = \frac{\beta \sigma^2[\Delta E_{\text{redox}}]}{2} = \frac{\langle \Delta E_{\text{red}} \rangle - \langle \Delta E_{\text{ox}} \rangle}{2}, \tag{3.4}$$

where $\sigma^2[\Delta E_{\text{redox}}]$ denotes the variance of the equilibrium probability distribution for ΔE, and $\langle \Delta E_{\text{red}} \rangle$ and $\langle \Delta E_{\text{ox}} \rangle$ are the average values of ΔE computed from the reduced or oxidized states, respectively. The second equality reflects a constraint that arises from assuming linear response, implying that ΔE obeys Gaussian statistics, which also leads to the property $\sigma^2[\Delta E_{\text{redox}}] = \sigma^2[\Delta E_{\text{red}}] = \sigma^2[\Delta E_{\text{ox}}]$. Gaussian statistics are expected when ΔE arises from numerous long-range charge-charge and dipole-charge interactions, typical of outer-sphere ET in an electrolyte medium.[19]

Equation 3.2 can be generalized to the case of interfacial ET (*i.e.*, where an electrode acts as an electron donor/acceptor) by integration over the Fermi distribution of electronic states within the electrode. This integration yields the Marcus-Hush-Chidsey (MHC) expression,[20–23]

$$k_{\text{ET}}^{(\text{MHC})} = \frac{4\pi^2}{\hbar}|H_{\text{redox}}|^2 \frac{1}{\sqrt{4\pi k_{\text{B}} T \lambda}} \int_{-\infty}^{\infty} \mathrm{d}\epsilon \, \frac{g(\epsilon)}{1 + e^{\beta \epsilon}} \cdot \exp\left[-\beta \Delta A^{\ddagger}(\epsilon, \mu_{\text{el}})\right], \tag{3.5}$$

where ϵ is the energy of the transferred electron relative to the Fermi level of the electrode, $g(\epsilon)$ is the density of electronic states (DOS) in the electrode, and $\Delta A^{\ddagger}(\epsilon, \mu_{\text{el}})$ denotes the activation energy, now expressed as a function of the the electronic energy and applied potential as,

$$\Delta A^{\ddagger}(\epsilon, \mu_{\text{el}}) = \frac{[\lambda - (\epsilon + \Delta q \cdot \mu_{\text{el}})]^2}{4\lambda}, \tag{3.6}$$

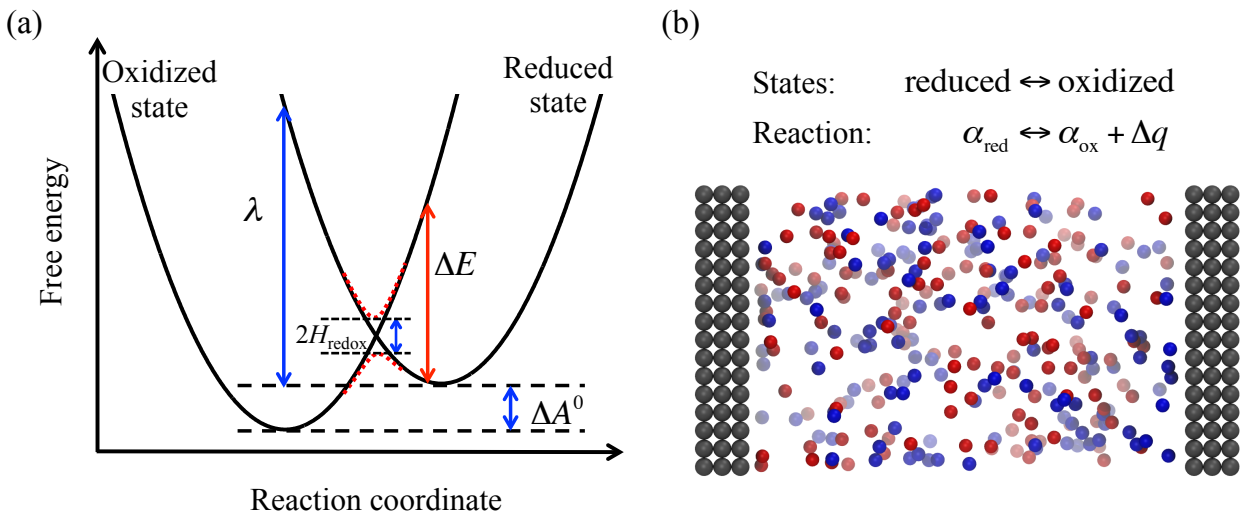

Figure 3.1: (a) Marcus curves for diabatic energy surfaces (black solid curves) of a redox reaction, with states red and ox representing the different location of the transferred charge. The red dotted lines trace out the avoided crossing in the adiabatic representation, with H_{redox} being the electronic coupling between the two diabatic states. (b) For a redox reaction in an electrochemical cell, a double-electrode configuration is employed, and the charge Δq is transferred between the redox species (blue and red spheres) and the polarizable electrodes (gray spheres).

where μ_{el} denotes the applied electrochemical potential, and Δq is the amount of transferred charge.

3.2.2 Computing reorganization energies from constant potential MD simulation

As Eqs. 3.2 and 3.5 reveal, the quantity λ plays a central role in setting the ET rate for weakly coupled condensed phase ET reactions. In the context of MD simulation, λ can be determined based on the equilibrium statistics of ΔE as sampled from the oxidized and reduced states. These statistics are quantified by the probability distributions $P_{\text{ox}}(\Delta E)$ and $P_{\text{red}}(\Delta E)$, respectively, which relate to the free energy functions, $A_{\text{ox}}(\Delta E)$ and $A_{\text{red}}(\Delta E)$, through the relationship,

$$P_{\alpha}(\Delta E) \propto \exp\left[-\beta A_{\alpha}(\Delta E)\right]. \tag{3.7}$$

For simulations of interfacial redox reactions, care must be taken when computing $P_{\text{ox}}(\Delta E)$ and $P_{\text{red}}(\Delta E)$, for example, to account for the effects of the electrode potential and to avoid artifacts from interactions with charges in neighboring periodic replicas. In this subsection, we formulate an expression for computing λ from simulations of a generic two-electrode system, such as illustrated in Fig. 3.1B. This expression properly accounts for the fact that the electrode, assumed to be an ideal conductor, can re-polarize immediately upon ET, whereas the surrounding solvent environment cannot.

To begin, we consider an electrolyte solution containing a single redox-active particle confined between two planar electrodes that are each held at fixed electrochemical potential, and are assumed to be ideally conducting. The system is periodically replicated in the two dimensions parallel to the electrode surface. We assume that the electrodes are in contact with an infinite reservoir of electrons with an electrochemical potential, μ_{el}, electrostatically neutral (*i.e.*, held at the potential of zero charge) and can polarize infinitely quickly in response to changes in the charge distribution of the electrolyte. We describe the electrode boundaries with the method of image charges by explicitly representing the reflections of all electrolyte particles in the electrode domain as oppositely signed point charges. In systems with parallel planar electrodes, the electrolyte system and its image charges can be represented with a series of infinite periodic images in the direction perpendicular to the electrodes (*i.e.*, the z-axis), as illustrated in Fig. 3.2.[24–27]

The primary contribution to the vertical energy gap, ΔE, for a redox reaction at a fixed nuclear configuration is the change of charge on the redox species and its associated influence on electrode polarization (*e.g.*, image charge interactions). Usually, ΔE is calculated by evaluating the difference in energy of the system before and after changing the charge states of the involved particles without modifying the nuclei configuration.[12] Previous studies used a particle switching scheme,[2,13,28] whereby an ion in a system configuration sampled from its equilibrium distribution is replaced by its redox counterpart, and the constant potential boundary condition is re-established without updating the nuclear configuration. The energy of the new system is evaluated, and the difference from that of the original system is taken to be ΔE.

When computing ΔE for a periodically replicated system, one must take care not to introduce artifacts due to electrostatic interactions across periodic replicas. In interfacial systems, electrode polarization can give rise to such artifacts. In Fig. 3.2, we present a sketch of the simulation system, its image region, and their tiled replicas under periodic boundary conditions (PBCs),[24,27] as well as how the system changes in the oxidation reaction $\alpha_{\text{red}} \rightarrow \alpha_{\text{ox}} + \Delta q$. In the reduced diabatic state (top part), the electrolyte (solid black boundaries) contains one reduced ion of interest (filled red circle) and few other electrolyte particles (filled black circles). Based on method of image charges, the conducting interface creates an image region (solid red boundaries) containing reflections of the particles in the electrolyte with equal magnitude but oppositely signed point charges (open circles). In accordance with prior work, the constant potential condition is implemented using standard PBC replicates of the electrolyte *and* image domain in the z direction (dashed black and red boundaries).[24] This generates an infinite series of the reduced ion and its image charges in the z direction.[26] In addition, PBCs are also applied in the x and y directions to simulate the effectively infinite electrode surface in the xy plane, creating tiled replicas (dashed blue boundaries) of the series of primary and image boxes.

When the redox ion in the electrolyte is oxidized (filled blue triangle in bottom part of Fig. 3.2), its image charges change as well (open blue triangles), since the electrode repolarizes instantly. Because the periodicity in the z direction is due to the double-interface image reflection, all the corresponding charges in this direction must also change accordingly. However, we do not wish to modify the charge state of the ions in the x and y replicas, i.e., the red circles in the dashed blue boxes must remain the same. This is to ensure that only one oxidation reaction occurs, whereas changing the charges in the x and y replicas

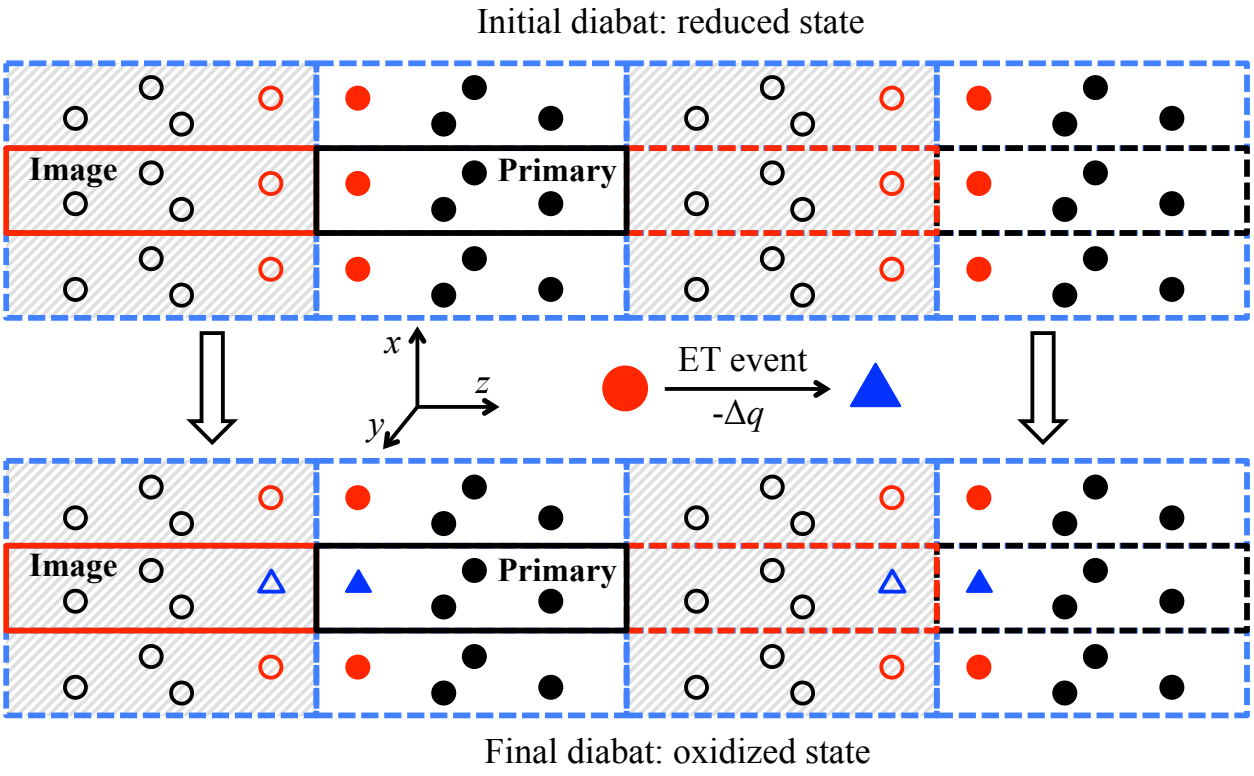

Figure 3.2: The change in charge states on relevant ions and images during an oxidation reaction: $\alpha_{\text{red}} \rightarrow \alpha_{\text{ox}} + \Delta q$. Primary box (solid black boundaries) includes the redox ion α (filled red circle for reduced state, filled blue triangle for oxidized state) and other electrolyte particles (filled black circles). Image box (solid red boundaries) contains the reflections of the particles from the primary box (open symbols). Replica boxes due to PBC are represented by dashed boundaries.

would imply that many oxidation reactions occur simultaneously, in a spuriously correlated fashion. Despite this fact, we do not expect significant error from this spurious correlation for simulations conducted in large primary boxes, because the electrostatic interactions between the switched ion and its x and y replicas are attenuated significantly over large distances by ionic and dielectric screening.

Based on this scheme, we obtain a new equation for ΔE (see Sec. 7.2 for a detailed derivation). As mentioned previously, only Coulombic interactions involving the redox ion need to be considered. By using the correct charges as illustrated in Fig. 3.2, the vertical energy gap of a particle α in the two states can be expressed as,

$$\Delta E_{\mathrm{red}}(\mathbf{r}^N) = \Delta q \left[\phi_{\mathrm{red}} + \frac{1}{2}\Delta q \cdot f(z, L)\right] - \mathrm{IE}_{\mathrm{red}} + \Delta q \cdot \mu_{\mathrm{el}}, \tag{3.8a}$$

$$\Delta E_{\mathrm{ox}}(\mathbf{r}^N) = \Delta q \left[\phi_{\mathrm{ox}} - \frac{1}{2}\Delta q \cdot f(z, L)\right] - \mathrm{EA}_{\mathrm{ox}} + \Delta q \cdot \mu_{\mathrm{el}}, \tag{3.8b}$$

where Δq is the amount of charge being transferred, μ_{el} is the applied electrochemical potential, $\mathrm{IE}_{\mathrm{red}}$ is the ionization energy of the reduced species, and $\mathrm{EA}_{\mathrm{ox}}$ is the electron affinity of the oxidized species. The Madelung potential, ϕ, is defined for the reduced species as,

$$\phi_{\mathrm{red}} = \sum_{j \neq \mathrm{red}} \frac{q_j}{|\mathbf{r}_j - \mathbf{r}_{\mathrm{red}}|}, \tag{3.9}$$

where the summation is taken over all other charges in the system (including image charges), q_j is the charge of particle j, and $|\mathbf{r}_j - \mathbf{r}_{\mathrm{red}}|$ is the distance between particle j and the reduced species. The correction function $f(z, L)$ is a deterministic function of the relative z-position of the redox species in the electrochemical cell that captures the double-image plane effect for electrodes separated by a distance L. The energy of this image effect is proportional to the Coulombic interaction energy between a point charge of Δq and two bare electrodes,[1,13] which, as shown by Cox and Geissler,[26] can be described by a conditionally-convergent infinite series of image charges. This charge series can be tamed by an alternating resummation (see Sec. 7.2) to glean a physically interpretable result, and to yield an exact expression for the correction function,

$$f(z, L) = \frac{1}{2L}\left[-\frac{1}{d_1 d_2} + 2\gamma + \psi(1 + d_1) + \psi(1 + d_2)\right] \tag{3.10}$$

where $d_1 = z/L$ and $d_2 = 1 - d_1$ are the non-dimensional distances from the redox particle to each of the two electrodes, $\psi(x) = \Gamma'(x)/\Gamma(x)$ is the digamma function, $\Gamma(x)$ is the Gamma function, and $\gamma = -\psi(1) \approx 0.577216$ is the Euler–Mascheroni constant.

By combining Eqs. 3.4 and 3.8, we find that the reorganization energy can be expressed as a function of the z position of the redox species:

$$\lambda = \frac{1}{2}\Delta q \left[\langle \phi_{\mathrm{red}} \rangle - \langle \phi_{\mathrm{ox}} \rangle + \Delta q \cdot f(z, L)\right], \tag{3.11}$$

where $\langle \phi_{\mathrm{red}} \rangle$ and $\langle \phi_{\mathrm{ox}} \rangle$ are the average values of the Madelung potential evaluated for the redox species at position z when it is in the reduced and oxidized states, respectively. Notably,

by exploiting the relationship between ΔE and ϕ for point charge systems (see Sec. 7.2), λ can also be described by the width of the Madelung potential distribution, as,

$$\lambda = \frac{\beta(\Delta q)^2}{2} \cdot \sigma^2[\phi_{\text{redox}}]. \tag{3.12}$$

This equation provides a prescription for computing the reorganization energy from the statistics of ϕ evaluated for the redox species. These statistics can be readily sampled from MD simulation data gathered at constant potential.

To evaluate the dependence of λ on the position relative to the electrode surface, we evaluate Eqns. 3.4 and 3.12 for a series of equilibrium simulations. Our simulations include an electrolyte solution in implicit solvent confined between two parallel constant potential electrodes. The results of the simulation are presented in the following subsection, and the simulation details are summarized below and fully described in Section 7.2.

3.2.3 Simulations results

The simulations are performed using the classical MD simulator LAMMPS,[29] with the Constant Potential package for simulating the electrolyte-electrode interactions.[1,30–32] A simulation box of size $80 \times 80 \times 100$ ($x \times y \times z$) is set up in the non-dimensional Lennard-Jones (LJ) style unit system as implemented in LAMMPS to maximize generality. Two parallel planar electrodes, each consisting of 3 layers of electrode atoms, are placed at $z = 10$ and $z = 90$, effectively creating a region of size $80 \times 80 \times 80$ in between. A group of positive and negative monovalent ions are confined in this region, and interact with the electrodes via both short-range LJ potential and electrostatic potential. The simulations provide equilibrium statistics of these ions for computing ΔE of redox reactions: the oxidization of negative ions and the reduction of positive ions. The results are discussed below.

Figure 3.3(a) contains a plot of $A(\Delta E)$, as computed from Eq. 3.7 for the reduced and oxidized species at different $z-$positions. Our results highlight that $A(\Delta E)$ is roughly parabolic for both the reduced and oxidized species, indicating that ΔE obeys Gaussian statistics. We find that the minimum and width of the parabolas depend on the z-position of the redox species. Specifically, $A_{\text{red}}(\Delta E)$ and $A_{\text{ox}}(\Delta E)$ are more closely spaced and narrower for redox species nearer to the electrode, as illustrated in Fig. 3.3B. The combined effect of these z-dependent changes in $A(\Delta E)$ is that the reorganization energy λ decreases as redox species approach the electrode. This result, plotted in Fig. 3.3C, is consistent with the finding of previous studies.[2,13,33]

Figure 3.3(b) presents the profile of such position dependence by displaying the means and variances of the two ΔE distributions for the two charge states, respectively. It is clear that $\langle \Delta E_{\text{red}} \rangle$ and $\langle \Delta E_{\text{ox}} \rangle$ are symmetric to each other around zero, as expected for the thermodynamically undriven oxidation and reduction reactions. In addition, the observations that $\sigma^2[\Delta E_{\text{red}}] = \sigma^2[\Delta E_{\text{ox}}]$ (red triangles overlaying blue dashed line) and that $\sigma^2 = k_B T(\langle \Delta E_{\text{red}} \rangle - \langle \Delta E_{\text{ox}} \rangle)$ (see Sec. 7.2) validate the linear response assumption that underlies the application of Marcus theory. More importantly, due to Eq. 3.12, the profile of $\sigma^2[\Delta E_{\text{red/ox}}]$ also represents the position-dependent profile of the reorganization energy λ, which exhibits maximum value near the cell center, and gradually reduces when approaching the electrode interfaces (see Fig. 3.3C, black line).

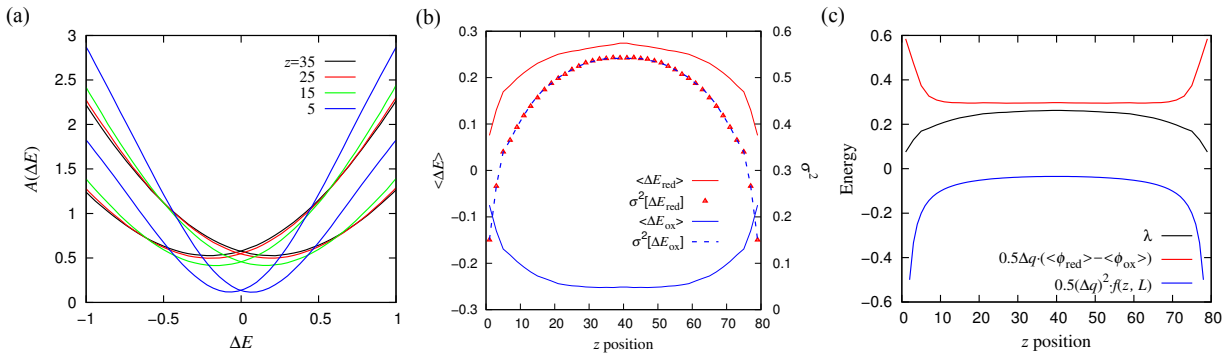

Figure 3.3: (a) Marcus parabolas for the reduced ($\langle \Delta E \rangle > 0$) and oxidized ($\langle \Delta E \rangle < 0$) states at different z values, where $z = 35$ is near the center of the cell, while $z = 5$ is near the electrode interface. (b) The position dependent profile of the mean and variance of ΔE. Note that $\sigma^2[\Delta E_{\text{red}}]$ (red triangles) overlays $\sigma^2[\Delta E_{\text{ox}}]$ (blue dashed line). (c) The position dependent profile of λ (black line), which can be decomposed into the term of $(\langle \phi_{\text{red}} \rangle - \langle \phi_{\text{ox}} \rangle)$ in Eq. 3.11 (red line) and the correction function $f(z, L)$ (blue line). Note: all quantities are in reduced non-dimensional Lennard-Jones system, which is unitless.

To evaluate the role of image charge interactions on $\lambda(z)$, we decompose it into its separate z-dependent contributions. Specifically, Fig. 3.3C depicts each term in Eq. 3.12 separately. We observe that the decrease in λ as redox species approach the electrode results from a balance between two competing effects. The contribution from local changes in electrostatic potential, $(1/2)\Delta q(\langle \phi_{\text{red}} \rangle - \langle \phi_{\text{ox}} \rangle)$ (red line), increases for species approaching the interface, while remaining the same for species at a distance more than about 5 length units away from either electrode. This effect, which contains the indirect influence of the image charges of other species, is localized to the interface. However, this increase is offset by a more significant decrease in the direct image charge term, $(1/2)(\Delta q)^2 f(z, L)$.

While the sign of $\langle \phi_{\text{red/ox}} \rangle$ is determined by the particle's environment and its own charge state, the function $f(z, L)$ is always negative with larger magnitude near the electrode interface (blue line in Fig. 3.3C). From Eq. 3.10, the position-dependence of $f(z, L)$ is determined by three functions of distance: $(d_1 d_2)^{-1}$, $\psi(1 + d_1)$, and $\psi(1 + d_2)$. Note that by definition, $0 \leq d_{1/2} \leq 1$ and $d_1 + d_2 = 1$. Hence, the value of two digamma functions only ranges from $\psi(1) \approx -0.577216$ to $\psi(2) \approx 0.422784$, and the sum of the two functions does not contribute significantly to $f(z, L)$. The general shape of $f(z, L)$ in fact is from the function of inverse distance from the interface ($1/d_1$ or $1/d_2$), and because of the double layer, it is symmetric around the center of the cell. Ultimately, the summation of the two quantities, $(1/2)\Delta q(\langle \phi_{\text{red}} \rangle - \langle \phi_{\text{ox}} \rangle)$ and $(1/2)(\Delta q)^2 \cdot f(z, L)$, results in the concave-down position-dependent profile of λ (black line).

3.3 A Statistical Field Theory Accounting for Constant-Potential Boundaries

The simulation results presented in Sec. 3.2 reveal that the Marcus reorganization energy, λ, is significantly attenuated in the vicinity of an electrode. This attenuation is a consequence of image charge effects arising from the constant potential condition that is imposed by a planar, ideally conducting boundary. In this section, we demonstrate the generality of this λ-attenuation by considering a statistical field theory of the charge density fluctuations constrained by idealized constant potential boundaries. By dispensing with atomistic details, we effectively isolate the fundamental role of the constant potential boundary, and image charge interactions in particular, in modifying ET rates near an electrochemical interface.

Following a general approach for formulating a field theory,[34] we represent the charge distribution of an electrolyte solution that is confined between two constant potential electrodes in terms of a continuous charge density field, $\rho(z)$, along the longitudinal direction of the cell (z-direction). This density field represents the spatial distribution of charge coarse grained over molecular length scales and resolved along a single axis perpendicular to the electrode surfaces. Atoms and molecules are not explicitly resolved under the field representation, so the reorganization energy is instead determined based on the fluctuations in the associated electrostatic potential field, $\varphi(z)$. In the limit that the electrolyte does not exhibit strong electrostatic correlations, the relationship between $\varphi(z)$ and $\rho(z)$ can be formulated from Debye-Hückel theory. This theory is encoded in the modified charge-potential relationship,

$$\nabla^2\varphi - 4\pi\kappa^2\varphi = -4\pi\rho, \tag{3.13}$$

where the electrolyte screening length (Debye length) $\lambda_{\mathrm{D}} = \kappa^{-1}$ identifies the characteristic distance beyond which the long-range electrostatic force exerted by a single charge is attenuated due to the effects of screening caused by other mobile charges.

3.3.1 Treating constant potential boundaries

We define the spatial coordinate of our density field using non-dimensionalized units of the inter-electrode spacing, so that one electrode is located at position $z = 0$ and the other at $z = 1$. We focus on the statistics of the charge density, $\rho(z)$, and the effect of these fluctuations on the potential, $\varphi(z)$, as given by Eq. 3.13. Assuming that the electrodes are each maintained at their potential of zero charge (PZC), the constant potential condition imposes a constraint on the potential field at the electrode surfaces, such that $\varphi(0) = \varphi(1) = 0$, and on the charge density field, such that it obeys a mirror symmetry across the planes of $z = 0$ and $z = 1$.

One way to satisfy these constraints is to encode them into the basis functions with which we study the fields $\rho(z)$ and $\varphi(z)$. In this work, we utilize a basis that includes a "mirror domain" ($z \in [-1, 0]$), and includes only functions that are odd upon reflection across $z = 0$, automatically enforcing $\varphi(0) = 0$, as well as satisfying $\varphi(1) = 0$ through periodicity of the domain of $-1 < z < 1$. These functions also ensure the natural emergence of image charge interactions within the charge density field. The Fourier sine series with integer frequencies comprises a complete basis for arbitrary odd functions g that also satisfy the constraint

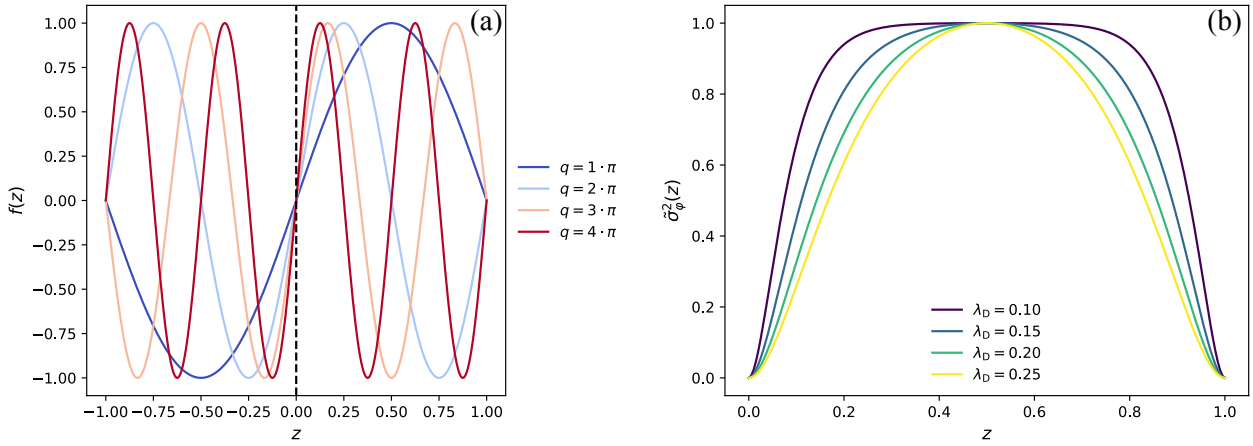

Figure 3.4: (a) Basis functions used in Fourier sine series expansion for the charge density and electrostatic potential field variables. (b) Individually normalized variance profiles computed from analytical evaluation of Eq. 3.21 (see Sec. 7.2 for an expression in terms of evaluable special functions), showing variance attenuation near the electrode interface, as well as plateau behavior upon exceeding a distance of a screening length away from the electrode interface. Values of λ_D are made non-dimensional by the electrode separation scale, L.

$g(0) = g(1) = 0$. These basis functions have the form,

$$\psi_q(z) = \sin(qz), \tag{3.14}$$

where $q \equiv n\pi$, with $n \in \mathbb{Z}^+$. These functions are orthogonal with respect to the ℓ^2 inner product, allowing us to define the Fourier sine transform $\hat{g}(q)$ of a function $g(z)$,

$$g(z) = \sum_{q=1}^{\infty} \hat{g}(q)\psi_q(z). \tag{3.15}$$

Figure 3.4(a) depicts a handful of the functions in the basis set, labeled by their frequencies. It is apparent that these functions satisfy the requisite boundary conditions. In this Fourier sine basis, the charge-potential relationship of Eq. 3.13 simplifies considerably, yielding,

$$\left(q^2 + 4\pi\kappa^2\right)\hat{\varphi}(q) = 4\pi\hat{\rho}(q). \tag{3.16}$$

3.3.2 Model formulation and results

We model the fluctuating charge density field as a point-wise Gaussian field with statistics given by,

$$\mathcal{P}\left[\rho(z); \sigma_\rho\right] \propto \exp\left[-\frac{1}{2\sigma_\rho^2} \cdot \int_{-1}^{1} \mathrm{d}z\, \rho(z)^2\right], \tag{3.17}$$

where σ_ρ parameterizes the variance of charge density fluctuations. This parameter depends on the implicit coarse-graining length scale and also encodes a significant amount of information about the physical and chemical details of the system being modeled. We assume that σ_ρ is independent of the approach coordinate, z, an assumption which is supported by empirical results from simulations (see Sec. 7.2). This parameter can, in principle, be tuned to describe a specific electrochemical system, however, in the results presented below we choose σ_ρ arbitrarily in order to highlight the general qualitative predictions of this field theoretic model.

In Fourier space, the distribution in Eq. 3.17 factorizes over the frequencies to yield,

$$\mathcal{P}\left[\hat{\rho}(q);\sigma_\rho\right] \propto \prod_{q=1}^{\infty} \exp\left[-\frac{\hat{\rho}(q)^2}{2\sigma_\rho^2}\right]. \tag{3.18}$$

In plain terms, every frequency component of the charge density is drawn independently from a Gaussian of equal variance. Under Debye-Hückel theory, the induced distribution over the electrostatic potential is independent, but not identically distributed over the frequency components. By applying Eq. 3.16, we arrive at an expression for the potential distribution in Fourier space,

$$\mathcal{P}\left[\hat{\varphi}(q)\right] \propto \prod_{q=1}^{\infty} \exp\left[-\frac{\left(q^2+4\pi\kappa^2\right)^2}{32\pi^2\sigma_\rho^2}\cdot\hat{\varphi}(q)^2\right], \tag{3.19}$$

which can be inverted to solve for the real space potential field. According to Eq. 3.19, the frequency components of the potential are random variables (RVs) drawn from normal distributions with different variances. Using $\mathcal{N}[\mu,\sigma^2]$ to denote a normal RV with mean μ and variance σ^2, we have

$$\varphi(z) = \sum_{q=1}^{\infty} \mathcal{N}\left[0, \frac{16\pi^2\sigma_\rho^2}{\left(q^2+4\pi\kappa^2\right)^2}\right]\cdot\sin(qz) \tag{3.20}$$

Employing standard Gaussian scaling rules and exploiting the fact that variances of independent RVs simply sum,

$$\sigma_\varphi^2(z) = \frac{16\sigma_\rho^2}{\pi^2}\sum_{n=1}^{\infty}\frac{\sin^2(n\pi z)}{\left(n^2+4\kappa^2/\pi\right)^2} \tag{3.21}$$

An analytical result for this summation can be expressed in terms of non-elementary functions.

Figure 3.4(b) depicts traces of the electrostatic potential variance profile from Eq. 3.21 as a function of the approach coordinate z. Qualitatively, the variance approaches zero at the cell boundaries $z=0$ and $z=1$, and plateaus to a constant value within a few screening lengths λ_D from the electrode surface. This behavior is consistent with physical intuition; at the level of Debye-Hückel theory, electrostatic correlations are exponentially attenuated for distances greater than the screening length, implying that the "bulk" region of the cell ($2\lambda \leq z \leq 1-2\lambda$) hardly feels the influence of the constant potential electrode. However, within the region of strong electrostatic influence from the electrode, the image plane constraint serves to significantly attenuate the range of possible electrostatic fluctuations.

The results presented in Sections 3.2 and 3.3 demonstrate the generality of reorganization energy attenuation near a constant potential electrode. The decomposition scheme presented in Section 3.2 indicates that the effect of image charges supported by the electrodes plays a dominant role in determining the vertical energy gap, and hence the reorganization energy, as one approaches the electrode surface. This observation explains why numerous studies with different representations of intermolecular forces between simulated particles all find a systematic attenuation of the reorganization energy with electrode approach. In Section 3.3, we build a mathematical framework based on a fluctuating field theory, entirely free of molecular detail, to show that this attenuation is purely a consequence of the constant potential boundary conditions. These results help build intuition about the manner in which an ideal electrode sculpts the landscape of electrostatic fluctuations near the interface.

3.4 References

[1] Stewart K Reed, Oliver J Lanning, and Paul A Madden. Electrochemical interface between an ionic liquid and a model metallic electrode. *J. Chem. Phys.*, 126(8):084704, 2007. ISSN 0021-9606. doi: 10.1063/1.2464084.

[2] Matt K Petersen, Revati Kumar, Henry S White, and Gregory A Voth. A computationally efficient treatment of polarizable electrochemical cells held at a constant potential. *J. Phys. Chem. C*, 116(7):4903–4912, 2012. ISSN 1932-7447. doi: 10.1021/jp210252g.

[3] Soumya Ghosh, Samantha Horvath, Alexander V Soudackov, and Hammes-Schiffer, Sharon. Electrochemical solvent reorganization energies in the framework of the polarizable continuum model. *J. Chem. Theory Comput.*, 10(5):2091–2102, 2014. ISSN 1549-9618. doi: 10.1021/ct500051e.

[4] R. A. Marcus. On the theory of Oxidation-Reduction reactions involving electron transfer. i. *J. Chem. Phys.*, 24(5):966–978, 1956. ISSN 0021-9606. doi: 10.1063/1.1742723.

[5] R. A. Marcus. Electrostatic free energy and other properties of states having nonequilibrium polarization. i. *J. Chem. Phys.*, 24(5):979–989, 1956. ISSN 0021-9606. doi: 10.1063/1.1742724.

[6] R. A. Marcus. On the theory of Electron-Transfer reactions. VI. unified treatment for homogeneous and electrode reactions. *J. Chem. Phys.*, 43(2):679–701, 1965. ISSN 0021-9606. doi: 10.1063/1.1696792.

[7] Wolfgang Schmickler and Elizabeth Santos. *Interfacial electrochemistry*. Springer Science & Business Media, 2010.

[8] Noel S. Hush. Electrode reactions of the methyl halides. *Z. Elektrochem.*, 61(6):734–738, 1957. ISSN 0005-9021. doi: 10.1002/bbpc.19570610606.

[9] Noel S. Hush. Adiabatic rate processes at electrodes. i. energy-charge relationships. *J. Chem. Phys.*, 28(5):962–972, 1958. ISSN 0021-9606. doi: 10.1063/1.1744305.

[10] Noel S. Hush. Adiabatic theory of outer sphere electron-transfer reactions in solution. *Trans. Faraday Soc.*, 57(0):557–580, 1961. ISSN 0014-7672. doi: 10.1039/tf9615700557.

[11] Christopher E. D. Chidsey. Free energy and temperature dependence of electron transfer at the Metal-Electrolyte interface. *Science*, 251(4996):919–922, 1991. ISSN 0036-8075. doi: 10.1126/science.251.4996.919.

[12] J Blumberger and M Sprik. *Redox Free Energies from Vertical Energy Gaps: Ab Initio Molecular Dynamics Implementation*, pages 481–506. Number 704. Springer, Berlin, Heidelberg., 2006. ISBN 9783540352839.

[13] Stewart K Reed, Paul A Madden, and Aristides Papadopoulos. Electrochemical charge transfer at a metallic electrode: a simulation study. *J. Chem. Phys.*, 128(12):124701, 2008. ISSN 0021-9606. doi: 10.1063/1.2844801.

[14] Arieh Warshel. Dynamics of reactions in polar solvents. semiclassical trajectory studies of electron-transfer and proton-transfer reactions. *J. Phys. Chem.*, 86(12):2218–2224, 1982. ISSN 0022-3654. doi: 10.1021/j100209a016.

[15] Arieh Warshel and Jenn-Kang Hwang. Simulation of the dynamics of electron transfer reactions in polar solvents: Semiclassical trajectories and dispersed polaron approaches. *J. Chem. Phys.*, 84(9):4938–4957, 1986. ISSN 0021-9606. doi: 10.1063/1.449981.

[16] Jenn Kang Hwang and Arieh Warshel. Microscopic examination of free-energy relationships for electron transfer in polar solvents. *J. Am. Chem. Soc.*, 109(3):715–720, 1987.

[17] Gregory King and Arieh Warshel. Investigation of the free energy functions for electron transfer reactions. *J. Chem. Phys.*, 93(12):8682–8692, 1990.

[18] Rachel E. Bangle, Jenny Schneider, Eric J. Piechota, Ludovic Troian-Gautier, and Gerald J. Meyer. Electron transfer reorganization energies in the electrode–electrolyte double layer. *J. Am. Chem. Soc.*, 142(2):674–679, 2020. doi: 10.1021/jacs.9b11815. URL `https://doi.org/10.1021/jacs.9b11815`. PMID: 31859498.

[19] David Chandler. Electron transfer in water and other polar environments, how it happens. In *Classical and Quantum Dynamics in Condensed Phase Simulations*, pages 25–49. WORLD SCIENTIFIC, jun 2010. ISBN 978-981-02-3498-0. doi: 10.1142/9789812839664_0002. URL `http://www.worldscientific.com/doi/abs/10.1142/9789812839664{_}0002`.

[20] Martin C Henstridge, Eduardo Laborda, Neil V Rees, and Richard G Compton. Marcus-Hush-Chidsey theory of electron transfer applied to voltammetry: A review. *Electrochim. Acta.*, 84:12–20, 2012. ISSN 0013-4686. doi: 10.1016/j.electacta.2011.10.026.

[21] Yi Zeng, Raymond B Smith, Peng Bai, and Martin Z Bazant. Simple formula for Marcus-Hush-Chidsey kinetics. *J. Electroanal. Chem.*, 735:77–83, 2014. ISSN 1572-6657. doi: 10.1016/j.jelechem.2014.09.038.

[22] H. O. Finklea, K. Yoon, E. Chamberlain, J. Allen, and R. Haddox. Effect of the metal on electron transfer across Self-Assembled monolayers. *J. Phys. Chem. B*, 105(15): 3088–3092, 2001. ISSN 1520-6106. doi: 10.1021/jp0041510.

[23] William J Royea, Thomas W Hamann, Bruce S Brunschwig, and Nathan S Lewis. A comparison between interfacial Electron-Transfer rate constants at metallic and graphite electrodes. *J. Phys. Chem. B*, 110(39):19433–19442, 2006. ISSN 1520-6106. doi: 10.1021/jp062141e.

[24] Kaitlyn A Dwelle and Adam P Willard. Constant potential, electrochemically active boundary conditions for electrochemical simulation. *J. Phys. Chem. C*, 123(39):24095–24103, 2019. ISSN 1932-7447. doi: 10.1021/acs.jpcc.9b06635.

[25] John David Jackson. *Classical electrodynamics*. AAPT, 1999.

[26] Stephen J Cox and Phillip L Geissler. Interfacial ion solvation: Obtaining the thermodynamic limit from molecular simulations. *J. Chem. Phys.*, 148(22):222823, 2018. ISSN 0021-9606. doi: 10.1063/1.5020563.

[27] J. W. Perram and Mark A Ratner. Simulations at conducting interfaces: Boundary conditions for electrodes and electrolytes. *J. Chem. Phys.*, 104(13):5174–5180, 1996. ISSN 0021-9606. doi: 10.1063/1.471144.

[28] Adam P Willard, Stewart K Reed, Paul A Madden, and David Chandler. Water at an electrochemical interface–a simulation study. *Faraday Discuss.*, 141:423–441, 2009. ISSN 1359-6640. doi: 10.1039/B805544K.

[29] Steve Plimpton. Fast parallel algorithms for Short-Range molecular dynamics. *J. Comput. Phys.*, 117(1):1–19, 1995. ISSN 0021-9991. doi: 10.1006/jcph.1995.1039.

[30] Zhenxing Wang, Yang Yang, David L Olmsted, Mark Asta, and Brian B Laird. Evaluation of the constant potential method in simulating electric double-layer capacitors. *J. Chem. Phys.*, 141(18):184102, 2014. ISSN 0021-9606. doi: 10.1063/1.4899176.

[31] Ilja J Siepmann and Michiel Sprik. Influence of surface topology and electrostatic potential on water/electrode systems. *J. Chem. Phys.*, 102(1):511–524, 1995. ISSN 0021-9606. doi: 10.1063/1.469429.

[32] Todd R Gingrich and Mark Wilson. On the ewald summation of gaussian charges for the simulation of metallic surfaces. *Chem. Phys. Lett.*, 500(1-3):178–183, 2010. ISSN 0009-2614. doi: 10.1016/j.cplett.2010.10.010.

[33] Soumya Ghosh, Alexander V Soudackov, and Hammes-Schiffer, Sharon. Electrochemical electron transfer and Proton-Coupled electron transfer: Effects of double layer and ionic environment on solvent reorganization energies. *J. Chem. Theory Comput.*, 12(6):2917–25, 2016. ISSN 1549-9618. doi: 10.1021/acs.jctc.6b00233.

[34] Mehran Kardar. *Statistical Physics of Fields*. Cambridge University Press, 2007. doi: 10.1017/CBO9780511815881.

Chapter 4

Electrostatic Screening in Moderately Concentrated Aqueous Electrolyte is Concentration-Independent and Microscopically Heterogeneous

4.1 Introduction

Electrochemical systems operate by maintaining an electrochemical potential difference between two electrodes of opposite polarity, typically separated by a liquid electrolyte. Under applied potential, the electrode surfaces typically acquire a surface charge, resulting in electric fields that exert directional forces on the solvent molecules and ions comprising the electrolyte. These fields elicit an electrolyte "screening response" characterized by the buildup of ionic counter-charge near the electrode, which serves to localize the electric field within a microscopically thin layer of electrolyte immediately adjacent to the electrodes. Commonly known as the electrochemical double-layer (EDL), this narrow interfacial region features stark spatial anisotropy and potent local electric fields, and serves as the backdrop for several interesting phenomena in interfacial electrochemistry.

Theoretical descriptions of electrostatic screening phenomena in the EDL, which focus on predicting spatially-resolved profiles of the electrostatic potential and the ionic concentration, have a rich history. Helmholtz and Perrin advanced the first mathematical model for the EDL, and assumed that the electrode surface charge was perfectly neutralized by a flat plane of ions residing at the "outer Helmholtz plane" (OHP), separated from the electrode by a distance ℓ_{OHP}. Under this assumption, the EDL is a microscopic parallel-plate capacitor, with a constant electric field between the electrode and the OHP, and no variation in the potential from the OHP onwards. A simple thermodynamic argument should convince us of the limitations of the Helmholtz picture: the plane–of–ions configuration carries a steep entropic penalty, and hence is un-representative of a typical ionic density in the EDL.

In fact, more typical electrostatic screening configurations must feature a diffuse cloud of neutralizing ionic density. The first successful description of potential variations in the EDL

that accounts for such entropic effects begins by applying the Poisson-Boltzmann equation,

$$\nabla^2\psi = \frac{c_0 \cdot e}{\epsilon \cdot \epsilon_0} \sum_k z_k \exp\left[-\beta e z_k \psi\right], \tag{4.1}$$

where ψ is the electrostatic potential, c_0 is the bulk ion concentration, e is the fundamental charge, β is the thermodynamic inverse temperature, and ϵ_0 and ϵ are the continuum dielectric permittivity and the permittivity of free space, respectively. The summation runs over all ionic components of the solution, indexed by k, where z_k represents the charge number of the ion (e.g. $z_k = +1$ for a monovalent cation). We can make analytical progress by linearizing the exponential term in Eq. (4.1), formally only valid for small electrolyte concentrations and modest applied potentials, and leveraging the fact that the salt formula is electroneutral (i.e. $\sum_k z_k = 0$). The resultant mathematical description predicts an exponentially decaying electrostatic potential,

$$\psi(z) = \psi_0 \exp\left[-z/\ell_{\mathrm{D}}\right], \tag{4.2}$$

where z is the separation from the electrode interface, ψ_0 is the applied potential, and $\ell_{\mathrm{D}} \propto c_{\mathrm{ion}}^{-1/2}$ is the Debye screening length of the electrolyte solution.

Debye-Hückel (DH) theory, as described in Eq. (4.2), is applied widely when considering screening phenomena in the EDL, especially when they are of relevance to interpreting the results of electrochemical experiments. DH theory is particularly attractive because it advances a simple physical picture of mobile-charge screening: a single tagged charge is surrounded by a diffuse "cloud" of mobile ionic counter-charges with a characteristic length scale identified by the Debye length ℓ_{D}. This results in a monotonically decreasing potential profile in the EDL. While physically intuitive, the theory for potential decay presented in Eq. (4.2) involves a number of strong assumptions, many of which may be violated in electrochemically-relevant electrolyte systems.

First, DH theory also assumes that the ions in the electrolyte can be modeled as point charges that occupy no volume. Second, DH theory assumes that the solvent environment can be faithfully represented by a dielectric continuum described by a single dielectric permittivity ϵ, neglecting both the finite size of solvent molecules as well as possible correlations between their positions and orientations. Although these assumptions are accurate on continuum lengthscales, they can result in qualitatively inaccurate predictions on the lengthscales relevant to the EDL in moderately concentrated electrolytes. For example, in 1M monovalent aqueous electrolyte, the Debye length $\ell_{\mathrm{D}} = 3$ Å, which is comparable to the hydrated radius of a single solvated ion; at this scale, the intuitive physical picture of a diffuse ionic charge screening cloud of radius ℓ_{D} around a tagged charge becomes untenable. Additionally, DH theory does not model the strong molecular interactions between a planar electrode surface and solvent dipoles, which have been shown to exhibit strong orientational preferences within a few molecular layers of an electrode surface. Some of the issues associated with the second assumption are remedied by the so-called Stern correction, which posits that there is a molecular layer (the "Stern layer") of specifically adsorbed, oriented solvent dipoles at the electrode surface. Including the Stern correction in the theory developed in Eq. (4.2) results in an electrostatic potential profile that decays linearly in the Stern layer, and then exponentially out to the bulk. Figure 4.1 depicts schematic descriptions of potential decay as described by each of the theories discussed.

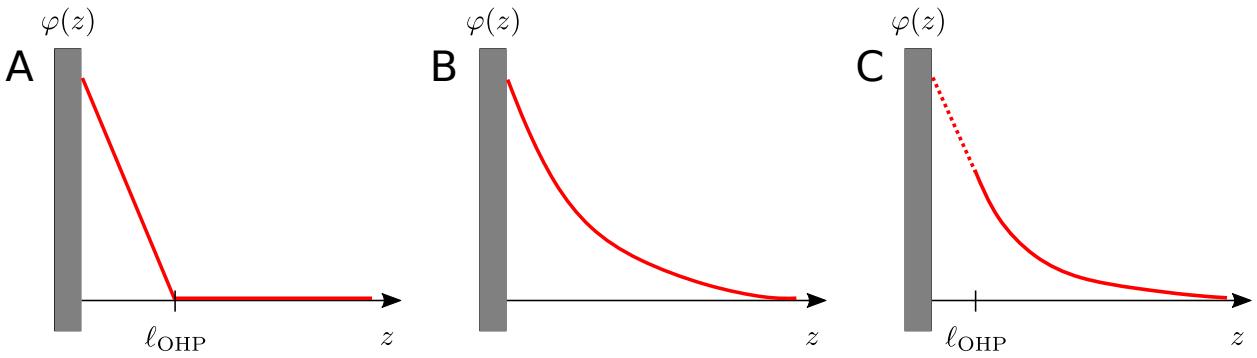

Figure 4.1: Schematic electrical potential profiles in the EDL predicted by (A) Helmholtz-Perrin theory, (B) DH theory, and (C) DH theory with the Stern correction, where the dashed section represents the linear decay in the Stern layer.

Here, we seek to evaluate how these continuum theories of electrostatic screening in the EDL compare with results from constant potential molecular dynamics simulations of moderately concentrated aqueous electrolytes. Since molecular dynamics simulations fully represent the finite size effects and molecular correlations of and between solvent molecules and ions, they are well positioned to examine the pitfalls of the assumptions advanced in deriving the electrostatic screening theories summarized in Fig. 4.1.

4.2 Results

We study the nature of electrostatic screening in the EDL using molecular dynamics (MD) simulations of aqueous NaCl electrolytes at various different concentrations sandwiched between two Pt electrodes. Figure 4.2A depicts a representative snapshot of the molecular simulation cell, with the z direction oriented normal to the planar electrode surface. In order to simulate connection to an external circuit that holds the electrodes at a constant potential difference, we use the well-developed fluctuating charges method to adjust the point charges on the electrode atoms at each timestep in order to obey a constant potential difference of $\Delta V = 1$ V between the two electrodes. The simulation box has dimensions $3.1\,\mathrm{nm} \times 3.1\,\mathrm{nm} \times 9.3\,\mathrm{nm}$, and is periodically replicated in the directions lateral to the electrode surface. This is a large enough simulation cell to host two non-overlapping EDLs at each of the electrodes, with a well-formed bulk in the central region. The intermolecular potential, or "force field" describing the water molecules is the standard TIP3P force field, whereas the ion and Pt atom interaction parameters are taken from studies reported in the literature. The results presented here are obviously dependent on the details of the intermolecular interaction potentials, but the qualitative screening structures reported here should be broadly conserved between force fields.

In order to compare the results of molecular simulations to the continuum theories summarized in Fig. 4.1, we must develop a way to compute the electrostatic potential profile from a single simulation snapshot. This is not an immediately straightforward problem, since the Poisson equation in three dimensions is a partial differential equation that is generally solved on a regular grid, whereas the atomic positions in an MD simulation are unconstrained

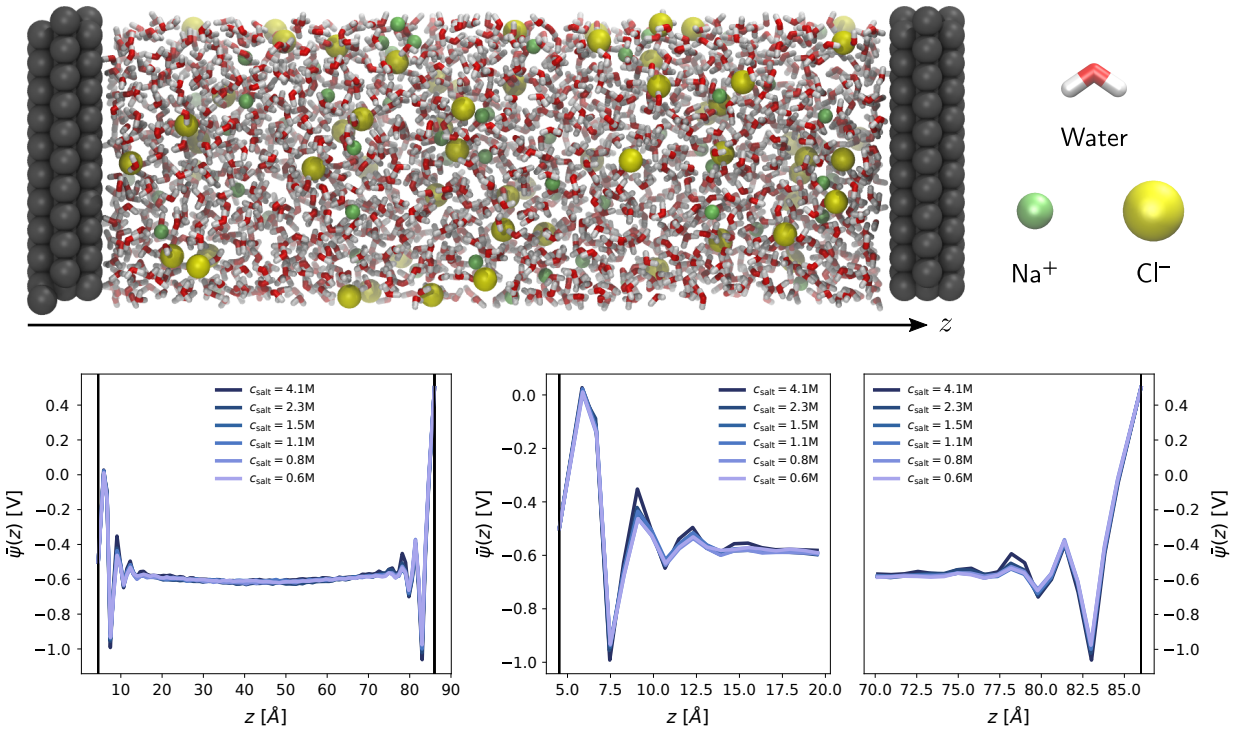

Figure 4.2: Poisson potential computations from molecular dynamics simulations. (A) Representative snapshot of a molecular dynamics simulation cell, depicting an aqueous 1M NaCl electrolyte between two Pt electrodes. The left electrode is the cathode (held at $V_{\text{left}} = -0.5$ V), and the right electrode is the anode (held at $V_{\text{right}} = -0.5$ V). By convention, the z axis runs perpendicular to the electrode surfaces. (B) Traces of the equilibrium-averaged, plane-averaged Poisson potential $\bar{\psi}(z)$, estimated from molecular dynamics simulations run at various electrolyte salt concentrations. (C) Traces of $\bar{\psi}(z)$ zoomed in on the cathode and anode, highlighting oscillatory and concentration independent short distance screening behavior.

relative to the grid points. In order to address this, we use a proportional spreading scheme, described in full detail in Sec. 7.3, to interpolate the charges at each timestep from the atom centers to the points on a regular grid. Once the charges are spread onto a regular grid, we can compute the instantaneous Poisson potential $\psi(x, y, z)$ in a single molecular simulation snapshot; to achieve correspondence with a one-dimensional continuum electrostatics theory, we define the plane-averaged Poisson potential,

$$\bar{\psi}(z) \equiv \frac{1}{L_x \cdot L_y} \int_0^{L_x} \int_0^{L_y} dxdy \; \psi(x, y, z), \tag{4.3}$$

where L_x and L_y are the length of the electrolyte region in the x and y directions, respectively. Finally, we run the molecular simulations for a total sampling time of 10 ns, and compute a time average of the plane-averaged Poisson potential $\bar{\psi}(z)$ using simulation snapshots saved every 100 ps.

Figure 4.2B depicts traces of the plane-averaged Poisson potential for several different

electrolyte ion concentrations (represented by different colors of the thick lines). The thin black lines represent the planes of constant potential imposed in the MD simulation, where the voltages are pinned at $V_{\text{left}} = -0.5$ and $V_{\text{right}} = +0.5$ V. It is apparent that the electrostatic screening structure is well-established over the course of the simulations, with two distinct EDL regions confined within 10-15 Åof the electrode surfaces, and a bulk region with a flat electrostatic potential profile. Figure 4.2C shows zoomed-in snapshots of the EDLs at the left and right electrodes, highlighting the electrostatic potential variation in these regions. Although the plane-averaged potential profiles exhibit electrostatic potential decay from the electrode surface to the bulk, in line with continuum descriptions of electrostatic screening, they are strikingly dissimilar from the profiles depicted in Fig. 4.1 in a couple different ways. First, the profiles are markedly non-monotonic, exhibiting relatively large oscillations in the local electrostatic potential on the scale of ΔV, the potential difference between the two electrodes. Second, and perhaps most strikingly, the electrostatic potential profiles show little variation over the entire range of ion concentrations studied here, instead of becoming more compact at higher concentrations, as predicted by DH theory.

The marked deviations from DH behavior in Fig. 4.2 raise the question: in what manner is DH-like screening observed in the MD simulation results presented here, if at all? Since DH theory treats the solvent molecules as a dielectric continuum, one way in which we may be able to recover signatures of DH screening in the MD simulations is if we focus solely on the positional statistics of the ions. We can achieve this by constructing an ionic screening function,

$$\mathcal{S}(z) = q_{\text{elec}} + \int_0^z ds \bar{\rho}_{\text{ion}}(s), \tag{4.4}$$

where $\bar{\rho}_{\text{ion}}(z)$ is the plane-averaged *ionic* charge density, obtained by applying the proportional spreading procedure described in Sec. 7.3 only to the atom-centered charges on the ionic species, and neglecting the solvent molecules entirely. Intuitively, the screening function $\mathcal{S}(z)$ tallies the amount of electrode charge that remains unscreened by the mobile ionic charges; it takes the value q_{elec} at the electrode surface $z = 0$, and vanishes upon reaching the bulk region of the simulation cell.

Figure 4.3A depicts traces of the normalized screening function $\bar{\mathcal{S}}(z) \equiv \mathcal{S}(z)/\mathcal{S}(0)$ for various different concentrations (represented by differently colored traces). According to DH screening theory, this normalized screening function should decay from unity to zero in an exponential manner, with associated length scale ℓ_{D}, the Debye length. The profiles in Fig. 4.3A show signatures of the DH screening behavior; the profiles are more diffuse at lower salt concentrations, and analysis of the length scale by exponential fitting shows that the decay length is roughly ℓ_{D} for each ion concentration. Although the ionic statistics are in line with expectations from DH theory, the molecular dynamics simulations provide ample evidence that the solvent molecules play an important role in electrostatic screening. Figure 4.3B shows traces of the bulk-normalized concentration of water molecules (solid lines) and sodium cations (dashed lines) in the simulation for the different ionic concentrations examined. At all concentrations examined, the first density peak of the water molecules appears closer to the left electrode than the first density peak of the cations. Additionally, the height of the peak, normalized to the bulk density of water, is roughly independent of the ion concentration, indicating that the water molecules are able to screen the electrode

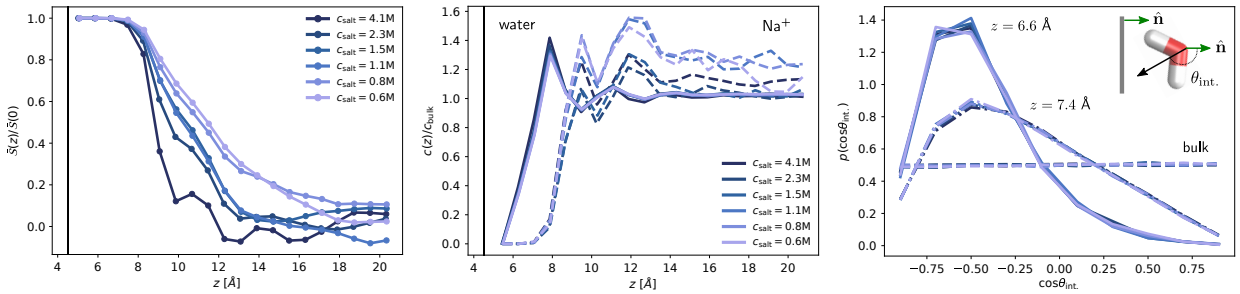

Figure 4.3: Signatures of ionic and dipolar screening behavior. (A) Traces of the normalized screening function, $\mathcal{S}(z)/\mathcal{S}(0)$ at various electrolyte concentrations, reflecting concentration dependent ionic screening behavior. (B) Traces of the local concentration of water molecules (solid lines) and Na^+ cations (dashed lines), normalized by their respective bulk concentrations, at various electrolyte concentrations. (C, inset) Schematic depicting the selected convention for water orientation computations; the molecular orientation vector (black) bisects the water molecule, pointing from oxygen to hydrogen, while the surface normal vector (green) points normal to the cathode. Negative values of $\cos\theta_{\text{int.}}$ indicate hydrogens-facing-cathode configurations. (C) Orientational distributions of water molecules situated at $z = 6.6$ Å(solid lines), $z = 7.4$ Å(dot-dashed lines), and in the bulk (dashed lines) at various electrolyte concentrations.

charge at distances closer than the typical cation approaches the electrode.

Finally, Fig. 4.3C shows orientational distributions of the water molecules at different values of the z coordinate (represented by solid, dashed, and dash-dotted lines), for various different ion concentrations (represented by different colors). The orientational order parameter, $\cos\theta_{\text{int}}$, captures the degree of alignment of the molecular dipole of a water molecule with the surface normal of the electrode, as represented schematically in the inset of Fig. 4.3C. For $\cos\theta_{\text{int}} = -1$, the hydrogen atoms in the water molecule are pointed towards the electrode, whereas $\cos\theta_{\text{int}} = +1$ represents an orientation where the oxygen atoms are pointed towards the electrode. Since the left electrode is the cathode (held at a negative potential), it stands to reason that the water molecules closest to the electrode show a distinct preference for orientations where the water dipole is aligned with the field, which decays rapidly into an un-oriented distribution in the bulk. Corresponding plots for the orientations at the anode are included in Sec. 7.3.

Chapter 5

Examining Cardinal Tafel Slope Preferences in CO_2 Reduction Electrocatalysis with Bayesian Data Analysis

5.1 Introduction

Modern tools in data science provide the capability to reduce or outright eliminate sources of human bias in the analysis and interpretation of experimental measurements. [1] Despite the wide availability of these tools, many communities continue to rely on more primitive and bias-prone methods of data analysis. The calculation of Tafel slopes through linear least squares fitting is one prominent example. Here, we present a robust Bayesian approach to analyzing electrochemical current-voltage measurements that (1) eliminates the need to manually exclude points in limiting-current regimes, and (2) provides a well-defined measure of uncertainty in the fitting parameters (e.g. the Tafel slope). By applying this approach to a large set of literature data, we identify a systematic but unjustified tendency for the assignment of Tafel slopes to specific "cardinal" values. This finding highlights the role that modern data science can play in uncovering and eliminating hidden sources of bias that exist within various scientific communities.

Current-voltage measurements are a fundamental characterization tool for electrochemical systems, as they report on the propensity for system response when pushed out of equilibrium by a thermodynamic driving force. In the context of electrochemical catalysis, current-voltage behavior is often summarized by the Tafel slope, a parameter that quantifies the amount of electrochemical driving force required to produce a logarithmic increase in the observed current.[1] Nearly all studies that develop a novel electrochemical catalyst report a Tafel slope, and it is considered an important figure of merit when comparing catalysts. In

[1]The material in this chapter is reproduced in part with permission from: Limaye, A. M.; Zeng, J. S.; Willard, A. P.; Manthiram, K., Bayesian data analysis reveals no preference for cardinal Tafel slopes in CO2 reduction electrocatalysis. *Nat. Commun.* **2021**, 12, 703. `https://doi.org/10.1038/s41467-021-20924-y`.

principle, the Tafel slope contains information about the microscopic mechanism underlying the operation of a catalyst. The elementary kinetic steps of idealized reaction mechanisms imply a strong tendency for Tafel slopes to exhibit certain "cardinal values" [2,3], and these cardinal values are frequently referenced in the kinetic analysis of catalytic materials. However, several notable studies have reported Tafel slopes that differ significantly from their predicted cardinal values.[4,5] Because the kinetic steps associated with these cardinal values are ubiquitous, there is a tendency to interpret Tafel slopes with off-cardinal values as if they represent a truly cardinal value that has been altered by sources of experimental error, despite relatively incomplete error quantification.[6–12] The flaw in this interpretive strategy is that it relies on the validity of idealizing assumptions about the underlying kinetic mechanism, and does not account for the numerous ways in which deviations from ideality can influence the Tafel slope.[13]

Despite the scientific and engineering relevance of the Tafel slope, current literature approaches for estimating this parameter from measured current-voltage data require subjective human intervention, and are susceptible to numerous sources of systematic error. Subjective considerations in the fitting procedure (namely, the manual demarcation of a linear fit region) make it impossible to determine, in a truly unbiased manner, the intrinsic distribution of Tafel slopes, and whether they cluster around cardinal values. Additionally, human interventions in the fitting procedure enable researcher bias, both inadvertent and intentional, to influence a quantitative catalyst benchmark. Such biases are difficult to recognize without re-examining primary source data.

To address these concerns, we advance an alternative Bayesian data analysis method that enables unbiased Tafel slope estimation. This method provides robust, distributional uncertainty quantification, elucidating the credible range of Tafel slope values consistent with the measured data. Because our method eliminates subjectivity in the fitting process, it enables us to fairly evaluate the prevalence of cardinal Tafel slopes within re-analyzed literature data.

In this manuscript, we begin by describing common literature practices for assigning Tafel slopes from experimental current-voltage data. Subsequently, we develop the mathematical formalism behind our Bayesian approach to Tafel slope estimation, and discuss its associated benefits compared to existing approaches. Using synthetic data, we illustrate the benefits of our approach, and show how it can be combined with iterative data acquisition procedures to systematically reduce uncertainty in Tafel slope estimates. Finally, we apply our approach to a large set of CO_2 reduction catalyst data from the literature, and compare our Tafel slope estimates to the reported values. We find that clustering of reported Tafel slopes around cardinal values is unjustified, and likely reflects systemic bias across the field. We conclude by hypothesizing several plausible sources of mechanistic nonideality and estimating their ability to modify Tafel slopes from their cardinal values.

5.2 Results

5.2.1 Tafel Slopes in Electrocatalysis

Electrochemical systems operate by converting the energy stored in chemical bonds into electrical work (or vice-versa) by means of electron transport through an external circuit. The electron transport process originates at an electrochemical interface, where a portion of the external circuit (an electrode) is contacted with a chemical system (a reactive electrolyte solution) in the presence of a catalyst. Catalyzed interfacial electron transfer serves to inextricably link the electrical dynamics of the external circuit to the chemical dynamics of the electrolyte. Electrochemical characterization techniques exploit this linkage, using the voltage and current measured in the external circuit to report on the thermodynamic driving forces and nonequilibrium currents in the chemical system. The simplest possible electrochemical experiment involves setting the applied potential at an electrode and measuring the resultant electrical current (or vice-versa), generating a current-voltage trace.

Several phenomena can influence the shape of current-voltage traces. For example, the electronic properties of the electrode, the chemical identity of the catalyst material, the transport characteristics of reactive species in the electrolyte, and myriad other factors all play an important role in structuring current-voltage behavior.[14] When characterizing the performance of a catalyst material, we are most interested in the kinetic control regime of a current-voltage trace, where the measured current reports directly on the intrinsic rate of a chemical reaction at the interface. Under kinetic control, the current is generally expected to follow an exponential asymptotic dependence on the overpotential η, which quantifies the difference between the applied electrode potential and the equilibrium potential for the chemical reaction.[1] In the high $|\eta|$ limit (specifically, $|\eta| \gg k_{\mathrm{B}}T/e$, the thermal voltage), the logarithm of the kinetic current, i_{kin}, should depend linearly on the applied potential. The (inverse) slope of this relationship is termed the Tafel slope,

$$\text{Tafel Slope} \equiv \left.\frac{d\eta}{d\log_{10} i_{\mathrm{kin}}}\right|_{|\eta| \gg k_{\mathrm{B}}T/e}, \tag{5.1}$$

and is generally reported in units of mV/decade.

The Tafel slope is an important parameter to judge the performance of a catalyst because it quantifies the amount of additional applied potential required to observe a logarithmic increase in the measured current. Hence, studies that develop a novel electrocatalytic material often measure current-voltage data in the kinetic control regime, and then use this data to estimate a Tafel slope for their catalytic system. Experimental limitations impose a number of practical constraints on the Tafel slope estimation procedure. First, for several electrochemical reactions (CO_2 reduction, N_2 reduction, organic electrosynthesis, etc.), accurately determining a kinetic current for a specific reaction requires product quantification after a constant potential/current hold. Due to throughput limitations for quantification techniques, the Tafel slope often must be estimated from just a handful of data points (roughly, 3–10). Another important practical constraint arises from limiting current phenomena observed in many electrocatalytic systems. At sufficiently high overpotentials, the reaction rate exceeds the rate of another physical process required for the reaction to proceed. In this regime, the system is no longer under kinetic control, and the measured current plateaus to a limiting

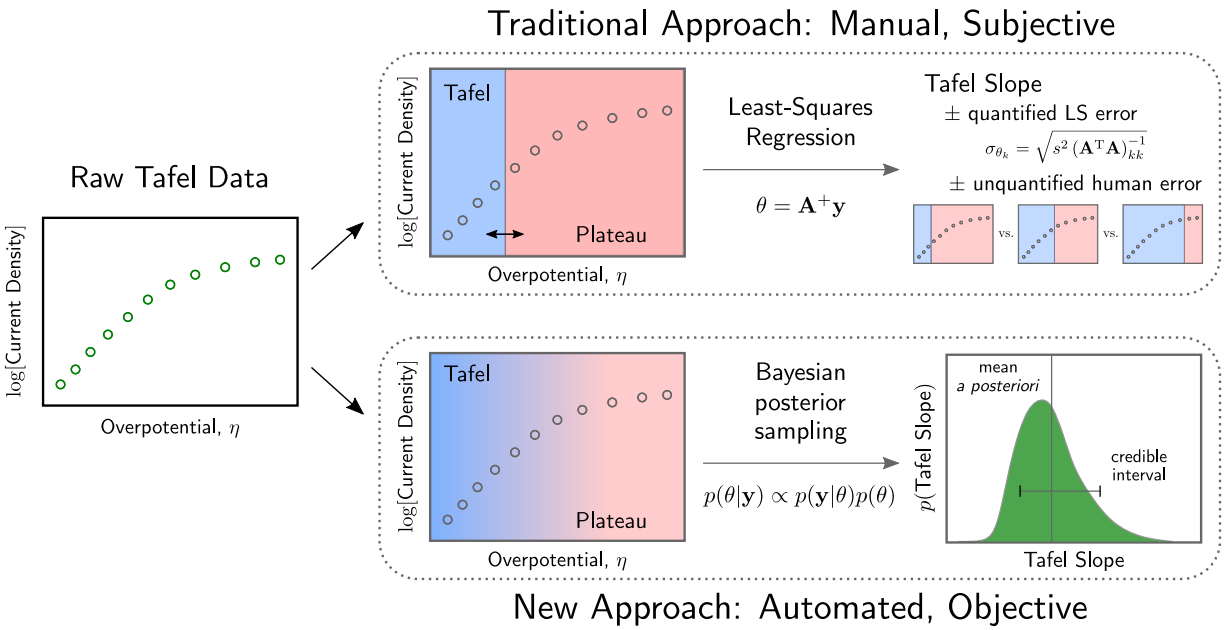

Figure 5.1: Schematic comparison of the traditional approach to Tafel fitting and the new approach we describe in this manuscript. Starting from raw current-voltage data on the left, the current literature approach begins with manual identification of a linear Tafel region on the plot. The rest of the data is discarded, and a linear fit to the Tafel region yields a Tafel slope, with an associated uncertainty corresponding to the standard error of the ordinary least squares (OLS) estimator. In addition to this quantified uncertainty, an additional unquantified source of uncertainty arises from manual selection of a Tafel region on the plot. The new approach described here considers all of the data in the context of a nonlinear model that smoothly interpolates between the traditional Tafel region and a plateaued region (e.g., due to mass transport limitations). Our approach uses a Monte Carlo method to sample from the Bayes posterior distribution over the parameters of the model, yielding a probabilistic distribution over Tafel slopes that are consistent with the measured data.

current, becoming independent of the applied voltage.[15] Most commonly, limiting currents in CO_2 reduction systems arise from diffusive transport limitations in the electrolyte, although several other physical reasons for plateau currents have been hypothesized and investigated in the literature.[16–20] Consequently, experimentally measured Tafel data usually starts out linear, but curves sub-linearly at sufficiently high overpotentials.

In the face of these practical limitations, studies in the literature use a relatively standard protocol for estimating the Tafel slope, depicted schematically in the upper half of Fig. 5.1. First, a researcher must manually identify an ad hoc cutoff between a linear, kinetically-controlled regime (the Tafel regime) and a limiting current (plateau) regime.[21] All data points in the plateau regime are subsequently discarded, and a Tafel slope is fitted by ordinary least squares (OLS) linear regression to the data in the Tafel regime. The OLS procedure offers a prescription for extracting the standard error of the Tafel slope; this standard error is sometimes used to construct a confidence interval for the Tafel slope estimate.[22,23]

We believe the current standard literature practice bears several drawbacks. First and foremost, manual identification of a cutoff between the kinetic and limiting-current regimes introduces subjectivity into Tafel slope estimation, potentially incorporating undesirable human influence into the quantification of an important metric for electrocatalyst performance. Second, reporting the error associated with a linear fit to a manually selected set of data points systematically under-estimates the actual error associated with estimating a Tafel slope from a small number of data points. The OLS slope standard error quantifies the uncertainty associated with the linear fit to a given set of data, but there is an additional unquantified error associated with selection of the linear regime. Third and finally, ad hoc selection of a regime cutoff can introduce a systematic bias in the Tafel slope, since the final few points of the kinetic regime will suffer at least some effects from limiting current curvature, causing the current at these points to deviate slightly from the true kinetic current.

5.2.2 Bayesian Data Analysis Algorithm

Our approach for Tafel slope estimation seeks to obviate manual demarcation between the linear and plateau regions in current voltage data. To this end, we choose to fit all current-voltage data measured in a Tafel experiment to a phenomenological model that smoothly interpolates between the kinetic control and plateau regimes. The model reads,

$$\frac{1}{i(\eta)} = \frac{1}{i_{\text{lim}}} + \frac{1}{i_0 \exp\left[m_{\text{T}}^{-1} \cdot |\eta|\right]}, \tag{5.2}$$

where $i(\eta)$ is the measured current density as a function of overpotential. The unknown parameters in the model are i_{lim}, the limiting current density, i_0, the exchange current density, and m_{T}^{-1}, the inverse Tafel slope. The mathematical structure of Eq. (5.2) can be shown to arise, for example, when the surface concentration of a redox-active species changes with applied overpotential due to diffusive transport effects. Alternatively, Eq. (5.2) could be motivated by interpreting the presence of limiting-current phenomena as an additional series resistance to current in the equivalent circuit for an electrochemical cell.[1] Most generally, this model can describe any physical phenomenon that imposes a "speed limit" on the passed current.[24]

Typically, the parameters in a model like Eq. (5.2) would be adjusted to achieve optimal agreement between the model and experimental data. Despite the nonlinearity inherent to the model, numerical optimization schemes for determining the optimal set of parameters are mature and well-studied. Here, we employ a different approach based on Bayesian sampling that can quantify not only an optimal set of parameters, but also a distribution over the likely values of the model parameters given the available experimental data.[25] Before carrying out any current-voltage measurements, we generally have at least some idea of the reasonable values of parameters in Eq. (5.2). For example, one would be very leery of a Tafel slope $m_{\text{T}} \notin [10^1, 10^3]$ mV/decade, and one can use tabulated values of a species diffusion coefficient and an estimate of the cell boundary layer thickness to compute a ballpark estimate of a limiting current, i_{lim}, arising from diffusive transport limitations.[1,24] For a general set of parameters θ, this knowledge is encoded in a prior distribution over the parameters $p(\theta)$. Upon observing some data $\mathbf{y}$, we can compute an updated posterior distribution $p(\theta|\mathbf{y})$ (the

probability of the parameters given the observed data) using Bayes' rule,[26]

$$p(\theta|\mathbf{y}) = \frac{p(\mathbf{y}|\theta) \times p(\theta)}{p(\mathbf{y})}. \tag{5.3}$$

The likelihood $p(\mathbf{y}|\theta)$ is supplied by a model like Eq. (5.2), in conjunction with an assumption about the distribution over the error at each data point. Here, we assume the error at each data point is independently normally distributed with a standard deviation $\sigma = 0.10$ log units, though our approach is flexible in this respect (see Sec. 7.4 for sensitivity analysis with respect to the σ parameter).

Despite the fact that the partition function $p(\mathbf{y})$ is an unknown constant, Eq. (5.3) yields a prescription for sampling from the posterior distribution over parameters $p(\theta|\mathbf{y})$. Briefly, one can use a Markov chain Monte Carlo sampling scheme[27] to glean several parameter samples from the posterior distribution, which are expected to concentrate in density around the optimal values of the parameters (additional detail on implementation can be found in Sec. 7.4). As depicted in the lower panel of Fig. 5.1, this Bayesian posterior sampling technique reveals both the optimal values of the model parameters and a distributional uncertainty estimate over their values, accounting for all sources of uncertainty in the model. If we truly want to collapse this distributional information to a single value of the parameter, say for quoting a Tafel slope associated with a catalyst, we can compute,

$$\langle\theta\rangle \equiv \int \mathrm{d}\theta \cdot \theta \cdot p(\theta|\mathbf{y}), \tag{5.4}$$

where $\langle\theta\rangle$ is termed the mean *a posteriori* (MAP) parameter estimate. When the posterior distribution $p(\theta|\mathbf{y})$ is strongly peaked around an optimal set of parameters, the MAP estimate will line up with the parameters gleaned from a nonlinear optimization technique. When the posterior distribution is broad or multimodal, the MAP estimate and the optimal parameter values may differ, signaling a high degree of uncertainty associated with the optimal parameter estimate.

The Bayesian posterior sampling approach offers several key advantages over the traditional approach to Tafel slope estimation. First, it removes subjectivity from the analysis of Tafel data: users of our algorithm need only select a model such as Eq. (5.2) to interpret the observed data, which can be justified on the basis of rigorous physical arguments, unlike a subjective delineation between linear and plateau regimes. Second, our approach yields accurate quantification the uncertainty associated with a Tafel slope estimate. Specifically, we believe the distributional uncertainty quantification afforded by our algorithm will be useful when assessing and discriminating between disparate sets of experimental data. Finally, because the model in Eq. (5.2) analytically extrapolates away curvature-related attenuation of the kinetic current, our approach is free of the systematic bias present in current literature practice.

As a caveat, we stress that while the model in Eq. (5.2) is appropriate for fitting some current-voltage data in the CO_2 reduction literature, experimental and theoretical studies have noted the possibility of multiple kinetic control regimes with distinct Tafel slopes before a limiting current plateau regime.[3,28,29] This phenomenon can arise due to potential-dependent surface coverage effects or a potential-dependent switch in the microscopic reaction mechanism. When multiple distinct Tafel regimes are present, the experimental data

must be interpreted under a model that allows for this possibility; once a suitable model is selected, the Bayesian posterior sampling approach can still be employed (see Sec. 7.4 for additional discussion on model flexibility).

5.2.3 Identifying and Addressing Data Insufficiency

As mentioned previously, practical throughput considerations imposed by product quantification and other experimental requirements limit the amount of data generally used in a Tafel analysis to 3–10 points. In a survey of Tafel data reported in CO_2 reduction studies in the literature, we found that a significant number of papers conduct Tafel analyses on a set of 3–5 data points within a narrow overpotential window. With such few data points, trends often appear linear, and so many studies simply extract the Tafel slope from a linear fit to all the data. While seemingly benign, estimating a Tafel slope without accounting for the possibility of limiting-current nonlinearity can lead to systematic error arising from data insufficiency. This phenomenon is elegantly identified and addressed by our Bayesian posterior sampling approach. For the sake of clarity, we illustrate how this systematic error can emerge by analyzing a set of synthetic data. The parable narrated by this data is easily relatable to a specific set of experimental data, and it emphasizes another distinct advantage of the Bayesian posterior sampling approach.

The inset of Fig. 5.2A depicts a set of (synthetic) Tafel data measured over a 100 mV overpotential window. To the eye, the data looks entirely linear, and fitting a Tafel slope to the entire dataset using OLS regression yields a Tafel slope of 130 mV/decade, with a standard error of 10 mV/decade. However, Fig. 5.2A illustrates the issue with this traditional Tafel analysis. Indeed, the original set of green data in the narrow overpotential regime is essentially entirely consistent, within experimental error, with two models possessing very different Tafel slopes. Model I has a Tafel slope of 80 mV/decade, while Model II has a Tafel slope of 120 mV/decade. Despite this wide berth in Tafel slope, the models align in the initial overpotential window because of their distinct limiting currents i_{lim}, which differ by a modest half order of magnitude. Clearly, the set of data measured in the inset of Fig. 5.2A is insufficient to distinguish between the two models, but this data insufficiency is entirely hidden by the traditional analysis approach.

Unlike the traditional analysis approach, Bayesian posterior sampling correctly identifies the Tafel slope ambiguity present in the original data. The green trace in Fig. 5.2B depicts the posterior distribution over the Tafel slope using solely the green data. This distribution is broad and markedly multimodal, with concentrations of probability density around the Model I and II Tafel slopes. In this manner, Bayesian posterior sampling correctly surmises that the original data is insufficient to pin down a value of the Tafel slope with high certainty. One possible solution to this issue is to measure additional data over a wider range of overpotentials. Depending on the true parameters of the electrochemical system under measurement, this experiment could yield either the blue data or the red data in Fig. 5.2A. When the Bayes posterior sampling algorithm is fed a combination of the green data and the red data, it correctly predicts a posterior distribution of Tafel slopes concentrated around the Model I Tafel slope. Conversely, when fed a combination of the green data and the blue data, it correctly predicts a posterior distribution of Tafel slopes concentrated around the Model II Tafel slope. In other words, multimodality in the posterior distribution predicted

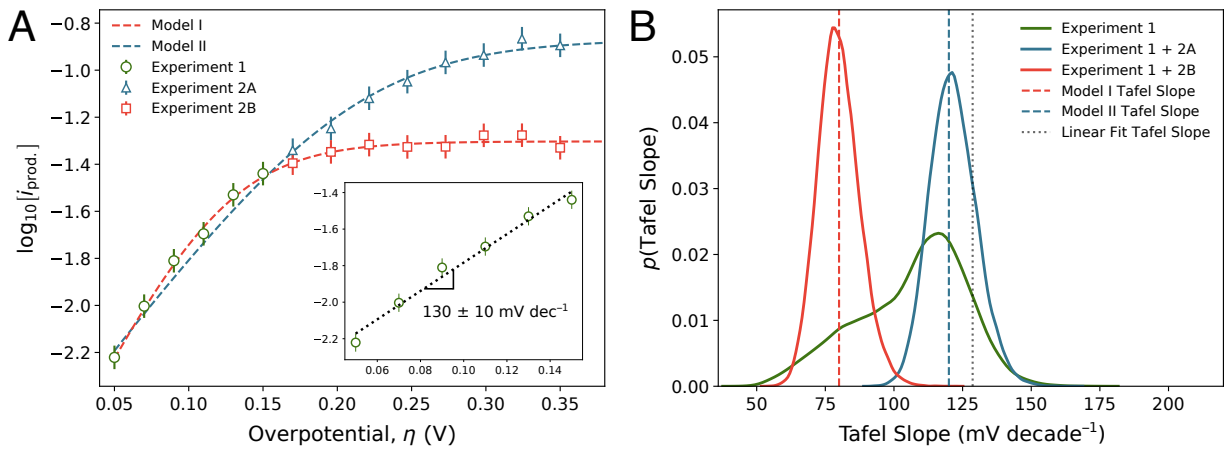

Figure 5.2: Bimodal posterior distributions signify Tafel slope ambiguity that cannot be clarified by the available data. (A, inset) Synthetic current-voltage data collected in hypothetical Experiment 1 appears linear over a 100 mV overpotential region, with a Tafel slope of 130 ± 10 mV/decade. (A) Synthetic current-voltage data over a broader range of overpotentials. The dashed lines show two models (I, II) with different Tafel slopes and plateau currents that could both reasonably fit the Experiment 1 data. Synthetic error bars represent one standard error of the mean of uncertainty in the synthetic data. Experiment 2A (blue triangles) and 2B (red squares) represent two possible outcomes of experiments that probe a broader range of overpotentials, which can clearly distinguish between Model I and Model II. (B) Bayes posterior distributions over the Tafel slope determined by our algorithm given various sets of observed data. If the algorithm is fed just the Experiment 1 data, the posterior distribution over the Tafel slope is broad and weakly bimodal, indicating that the Experiment 1 data is insufficient to discriminate between Model I and Model II. When fit to the Experiment 2A or 2B data in addition to the Experiment 1 data, this bimodality splits cleanly into two separate modes centered at the Model I and Model II Tafel slopes. Note that the linear fit to just the Experiment 1 data is distinct from both the Model I and Model II Tafel slopes.

by our algorithm is a hallmark of data insufficiency; when the underlying insufficiency is addressed, the algorithm neatly splits the distributional modes according to the observed data.

We highlight a couple of important conclusions from the synthetic data analysis presented in Fig. 5.2. First, current-voltage data used for Tafel slope estimation should ideally be measured until clear curvature is observed. If such a measurement is unnecessarily inconvenient or impossible, one should attempt to quantify the limiting current either through back-of-the-envelope estimates or through direct experimental control over the limiting current (e.g. with a rotating-disk electrode), and ensure that data used to estimate Tafel slopes is collected well below the limiting current density. Without information that elucidates the magnitude of the limiting current, it is impossible to ascertain the degree of limiting current-induced attenuation suffered by the current measured in the Tafel regime. Consequently, Tafel slopes estimated on the basis of a linear Tafel plot measured in a small overpotential window are likely systematically unreliable, and can harbor significant unquantified uncertainty. Second, the synthetic data analysis illustrates how the Bayesian posterior sampling approach can be employed iteratively with data acquisition efforts. Since the posterior distributions accurately quantify the uncertainty associated with a Tafel slope estimated given available data, an experimentalist can use this uncertainty information to guide future data acquisition until a desirable uncertainty threshold is achieved.

5.2.4 Evaluating Cardinal Preferences in Literature Data

In addition to being an important metric in assessing catalyst performance, the Tafel slope can be valuable because it may yield insight into the mechanism of a catalyzed electrochemical reaction. The connection between the Tafel slope, a macroscopically-measurable quantity, and the microscopic reaction mechanism is derived using microkinetic analysis invoking a whole host of ideality assumptions.[2,3] For an electrochemical reaction that proceeds through a number of elementary steps, one must assume that a single step determines the rate, and that all steps prior to the rate-determining step (RDS) are in quasi-equilibrium. Each of the quasi-equilibrated elementary steps carries an associated equilibrium constant which is possibly dependent on the applied potential. For potential-dependent equilibrium constants, one must additionally assume that the potential dependence goes exponentially in the (strictly integer) number of electrons transferred in the elementary step. The RDS has an associated forward rate constant, which is assumed to have a Butler-Volmer-like dependence on the applied potential, with a symmetry coefficient $\alpha = 1/2$.[1] Under these restrictive assumptions, one can derive (see Sec. 7.4) an equation for the Tafel slope of the entire chemical reaction (at $T = 298$ K),

$$\text{Tafel Slope} = \frac{60 \text{ mV/decade}}{n + q/2}, \tag{5.5}$$

where n is the total number of electrons transferred in elementary steps prior to the RDS, and q is the number of electrons transferred in the RDS.

Equation (5.5) gives rise to so-called "cardinal values" of the Tafel slope, which arise from evaluating the Tafel slope for different values of (n, q). Tafel slope values of 120, 60, and 40 mV/decade are familiar to most electrochemists, and arise from $(n, q) = (0, 1), (1, 0)$

and $(1, 1)$, respectively. Researchers routinely appeal to cardinal values to extract microscopic insight from experimentally-measured Tafel slopes. A common argumentative thrust goes: "my catalyst has a Tafel slope of 110 mV/decade, which is reasonably close to 120 mV/decade, indicating that the reaction proceeds through a rate-limiting first electron transfer step." This line of reasoning is only truly valid if the typical catalyst satisfies the ideality assumptions involved in deriving Eq. (5.5), a point that has been emphasized several times in the literature.[3–5] Comprehensive analysis of literature Tafel data can shed light on whether a typical catalyst satisfies these strict assumptions; if this is indeed true, then literature Tafel slopes should tend to cluster around the cardinal Tafel values predicted by Eq. (5.5).

Our Bayesian posterior sampling algorithm for Tafel slope fitting allows us to carry out an unbiased, automated survey of literature Tafel data to quantitatively test whether Tafel slope values reported in the literature show any preference for cardinal values. In this study, we choose to focus on re-analyzing Tafel data from the CO_2 reduction literature. We focus on this subsection of the literature because CO_2 reduction is a burgeoning field with diverse catalyst materials and morphologies,[30] and because product quantification requirements place Tafel analysis in this field in the low-data regime, as discussed previously. To carry out the literature survey, we digitized 344 distinct Tafel datasets from the CO_2 reduction literature and fed the resultant data to the Bayesian posterior sampling algorithm to produce re-analyzed estimates of the Tafel slope. Further information on the data mining and analysis procedure can be found in the Methods section.

Our re-analysis procedure uses Eq. (5.2) to interpret the literature Tafel datasets. As mentioned earlier, this model is only truly appropriate in the case of one kinetic control regime associated with a single Tafel slope; it cannot accurately capture current-voltage behavior under multiple kinetic regimes, which may be operative in at least some of the datasets we have analyzed. However, absent independent experimental confirmation of the physical mechanism underlying the observed multiple kinetic regimes (e.g. from spectroscopy or surface imaging), it is difficult to rigorously select a single model from the plethora that arise from enumerating microkinetic possibilities for intermediates in CO_2 reduction. Since the papers from the literature that we have re-analyzed fit a single Tafel slope to their data, and because they lack the experimental evidence required to pin down a richer physical model describing their data, we believe that uniform application of the model in Eq. (5.2) is an appropriate choice for our literature survey study. Our usage of Eq. (5.2) to interpret the data should not be construed as a blanket endorsement of this model in Tafel analysis. Indeed, if there is solid experimental evidence motivating the usage of a different kinetic model for a specific CO_2 reduction catalyst system, it can and should be employed under our Bayesian framework.

Figure 5.3A depicts a correlation plot of the MAP Tafel slope estimated by the Bayes posterior sampling approach versus the literature-reported Tafel slope. A significant fraction of the datasets fall within the 20% parity line, a strong sign that our algorithm produces Tafel slopes that are consistent with literature values when seeing identical data. Additionally, the MAP Tafel slope does not seem to systematically overestimate or underestimate the literature-reported value over a wide range of reported Tafel slopes. We note that complete parity between the MAP and literature Tafel slopes should not be expected; as explained previously, due to the possibility for subjectivity and systematic error with current literature practice for Tafel estimation, the MAP estimates derived by our algorithm are arguably more

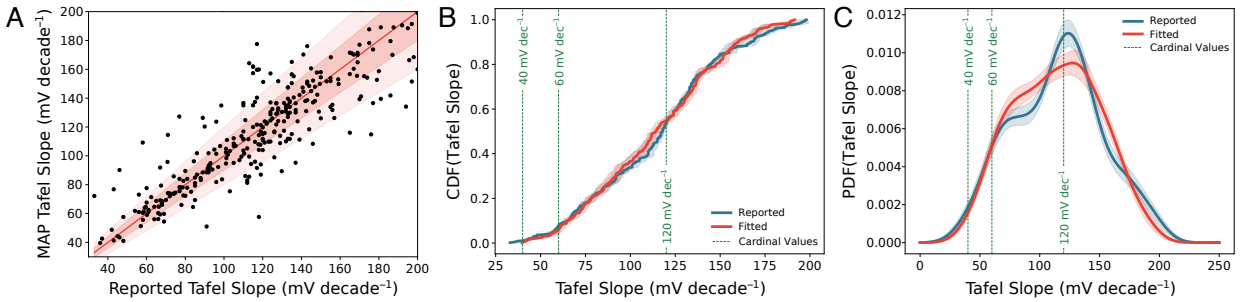

Figure 5.3: Unbiased refit of literature data using our Bayesian analysis approach reveals little preference for cardinal values of the Tafel slope for CO_2 reduction catalysts. (A) Correlation plot of reported Tafel slopes from the literature against MAP Tafel slopes fitted by our algorithm on identical data. The solid red line represents perfect agreement, while the red filled intervals are lines representing 10% and 20% relative error. (B) Cumulative distribution function of the Tafel slopes reported in literature data (blue), and those refitted by our algorithm (red). Error intervals correspond to one standard deviation of bootstrapped resamples. (C) Kernel density estimates (KDE) of the empirical probability distribution function of Tafel slopes reported in literature data (blue) and MAP Tafel slopes refitted by our algorithm (red). Error intervals correspond to one standard deviation of bootstrapped resamples. Green dashed lines in both (B, C) correspond to cardinal values of the Tafel slope predicted by Eq. (5.5).

trustworthy than the literature-reported values.

Figures 5.3B and 5.3C depict estimates of the distributional tendencies of the MAP and literature-reported Tafel slopes. Figure 5.3B plots the empirical cumulative distribution function (CDF) of the MAP Tafel slope (red trace) and the literature-reported Tafel slopes (blue trace). The low-opacity intervals in both Fig. 5.3B and Fig. 5.3C span one standard deviation of several bootstrapped resamples drawn with replacement (see Methods section for additional detail on the bootstrapping procedure), and are useful for examining the sensitivity of our distributional results to the specific subsampling of literature data we have chosen to analyze.[31] The CDF value for a given Tafel slope value m_{T} tallies the running fraction of datasets that have a Tafel slope value of at most m_{T}. If Tafel slopes truly cluster around cardinal values, the running fraction should increase sharply around those preferred values, and one would expect to see sigmoidal features in the CDF at the cardinal values. Figure 5.3 shows little evidence of such locally sigmoidal behavior; rather, we see something resembling a straight line, corresponding to a roughly uniform distribution over the range of Tafel slopes considered.

We can visualize the distributional data in a different way by examining the empirical probability distribution function (PDF) of the Tafel slopes. Estimating the PDF of a distribution given a set of samples is a notoriously difficult problem in statistics, because relatively small amounts of sampling noise can result in the presence of spurious peaks in the PDF. Several techniques exist for tackling this problem; here, we employ Gaussian kernel density estimation, which constructs an estimate of the PDF by summing appropriately-normalized Gaussian kernel functions centered at each of the observed data points. Additional details

on the kernel density estimation procedure are reported in the Methods section. Figure 5.3C shows a kernel density estimate of the PDF of the MAP (red trace) and literature-reported (blue trace) Tafel slopes. Based on the shape of the PDFs and their corresponding standard errors, we conclude that there is a slight preference to assign Tafel slope values around 70 and 125 mV/decade in the literature that essentially disappears when the same data is re-analyzed with our approach. While a small peak persists around 125 mV/decade in the MAP Tafel slopes, the height of the peak is roughly within the error bound. We also note that any residual preference for cardinal values in the MAP Tafel slopes can possibly be explained by data acquisition biases. While the Bayesian approach we develop removes subjectivity from data analysis, we cannot remove biases introduced during data collection; it is at least plausible that such biases exist given that the literature-reported values significantly overestimate the concentration of Tafel slopes around 120 mV/decade compared to the MAP values.

The results presented in Fig. 5.3 combine data from several studies using different catalyst materials to assess whether or not a preference for cardinal Tafel slopes exists broadly across all CO_2 reduction catalysts. In order to confirm that this apparent lack of cardinal preference in the entire dataset is not simply an artifact introduced by pooling together separate catalyst materials which each individually exhibit a cardinal preference, we broke out the PDF analysis in Fig. 5.3 according to catalyst material identity. Upon examining the results from the breakout analysis (see Sec. 7.4), we conclude that the apparent lack of cardinality we find in Fig. 5.3 indeed persists when separately examining Tafel slopes from common materials used in CO_2 reduction catalysts: Ag, Au, Cu, Sn, Zn. Curiously, it appears that Bi-based materials do show a preference for Tafel slope values around 120 mV/decade, which may inform future mechanistic studies on these catalysts. As a caveat, we note our Bi results comprise only 27 distinct Tafel datasets, and are hence subject to a high degree of variability arising from the specific set of studies we chose to re-analyze; future work that attempts to weigh in on this question should ideally perform new experiments on well-controlled Bi surfaces and use the data acquisition and analysis recommendations identified in this work. Taken together, the results presented in Fig. 3 and the material breakout analysis in Sec. 7.4 lead us to conclude that, when analyzed in an unbiased fashion, experimental data in the literature does not support a systematic preference for cardinal values of the Tafel slope among CO_2 reduction catalysts.

While we are not in a position to identify the cause for deviation from cardinal Tafel slope values in each specific Tafel dataset comprising Fig. 5.3, we advance the hypothesis that these deviations could originate from physical non-idealities that violate the assumptions involved in deriving Eq. (5.5). To test this hypothesis, we attempt to ascertain the manner in which a select few simple physical non-idealities can adjust the PDF of Tafel slopes that would otherwise be concentrated around cardinal values. In this regard, we consider three possible physical effects that violate the ideality assumptions used to arrive at Eq. (5.5). These three effects comprise a very small subset of the menagerie of physical non-idealities that could operate in CO_2 reduction electrocatalysis; our goal is simply to show that these effects can spoil a preference for cardinal values of the Tafel slope, not to single out these particular effects as the only non-idealities present in CO_2 reduction.

First, we consider the possibility that the symmetry coefficient $\alpha \neq 1/2$. Such deviations could arise, for example, due to disparate local slopes of the Marcus free energy surfaces at

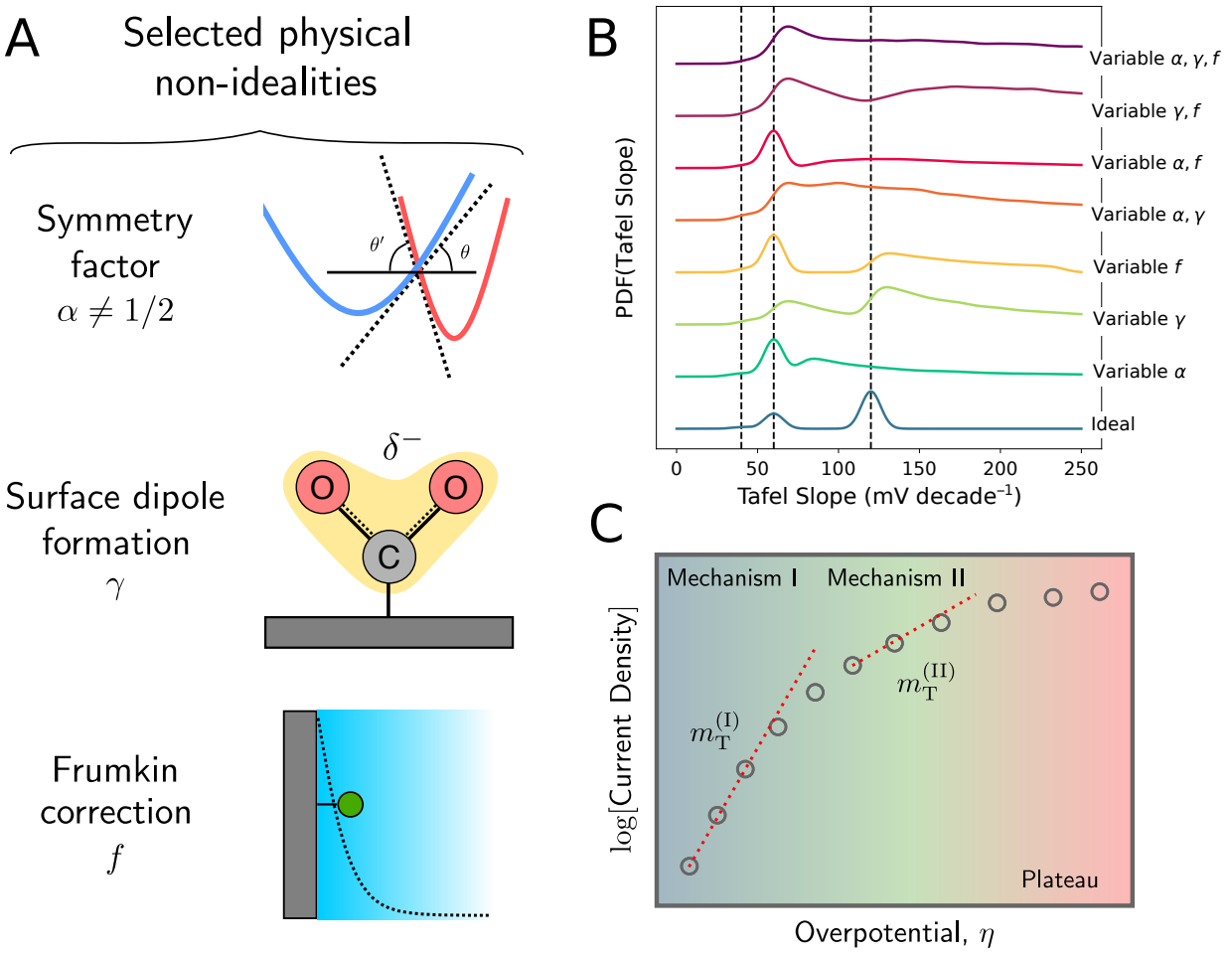

Figure 5.4: Physical hypotheses for the lack of observed cardinality in literature Tafel slopes. (A) Schematic of three selected physical non-idealities which can affect the measured Tafel slope. (B, blue trace) Synthetic kernel density estimate of the probability distribution over Tafel slopes for a "random" CO_2 reduction catalyst, peaked around the cardinal values predicted by Eq. (5.5). (B, other traces) Several synthetic kernel density estimates of the probability distributions over the Tafel slope generated from including random values of different parameters governing physical non-idealities. (C) Schematic illustrating the possibility of measuring data across separate kinetic regimes in a Tafel analysis. Due to a switch in mechanism, different overpotential regimes exhibit different Tafel slopes, complicating interpretation of a single Tafel slope value fit straddling both regimes.

their crossing point, or reactant species position fluctuations in the electrochemical double layer.[32–35] Second, we examine the effect of partial charge transfer or surface dipole formation in the adsorption of CO_2 to the electrode surface, phenomena that have been hypothesized and characterized in prior studies on CO_2 reduction.[29,36] Mathematically, the formation of a surface dipole introduces a potential dependence in the adsorption equilibrium constant which mathematically resembles a partial charge transfer parameter γ. Third, we introduce a possible Frumkin correction f originating from the protrusion of an electrode-adsorbed species into the electrochemical double layer, which attenuates the applied potential due to electrostatic screening effects.[1] The Frumkin correction is most important at low supporting salt concentration (and hence large resultant electrolyte screening length), but it has been considered in the context of CO_2 reduction electrocatalysis.[29] Each of these non-idealities depends on the value of a non-ideality parameter. Of course, we have no idea, at least a priori, about the distribution of values these non-ideality parameters can take in typical CO_2 reduction catalyst systems. In the absence of information, we make the maximally ignorant choice, and assume that the non-ideality parameters are drawn from uniform distributions within a reasonable set of bounds. Once we postulate these uniform distributions, we can examine how randomly selected non-ideality parameters deform a distribution of Tafel slopes that begins concentrated around cardinal values.

The blue trace in Fig. 5.4B shows a distribution of Tafel slopes concentrated around the cardinal values predicted by Eq. (5.5). The relative heights of the cardinal value peaks are selected by artificially binning the distribution over MAP Tafel slopes into buckets centered around the cardinal values. The effects of randomly drawn physical non-idealities on this distribution can be examined using Monte Carlo simulation. Briefly, we sample a Tafel slope from the distribution depicted in the blue trace, sample the values of one or more non-ideality parameters, and finally calculate the resultant Tafel slope in the presence of non-idealities (see Methods section for additional details). Repeating the sampling procedure several times yields distributions over the Tafel slope, depicted as multicolored traces in Fig. 5.4B for different sets of non-idealities. Evidently, even rather mundane pieces of additional physics like the ones discussed above can produce stark changes in the distribution of Tafel slopes, spanning a range of behavior from moving certain peaks away from cardinal values to smearing out the entire distribution. While we cannot prove with certainty that physical non-idealities are responsible for the lack of observed Tafel cardinality in the literature, the results in Fig. 5.4B demonstrate that this is at least a plausible explanation for the observed behavior.

Alternatively, the observed lack of cardinality may also be a consequence of interpreting current-voltage data measured under several disparate kinetic regimes through the lens of Eq. (5.2), which cannot capture these intricacies. As illustrated schematically in Fig. 5.4C, the kinetic regimes may exhibit different Tafel slopes; in this case, mechanistic interpretation of a single Tafel slope extracted by fitting Eq. (5.2) to the data is inappropriate. Indeed, as examined in more detail in Sec. 7.4, fitting synthetic data generated from a model with multiple cardinal Tafel slope regimes using Eq. (5.2) can produce an off-cardinal Tafel slope value. This underscores the need to rigorously characterize the several physical complexities present in catalytic systems for CO_2 reduction, as they can complicate mechanistic interpretation guided solely by the Tafel slope.

Taken in their entirety, the results presented in Figures 5.3 and 5.4 present some com-

pelling reasons for the community to rethink the current approach of deducing mechanistic information purely from Tafel slope data. Indeed, the prevalence of Tafel slopes in the CO_2 reduction literature that do not fall neatly on cardinal values suggests that physical non-idealities, omitted by Eq. (5.5), may be commonplace in typical catalytic systems. The familiar approach of "rounding" experimentally-measured Tafel slopes to their nearest cardinal value to guide mechanistic interpretation, then, leaves one prone to interpreting experimental data in an overly simplistic manner. Rather than hand-wave away the physical complexities present in catalytic systems with strong ideality assumptions, we believe it is important to interpret Tafel data alongside several other pieces of experimental data (e.g. more diverse electrochemical kinetic data, surface-sensitive spectroscopy, materials characterization, etc.). In this manner, one can take a non-cardinal Tafel slope (and its associated uncertainty based on the data) at face value, and build a holistic physical picture that attempts to explain the deviation from cardinality in a manner consistent with all other experimental observations. Ideally, all these observations can be interpreted in the context of a richer model that allows one to determine the true breadth of physical phenomena present across a wide range of operating parameters, as has been done in some select studies in the literature.[2,28,37] We believe our Bayesian data analysis approach will be equally useful for rigorously quantifying parametric uncertainties in the suggested new paradigm for kinetic data interpretation.

5.3 Methods

5.3.1 Data Mining and Re-Analysis

We built up a dataset of Tafel measurements reported in the literature by manually extracting figures from published papers and digitizing them using the WebPlotDigitizer tool.[38] A full accounting of all papers and corresponding figures can be found in Sec. 7.4. When selecting datasets to analyze, we excluded those that reported continuous current-voltage data, because it is difficult to ascertain the underlying data density associated with a continuous curve, because our method is meant to address the unique challenges of estimating Tafel slopes with a small amount of data, and because continuous current-voltage data may be unreliable because product selectivity is not always 100%, especially in CO_2 reduction. We also excluded datasets that reported current-voltage data but did not report an explicit value of the Tafel slope. We assumed that all datasets were collected with appropriate experimental techniques (IR-correction for solution resistance has already been applied, etc.), and did not modify or omit any data from a figure during the digitization process. After digitization, each dataset was tagged with manually entered metadata to facilitate re-analysis. A full accounting of the metadata fields, as well as a complete record of all scraped data and metadata, is available in Sec. 7.4.

Re-analysis of the data was carried out using the Python-based `julius` package, developed in-house to handle data collation and Bayesian posterior sampling workflows. In order to determine prior distributions for the parameters, we first find an optimal set of parameters θ^* for the limiting current model using an implementation of the trust-region reflective (TRF) algorithm implemented in the optimization and root finding package included in SciPy.[39] For each model parameter θ_i, we select uniform prior distributions supported on

the interval $[0, a \times \theta_i^*]$, with $a = 10$ (note that all parameters we fit in this study are strictly non-negative). For all models studied here, we find that the posterior distribution does not depend on the value of a, indicating that the data imposes strong preferences on the optimal model fit (see Sec. 7.4 for detailed sensitivity analysis). For each dataset, we draw $N = 4 \times 10^4$ total samples (10^4 samples from four independent chains, each burning their first 2000 samples) from the posterior distribution using the No-U-Turn Hamiltonian Monte Carlo sampler (NUTS) implemented in the PyMC3 probabilistic programming package.[40]

In total, we re-analyzed 344 distinct Tafel datasets. Figure 5.3A restricts to both reported and MAP Tafel slopes $m_{\mathrm{T}} \in [0, 200]$, which comprises 300 distinct Tafel datasets. A correlation plot including all analyzed Tafel datasets is reported in Sec. 7.4.

5.3.2 Kernel Density Estimation

We use kernel density estimation (KDE) to estimate probability distributions given a finite set of samples. KDEs are used in the distributional visualizations in Figs. 5.2, 5.3, and 5.4. We use the Gaussian KDE function in the statistics package included in SciPy, and use Scott's rule for bandwidth selection in Figs. 5.2 and 5.3. Since the estimates in Fig. 5.4 are meant to emulate the result of a single simulated experimental observation with some associated error, here we use a pre-specified bandwidth of 6 mV/decade.

5.3.3 Bootstrap Resampling

We carry out a bootstrap resampling procedure to quantify the degree of variability of the results in Fig. 5.3 associated with our choice of a specific subset of literature data.[31] Essentially, we posit that the observed distribution over the Tafel slope is a good estimate of the true underlying distribution, and then resample several datasets of the same size as the original dataset from this distribution with replacement (i.e. samples can show up more than once, or not at all). The error intervals presented in Figs. 5.3A and 5.3B are gleaned from one standard deviation of 20 such bootstrapped resamples.

5.3.4 Monte Carlo Simulation

We use Monte Carlo simulation to estimate the distributional changes precipitated in a Tafel slope distribution by the physical non-idealities identified in the main text. To carry out this procedure, we begin with the distribution presented in Fig. 5.4A, which is generated by artificially bucketing the MAP Tafel slopes from the literature analysis into the bins $\{[0, 50), [50, 90), [90, \infty)\}$. We sample the physical non-ideality parameters according to $\alpha \sim \mathrm{Unif}[0.20, 0.80]$, $\gamma \sim \mathrm{Unif}[0, 1]$, $f \sim \mathrm{Unif}[0.50, 1.00]$, where $\mathrm{Unif}[a, b]$ signifies a uniform distribution supported on the interval $[a, b]$. For each set of non-idealities, we draw $N = 4 \times 10^4$ total posterior samples (10^4 samples from four independent chains, each burning their first 500 samples). The equations governing modifications to the Tafel slope based on physical nonidealities are worked out in Sec. 7.4. A sensitivity analysis of the Tafel slope distributions including non-idealities with respect to the bounds of the uniform distributions over non-ideality parameters is also reported in Sec. 7.4. All Monte Carlo simulation is again carried out using the PyMC3 probabilistic programming package.[40]

5.4 References

[1] Allen J Bard, Larry R Faulkner, Johna Leddy, and Cynthia G Zoski. *Electrochemical methods: fundamentals and applications*, volume 2. Wiley New York, 1980.

[2] Aaron T Marshall. Using microkinetic models to understand electrocatalytic reactions. *Curr. Opin. Electrochem.*, 7:75–80, 2018.

[3] Tatsuya Shinagawa, Angel T Garcia-Esparza, and Kazuhiro Takanabe. Insight on tafel slopes from a microkinetic analysis of aqueous electrocatalysis for energy conversion. *Sci. Rep.*

[4] Ya-Hui Fang and Zhi-Pan Liu. Tafel kinetics of electrocatalytic reactions: from experiment to first-principles. *ACS Catal.*, 4(12):4364–4376, 2014.

[5] Marco Dunwell, Wesley Luc, Yushan Yan, Feng Jiao, and Bingjun Xu. Understanding surface-mediated electrochemical reactions: Co2 reduction and beyond. *ACS Catal.*, 8 (9):8121–8129, 2018.

[6] M Gattrell, N Gupta, and A Co. A review of the aqueous electrochemical reduction of co2 to hydrocarbons at copper. *J. Electroanal. Chem.*, 594(1):1–19, 2006.

[7] Xiaoxia Chang, Tuo Wang, Zhi-Jian Zhao, Piaoping Yang, Jeffrey Greeley, Rentao Mu, Gong Zhang, Zhongmiao Gong, Zhibin Luo, Jun Chen, et al. Tuning cu/cu2o interfaces for the reduction of carbon dioxide to methanol in aqueous solutions. *Angew. Chem.*, 130(47):15641–15645, 2018.

[8] Lei Zhang, Zhi-Jian Zhao, and Jinlong Gong. Nanostructured materials for heterogeneous electrocatalytic co2 reduction and their related reaction mechanisms. *Angew. Chem. Int. Ed.*, 56(38):11326–11353, 2017.

[9] Chan Woo Lee, Nam Heon Cho, Ki Dong Yang, and Ki Tae Nam. Reaction mechanisms of the electrochemical conversion of carbon dioxide to formic acid on tin oxide electrodes. *ChemElectroChem*, 4(9):2130–2136, 2017.

[10] Qi Lu, Jonathan Rosen, and Feng Jiao. Nanostructured metallic electrocatalysts for carbon dioxide reduction. *ChemCatChem*, 7(1):38–47, 2015.

[11] Chan Woo Lee, Nam Heon Cho, Sang Won Im, Michael Shincheon Jee, Yun Jeong Hwang, Byoung Koun Min, and Ki Tae Nam. New challenges of electrokinetic studies in investigating the reaction mechanism of electrochemical co 2 reduction. *J. Mat. Chem. A*, 6(29):14043–14057, 2018.

[12] Nathan Corbin, Joy Zeng, Kindle Williams, and Karthish Manthiram. Heterogeneous molecular catalysts for electrocatalytic co 2 reduction. *Nano Res.*, pages 1–33, 2019.

[13] Qi Lu and Feng Jiao. Electrochemical co2 reduction: Electrocatalyst, reaction mechanism, and process engineering. *Nano Energy*, 29:439–456, 2016.

[14] Wolfgang Schmickler and Elizabeth Santos. *Interfacial electrochemistry*. Springer Science & Business Media, 2010.

[15] Ezra L Clark, Joaquin Resasco, Alan Landers, John Lin, Linh-Thao Chung, Amber Walton, Christopher Hahn, Thomas F Jaramillo, and Alexis T Bell. Standards and protocols for data acquisition and reporting for studies of the electrochemical reduction of carbon dioxide. *ACS Catal.*, 8(7):6560–6570, 2018.

[16] Kindle Williams, Nathan Corbin, Joy Zeng, Nikifar Lazouski, Deng-Tao Yang, and Karthish Manthiram. Protecting effect of mass transport during electrochemical reduction of oxygenated carbon dioxide feedstocks. *Sustain. Energy Fuels*, 3(5):1225–1232, 2019.

[17] Meenesh R Singh, Ezra L Clark, and Alexis T Bell. Effects of electrolyte, catalyst, and membrane composition and operating conditions on the performance of solar-driven electrochemical reduction of carbon dioxide. *Phys. Chem. Chem. Phys.*, 17(29):18924–18936, 2015.

[18] Meenesh R Singh, Jason D Goodpaster, Adam Z Weber, Martin Head-Gordon, and Alexis T Bell. Mechanistic insights into electrochemical reduction of co2 over ag using density functional theory and transport models. *Proc. Natl. Acad. Sci.*, 114(42):E8812–E8821, 2017.

[19] Benjamin A Zhang, Tuncay Ozel, Joseph S Elias, Cyrille Costentin, and Daniel G Nocera. Interplay of homogeneous reactions, mass transport, and kinetics in determining selectivity of the reduction of co2 on gold electrodes. *ACS Cent. Sci.*, 5(6):1097–1105, 2019.

[20] Steven Michael Brown. *Catalysis and reactor engineering for the electrochemical conversion of carbon dioxide to carbon monoxide*. PhD thesis, Massachusetts Institute of Technology, 2019.

[21] Damien Voiry, Manish Chhowalla, Yury Gogotsi, Nicholas A Kotov, Yan Li, Reginald M Penner, Raymond E Schaak, and Paul S Weiss. Best practices for reporting electrocatalytic performance of nanomaterials, 2018.

[22] Michael J. Rosenfeld. Ols in matrix form. `https://web.stanford.edu/~mrosenfe/soc_meth_proj3/matrix_OLS_NYU_notes.pdf`.

[23] Karthish Manthiram, Brandon J Beberwyck, and A Paul Alivisatos. Enhanced electrochemical methanation of carbon dioxide with a dispersible nanoscale copper catalyst. *J. Am. Chem. Soc.*, 136(38):13319–13325, 2014.

[24] W.M. Deen. *Analysis of Transport Phenomena*. Topics in chemical engineering. Oxford University Press, 2012. ISBN 9780199740284. URL `https://books.google.com/books?id=60YsAwEACAAJ`.

[25] Shuo-Huan Hsu, Stephen D Stamatis, James M Caruthers, W Nicholas Delgass, Venkat Venkatasubramanian, Gary E Blau, Mike Lasinski, and Seza Orcun. Bayesian framework for building kinetic models of catalytic systems. *Ind. Eng. Chem. Res.*, 48(10):4768–4790, 2009.

[26] Charles Miller Grinstead and James Laurie Snell. *Introduction to probability*. American Mathematical Soc., 2012.

[27] D.L. Chandler and D. Wu. *Introduction to Modern Statistical Mechanics*. Oxford University Press, 1987. ISBN 9780195042771. URL `https://books.google.com/books?id=3taTh5D-CDsC`.

[28] Joy S Zeng, Nathan Corbin, Kindle Williams, and Karthish Manthiram. Kinetic analysis on the role of bicarbonate in carbon dioxide electroreduction at immobilized cobalt phthalocyanine. *ACS Catal.*, 10(7):4326–4336, 2020.

[29] Stefan Ringe, Carlos G Morales-Guio, Leanne D Chen, Meredith Fields, Thomas F Jaramillo, Christopher Hahn, and Karen Chan. Double layer charging driven carbon dioxide adsorption limits the rate of electrochemical carbon dioxide reduction on gold. *Nat. Commun.*, 11(1):1–11, 2020.

[30] Rern Jern Lim, Mingshi Xie, Mahasin Alam Sk, Jong-Min Lee, Adrian Fisher, Xin Wang, and Kok Hwa Lim. A review on the electrochemical reduction of co2 in fuel cells, metal electrodes and molecular catalysts. *Catal. Today*, 233:169–180, 2014.

[31] Bradley Efron and Robert J Tibshirani. *An introduction to the bootstrap*. CRC press, 1994.

[32] J O'M Bockris and Z Nagy. Symmetry factor and transfer coefficient. a source of confusion in electrode kinetics. *J. Chem. Ed.*, 50(12):839, 1973.

[33] David Chandler. Electron transfer in water and other polar environments, how it happens. In *Classical and Quantum Dynamics in Condensed Phase Simulations*, pages 25–49. WORLD SCIENTIFIC, jun 2010. ISBN 978-981-02-3498-0. doi: 10.1142/9789812839664_0002. URL `http://www.worldscientific.com/doi/abs/10.1142/9789812839664{_}0002`.

[34] Rolando Guidelli, Richard G Compton, Juan M Feliu, Eliezer Gileadi, Jacek Lipkowski, Wolfgang Schmickler, and Sergio Trasatti. Defining the transfer coefficient in electrochemistry: An assessment (iupac technical report). *Pure Appl. Chem.*, 86(2):245–258, 2014.

[35] Aditya M Limaye and Adam P Willard. Modeling interfacial electron transfer in the double layer: the interplay between electrode coupling and electrostatic driving. *J. Phys. Chem. C*, 2019.

[36] Rolando Guidelli and Wolfgang Schmickler. Electrosorption valency and partial charge transfer. In *Modern Aspects of Electrochemistry*, pages 303–371. Springer, 2005.

[37] Prosper K Adanuvor and Ralph E White. Analysis of electrokinetic data by parameter estimation and model discrimination technqiues. *J. Electrochem. Soc.*, 135(8):1887, 1988.

[38] Ankit Rohatgi. Webplotdigitizer, 2017.

[39] Pauli Virtanen, Ralf Gommers, Travis E Oliphant, Matt Haberland, Tyler Reddy, David Cournapeau, Evgeni Burovski, Pearu Peterson, Warren Weckesser, Jonathan Bright, et al. Scipy 1.0: fundamental algorithms for scientific computing in python. *Nat. Methods*, 17(3):261–272, 2020.

[40] John Salvatier, Thomas V Wiecki, and Christopher Fonnesbeck. Probabilistic programming in python using pymc3. *PeerJ Comput. Sci.*, 2:e55, 2016.

Chapter 6

Electrochemical Characterization Using Analysis of Weakly Nonlinear Response to Small Amplitude Oscillating Voltage Signals

6.1 Introduction

Electrochemical characterization techniques have enjoyed increased use as electrochemical approaches begin to find more productive applications in energy storage, catalysis, biochemical sensing, and several other related fields. Fundamentally, all of these applications rely on optimizing the rate of an interfacial electron transfer (ET) reaction by turning a number of physical handles, such as the identity of the ET catalyst material or the chemical composition of the environment. Research efforts to optimally design chemicals and materials for these applications are crucially dependent on effective electrochemical characterization techniques, which extract the values of microscopic parameters that describe system performance from macroscopic electrochemical measurements. Electrochemical characterization techniques have a storied history, with modern polarographic techniques first arising in the early 1900s, which ultimately gave rise to the staple characterization tool of today, the cyclic voltammetry (CV) experiment. Although CV is taught and used widely, it comes with a number of mathematical and physical drawbacks, stemming from the fact that CV is based on analyzing electrochemical system response to a large voltage driving force. First of all, since analytical methods to analyze large driving force response are limited, CV parameter extraction techniques can only utilize certain features of a voltammogram (peak positions, peak voltages) and simply throw out the remaining measured data. Additionally, a number of practical difficulties can arise when the driving force in a CV experiment exceeds the electrochemical stability window of the solvent, resulting in occluded peaks and more inexact parameter extraction.

We develop an alternative, modern technique for electrochemical characterization that is predicated on probing systems with controllably small amplitude voltage driving forces. Restricting ourselves to small amplitude driving allows us to employ the tools of time-dependent

perturbation theory, which we use to derive a set of analytical relationships that predict the nonlinear electrochemical current response to an oscillatory voltage signal. These relationships can be used to extract electrochemical system parameters in an accurate manner that efficiently uses all the measured data, without running into the drawbacks typically associated with CV techniques. Our oscillating voltage characterization technique can be used alongside traditional CV experiments, and it is especially well-suited to a high-throughput data collection context, when minimizing experimental acquisition time and data efficiency are imperative.

In this manuscript, we begin by describing the well-developed, textbook approaches to electrochemical characterization. Subsequently, we derive a mathematical framework, based on Fourier analysis and time-dependent perturbation theory, which can be employed to predict the nonlinear response of an electrochemical system to an oscillatory voltage input. By comparison to results from numerical simulations, we demonstrate that our approach can accurately predict the response of an electrochemical system given a known set of underlying parameters. Finally, we apply our approach to extract the microscopic parameters of the ferrocyanide/ferricyanide redox couple, using both sinusoidal voltage inputs as well as windowed chirp voltage inputs, which can probe the system at multiple frequencies simultaneously. We find that our approach produces parameter values that are in line with those reported in the literature and those predicted by alternative methods of electrochemical characterization.

6.2 Approaches to Electrochemical Characterization

Electrochemical reactions generally take place at a solid-electrolyte interface, where a reactive species either donates or accepts an electron from an electrode material. The kinetics of this process are generally modeled phenomenologically using the Butler-Volmer kinetic expression, which involves certain microscopic parameters that encapsulate the chemical details of the system.[1] The goal of electrochemical characterization techniques is to carry out macroscopic measurements that can supply information about the values of the microscopic kinetic parameters. Generally, most measurements of this sort involve imposing a controlled potential difference between a working and reference electrode in an electrochemical cell, and measuring the resultant current density, or vice-versa. Since the current density quantifies the magnitude of electron flux through the electrode material, it may be related to the total rate of the electrochemical reaction at the interface. Although the total rate of reaction is influenced by the kinetics of the interfacial reaction, it may also, in certain potential regimes, be controlled by the rate of diffusive reactant (product) transport to (from) the interface. Hence, electrochemical characterization techniques must effectively deconvolute the effects of interfacial reaction kinetics from diffusive transport effects in order to accurately determine the microscopic kinetic parameters of the reaction of interest.[2]

Cyclic voltammetry (CV) is a workhorse tool of electrochemical characterization, used in several different contexts including, discovering more active catalysts for electrochemical synthesis[3,4], screening active compounds for flow batteries[5,6], and developing improved biological sensors.[7,8] CV experiments apply a time-varying triangular waveform between the working and reference electrodes of a cell, which sweeps across a potential window of several

100 mV at a predefined scan rate, which can vary over several orders of magnitude depending on the system under study.[9] If the electrochemical reaction at the boundary involves a simple redox couple described accurately by Butler-Volmer kinetics, the resultant current waveform initially rises exponentially, and then peaks and falls as the current response becomes transport-controlled. On the reverse portion of the triangular voltage waveform, the system passes current in the opposite direction, again rising exponentially and then peaking, resulting in a familiar peak-and-trough duck-shaped voltammogram curve (a current vs. voltage phase plot). There is a rich history of techniques developed to determine parameters by graphical analysis of voltammograms. For example, the equilibrium potential of the redox couple may be determined by averaging the positions of the reductive and oxidative peaks on the voltammogram.[9,10] Determining the kinetic rate constant is slightly more involved; one must carry out a series of CV experiments at successively increasing scan rates, and extract its value by means of linear regression on the voltages and currents of all the CV peaks.[5,10,11]

While parameter extraction from CV is well-developed in the literature, it suffers some drawbacks resulting from its reliance on applying a large amplitude voltage waveform. For one, due to the nonlinear nature of the reaction-diffusion problem encoding the mathematical relationship between the voltage input and the current response, analytical tools are extremely limited in the high amplitude voltage regime. Existing approaches must rely on asymptotic analysis techniques which relate characteristics of the voltammogram peaks to the underlying microscopic parameters.[2,11] While such relationships are useful, they inherently imply low data utilization; despite measuring an entire voltammogram curve in the lab, one can only quantitatively use the information encoded in the peaks, discarding the majority of the measured dataset. A second difficulty may arise when the equilibrium potential of the redox couple of interest lies near an edge of the electrochemical stability window of the electrolyte solution. If the potential window swept out by the triangular voltage waveform lies outside the stability window, the voltammetric data will be polluted by current from an adventitious electrochemical reaction involving solvent.[9] Since the solvent is present at much larger concentration than the redox couple, its current response swamps the signal from the solvent, cloaking the voltammogram peak required for parameter extraction. Taken together, these difficulties can make parameter extraction from CV either impossible entirely, or inefficient with respect to the measured data.

Potentiostatic electrochemical impedance spectroscopy (PEIS) is a complementary technique to CV that is also used widely for electrochemical characterization. PEIS experiments typically proceed by applying low amplitude (1–5 mV) voltage waveforms at a wide range of frequencies between the working and reference electrodes of a cell.[12] At low enough amplitudes, the system responds in a linear manner, producing an output current waveform at the same frequency as the input voltage waveform, usually with a different amplitude and phase. The results of a PEIS experiment are analyzed under the formalism of linear circuit theory, which represents both the voltage and current waveforms at a single frequency as complex-valued "phasors." The impedance Z is the (complex) ratio of the current and voltage phasors, and can take on different values at different frequencies, resulting in an impedance spectrum, the main product of a PEIS experiment. While impedance spectra are often used to characterize electrochemical systems, the models employed in the analysis are generally phenomenological, introducing fictive quantities like a charge-transfer resistance

or a constant-phase element, which can be difficult to relate to the underlying microscopic parameters of the Butler-Volmer equation.[13,14]

We develop a new characterization technique based around applying a small amplitude oscillating voltage input signal $V(t)$ to an electrochemical system, and observing the resultant oscillatory current density response signal, $J(t)$. As depicted in the top row of Fig. 6.1, the relationship between the input voltage and output current in the time domain is encoded by a coupled reaction-diffusion partial differential equation (PDE) model that involves the microscopic parameters of the electrochemical reaction. While the PDE model is difficult to solve analytically in the time domain, it can be analyzed readily in the frequency domain by means of a perturbative expansion in powers of ϵ, a small parameter associated with the amplitude of the input voltage signal $V(t)$, as depicted in the bottom row of Fig. 6.1. The perturbative expansion links the frequency domain representations of the voltage, $\hat{V}(\nu)$ and the current density $\hat{J}(\nu)$ in an analytical Volterra series structure that explicitly involves the microscopic parameters of the electrochemical system.[15] Armed with this analytical relationship between the current output and voltage input in the frequency domain, we can analyze the results of an oscillating voltage experiment to extract information about the microscopic parameters of an electrochemical reaction.

6.3 Theory and Numerical Validation

For the purposes of illustrating our approach, we choose to focus here on a simple model electrochemical system: a quiescent electrolyte solution prepared with both the oxidized and reduced states of a redox couple at known, dilute concentrations. Under these conditions, transport of the two species may be modeled by the time-dependent diffusion equation in one spatial dimension,[16]

$$\frac{\partial}{\partial t}c_k(t,z) = \mathcal{D}\frac{\partial^2}{\partial z^2}c_k(t,z) \tag{6.1}$$

where $c_k(t,z)$ describes the concentration of species $k \in (1,2)$ at time $t \in [0,\infty)$ and spatial position $z \in [0,\infty)$, and $\mathcal{D}$ is the Fickian diffusion coefficient (assumed to be identical for both species). Solving the pair of PDEs in Eq. (6.1) requires specification of boundary and initial conditions corresponding to the quiescent electrolyte system. The most salient boundary condition is specified at the electrode-electrolyte boundary, where the redox couple participates in an electrochemical reaction whose rate is described by the Butler-Volmer kinetic expression,[1]

$$-\mathcal{D}\left.\frac{\partial}{\partial z}c_1(t,z)\right|_{z=0} = k_0\left[c_1(t,z=0)e^{-\beta e\alpha(V(t)-E_{\text{eq}})} - c_2(t,z=0)e^{+\beta e(1-\alpha)(V(t)-E_{\text{eq}})}\right] \tag{6.2}$$

where $\beta \equiv (k_{\text{B}}T)^{-1}$ is the thermodynamic inverse temperature, e is the fundamental charge, k_0 is the rate constant, α is the transfer coefficient, E_{eq} is the equilibrium potential of the redox couple, and $V(t)$ is the time-dependent voltage input signal. The remaining boundary and initial conditions encode the mathematical requirements imposed by reaction stoichiometry and the physical setting of a quiescent solution with a fixed ratio of bulk species concentrations, $\gamma \equiv c_{1,\text{bulk}}/c_{2,\text{bulk}}$; these are described in full detail in the Supplementary

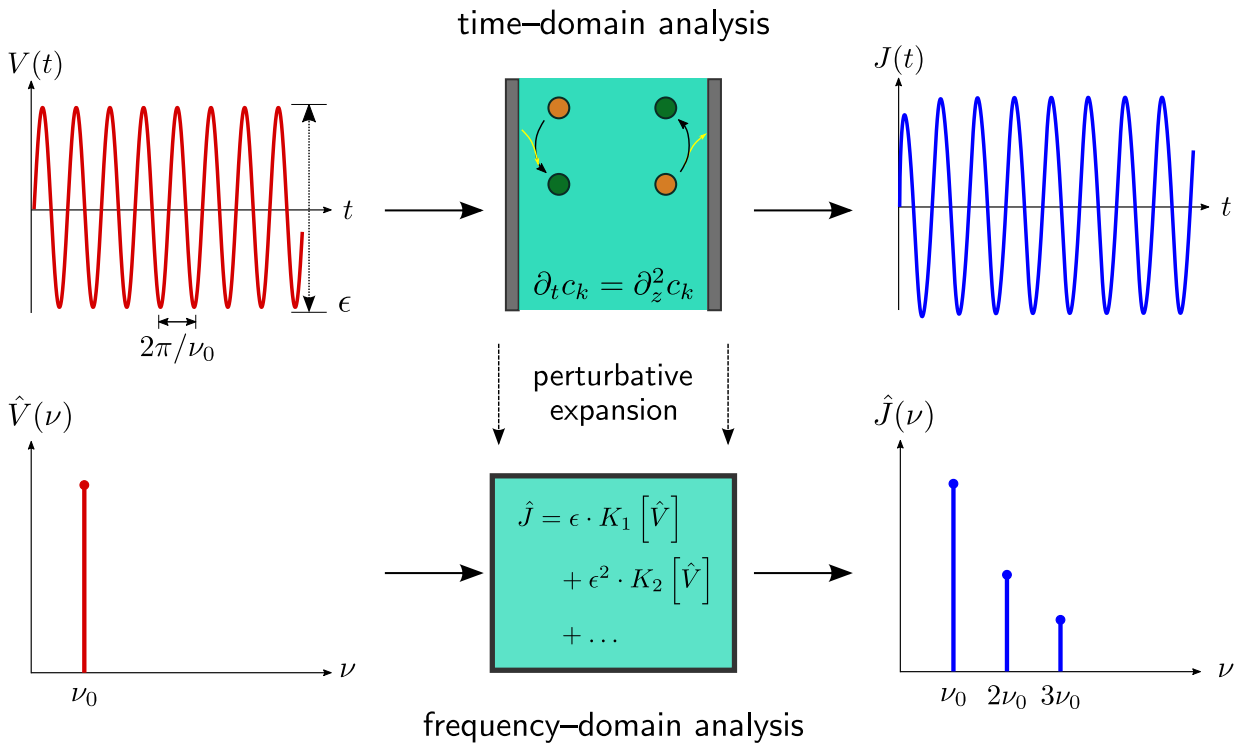

Figure 6.1: Schematic diagram of the medium amplitude oscillating voltage approach to electrochemical characterization. The top row shows the time-domain picture, where a small (specifically, $O(\epsilon)$) sinusoidal input voltage $V(t)$ is applied between the working and reference electrodes of an electrochemical system, producing a periodic output current density signal $J(t)$. In the time-domain, the relationship between the voltage and current signals is encoded by the dynamics of the time-dependent diffusion equation in Eq. (6.1), under the boundary conditions specified in Eqns. (6.7)–(6.9). The bottom row shows the frequency-domain picture; the input voltage $\hat{V}(\nu)$ is represented by a delta function at the input sinusoid frequency ν_0, producing an output current density $\hat{J}(\nu)$ which has a linear response component at ν_0, and additional intermodulatory response components at integer multiples of ν_0. The relationship between $\hat{V}(\nu)$ and $\hat{J}(\nu)$ is encoded by a set of convolution kernels $K^{(n)}$ that arise from a perturbative analysis of Eq. (6.1), which are organized in rising powers of the small parameter ϵ.

Information. Finally, the time-dependent output current density signal is extracted by evaluating the species flux at the boundary,

$$J(t) = -e\mathcal{D}\left.\frac{\partial}{\partial z}c_1(t,z)\right|_{z=0}. \tag{6.3}$$

Our mathematical approach operates by assuming that the input voltage signal $V(t)$ is a small disturbance around a reference potential E_{hold}. More specifically, we assert that the non-dimensional deviation of the signal from its reference value, $\beta e\left[V(t) - E_{\text{hold}}\right]$, is $O(\epsilon)$ at all times t. In this scenario, we may apply a time-dependent perturbative analysis by expanding the concentration profiles $c_k(t,z)$ in power series,

$$c_k(t,z) = c_k^{(0)}(t,z) + \epsilon \cdot c_k^{(1)}(t,z) + \epsilon^2 \cdot c_k^{(2)}(t,z) + \ldots \tag{6.4}$$

where $c_k^{(n)}(t,z)$ represents the n'th order correction to the time-dependent concentration profile for species k. The output current density signal, $J(t)$, may also be organized into a power series,

$$J(t) = J^{(0)}(t) + \epsilon \cdot J^{(1)}(t) + \epsilon^2 \cdot J^{(2)}(t) + \ldots, \tag{6.5}$$

where $J^{(n)}(t,z)$ now represents the n'th order correction to the time-dependent current density. For small enough voltage signals (i.e. $\epsilon \ll 1$), the power series in Eq. (6.5) is convergent, and may, to a good approximation, be truncated at finite order. While we do not derive any formal convergence guarantees in this work, all the numerical and experimental results we present are consistent with a convergent power series for the current at all magnitudes of applied voltage signals studied here.

So far, we have developed the problem formulation in the time domain, seeking to relate the output current density signal $J(t)$, to the input voltage signal $V(t)$. Due to the mathematical structure of the time-dependent diffusion problem stated in Eq. (6.1), it is much simpler to derive an analytical relationship between the Fourier representations of the current density and voltage signals. Given a signal $f(t)$, we define its Fourier representation $\hat{f}(\nu)$ as the function that satisfies the following relationship,

$$f(t) = \int_{-\infty}^{\infty} d\nu\, e^{2\pi i\nu t}\hat{f}(\nu) \tag{6.6}$$

where $i \equiv \sqrt{-1}$ is the imaginary unit.

Upon taking the Fourier transform of Eq. (6.1) and expanding the boundary condition stated in Eq. (6.2) to desired order, we can extract analytical relationships between $\hat{J}(\nu)$, the Fourier representation of the current density signal, and $\hat{V}(\nu)$, the Fourier representation of the voltage signal, to desired order (full details of the derivation can be found in the Sec. 7.5). At $O(\epsilon^0)$, we recover the familiar Cottrell current output signal in response to a flat voltage step input, represented in frequency space as,

$$\hat{J}^{(0)}(\nu) = \frac{1}{\sqrt{2\pi i\nu}} \cdot \frac{\zeta \cdot \left(\gamma e^{\bar{E}_{\text{hold}}} - 1\right)}{e^{\alpha\bar{E}_{\text{hold}}}\sqrt{2\pi i\nu} + \zeta(1 + e^{\bar{E}_{\text{hold}}})}. \tag{6.7}$$

At $O(\epsilon^1)$, we arrive at an expression that depends linearly on the input voltage signal,

$$\hat{J}^{(1)}(\nu) = \frac{\zeta(1+\gamma)e^{\bar{E}_{\text{hold}}}}{(1+e^{\bar{E}_{\text{hold}}})\left[\zeta(1+e^{\bar{E}_{\text{hold}}}) + e^{\alpha\bar{E}_{\text{hold}}}\sqrt{2\pi i\nu}\right]}\ \sqrt{2\pi i\nu}\cdot\hat{V}(\nu), \tag{6.8}$$

where $\bar{E}_{\text{hold}} \equiv \beta e\left[E_{\text{hold}} - E_{\text{eq}}\right]$ is the (non-dimensional) reference potential offset by the reaction equilibrium potential, and $\zeta \equiv k_0\left(\mathcal{D}\nu^*\right)^{-1/2}$ is the reaction rate constant made non-dimensional by a reference frequency, which we set to be $\nu^* = 1\,\text{Hz}$ for all results presented in this work. In the linear regime, only frequencies that are present in the input signal may be observed in the output signal; this is a general behavior of linear systems, and is exploited in the PEIS electrochemical characterization technique.

The power of our analytical approach lies in its ability to also extract current–voltage relationships to nonlinear orders, that is, $n > 1$. At $O(\epsilon^2)$, we obtain an expression of the form,

$$\hat{J}^{(2)}(\nu) = \int d\eta_1 K^{(2)}(\eta_1; k_0, \alpha, E_{\text{eq}})\hat{V}(\eta_1)\hat{V}(\nu-\eta_1), \tag{6.9}$$

where $K^{(2)}(\eta_1; k_0, \alpha, E_{\text{eq}})$ is a convolution kernel function that is parametrically dependent on the microscopic physical parameters, whose explicit form is detailed in the Sec. 7.5. As expected, the current density signal at this order now goes quadratically with the magnitude of the applied voltage signal. The convolutional integral in Eq. (6.9) introduces salient mathematical structure which captures an important signature of nonlinear systems. Specifically, if the voltage signal contains a single input frequency ν_0, then the convolutional integral at this order will not only produce a response at the original frequency ν_0, but also generate response at an "overtone" frequency $2\nu_0$. This phenomenon, known as intermodulation, is a general characteristic of nonlinear systems, and has been well-documented in nonlinear fluid rheology[17–20], nonlinear spectroscopy[21], and elsewhere; it is depicted schematically in the bottom row of Fig. 6.1. Relationships between the Fourier representations of the current and voltage signals can be derived to arbitrarily high order; the expression at $O(\epsilon^3)$ is presented in the Sec. 7.5. The mathematical structure of these expressions at $O(\epsilon^n)$ involves $(n-1)$'th order convolutional integrals, which result in additional output signals at higher integer multiple overtones of the frequency of the input signal.[17]

Zooming out from the mathematical details, the important result furnished by our perturbative analysis is the hierarchy of current-voltage relationships at various orders, as presented in Eqns. (6.7) – (6.9). These expressions are analytical and closed-form, and explicitly depend on the microscopic physical parameters of the system. One manner in which we can apply these relationships, and confirm their validity, is to use them to solve the "forward" problem of electrochemical modeling: given a known set of underlying physical parameters, we can attempt to predict the output current density signal produced by an electrochemical system subject to a known input voltage signal. Here, we seek to compare the predictions from the perturbative analysis to those from numerical time domain simulations of the diffusive transport problem presented in Eq. (6.1).

Briefly, the time domain simulation procedure employs the numerical method of lines; it couples a grid discretization of the spatial coordinate with high-order adaptive Runge-Kutta time domain integration. Additional details regarding the time domain numerical simulations are reported in the Sec. 7.5. For a given voltage input signal, we extract the

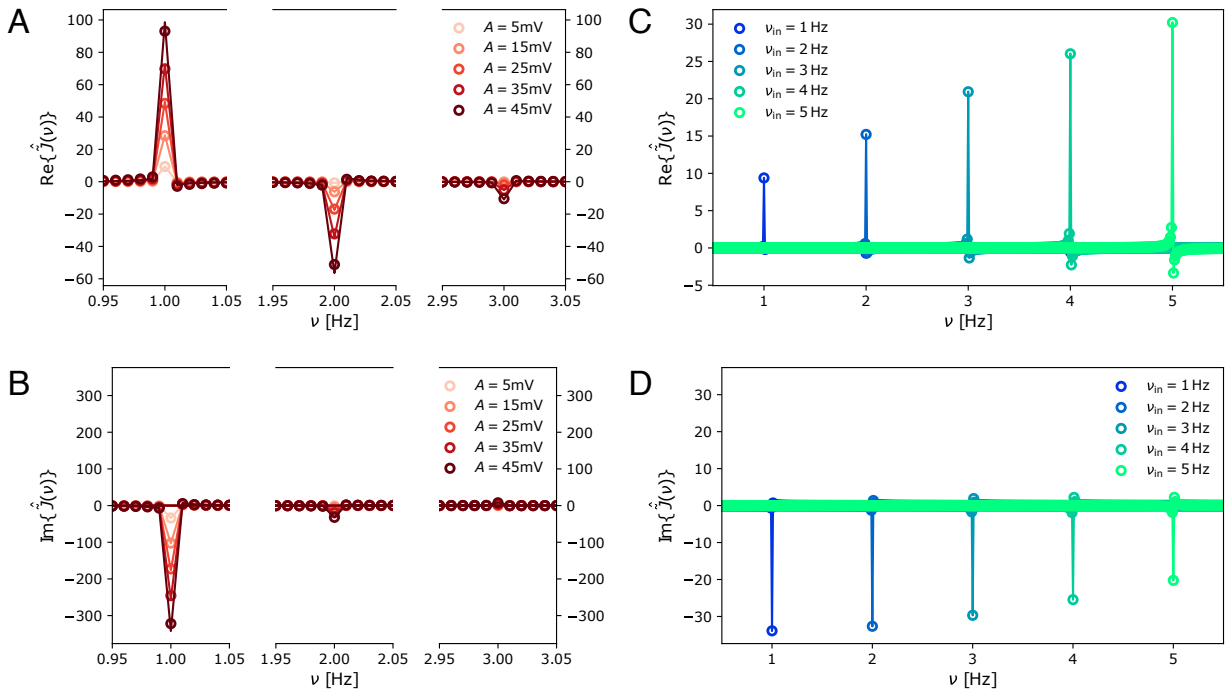

Figure 6.2: Quantitative comparison between time-domain numerical simulation and predictions from the perturbative analytical model. All results are presented in the frequency domain. (A, B) Real and imaginary parts of the current density $\hat{J}(\nu)$ output resultant from an input signal with a single frequency $\nu_{\text{in}} = 1\,\text{Hz}$. Open circles represent frequency-domain current densities extracted from taking the discrete Fourier Transform of time-domain numerical simulation data, whereas solid lines represent predictions from the analytical model. The color scale represents input sinusoids of different amplitudes A, illustrating an increase in intermodulatory response at larger frequencies. (C, D) Real and imaginary parts of the current density $\hat{J}(\nu)$ output resultant from an input signal with various different input frequencies ν_{in} (represented by the color scale). Open circles represent frequency-domain current densities extracted from taking the discrete Fourier Transform of time-domain numerical simulation data, whereas solid lines represent predictions from the analytical model.

corresponding time domain current density output signal from numerical simulation, and then apply a discrete Fourier transform to move the results into the frequency domain, where they can be easily compared with predictions from the analytical model. The Fourier transform of a real time domain signal $f(t)$ is a complex-valued function with Hermitian symmetry, $\hat{f}(\nu) = \left[\hat{f}(-\nu)\right]^*$, where the $[\cdot]^*$ operator denotes complex conjugation. Hence, we need only examine the frequency domain signal for $\nu \geq 0$, but we must check agreement between both the real and imaginary portions of the Fourier representations of two signals.

Figures 6.2 A and B depict a comparison between results from numerical simulation and the analytical model (truncated at $O(\epsilon^3)$) for a series of voltage input signals of the form,

$$V(t) = A \cdot \sin(2\pi\nu_0 t), \tag{6.10}$$

where A is a variable amplitude, and $\nu_0 = 1\,\text{Hz}$. Figure 6.2A (B) shows a comparison of the real (imaginary) portion of the Fourier representation of the output current density signal $\hat{J}(\nu)$, where open circles represent the results from numerical simulation, while solid lines represent the results of the analytical model. A majority of the current density response is concentrated on the input voltage frequency ν_0, with minor additional loadings at the intermodulatory response frequencies $2\nu_0$ and $3\nu_0$. As expected, the magnitude of the intermodulatory response grows larger with increasing amplitude A, reflecting a greater degree of nonlinear system driving. Figures 6.2 C and D depict a comparison between numerics and the analytical model for a series of voltage input signals following the form presented in Eq. (6.10), for ν_0 taking various values between 1–5 Hz, with the amplitude A fixed at 5 mV. Again, the open circles represent results collected from numerical simulation, while the solid lines denote results from the analytical model. At this amplitude, $\beta e|V(t)|_\infty \approx 0.20 \ll 1$, and so we expect a majority of the current response to be concentrated at the input voltage frequency ν_0, which is borne out in the numerical and analytical results.

Across all the input signal amplitudes and frequencies studied in Fig. 6.2, we observe excellent agreement between the numerical simulation results and the predictions of the analytical model. This result demonstrates the validity of the analytical model (evaluated up to $O(\epsilon^3)$) for voltage input signals within the amplitude range $A \in [5, 45]\,\text{mV}$ in predicting both the real and imaginary components of the complex current response signal. In a more conceptual sense, this confirms that in the parameter regime studied here, the perturbative analytical model presented in Eqns. (6.7) – (6.9) is an effective tool for solving the "forward problem" presented earlier: predicting the nonlinear response behavior of electrochemical systems with a known set of underlying parameters.

6.4 Experimental Validation

Typically, in the context of an electrochemical characterization experiment, we are interested in solving the "inverse problem": predicting the (unknown) underlying parameters of an electrochemical system on the basis of its current response to a known input voltage signal. Since our mathematical framework can produce predictions of the current response as a function of the underlying parameters, we can construct an objective function that quantifies the difference between the experimentally-observed and model-predicted current response.

Using standard nonlinear optimization techniques, we can minimize this objective function to glean a set of parameter values that best explain the experimental data. In this section, we provide a proof-of-concept demonstration by applying our Fourier space analytical formalism to extract the microscopic electrochemical parameters for a simple and well-characterized aqueous redox couple. All experimental results presented were taken in a one-compartment cell with a glassy carbon working electrode, Pt counter electrode, and an Ag/AgCl reference electrode. The electrolyte solution was prepared from deionized water, 1M NaCl supporting salt, and 5 mM of potassium ferrocyanide and potassium hexacyanoferrate, comprising both the oxidized and reduced states of the ferrocyanide/ferricyanide redox couple. Further details on the experimental setup are included in the Sec. 7.5.

In correspondence with the numerical simulation results presented in Fig. 6.2, we first attempted to quantify parameters on the basis of current response to a sinusoidal voltage oscillation around a reference potential E_{hold}. As derived in Eq. (6.7), simply holding an electrochemical system at a reference potential produces a current response often known as the Cottrell current, which decays as $t^{-1/2}$ at large times. For the sake of simplicity, we choose to simply hold at the reference potential for a time $t_{\text{hold}} = 100$ s until the Cottrell current has decayed to a suitably small value, and then apply an oscillating sinusoidal signal. Mathematically, the full voltage signal may be represented in the time domain as,

$$V(t) = E_{\text{hold}} + H\left(t - t_{\text{hold}}\right) \cdot \left\{A \sin\left[2\pi\nu_{\text{in}}\left(t - t_{\text{hold}}\right)\right]\right\}, \tag{6.11}$$

where $H(\cdot)$ denotes the Heaviside step function, A is the amplitude, and ν_{in} is the input frequency. For the sake of simplicity, we choose to fix the amplitude $A = 25$ mV and $\nu_{\text{in}} = 3$ Hz, while varying $E_{\text{hold}} \in \{203, 253, 303\}$ mV over a series of three experiments. Figure 6.3A depicts the voltage signals for these three experiments in the time domain, where the time traces are colored by their respective hold potentials. Figure 6.3B depicts the current density response to these signals in the time domain, and provides a stark illustration of the dependence of the response on the hold potential E_{hold}.

In order to apply the Fourier space perturbative model, we must transform the experimental data measured in the time domain into the frequency domain. We accomplish this task by using the standard discrete Fourier transform[22] applied over the time window $t \in [t_{\text{hold}}, t_{\text{hold}} + t_{\text{window}}]$, where $t_{\text{window}} = 10\,\text{s}$. Choosing a larger value of t_{window} would result in greater frequency resolution at the expense of longer experimental acquisition time; we present results for different values of t_{window} in the Sec. 7.5. Most importantly, t_{window} should be chosen such that it encompasses an integer multiple of sinusoidal periods, else the Fourier transformed data will be polluted by "spectral leakage" artifacts which are well-characterized in the analog signal processing literature.[23] Figure 6.3 C (D) depicts the real (imaginary) part of the appropriately non-dimensionalized current density response signal in the frequency domain, where the open circles represent the experimental data, whereas the solid lines represent predictions from the model with parameters that minimize the squared deviation against the experimental data. Agreement between the experimental results and the best fit model is visually quite satisfactory, with a majority of the current response at these frequencies being concentrated on the input frequency ν_{in}, and a smaller component at the overtone $2\nu_{\text{i}}$. The best-fit parameter values are determined to be $\hat{E}_{\text{eq}} = 188\,\text{mV}$, $\hat{\alpha} = 0.49$, and $\hat{k}_0 = 17\,\mu\text{m}\,\text{s}^{-1}$, which are in reasonable agreement with a standard cyclic

voltammetry analysis, theoretical prediction, and literature results, respectively[24]. We note that further parametric uncertainty quantification efforts could be carried out in a relatively straightforward manner using a Bayesian framework, although these are outside the scope of the current work.[25]

So far, all the numerical and experimental results presented here employ pure-tone signals that contain a single frequency, denoted ν_{in}. However, a distinct advantage of the Fourier space analytical formalism we develop here is that it is not limited to simple pure-tone signals; indeed, we may employ it to analyze any input voltage signal that admits a Fourier transform. In particular, inspection of Eqns. (6.7)–(6.9) reveals that the output current density signal is nontrivially dependent on the value of ν_{in}, implying that a signal that contains loading at multiple different frequencies can yield a richer picture of the electrochemical system response. The simplest possible signal with multi-frequency loading is a linear superposition of sinusoidal oscillations, which is represented in the frequency domain as a summed "comb" of delta functions at the individual frequencies in the signal. While our method may be applied to such input signals, here we choose to demonstrate its application to a slightly more sophisticated multi-frequency signal, the "chirped" waveform, which is well-studied and widely employed in rheology[26,27], spectroscopy[28], and analog signal processing.[29] Chirped waveforms are characterized by an instantaneous frequency that continuously sweeps over a range of frequencies over the course of the signal; if sweeping from low to high frequencies, this produces an auditory signal that becomes more shrill over time, much like a bird's chirp. Mathematically, a chirped waveform is represented as,

$$V(t) = A \sin\left\{2\pi\left[\frac{(\nu_2 - \nu_1)}{2t_{\text{window}}} \cdot t^2 + \nu_1 \cdot t\right]\right\} \tag{6.12}$$

where ν_1 and ν_2 are the initial and final frequencies, respectively, A is the amplitude, and t_{window}, as before, represents the experimental acquisition time. Additionally, following standard practice to avoid issues with spectral leakage, we apply a Tukey window function[26] with $r = 0.8$ to the final chirped voltage waveform (additional detail in the Sec. 7.5).

Figure 6.4A depicts the chirped voltage signals in the time domain for three experiments sweeping over different values of E_{hold}; by eye, one can distinguish that the oscillations in the voltage waveform become more frequent over time In all experiments, $A = 25\,\text{mV}$, $\nu_1 = 2\,\text{Hz}$, $\nu_2 = 5\,\text{Hz}$, and $t_{\text{window}} = 40\,\text{s}$. Figure 6.4B depicts the current density response signals in the time domain, where we can again observe a stark dependence on the hold potential E_{hold}. Chirped waveform signals are most easily visualized in the Fourier domain by analyzing the magnitude and phase of the complex Fourier transform data, where $\text{Phase}(z) \equiv \tan^{-1}\left[\text{Im}\{z\}/\text{Re}\{z\}\right] \in [-\pi, \pi)$. As shown in Fig. 6.4C, the magnitude signature of the chirped waveforms is supported over a range slightly larger than the interval $[\nu_1, \nu_2]$; the open circles, which represent experimental data, and the solid lines, which represent model predictions with best-fit parameter values, are in excellent agreement. Figure 6.4D depicts the phase signature of the current density signals in the frequency domain, highlighting some of the differences at various values of E_{hold} while still demonstrating agreement between the experimental data and the model predictions. Finally, although Figs. 6.4C and 6.4D cut off the frequency axis at ν_2 for the sake of clarity of presentation, we do observe (and can fit) intermodulatory response signatures over the interval $[\nu_2, 2\nu_2]$. These are presented in greater detail in the Sec. 7.5. The best-fit parameter values are determined to be $\hat{E}_{\text{eq}} = 190\,\text{mV}$,

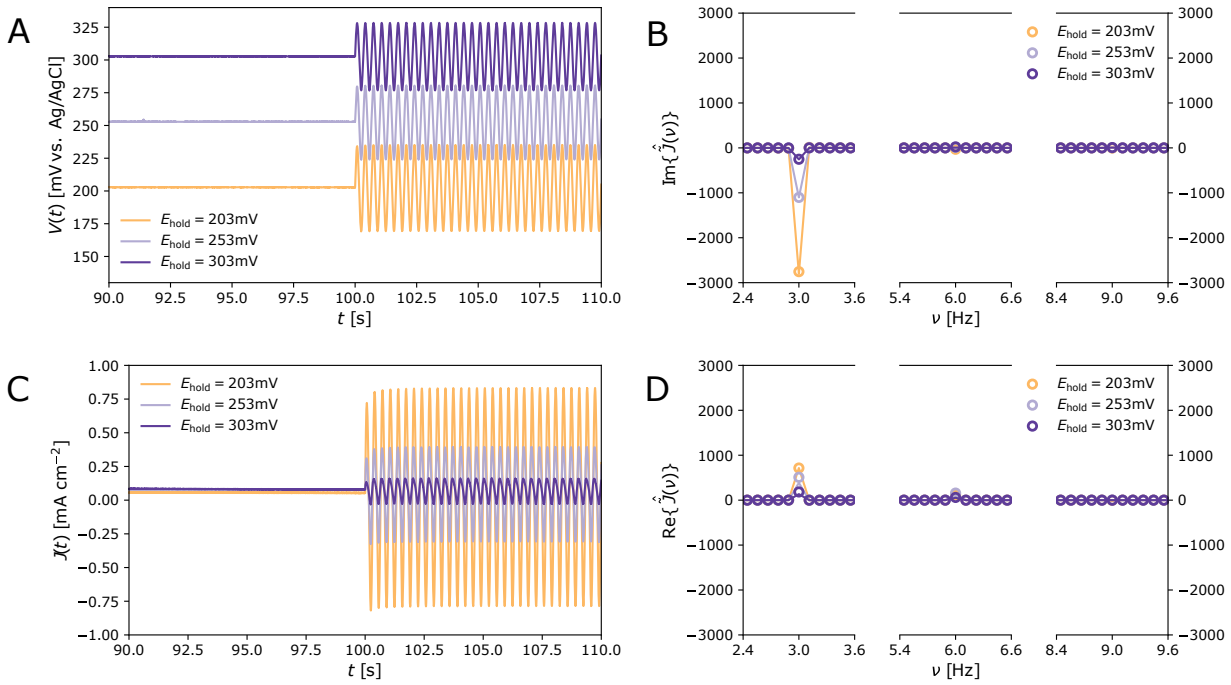

Figure 6.3: Extracting microscopic electrochemical parameters by analysis of current density response to a sinusoidal voltage input signal. (A) Time-domain representation of the input voltage signals, which start off as constant potential holds at various increasing values of the hold potential, E_{hold} (depicted by color-coding). A purely sinusoidal input voltage signal of the form presented in Eq. (6.11), with amplitude $A = 25\text{mV}$ and $\nu_{\text{in}} = 3\,\text{Hz}$ is switched on at $t = 100\text{s}$ and applied for 10 s; the Fourier analysis window is $t \in [100, 110]$ s. (B) Time-domain representation of the associated output current density responses. The magnitude of the observed current is strongly dependent on the hold potential; by eye it is apparent that the current response contains harmonics at frequencies higher than ν_{in}. (C, D) (Imaginary, real) components of the Fourier representations of the current output signal are depicted in open circles, whereas the predictions from fitting the analytical model to this data are represented as solid lines. All the Fourier space content of the current signal is concentrated at the first three integer multiples of ν_{in}; agreement between the data and the fitted model is excellent.

$\hat{\alpha} = 0.49$, and $\hat{k}_0 = 17\,\mu\mathrm{m\,s^{-1}}$, which are in agreement with the results from the single sinusoid experiments, demonstrating that our technique is applicable with a variety of different input waveforms.

6.5 References

[1] Allen J Bard, Larry R Faulkner, Johna Leddy, and Cynthia G Zoski. *Electrochemical methods: fundamentals and applications*, volume 2. Wiley New York, 1980.

[2] Jean-Michel Savéant. *Elements of molecular and biomolecular electrochemistry: an electrochemical approach to electron transfer chemistry*. John Wiley & Sons, 2006.

[3] Timothy R Cook, Dilek K Dogutan, Steven Y Reece, Yogesh Surendranath, Thomas S Teets, and Daniel G Nocera. Solar energy supply and storage for the legacy and nonlegacy worlds. *Chemical reviews*, 110(11):6474–6502, 2010.

[4] Matthew E O'Reilly, R Soyoung Kim, Seokjoon Oh, and Yogesh Surendranath. Catalytic methane monofunctionalization by an electrogenerated high-valent pd intermediate. *ACS central science*, 3(11):1174–1179, 2017.

[5] Hao Wang, Sayed Youssef Sayed, Erik J Luber, Brian C Olsen, Shubham M Shirurkar, Sankaranarayanan Venkatakrishnan, Ushula M Tefashe, Anna K Farquhar, Eugene S Smotkin, Richard L McCreery, et al. Redox flow batteries: how to determine electrochemical kinetic parameters. *ACS nano*, 14(3):2575–2584, 2020.

[6] MH Chakrabarti, RAW Dryfe, and EPL Roberts. Evaluation of electrolytes for redox flow battery applications. *Electrochimica Acta*, 52(5):2189–2195, 2007.

[7] Miguel Aller Pellitero, Samuel D Curtis, and Netzahualcóyotl Arroyo-Currás. Interrogation of electrochemical aptamer-based sensors via peak-to-peak separation in cyclic voltammetry improves the temporal stability and batch-to-batch variability in biological fluids. *ACS sensors*, 6(3):1199–1207, 2021.

[8] Amruta A Karbelkar and Ariel L Furst. Electrochemical diagnostics for bacterial infectious diseases. *ACS Infectious Diseases*, 6(7):1567–1571, 2020.

[9] Noémie Elgrishi, Kelley J Rountree, Brian D McCarthy, Eric S Rountree, Thomas T Eisenhart, and Jillian L Dempsey. A practical beginner's guide to cyclic voltammetry. *Journal of chemical education*, 95(2):197–206, 2018.

[10] Eric S Rountree, Brian D McCarthy, Thomas T Eisenhart, and Jillian L Dempsey. Evaluation of homogeneous electrocatalysts by cyclic voltammetry. *Inorganic chemistry*, 53(19):9983–10002, 2014.

[11] Richard S Nicholson. Theory and application of cyclic voltammetry for measurement of electrode reaction kinetics. *Analytical chemistry*, 37(11):1351–1355, 1965.

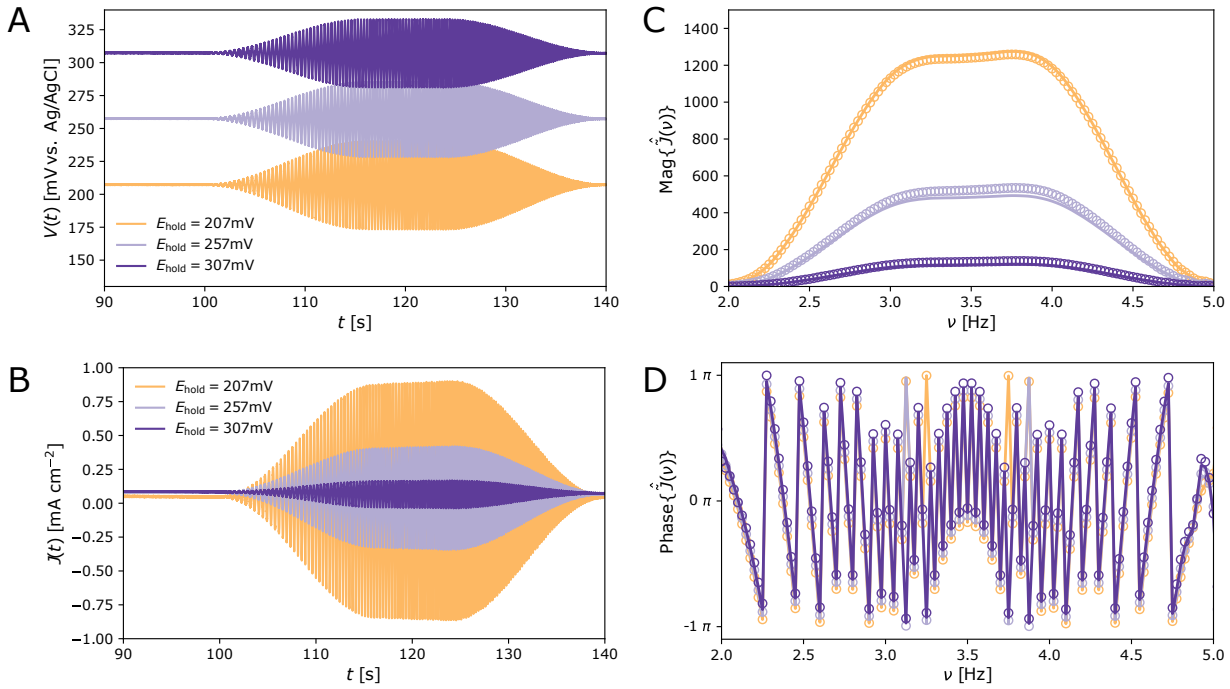

Figure 6.4: Extracting microscopic electrochemical parameters by analysis of current density response to a windowed chirp voltage input signal. (A) Time-domain representation of the input voltage signals, which start off as constant potential holds at various increasing values of the hold potential, E_{hold} (depicted by color-coding). A windowed chirp input voltage signal of the form presented in Eq. (6.12), with amplitude $A = 25\text{mV}$ and $\nu_1 = 2\,\text{Hz}$ and $\nu_2 = 2\,\text{Hz}$ is switched on at $t = 100\text{s}$ and applied for 40 s; the Fourier analysis window is $t \in [100, 140]$ s. (B) Time-domain representation of the associated output current density responses. The magnitude of the observed current is strongly dependent on the hold potential. (C, D) (Magnitude, phase) components of the Fourier representations of the current output signal are depicted in open circles, whereas the predictions from fitting the analytical model to this data are represented as solid lines. The Fourier space content of the output signals is concentrated between frequencies ν_1 and ν_2; agreement between the data and the fitted model is excellent.

[12] *Equivalent Circuit Analogs*, chapter 9, pages 153–162. John Wiley & Sons, Ltd, 2008. ISBN 9780470381588. doi: https://doi.org/10.1002/9780470381588.ch9. URL https://onlinelibrary.wiley.com/doi/abs/10.1002/9780470381588.ch9.

[13] Mark E Orazem, Pankaj Agarwal, and Luis H Garcia-Rubio. Critical issues associated with interpretation of impedance spectra. *Journal of Electroanalytical Chemistry*, 378 (1-2):51–62, 1994.

[14] Digby D Macdonald, Elzbieta Sikora, and George Engelhardt. Characterizing electrochemical systems in the frequency domain. *Electrochimica Acta*, 43(1-2):87–107, 1998.

[15] STEPHEN BOYD, L. O. CHUA, and C. A. DESOER. Analytical Foundations of Volterra Series *. *IMA Journal of Mathematical Control and Information*, 1(3):243–282, 09 1984. ISSN 0265-0754. doi: 10.1093/imamci/1.3.243. URL https://doi.org/10.1093/imamci/1.3.243.

[16] W.M. Deen. *Analysis of Transport Phenomena*. Topics in chemical engineering. Oxford University Press, 2012. ISBN 9780199740284. URL https://books.google.com/books?id=60YsAwEACAAJ.

[17] Kyle R Lennon, Gareth H McKinley, and James W Swan. Medium amplitude parallel superposition (maps) rheology. part 1: Mathematical framework and theoretical examples. *Journal of Rheology*, 64(3):551–579, 2020.

[18] Kyle R Lennon, Michela Geri, Gareth H McKinley, and James W Swan. Medium amplitude parallel superposition (maps) rheology. part 2: Experimental protocols and data analysis. *Journal of Rheology*, 64(5):1263–1293, 2020.

[19] Satish Kumar Gupta, Kyle R Lennon, Mary A Joens, Hari Bandi, Martijn Van Galen, YuLong Han, Wenhui Tang, Yiwei Li, Steven Charles Wasserman, James W Swan, et al. Optical tweezer measurements of asymptotic nonlinearities in complex fluids. *Physical Review E*, 104(6):064604, 2021.

[20] Kyle R Lennon, Gareth H McKinley, and James W Swan. Medium amplitude parallel superposition (maps) rheology of a wormlike micellar solution. *Rheologica Acta*, 60(12): 729–739, 2021.

[21] Carsten Hutter, Daniel Platz, EA Tholén, TH Hansson, and DB Haviland. Reconstructing nonlinearities with intermodulation spectroscopy. *Physical review letters*, 104 (5):050801, 2010.

[22] Matteo Frigo and Steven G Johnson. The fastest fourier transform in the west. Technical report, MASSACHUSETTS INST OF TECH CAMBRIDGE, 1997.

[23] Douglas A Lyon. The discrete fourier transform, part 4: spectral leakage. *Journal of object technology*, 8(7), 2009.

[24] Botao Huang, Kyaw Hpone Myint, Yanming Wang, Yirui Zhang, Reshma R Rao, Jame Sun, Sokseiha Muy, Yu Katayama, Juan Corchado Garcia, Dimitrios Fraggedakis, et al. Cation-dependent interfacial structures and kinetics for outer-sphere electron-transfer reactions. *The Journal of Physical Chemistry C*, 125(8):4397–4411, 2021.

[25] Aditya M Limaye, Joy S Zeng, Adam P Willard, and Karthish Manthiram. Bayesian data analysis reveals no preference for cardinal tafel slopes in co2 reduction electrocatalysis. *Nature communications*, 12(1):1–10, 2021.

[26] Michela Geri, Bavand Keshavarz, Thibaut Divoux, Christian Clasen, Daniel J Curtis, and Gareth H McKinley. Time-resolved mechanical spectroscopy of soft materials via optimally windowed chirps. *Physical Review X*, 8(4):041042, 2018.

[27] Mehdi Bouzid, Bavand Keshavarz, Michela Geri, Thibaut Divoux, Emanuela Del Gado, and Gareth H McKinley. Computing the linear viscoelastic properties of soft gels using an optimally windowed chirp protocol. *Journal of Rheology*, 62(4):1037–1050, 2018.

[28] Eyal Gerecht, Kevin O Douglass, and David F Plusquellic. Chirped-pulse terahertz spectroscopy for broadband trace gas sensing. *Optics express*, 19(9):8973–8984, 2011.

[29] Richard S Withers. Wideband analog signal processing. *Superconducting Devices*, pages 227–272, 1990.

Chapter 7

Appendices

7.1 Additional Information: Expanding Marcus Theory to Account for Transport Phenomena in the Electrochemical Double Layer

7.1.1 Non-Dimensionalization Procedure

Conservation of probability mass yields the set of partial differential equations

$$\frac{\partial P_i}{\partial t} = \hat{\mathcal{L}}_i P_i + \sum_{j \neq i} \left[\zeta_{j \to i} P_j - \zeta_{i \to j} P_i \right]. \tag{7.1}$$

Expanding the shorthand for the Smoluchowski propagator,

$$\frac{\partial P_i}{\partial t} = \mathcal{D} \nabla \cdot \left[e^{-\beta F_i} \nabla \left(e^{\beta F_i} P_i \right) \right] + \sum_{j \neq i} \left[\zeta_{j \to i} P_j - \zeta_{i \to j} P_i \right]. \tag{7.2}$$

Non-dimensionalizing the gradient operators $\tilde{\nabla} \equiv L \cdot \nabla$,

$$\frac{\partial P_i}{\partial t} = \frac{\mathcal{D}}{L^2} \tilde{\nabla} \cdot \left[e^{-\beta F_i} \tilde{\nabla} \left(e^{\beta F_i} P_i \right) \right] + \sum_{j \neq i} \left[\zeta_{j \to i} P_j - \zeta_{i \to j} P_i \right]. \tag{7.3}$$

As explained in the main text, the diffusive timescale $\tau \equiv \mathcal{D}/L^2$, implying

$$\tau \frac{\partial P_i}{\partial t} = \tilde{\nabla} \cdot \left[e^{-\beta F_i} \tilde{\nabla} \left(e^{\beta F_i} P_i \right) \right] + \sum_{j \neq i} \left[\tau \cdot \zeta_{j \to i} P_j - \tau \cdot \zeta_{i \to j} P_i \right]. \tag{7.4}$$

Introducing the non-dimensional time and sink/source rates ($\tilde{t} \equiv t/\tau$ and $\tilde{\zeta_{ij}} \equiv \tau \cdot \zeta_{ij}$) yields the final non-dimensionalized equations

$$\frac{\partial P_i}{\partial \tilde{t}} = \tilde{\nabla} \cdot \left[e^{-\beta F_i} \tilde{\nabla} \left(e^{\beta F_i} P_i \right) \right] + \sum_{j \neq i} \left[\tilde{\zeta}_{j \to i} P_j - \tilde{\zeta}_{i \to j} P_i \right]. \tag{7.5}$$

7.1.2 Computational Details

Similarity Transformation

The Smoluchowski diffusion operator from the main text reads

$$\hat{\mathcal{L}}_i P_i \equiv \mathcal{D} \nabla \cdot \left[e^{-\beta F_i} \nabla \left(e^{\beta F_i} P_i \right) \right]. \tag{7.6}$$

As written, this operator is not self-adjoint. This makes numerical solution more difficult, and makes a diagonalization procedure unstable[1]. A standard similarity transformation[2] can be employed to write $\hat{\mathcal{L}}_i$ in a self-adjoint form $\hat{\mathcal{L}}_i^H$, formally written as

$$\hat{\mathcal{L}}_i = \exp\left(-\beta F_i/2\right) \hat{\mathcal{L}}_i^H \exp\left(\beta F_i/2\right) \tag{7.7}$$

Recasting the full population dynamics equations in terms of $\hat{\mathcal{L}}_i^H$ creates some changes to the sink and source terms which render the entire propagator self-adjoint, the details of this transformation have been worked out by Ouyang and Subotnik[1]. Since the self-adjoint form of the operator is the one we actually use when carrying out numerical calculations, we report a discretization scheme for $\hat{\mathcal{L}}_i^H$, rather than the original propagator.

Interior Point Discretization

We choose a finite-volume discretization of the SME because it explicitly conserves mass to numerical precision and also naturally incorporates no-flux boundary conditions, which are employed at most boundaries in this model. Fig. 7.1 shows a schematic of one of the node points hosting a finite volume. Our charge is to discretize the self-adjoint version of the Smoluchowski propagator, written as

$$\hat{\mathcal{L}}^H = e^{\beta F/2}\frac{\partial}{\partial x_i}e^{-\beta F}\frac{\partial}{\partial x_i}e^{\beta F/2}, \tag{7.8}$$

where x_i is a generalized coordinate (here, refers to either x or z), and Einstein summation is implied. Inspection reveals that the operator in Eq. (7.8) is a (weighted) divergence of flux terms.

Using a two-point forward difference stencil, the appropriately-weighted fluxes piercing the boundary surfaces in Fig. 7.1 of an interior point can be expressed as

$$\mathcal{F}_{x-\delta x/2,y} = \exp\left[-\beta F(x-\delta x/2,y)\right]\left[\frac{\exp\left[\beta F(x,y)/2\right]P(x,y) - \exp\left[\beta F(x-\delta x,y)/2\right]P(x-\delta x,y)}{\delta x}\right] \tag{7.9}$$

$$\mathcal{F}_{x+\delta x/2,y} = \exp\left[-\beta F(x+\delta x/2,y)\right]\left[\frac{\exp\left[\beta F(x+\delta x,y)/2\right]P(x+\delta x,y) - \exp\left[\beta F(x,y)/2\right]P(x,y)}{\delta x}\right] \tag{7.10}$$

$$\mathcal{F}_{x,y-\delta y/2} = \exp\left[-\beta F(x,y-\delta y/2)\right]\left[\frac{\exp\left[\beta F(x,y)/2\right]P(x,y) - \exp\left[\beta F(x,y-\delta y)/2\right]P(x,y-\delta y)}{\delta y}\right] \tag{7.11}$$

$$\mathcal{F}_{x,y+\delta y/2} = \exp\left[-\beta F(x,y+\delta y/2)\right]\left[\frac{\exp\left[\beta F(x,y+\delta y)/2\right]P(x,y+\delta y) - \exp\left[\beta F(x,y)/2\right]P(x,y)}{\delta y}\right] \tag{7.12}$$

The diffusion operator can now be assembled by weighting the fluxes by their appropriate Boltzmann weight from Eq. (7.6) and making a first order central finite difference approximation for the divergence. The diffusion operator at a node point centered at (x,y) can be expressed as

$$\begin{aligned}\mathcal{L}^H(x,y) = &\frac{\exp\left[\beta F(x+\delta x/2,y)/2\right]\mathcal{F}_{x+\delta x/2,y} - \exp\left[\beta F(x-\delta x/2,y)/2\right]\mathcal{F}_{x-\delta x/2,y}}{\delta x} \\ &+ \frac{\exp\left[\beta F(x,y+\delta y/2)/2\right]\mathcal{F}_{x,y+\delta y/2} - \exp\left[\beta F(x,y-\delta y/2)/2\right]\mathcal{F}_{x,y-\delta y/2}}{\delta y}\end{aligned} \tag{7.13}$$

Note that Eq. (7.13) requires evaluating the free energy on the dual grid of the grid defining the node points; this is not difficult if the free energy can be expressed as an analytical function in closed form, as in this work.

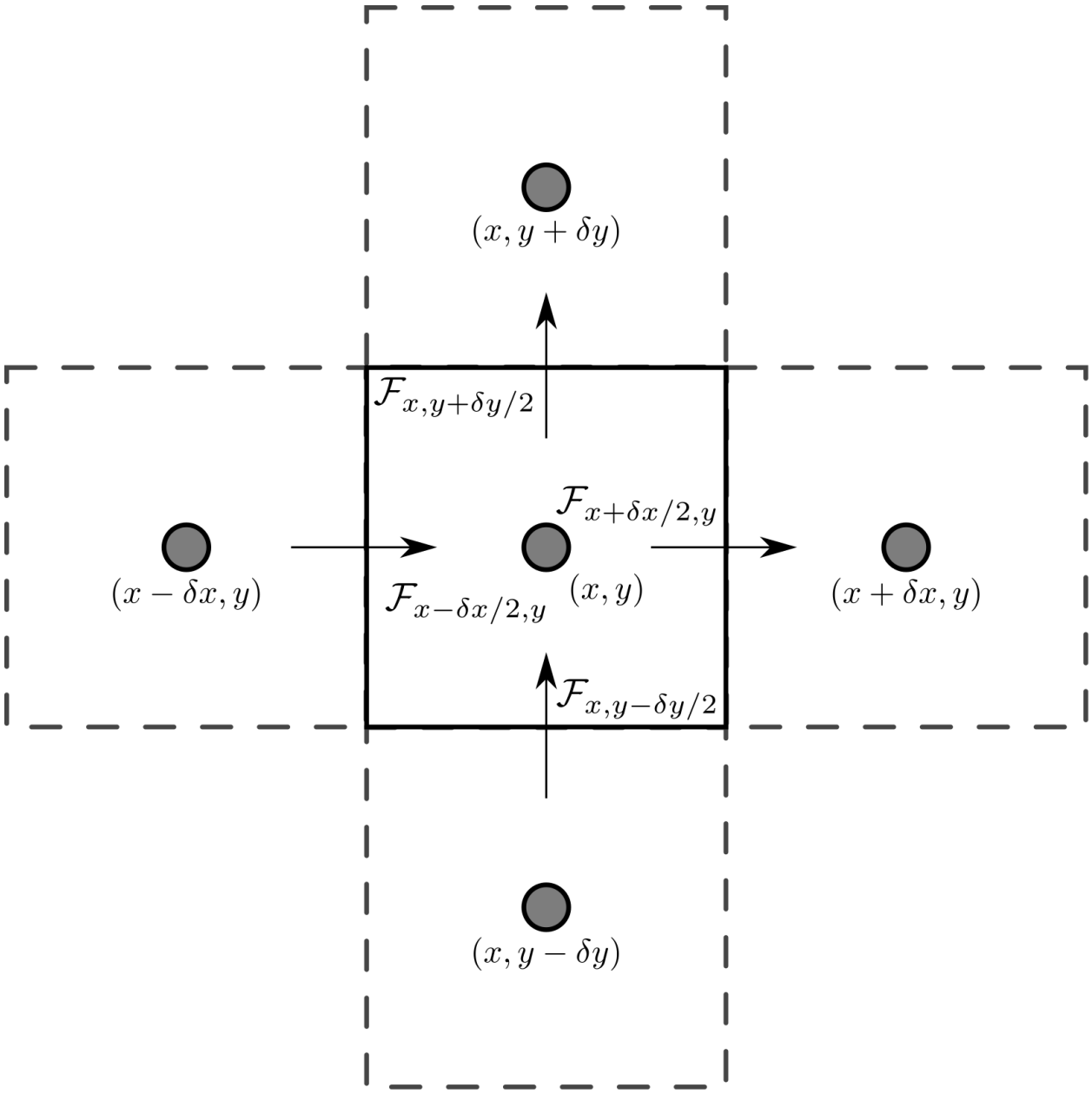

Figure 7.1: Schematic of the finite-volume discretization used for numerical solution of the Smoluchowski master equation.

Boundary Point Discretization

At boundary points, we have to take additional care to implement the appropriate boundary condition. No-flux (Neumann) conditions are simple to incorporate into the discretization scheme, we simply need to set the corresponding boundary flux term in Eq. (7.13) to zero. This results in a closed set of equations; the values of the probability field at the interior points are the only dependent variables involved.

Concentration (Dirichlet) boundary conditions are slightly more difficult to implement. The two-point central difference flux stencils in Eqns. (7.9)–(7.12) must be changed to two-point *forward* difference stencils that involve the specified boundary probability. For the flux $\mathcal{F}_{x,y+\delta y/2}$ out of a top boundary with a specified boundary probability,

$$\mathcal{F}_{x,y+\delta y/2} = \exp\left[-\beta F(x, y+\delta y/2)\right] \left[\frac{\exp\left[\beta F(x, y+\delta y/2)/2\right] P_{\text{bdy.}}(x) - \exp\left[\beta F(x,y)/2\right] P(x,y)}{(\delta y/2)}\right], \tag{7.14}$$

where $P_{\text{bdy.}}(x)$ is the boundary probability. Note that the first term in the bracketed expression is a constant, while the second term involves a dependent field variable. The first term comprises an inhomogeneity in the propagator, and leads to the existence of a non-trivial steady state solution.

Steady-State Solution

The discretization scheme described in the previous two sections approximates the unbounded Smoluchowski diffusion operator in Eq. (7.6) by a bounded finite difference operator. The hopping terms can be included straightforwardly[1] into the bounded difference operator, reducing the population dynamics partial differential equation to the matrix equation

$$\frac{\mathrm{d}\mathbf{p}}{\mathrm{d}t} = \mathbf{L}\mathbf{p} + \mathbf{c}, \tag{7.15}$$

where $\mathbf{L}$ is the matrix encoding the bounded propagator, $\mathbf{p}$ is the probability distribution evaluated at the finite difference nodes, and $\mathbf{c}$ is a constant inhomogeneity vector arising from the Dirichlet boundary conditions. The solution of the system

$$\mathbf{L}\mathbf{p} = -\mathbf{c} \tag{7.16}$$

comprises a steady-state of the SME model. In practice, the $\mathbf{L}$ operator is very sparse with a predictable structure (block-diagonal with appropriate bandwidth), and so sparse matrix algorithms can be used to efficiently solve the system in Eq. (7.16).

Computing Current

Comparing results from the SME model to experimental current-voltage data requires a working definition for net ET current towards a single species. If we let $P_i(x,z)$ denote the steady-state probability distributions of the species given the appropriate boundary conditions, an intuitive definition of the net ET current towards species k is:

$$\mathcal{J}_k \equiv \int \mathrm{d}x\mathrm{d}z \sum_{j\neq k} \left[P_j \cdot \zeta_{j\to k} - P_k \cdot \zeta_{k\to j}\right] \tag{7.17}$$

Alternatively, we can compute the current by integrating the net probability flux out of the $z = 1$ boundary for species k. While appropriate as a definition for the current, this is more numerically ill-conditioned since it involves a finite difference expression at a point where the potential profile has a corner. This ill-conditioning becomes worse at higher values of the applied potential. For all current-voltage curves measured here, we use the definition in Eq. (7.17), which is numerically robust over a wide range of applied potentials.

7.1.3 Transfer Coefficients

Traditional Marcus Theory

Marcus theory provides a prediction for the dependence of the transfer coefficient on the applied potential. I will reproduce the derivation of this dependence here using the parameters defined in the two-surface model; the end result is identical to the textbook result[3] with appropriate redefinition of variables. Take two Marcus free energies defined on a single coordinate x:

$$f_1(x) = \frac{k_{\text{reorg}}}{2} \cdot (x-1)^2 \tag{7.18}$$

$$f_2(x) = \frac{k_{\text{reorg}}}{2} \cdot x^2 + \Delta E_{\text{int}} + eV, \tag{7.19}$$

where V is the applied potential. The two curves intersect at:

$$x^* = \frac{1}{2} - \frac{\Delta E_{\text{int}} + eV}{k_{\text{reorg}}} \tag{7.20}$$

The free energy at this point referenced to the minimum of f_1 is exactly the activation energy E_a, and is given by:

$$E_a = \frac{k_{\text{reorg}}}{2} \left[\frac{1}{2} + \frac{\Delta E_{\text{int}} + eV}{k_{\text{reorg}}} \right]^2 \tag{7.21}$$

Therefore,

$$\alpha_{\text{Marcus}} = -\frac{\partial E_a}{\partial (eV)} = \left[\frac{1}{2} + \frac{\Delta E_{\text{int}} + eV}{k_{\text{reorg}}} \right]. \tag{7.22}$$

Eq. (7.22) is identical to the one produced in the main text.

Model for Transfer Coefficient Attenuation

The model for transfer coefficient attenuation relies on the calculation of an activation energy profile over the approach coordinate. We can derive this in a similar manner to the traditional Marcus derivation. The two Marcus free energies are now defined over the product space (x, z):

$$f_1(x, z) = \frac{k_{\text{reorg}}}{2} \cdot (x-1)^2 \tag{7.23}$$

$$f_2(x, z) = \frac{k_{\text{reorg}}}{2} \cdot x^2 + \Delta E_{\text{int}} + eVz, \tag{7.24}$$

The two curves intersect at:

$$x^* = \frac{1}{2} - \frac{\Delta E_{\text{int}} + eVz}{k_{\text{reorg}}} \tag{7.25}$$

The activation energy profile is straightforward to calculate from here:

$$E_a(z) = \frac{k_{\text{reorg}}}{2}\left[\frac{1}{2} + \frac{\Delta E_{\text{int}} + eVz}{k_{\text{reorg}}}\right]^2 \tag{7.26}$$

Applying the Leibniz rule requires computing

$$\frac{\mathrm{d}E_a}{\mathrm{d}(eV)} = z\left[\frac{1}{2} + \frac{\Delta E_{\text{int}} + Vz}{k_{\text{reorg}}}\right] \tag{7.27}$$

The final transfer coefficient expression from the main text is

$$\alpha = -\int \mathrm{d}z\ \tilde{\tilde{\Delta}}(z) \cdot \left[\frac{\mathrm{d}E_a}{\mathrm{d}(eV)}\right]\ , \tag{7.28}$$

Fig. 7.2 depicts a graphical representation of the integral in Eq. (7.28), using the same parameters discussed in the main text, for $V = -0.20$ V (zero overpotential). Current distributions that are highly localized near the electrode surface ($z = 0$) overlap with the initial, increasing branch of this function, and lead to low transfer coefficients. When the ET event is entirely localized to the EDL boundary, implying that $\tilde{\tilde{\Delta}}(z) = \delta[z-1]$, then the integration "sifts out" the value of Eq. (7.27) at $z = 1$. At zero overpotential, this value is exactly 1/2, implying that we recover the Marcus result from Eq. (7.22) in the appropriate limit.

Potential Dependence of the Net Current Profile

The derivation of the transfer coefficient model in the main text employed an assumption that the normalized net current marginal $\tilde{\tilde{\Delta}}(z)$ was roughly independent of the applied voltage. Figure 7.3 provides numerical confirmation that the net current marginal profile is only a weak function of voltage over the voltage range studied. Note that this is only an appropriate assumption when the reactant species does not carry a charge. For a charged reactant, the ET localization behavior is a strong function of potential, as discussed in the main text.

Additional Intuition

The main text makes reference to a "pinning" effect that attenuates the transfer coefficient as a consequence of ET localization near the electrode surface. Fig. 7.4 provides some schematic intuition for this phenomenon. Since the driving force is constrained to be exactly zero at the electrode surface, modulating the voltage yields less "bang for the buck" activation energy-wise when the ET event is constrained to occur near the electrode.

Results for Higher Reorganization Energy

A replication of Figure 3 from the main text, but with $k = 2.00$ eV. As expected, for higher reorganization energies, the current-voltage curves are linear over a broader voltage range, and the transfer coefficient prediction from Eq. (7.28) is more quantitatively correct.

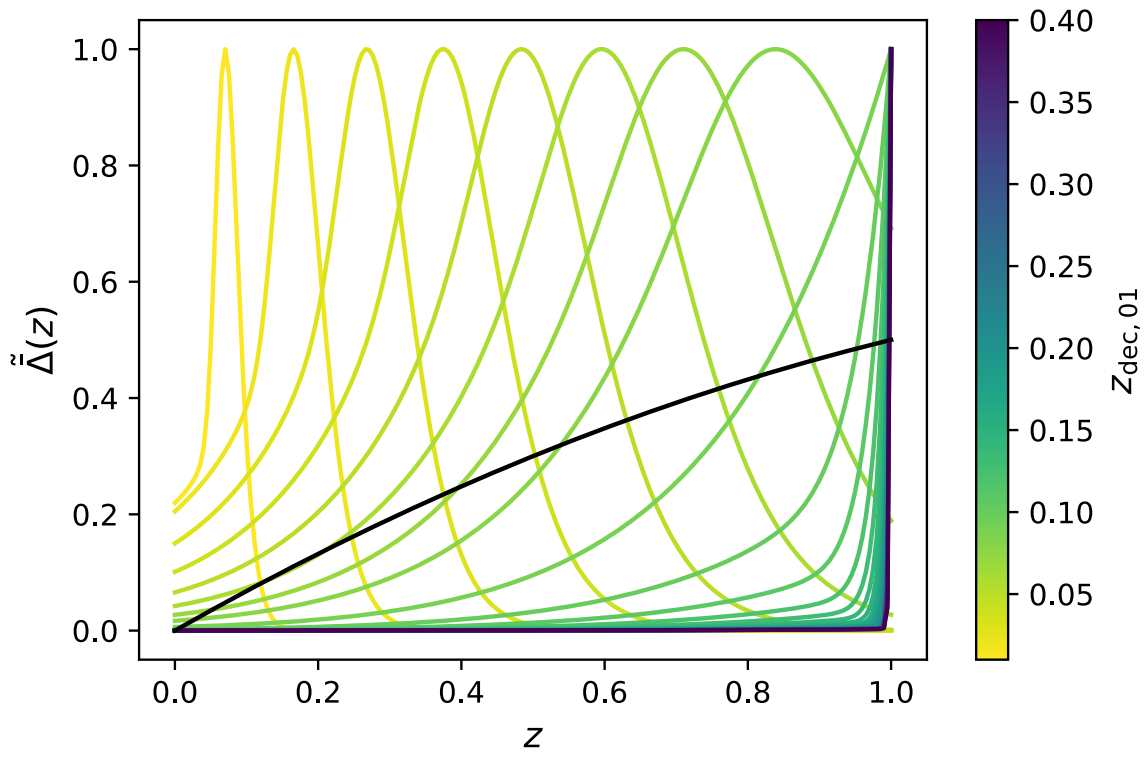

Figure 7.2: Traces of the normalized marginal current $\tilde{\tilde{\Delta}}(z)$ for values of $z_{\mathrm{dec},01} \in [0.01, 0.40]$, as well as a plot of the integration weight function in Eq. (7.27).

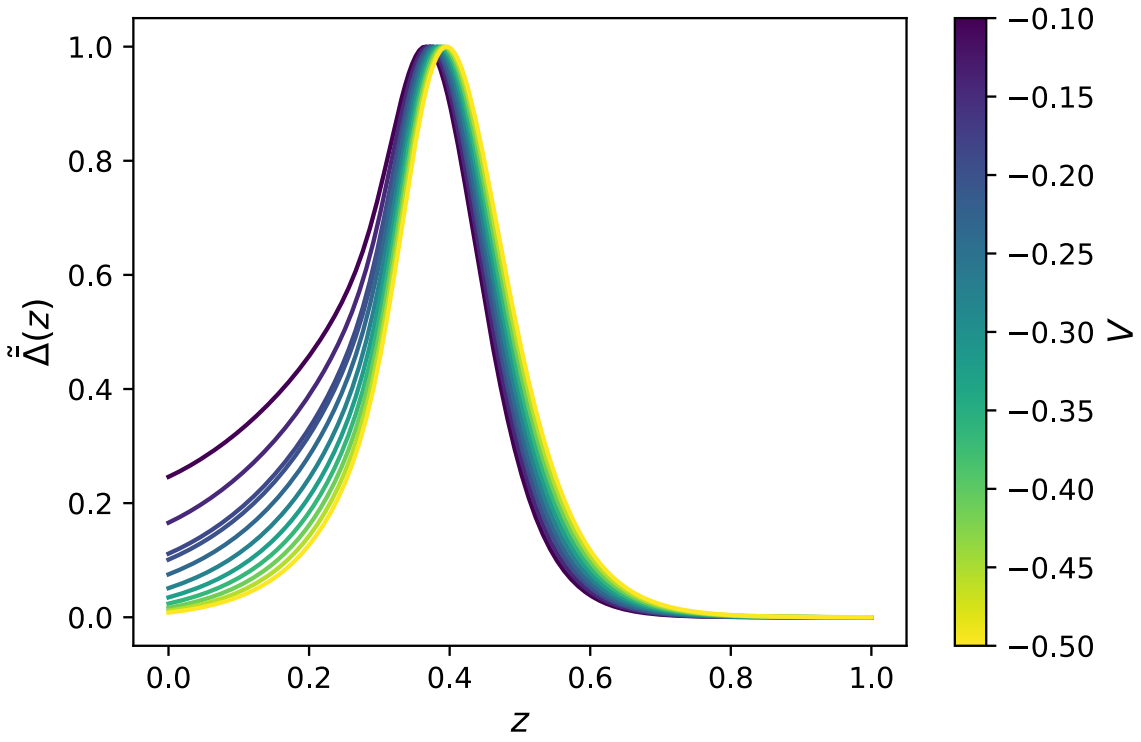

Figure 7.3: Normalized net current marginal profiles for a range of values of the applied voltage, using the same parameters as the main text. The shape of the profile is a weak function of the applied voltage.

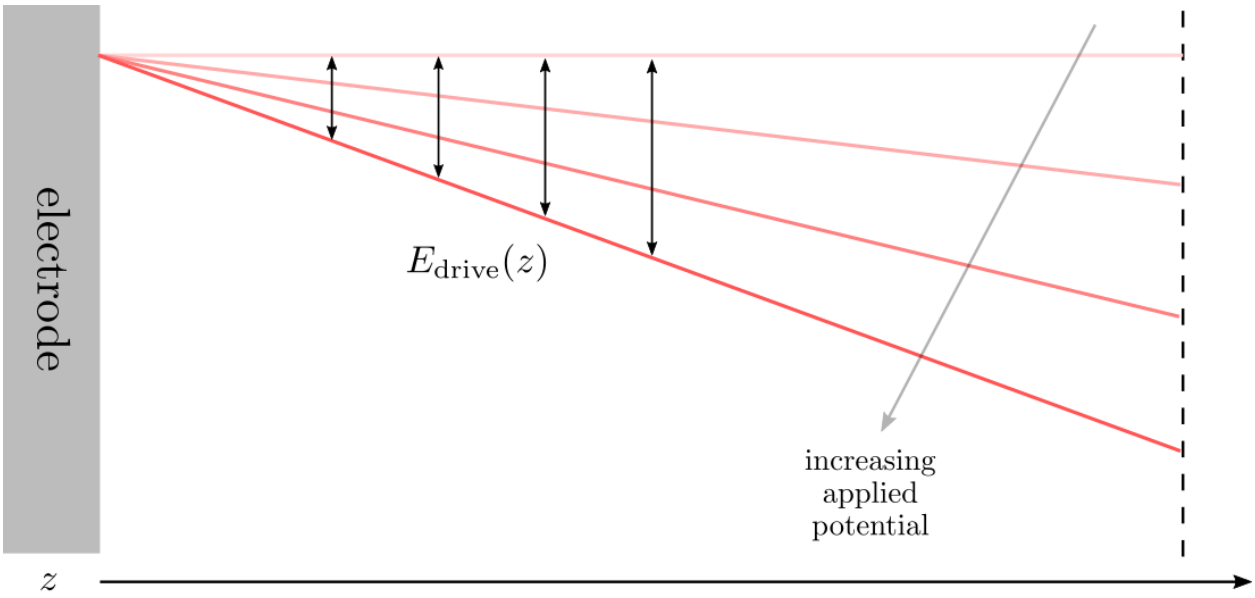

Figure 7.4: Schematic picture of the distance-dependent potential driving force in the SME model with linear potential decay. As ET occurs closer to the electrode, modulating the external potential has a smaller effect on the potential driving force felt by the redox-active species.

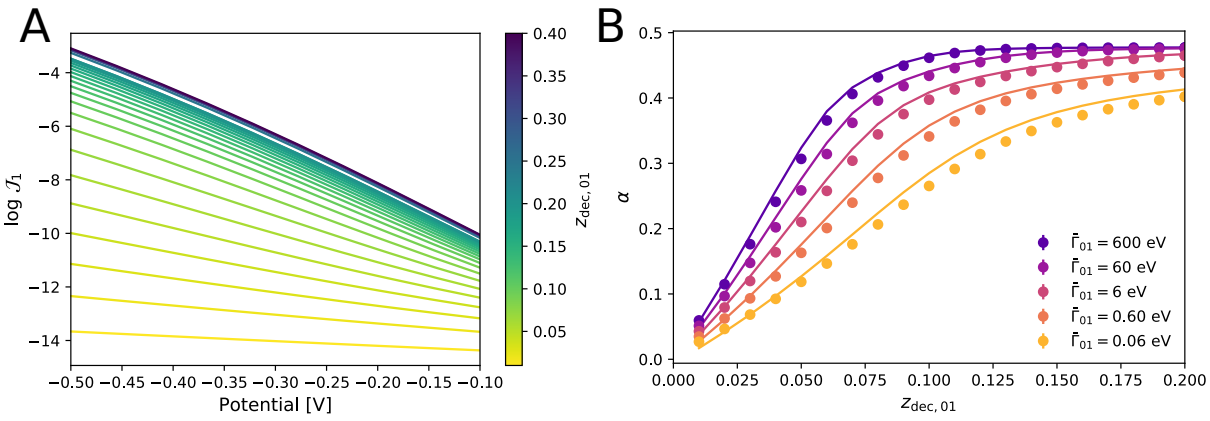

Figure 7.5: Current-voltage curves and transfer coefficient predictions from the two-surface model, for $k_{\text{reorg}} = 2.00$ eV. (A) Several current-voltage curves measured for different values of the coupling localization parameter $z_{\text{dec},01}$, with $\bar{\Gamma}_{01} = 6$ eV. (B) Transfer coefficients determined by linear fitting for a number of different coupling strengths are shown as colored dots. The solid lines are predictions from the simple model/approximation developed in Eq. (7.28).

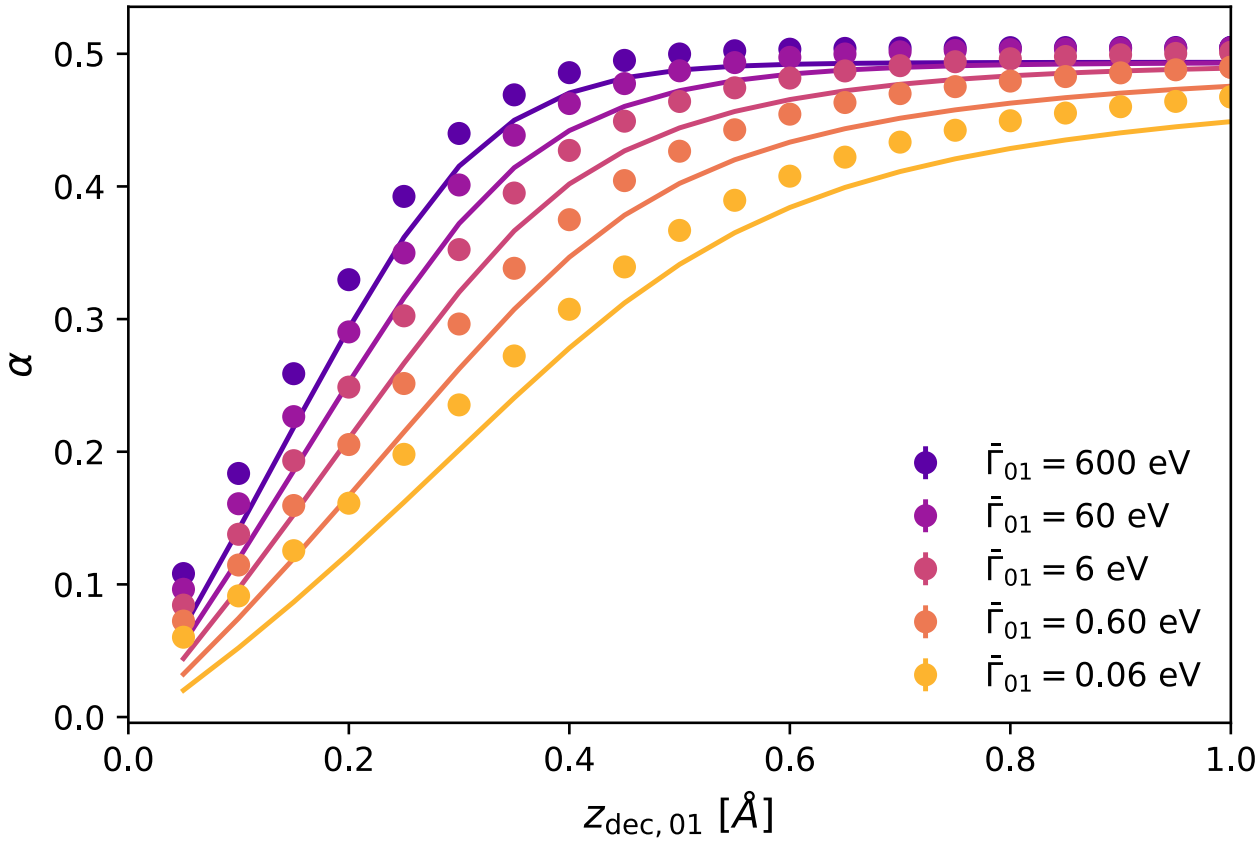

Figure 7.6: Transfer coefficients determined from linear fitting of current-voltage behavior versus $z_{\mathrm{dec},01}$, presented here on a dimensional scale, assuming $L = 5$ Å.

Dimensionalized Results for Transfer Coefficient Attenuation

A replication of Figure 3B from the main text, but this time with the parameter $z_{\mathrm{dec},01}$ presented on a dimensional scale, taking $L = 5$ Å, characteristic for an aqueous electrolyte with a 1M concentration of monovalent salt. We hope this helps contextualize the results presented in the main text in terms of length scales familiar to electrochemical literature.

Results for Exponential Potential Decay Profile

A replication of Figure 3B from the main text, but with an augmented potential profile,

$$\phi(z) = V \exp\left[-\frac{z}{\nu}\right], \tag{7.29}$$

representing the Gouy-Chapman solution to potential decay in an electrolyte with mobile charges at a plane interface held at constant potential. In these simulations, we set $\nu = 0.285L$. Note that the solid lines from the main-text figure are derived from an analytical approximation that only holds for the linear decay profile presented in the main text, so the solid lines are omitted from this figure.

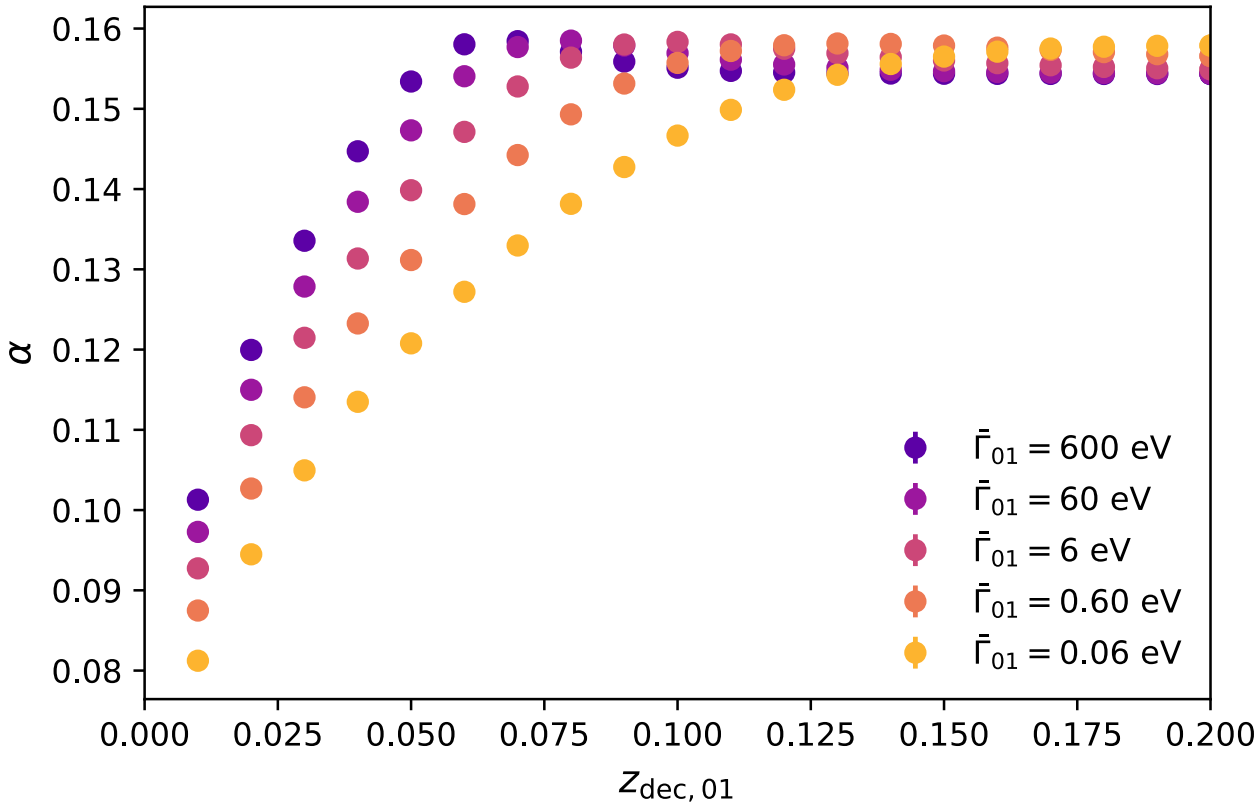

Figure 7.7: Transfer coefficients determined from linear fitting of current-voltage behavior versus $z_{\mathrm{dec},01}$ from a model using the Gouy-Chapman potential decay profile in Eq. (7.29).

7.1.4 References

[1] Wenjun Ouyang and Joseph E Subotnik. The dynamics of charge transfer with and without a barrier: A very simplified model of cyclic voltammetry. *The Journal of chemical physics*, 146(17):174103, 2017.

[2] Hannes Risken and Till Frank. The Fokker-Planck Equation: Methods of Solutions and Applications (Springer Series in Synergetics). *Springer*, 1996. ISSN 03233847. doi: 10.1007/978-3-642-61544-3. URL `http://www.amazon.ca/exec/obidos/redirect?tag=citeulike09-20{&}path=ASIN/354061530X`.

[3] Allen J Bard, Larry R Faulkner, Johna Leddy, and Cynthia G Zoski. *Electrochemical methods: fundamentals and applications*, volume 2. Wiley New York, 1980.

7.2 Additional Information: Understanding Attenuated Marcus Reorganization Energies in the Electrochemical Double Layer

7.2.1 Resummation Procedure for Image Charge Series

The Madelung potential as defined is computed with the image charges from the *initial* state. To get the appropriate vertical energy gap for a system with constant potential boundaries, we need to subtract away the interaction energy of the initial charge in the "primary cell" (see Fig. 2 in the main text) with its image charges in the z-direction, and then add back the interaction energy of the final charge in the "primary cell" with its image charges in the z-direction. Let $\phi_{k,\text{img.}}(z)$ denote the electrostatic potential at position $\mathbf{r}_k$ induced by all image charges of the copy of species k in the "primary cell", when species k carries charge z. Formally,

$$\Delta E_{\text{gap}} = \underbrace{q_f \left[\underbrace{\phi_{k,\text{Mad.}}}_{\substack{\text{potential from}\\ \text{initial's images}}} \quad \underbrace{-\phi_{k,\text{img.}}(q_i)}_{\substack{\text{remove potential from}\\ \text{homebox initial's images}}} \quad \underbrace{+\phi_{k,\text{img.}}(q_f)}_{\substack{\text{add back potential from}\\ \text{homebox final's images}}} \right]}_{\text{final energy}} - \underbrace{q_i \phi_{k,\text{Mad.}}}_{\text{initial energy}} \tag{7.30}$$

To proceed, we needs some way to evaluate $\phi_{k,\text{img.}}(z)$. Cox and Geissler developed the following expression by explicitly writing an infinite series accounting for all image contributions.[1]

$$\phi_{k,\text{img.}}(q) = \sum_{n=0}^{\infty} \frac{(-1)^{2n+1} \cdot q}{2 \cdot (nL + \hat{d}_1)} + \sum_{n=1}^{\infty} \frac{(-1)^{2n} \cdot q}{2 \cdot nL} + \sum_{n=0}^{\infty} \frac{(-1)^{2n+1} \cdot q}{2 \cdot (nL + \hat{d}_2)} + \sum_{n=1}^{\infty} \frac{(-1)^{2n} \cdot q}{2 \cdot nL} \tag{7.31}$$

$$\phi_{k,\text{img.}}(q) = \frac{q}{2L} \left[\sum_{n=0}^{\infty} \frac{(-1)^{2n+1}}{(n + d_1)} + \sum_{n=1}^{\infty} \frac{(-1)^{2n}}{n} + \sum_{n=0}^{\infty} \frac{(-1)^{2n+1}}{(n + d_2)} + \sum_{n=1}^{\infty} \frac{(-1)^{2n}}{n} \right] \tag{7.32}$$

Here, $\hat{d}_1$ is the z-distance from the nearest electrode boundary, and $\hat{d}_2 \equiv L - \hat{d}_1$, its complement. The quantities $d_1 \equiv \hat{d}_1/L$ and $d_2 \equiv \hat{d}_2/L$ are their non-dimensional counterparts. The series summations in Eq. 7.32 are conditionally convergent. As written, each series is a divergent harmonic series. The following resummation organizes the series into a pair of alternating harmonic series, which are summable.

$$\phi_{k,\text{img.}}(z) = \frac{z}{2L} \left[-\frac{1}{d_1} + \sum_{n=1}^{\infty} \left(\frac{1}{n} - \frac{1}{(n + d_1)} \right) - \frac{1}{d_2} + \sum_{n=1}^{\infty} \left(\frac{1}{n} - \frac{1}{(n + d_2)} \right) \right]$$

$$\phi_{k,\text{img.}}(z) = \frac{z}{2L} \left[-\frac{1}{d_1} - \frac{1}{d_2} + \sum_{n=1}^{\infty} \frac{d_1}{n^2 + n d_1} + \sum_{n=1}^{\infty} \frac{d_2}{n^2 + n d_2} \right]$$

Isolating the summation and identifying a closed-form result,

$$\mathcal{S}[d] = \sum_{n=1}^{\infty} \frac{d}{n^2 + nd}, \tag{7.33}$$

$$\mathcal{S}[d] = \gamma + \psi(1 + d), \tag{7.34}$$

where $\psi(z)$ is the digamma function, and $\gamma = 0.577216\ldots$ is the Euler-Mascheroni constant. Using this result, Equation 7.33 becomes

$$\phi_{k,\text{img.}}(q) = \frac{q}{2L}\left[-\frac{1}{d_1} - \frac{1}{d_2} + 2\gamma + \psi(1 + d_1) + \psi(1 + d_2)\right]$$

$$\phi_{k,\text{img.}}(q) = \frac{q}{2L}\left[-\frac{d_1 + d_2}{d_1 d_2} + 2\gamma + \psi(1 + d_1) + \psi(1 + d_2)\right]$$

Note that the potential due to the image charges immediately factorizes as

$$\phi_{k,\text{img.}}(q) = q \cdot f(d_1, d_2)$$

where $f(d_1, d_2)$ is the correction function

$$f(d_1, d_2) \equiv \frac{1}{2L}\left[-\frac{d_1 + d_2}{d_1 d_2} + 2\gamma + \psi(1 + d_1) + \psi(1 + d_2)\right]. \tag{7.35}$$

7.2.2 Simulation Details

The simulations are performed using the classical MD simulator LAMMPS,[2] with the Constant Potential package for simulating the electrolyte-electrode interactions.[3] To distance our study from any particular type of molecular system, we use the non-dimensional Lennard-Jones (LJ) style unit system as implemented in LAMMPS. A simulation box of size $80 \times 80 \times 100$ ($x \times y \times z$) includes two parallel planar electrodes, each comprised of 3 layers of electrode atoms, which are placed at $z = 10$ and $z = 90$, effectively creating a region of size $80 \times 80 \times 80$ between the electrodes. The positions of the electrode atoms are held fixed, and the electrodes are kept at a constant potential, with no applied voltage bias between the two electrodes. A group of positive and negative monovalent ions are confined in inter-electrode region, and interact with the electrode atoms via both a short-range LJ potential (with $\epsilon = 0.2$ and $\sigma = 2.5$) and long-range electrostatics. The ions are generic LJ spheres, interacting with each other with LJ parameters $\epsilon = 1$ and $\sigma = 1$. The density for each type of ion (number of ions/volume) in the region between the electrode is 0.001, *i.e.*, there are 512 positive ions and 512 negative ions in the $80 \times 80 \times 80$ volume. The dynamics of ions are evolved in the NVE ensemble with a Langevin thermostat fixed at a temperature of 1. All particles are assigned a mass of 1. Periodic boundary conditions are used for the x and y directions, while non-periodic boundary conditions are used for the z direction, and the slab version of particle-particle particle-mesh (PPPM) is used for the k-space Ewald summation algorithm. The electrodes are simulated by using the constant potential method, first introduced by Siepmann and Sprik[4], and the further developed by Reed *et al*[5] and Gingrich *et*

al.[6] In this method, the charges on the electrode atoms fluctuate according to the electrolyte environment close to the interface, in order to maintain constant electric potential on the electrodes. The fluctuating charges are determined at specified time steps by solving for the electrostatic interactions between the electrode atoms and the electrolyte ions. Further constraint from applied potential bias can be easily added to the electrode charges. The utilized package of such method in LAMMPS is implemented by Wang *et al.*[3]

7.2.3 Analytical Theory Details

In this section, we work out in detail some common Fourier space manipulations used in the main text, and quote the result for the summation in Eq. 21 in terms of non-elementary functions.

Charge–Potential Relationship in Fourier Space

Starting from Eq. 13 in the main text,

$$
\begin{aligned}
\nabla^2\varphi - 4\pi\kappa^2\varphi &= -4\pi\rho \\
\nabla^2\left[\sum_{q=1}^{\infty}\hat{\varphi}(q)\psi_q(z)\right] - 4\pi\kappa^2\sum_{q=1}^{\infty}\hat{\varphi}(q)\psi_q(z) &= -4\pi\sum_{q=1}^{\infty}\hat{\rho}(q)\psi_q(z) \\
\int_{-1}^{1}dz\,\psi_\ell(z)\left\{-\sum_{q=1}^{\infty}q^2\hat{\varphi}(q)\psi_q(z) - 4\pi\kappa^2\sum_{q=1}^{\infty}\hat{\varphi}(q)\psi_q(z)\right\} &= -4\pi\int_{-1}^{1}dz\,\psi_\ell(z)\left\{\sum_{q=1}^{\infty}\hat{\rho}(q)\psi_q(z)\right\} \\
\sum_{q=1}^{\infty}q^2\hat{\varphi}(q)\int_{-1}^{1}dz\,\psi_\ell(z)\psi_q(z) + 4\pi\kappa^2\sum_{q=1}^{\infty}\hat{\varphi}(q)\int_{-1}^{1}dz\,\psi_\ell(z)\psi_q(z) &= 4\pi\sum_{q=1}^{\infty}\hat{\rho}(q)\int_{-1}^{1}dz\,\psi_\ell(z)\psi_q(z) \\
\sum_{q=1}^{\infty}q^2\hat{\varphi}(q)\delta_{q\ell} + 4\pi\kappa^2\sum_{q=1}^{\infty}\hat{\varphi}(q)\delta_{q\ell} &= 4\pi\sum_{q=1}^{\infty}\hat{\rho}(q)\delta_{q\ell} \\
\ell^2\hat{\varphi}(\ell) + 4\pi\kappa^2\hat{\varphi}(\ell) &= 4\pi\hat{\rho}(\ell) \\
\left(q^2 + 4\pi\kappa^2\right)\hat{\varphi}(q) &= 4\pi\hat{\rho}(q),
\end{aligned}
$$

where the final equation is the Fourier space relationship between the free charge density and the potential, quoted as Eq. 16 in the main text.

Factorization of Pointwise Gaussian Field Distribution

Starting from Eq. 17,

$$\begin{aligned}
\mathcal{P}\left[\rho(z);\sigma_\rho\right] &\propto \exp\left[-\frac{1}{2\sigma_\rho^2}\cdot\int_{-1}^{1}\mathrm{d}z\,\rho(z)^2\right] \\
\mathcal{P}\left[\hat{\rho}(q);\sigma_\rho\right] &\propto \exp\left[-\frac{1}{2\sigma_\rho^2}\cdot\int_{-1}^{1}\mathrm{d}z\,\left[\sum_{q=1}^{\infty}\hat{\rho}(q)\psi_q(z)\right]\cdot\left[\sum_{\ell=1}^{\infty}\hat{\rho}(\ell)\psi_\ell(z)\right]\right] \\
\mathcal{P}\left[\hat{\rho}(q);\sigma_\rho\right] &\propto \exp\left[-\frac{1}{2\sigma_\rho^2}\cdot\sum_{(q,\ell)=(1,1)}^{\infty}\hat{\rho}(q)\hat{\rho}(\ell)\int_{-1}^{1}\mathrm{d}z\,\psi_q(z)\psi_\ell(z)\right] \\
\mathcal{P}\left[\hat{\rho}(q);\sigma_\rho\right] &\propto \exp\left[-\frac{1}{2\sigma_\rho^2}\cdot\sum_{(q,\ell)=(1,1)}^{\infty}\hat{\rho}(q)\hat{\rho}(\ell)\delta_{q\ell}\right] \\
\mathcal{P}\left[\hat{\rho}(q);\sigma_\rho\right] &\propto \exp\left[-\frac{1}{2\sigma_\rho^2}\cdot\sum_{q=1}^{\infty}\hat{\rho}(q)^2\right] \\
\mathcal{P}\left[\hat{\rho}(q);\sigma_\rho\right] &\propto \prod_{q=1}^{\infty}\exp\left[-\frac{\hat{\rho}(q)^2}{2\sigma_\rho^2}\right],
\end{aligned}$$

which is quoted as Eq. 18 in the main text.

Analytical Result for Variance Profile

The analytical result for the summation encountered when performing Fourier inversion are reported here. The result are expressed in terms of certain special functions, which we will define prior to presenting the final result. The Hurwitz-Lerch transcendent,

$$\Phi_{\mathrm{HL}}(z,s,\alpha)\equiv\sum_{n=0}^{\infty}\frac{z^n}{(n+\alpha)^s}. \tag{7.36}$$

The Gamma function,

$$\Gamma(z)\equiv\int_0^{\infty}\mathrm{d}x\,x^{z-1}e^{-x}. \tag{7.37}$$

Finally, the Gauss hypergeometric function:

$${}_2F_1(a,b;c;z) \;\equiv\; \frac{\Gamma(c)}{\Gamma(b)\Gamma(c-b)}\cdot\int_0^1\mathrm{d}t\,\frac{t^{b-1}(1-t)^{c-b-1}}{(1-tz)^a}. \tag{7.38}$$

Practically, these functions are evaluated using the `mpmath` library in Python for constructing the figures displayed in the main text.[7] The analytical result is,

$$\begin{aligned}\sigma_\varphi^2(z) \;=\; \frac{\sigma_\rho^2}{4\kappa^4}\Bigg\{ & -1+\sqrt{\pi}\kappa\cdot\coth\left(2\sqrt{\pi}\kappa\right)+2\pi\kappa^2\cdot\operatorname{csch}^2\left(2\sqrt{\pi}\kappa\right)^2 \\ & +\pi^{-1}e^{-2\pi iz}\kappa^2\cdot\Bigg[\Phi_{\mathrm{HL}}\left(e^{2\pi iz},2,1-\frac{2i\kappa}{\sqrt{\pi}}\right)+\Phi_{\mathrm{HL}}\left(e^{-2\pi iz},2,1+\frac{2i\kappa}{\sqrt{\pi}}\right) \\ & \quad +\Gamma\left(-\frac{2i\kappa}{\sqrt{\pi}}\right){}_2F_1\left(1,1-\frac{2i\kappa}{\sqrt{\pi}};2-\frac{2i\kappa}{\sqrt{\pi}};e^{-2\pi iz}\right) \\ & \quad +\Gamma\left(+\frac{2i\kappa}{\sqrt{\pi}}\right){}_2F_1\left(1,1+\frac{2i\kappa}{\sqrt{\pi}};2+\frac{2i\kappa}{\sqrt{\pi}};e^{-2\pi iz}\right)\Bigg] \\ & +\pi^{-1}e^{+2\pi iz}\kappa^2\cdot\Bigg[\Phi_{\mathrm{HL}}\left(e^{2\pi iz},2,1-\frac{2i\kappa}{\sqrt{\pi}}\right)+\Phi_{\mathrm{HL}}\left(e^{-2\pi iz},2,1+\frac{2i\kappa}{\sqrt{\pi}}\right) \\ & \quad +\Gamma\left(-\frac{2i\kappa}{\sqrt{\pi}}\right){}_2F_1\left(1,1-\frac{2i\kappa}{\sqrt{\pi}};2-\frac{2i\kappa}{\sqrt{\pi}};e^{-2\pi iz}\right) \\ & \quad +\Gamma\left(+\frac{2i\kappa}{\sqrt{\pi}}\right){}_2F_1\left(1,1+\frac{2i\kappa}{\sqrt{\pi}};2+\frac{2i\kappa}{\sqrt{\pi}};e^{-2\pi iz}\right)\Bigg]\Bigg\}.\end{aligned} \tag{7.39}$$

The expression in Eq. 7.39 is rather opaque. We can extract the qualitative behavior of this function by examining the original summation in Eq. 21, reproduced as,

$$\sigma_\varphi^2(z)=\frac{16\sigma_\rho^2}{\pi^2}\sum_{n=1}^{\infty}\frac{\sin^2(n\pi z)}{\left(n^2+4\kappa^2/\pi\right)^2}. \tag{7.40}$$

Symmetry of the problem demands that the function is symmetric around $z=0.5$. It is also apparent that $\mathrm{Var}[\varphi(0)]=0$, since $\sin(0)=0$. Perhaps less apparently, this function must plateau for values of $\kappa z>1$. To see why, first note that the sum is well-approximated by only considering frequencies up to a cutoff κ, since higher frequency components are killed quickly by a factor of n^4. These "relevant" frequency components can all be linearized to good approximation by qz for $\kappa z\ll 1$. In this range, all of these frequency components are increasing, and so $\mathrm{Var}[\varphi(z)]$ is also increasing. The linearization fails after $\kappa z\approx 1$, since the highest relevant frequency component begins to plateau and then decrease. For $z\gg\kappa^{-1}$, the sum runs over nearly orthogonal functions, and hence does not change much with z. This is indeed the behavior observed in Fig. 4 in the main text.

7.2.4 Additional Figures

Ratio between reorganization energies computed by using $\sigma^2[\Delta E]$ and using $\langle \Delta E \rangle$

As described in the main text (Sec. IIA), the reorganization energy, λ, can be obtained by the following two equations, by the courtesy of linear response theory:

$$\lambda_1 = \frac{\beta\sigma^2[\Delta E_{\text{red}}]}{2} = \frac{\beta\sigma^2[\Delta E_{\text{ox}}]}{2}, \tag{7.41a}$$

$$\lambda_2 = \frac{\langle \Delta E_{\text{red}} \rangle - \langle \Delta E_{\text{ox}} \rangle}{2}. \tag{7.41b}$$

Therefore, one way to validate the linear response assumption for a particular system is to compare λ_1 and λ_2 calculated using $\sigma^2[\Delta E]$ and $\langle \Delta E \rangle$ obtained from MD simulations, respectively. Figure 7.8 shows that λ_1 and λ_2 largely overlap, and that the ratio λ_1/λ_2 is close to 1 for all z positions.

MD simulation results of reorganization energy for systems with different Debye length

As shown by field theory in Sec. IIIB, the exact profile for $\sigma^2[\Delta E]$ changes as the Debye length, λ_D, of the electrolyte system changes. In particular, the size of the bulk region is larger for systems with smaller Debye length. This effect can be captured by MD simulations. Keeping the size of the simulation box the same, different Debye lengths can be achieved by changing the ion concentration in the electrolyte, according to the following relation:

$$\lambda_D = \left(\frac{k_B T}{\sum_{j=1}^{N} n_j^0 q_j^2} \right) \tag{7.42}$$

where k_B is the Boltzmann constant, T is temperature, n_j^0 is the mean concentration of species j, q_j is the charge of species j, and N is the total number of charged species. From the relation, it is clear that λ_D is smaller for systems with higher ionic strength ($\sum_{j=1}^{N} n_j^0 q_j^2$). Because the charges of the ions are kept constant for different systems, higher concentration in our simulation is equivalent to larger ionic strength. Figure 7.9 presents the profiles of normalized reorganization energy λ for systems with different ion concentration. Compared to Fig. 4(b), the MD results qualitatively match those from field theory, *i.e.*, bulk region is larger for systems with higher ion concentration.

Empirical free charge distributions from MD simulations

We computed free charge distributions from simulations by applying a spatial binning procedure to the ionic charges in the MD simulation cell. Figure 7.10 depicts a family of traces of the empirically-observed free energy profiles of the free charge density for various values of the z distance from the electrode. Modulo sampling artifacts, the charge density distributions all have roughly equivalent variance. This lends some empirical support toward employing a position-independent charge density field variance when constructing a fluctuating field theory.

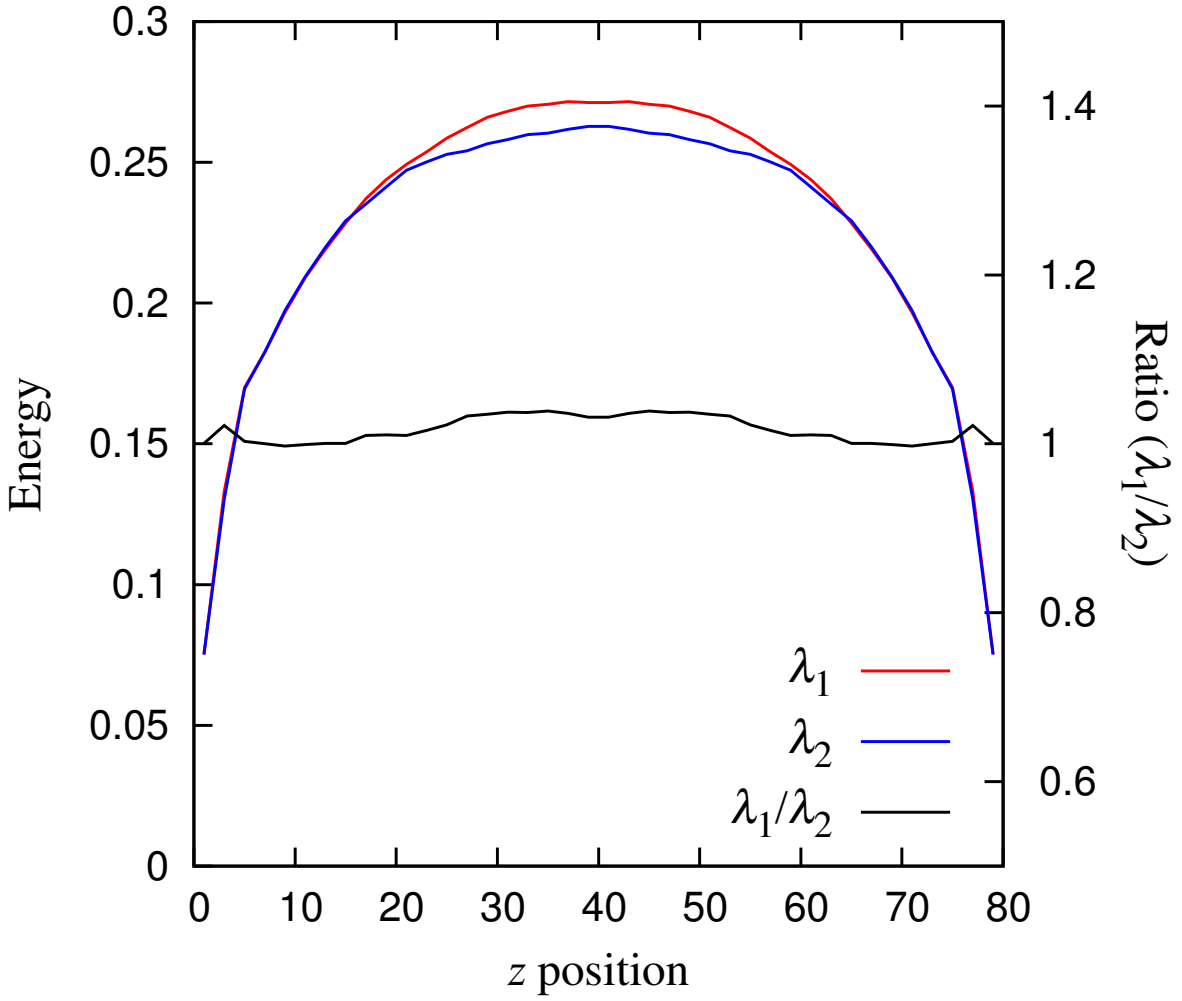

Figure 7.8: The reorganization energies, λ_1 (red line) and λ_2 (blue line), calculated using $\sigma^2[\Delta E]$ and $\langle \Delta E \rangle$ obtained from MD simulations, respectively. The black line is the ratio between λ_1 and λ_2.

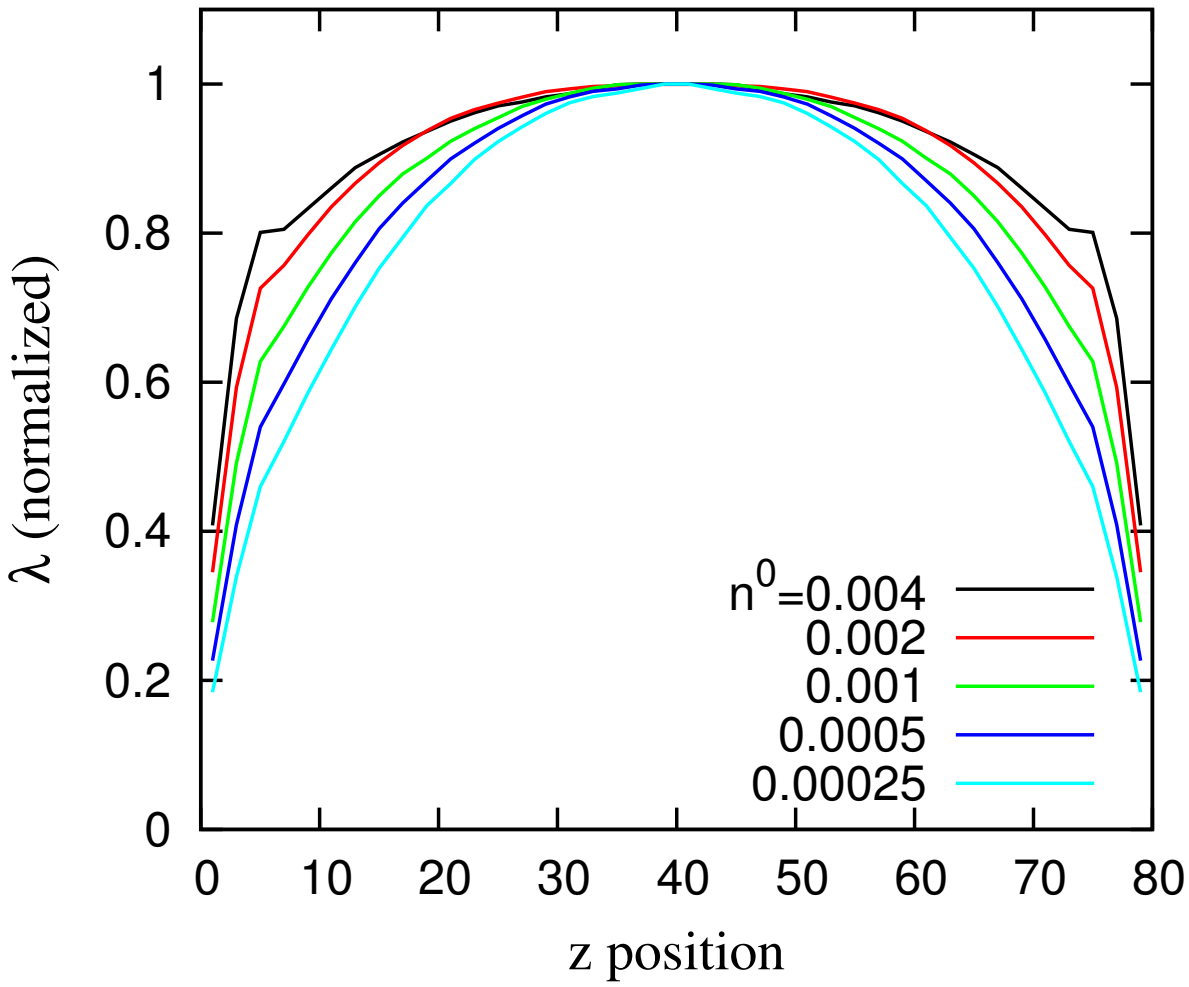

Figure 7.9: The normalized reorganization energies, λ, for systems with different ionic strength obtained from MD simulations.

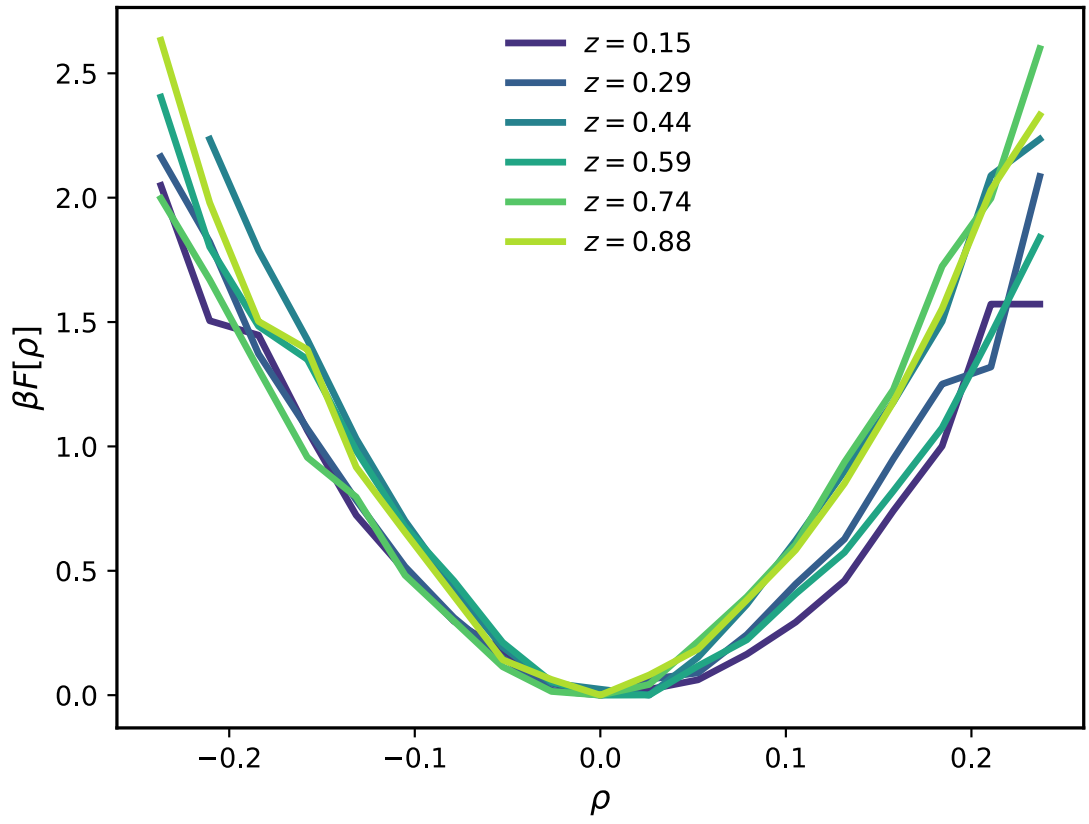

Figure 7.10: Traces of the empirically observed free energy for a free charge density ρ, colored by z-position along the simulated electrochemical system, made non-dimensional by the electrode length scale, L.

7.2.5 References

[1] Stephen J Cox and Phillip L Geissler. Interfacial ion solvation: Obtaining the thermodynamic limit from molecular simulations. *J. Chem. Phys.*, 148(22):222823, 2018. ISSN 0021-9606. doi: 10.1063/1.5020563.

[2] Steve Plimpton. Fast parallel algorithms for Short-Range molecular dynamics. *J. Comput. Phys.*, 117(1):1–19, 1995. ISSN 0021-9991. doi: 10.1006/jcph.1995.1039.

[3] Zhenxing Wang, Yang Yang, David L Olmsted, Mark Asta, and Brian B Laird. Evaluation of the constant potential method in simulating electric double-layer capacitors. *J. Chem. Phys.*, 141(18):184102, 2014. ISSN 0021-9606. doi: 10.1063/1.4899176.

[4] Ilja J Siepmann and Michiel Sprik. Influence of surface topology and electrostatic potential on water/electrode systems. *J. Chem. Phys.*, 102(1):511–524, 1995. ISSN 0021-9606. doi: 10.1063/1.469429.

[5] Stewart K Reed, Oliver J Lanning, and Paul A Madden. Electrochemical interface between an ionic liquid and a model metallic electrode. *J. Chem. Phys.*, 126(8):084704, 2007. ISSN 0021-9606. doi: 10.1063/1.2464084.

[6] Todd R Gingrich and Mark Wilson. On the ewald summation of gaussian charges for the simulation of metallic surfaces. *Chem. Phys. Lett.*, 500(1-3):178–183, 2010. ISSN 0009-2614. doi: 10.1016/j.cplett.2010.10.010.

[7] Fredrik Johansson et al. *mpmath: a Python library for arbitrary-precision floating-point arithmetic (version 0.18)*, December 2013. `http://mpmath.org/`.

7.3 Additional Information: Electrostatic Screening in Moderately Concentrated Aqueous Electrolyte is Concentration-Independent and Microscopically Heterogeneous

7.3.1 Computational Details for Poisson Potential Computation

Given a molecular simulation trajectory, we would like to devise a numerical scheme to determine the Poisson potential at any point in the simulation volume. The Poisson potential φ is defined by the Poisson equation,

$$\nabla^2 \varphi = \rho, \tag{7.43}$$

where ρ is the free charge density field. The geometry under consideration has two periodic dimensions, denoted x and y, and one closed dimension z, which is the coordinate normal to the planar electrodes. The appropriate boundary conditions are,

$$\varphi(0, y, z) = \varphi(L_x, y, z) \tag{7.44}$$
$$\varphi(x, 0, z) = \varphi(x, L_y, z) \tag{7.45}$$
$$\partial_x \varphi(0, y, z) = \partial_x \varphi(L_x, y, z) \tag{7.46}$$
$$\partial_y \varphi(x, 0, z) = \partial_y \varphi(x, L_y, z) \tag{7.47}$$
$$\varphi(x, y, 0) = V_{\text{left}} \tag{7.48}$$
$$\varphi(x, y, L_z) = V_{\text{right}}, \tag{7.49}$$

where V_{left} and V_{right} are the applied potentials on the left and right electrodes, situated at $z = 0$ and $z = L_z$, respectively.

To start developing a numerical scheme, we can discretize Eq. (7.43) on a three-dimensional rectangular grid. Given a specification of the number of grid points $\mathbf{N} = (N_x, N_y, N_z)$, we can define a vector of grid spacings $\boldsymbol{\Delta} \equiv \left(N_x^{-1}, N_y^{-1}, [N_z + 1]^{-1}\right)$. Note that the z-coordinate has a slightly different grid spacing because we would like to impose Dirichlet boundary conditions in this coordinate, requiring an extra boundary point. Now, grid points can be indexed by an index tuple $\mathbf{n} \in \{0, \ldots, N_x - 1\} \times \{0, \ldots, N_y - 1\} \times \{0, \ldots, N_z\}$. The spatial location of a grid point with index tuple $\mathbf{n}$ is simply $\mathbf{r}_{\mathbf{n}} = \boldsymbol{\Delta} \cdot \mathbf{n}$. Equation (7.43) can be naturally discretized using a second-order Laplacian stencil. Under a row-major indexing scheme for the coordinates, this produces a sparse representation of the Laplacian operator, whose sparsity pattern is depicted in Fig. 7.11A.

Solving Eq. (7.43), discretized on a grid, is relatively straightforward if we have a way to evaluate the free charge density field, ρ, on the grid points. However, particles in a molecular simulation are, in general, not situated on a uniform grid. Hence, we need a scheme for interpolating a non-uniform charge density field onto a uniform grid of points. Figure 7.11B describes the scheme pictorially in two dimensions; extension to three dimensions is straightforward. Formally, for a particle with index k carrying charge q_k localized at position $\mathbf{r}_k = (x_k, y_k, z_k)$, we identify eight points bounding the voxel containing the particle. The

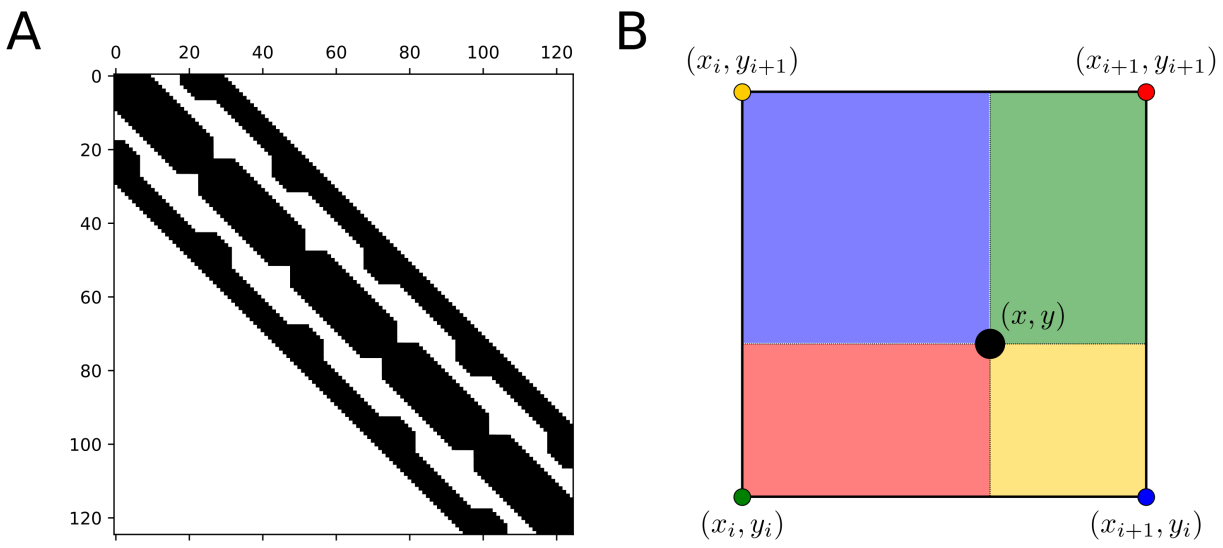

Figure 7.11: (A) Sparsity pattern for discretized Laplacian operator, for $\mathbf{N} = (5, 5, 4)$. (B) Schematic depiction of charge interpolation scheme in two dimensions. Each boundary point receives a fraction of the charge proportional to the ratio of its correspondingly colored rectangle area to the entire voxel area.

index tuples of these eight points can be computed using the following equations,

$$\mathbf{n}_1^k = (\lceil x_k/L_x \rceil, \lfloor y_k/L_y \rfloor, \lfloor z_k/L_z \rfloor) \tag{7.50}$$
$$\mathbf{n}_2^k = (\lfloor x_k/L_x \rfloor, \lfloor y_k/L_y \rfloor, \lfloor z_k/L_z \rfloor) \tag{7.51}$$
$$\mathbf{n}_3^k = (\lceil x_k/L_x \rceil, \lceil y_k/L_y \rceil, \lfloor z_k/L_z \rfloor) \tag{7.52}$$
$$\mathbf{n}_4^k = (\lfloor x_k/L_x \rfloor, \lceil y_k/L_y \rceil, \lfloor z_k/L_z \rfloor) \tag{7.53}$$
$$\mathbf{n}_5^k = (\lceil x_k/L_x \rceil, \lfloor y_k/L_y \rfloor, \lceil z_k/L_z \rceil) \tag{7.54}$$
$$\mathbf{n}_6^k = (\lfloor x_k/L_x \rfloor, \lfloor y_k/L_y \rfloor, \lceil z_k/L_z \rceil) \tag{7.55}$$
$$\mathbf{n}_7^k = (\lceil x_k/L_x \rceil, \lceil y_k/L_y \rceil, \lceil z_k/L_z \rceil) \tag{7.56}$$
$$\mathbf{n}_8^k = (\lfloor x_k/L_x \rfloor, \lceil y_k/L_y \rceil, \lceil z_k/L_z \rceil)\,, \tag{7.57}$$

where $\lfloor \cdot \rfloor$ and $\lceil \cdot \rceil$ represent the integer floor and integer ceiling functions, respectively. Along each dimension $d \in (x, y, z)$, the particle position partitions the line segment connecting two adjacent grid points into two segments, one of length $\ell_\downarrow^{(d)} = \mathbf{r}_k^{(d)} - \lfloor \mathbf{r}_k^{(d)}/L_d \rfloor \cdot \mathbf{\Delta}^{(d)}$, and another of length $\ell_\uparrow^{(d)} = \lceil \mathbf{r}_k^{(d)}/L_d \rceil \cdot \mathbf{\Delta}^{(d)} - \mathbf{r}_k^{(d)}$. Note that $\mathbf{\Delta}^{(d)} = \ell_\downarrow^{(d)} + \ell_\uparrow^{(d)}$, due to the properties of the ceiling and floor functions. For notational convenience, define,

$$\delta = \prod_d \mathbf{\Delta}^{(d)} \tag{7.58}$$

Now, we assign each point bounding the voxel a weight,

$$w_1^k = \delta^{-1} \cdot \ell_\uparrow^{(x)} \ell_\downarrow^{(y)} \ell_\downarrow^{(z)} \tag{7.59}$$
$$w_2^k = \delta^{-1} \cdot \ell_\downarrow^{(x)} \ell_\downarrow^{(y)} \ell_\downarrow^{(z)} \tag{7.60}$$
$$w_3^k = \delta^{-1} \cdot \ell_\uparrow^{(x)} \ell_\uparrow^{(y)} \ell_\downarrow^{(z)} \tag{7.61}$$
$$w_4^k = \delta^{-1} \cdot \ell_\downarrow^{(x)} \ell_\uparrow^{(y)} \ell_\downarrow^{(z)} \tag{7.62}$$
$$w_5^k = \delta^{-1} \cdot \ell_\uparrow^{(x)} \ell_\downarrow^{(y)} \ell_\uparrow^{(z)} \tag{7.63}$$
$$w_6^k = \delta^{-1} \cdot \ell_\downarrow^{(x)} \ell_\downarrow^{(y)} \ell_\uparrow^{(z)} \tag{7.64}$$
$$w_7^k = \delta^{-1} \cdot \ell_\uparrow^{(x)} \ell_\uparrow^{(y)} \ell_\uparrow^{(z)} \tag{7.65}$$
$$w_8^k = \delta^{-1} \cdot \ell_\downarrow^{(x)} \ell_\uparrow^{(y)} \ell_\uparrow^{(z)}. \tag{7.66}$$

The charge density on all grid points is computed by incrementing the charge density on each point $i \in 1, \ldots, 8$ bounding the voxel containing particle k by its charge weight $q_k w_i^k$, and repeating for all particles in the simulation.

7.4 Additional Information: Examining Cardinal Tafel Slope Preferences in CO_2 Reduction Electrocatalysis with Bayesian Data Analysis

7.4.1 Literature Analysis

Residuals vs. Literature-Reported Values

Residual analysis can help sniff out systematic or correlated errors in the results presented in Fig. 3A of the main text. We can define residuals between the literature-reported values and the MAP values in several different ways. Here, we will consider two definitions of the residuals, normalized either to the literature-reported Tafel slopes,

$$\text{Residual Normalized to Reported} = \frac{T_{\text{reported}} - T_{\text{MAP}}}{T_{\text{reported}}}, \tag{7.67}$$

or to the MAP Tafel slopes,

$$\text{Residual Normalized to MAP} = \frac{T_{\text{reported}} - T_{\text{MAP}}}{T_{\text{MAP}}}. \tag{7.68}$$

Figure 7.12 depicts plots of the residuals versus the literature-reported and MAP Tafel slopes (A and C, respectively), as well as kernel density estimates of the distribution over the residuals normalized to the literature-reported and MAP Tafel slopes (B and D, respectively). To the eye, the residuals appear roughly unbiased around zero, and there appear to be no spurious correlations between the residuals.

Correlation Plot over Full Range

Figure 7.13 depicts a correlation plot of the MAP Tafel slope versus the literature-reported Tafel slope, including all datasets considered in this study.

PDF Plot Using all Posterior Samples

For every single dataset considered in the study, we draw $N = 4 \times 10^4$ samples from the posterior distribution over the Tafel slope. In Fig. 3C in the main text, we depict a kernel density estimate of the distribution over the MAP Tafel slope from each of these posterior distributions. We choose to display this data because the MAP Tafel slope is a straightforward point estimate of the Tafel slope given a posterior distribution over the parameter, and hence is likely the quantity one would quote if asked what *the* Tafel slope of a catalyst is. However, the averaging operation involved in computing the MAP Tafel slope can collapse broad features in the posterior distribution down to a single value; this is especially true in the case of bimodal posterior distributions arising from insufficient datasets. Figure 7.14 depicts a kernel density estimate of the distribution over the Tafel slope using all samples collected from the posterior distribution for each dataset. The essential conclusions reported in the main text are upheld when examining the data in Fig. 7.14. A very small preference for Tafel slopes around 45 mV/decade emerges in this analysis. However, given the small

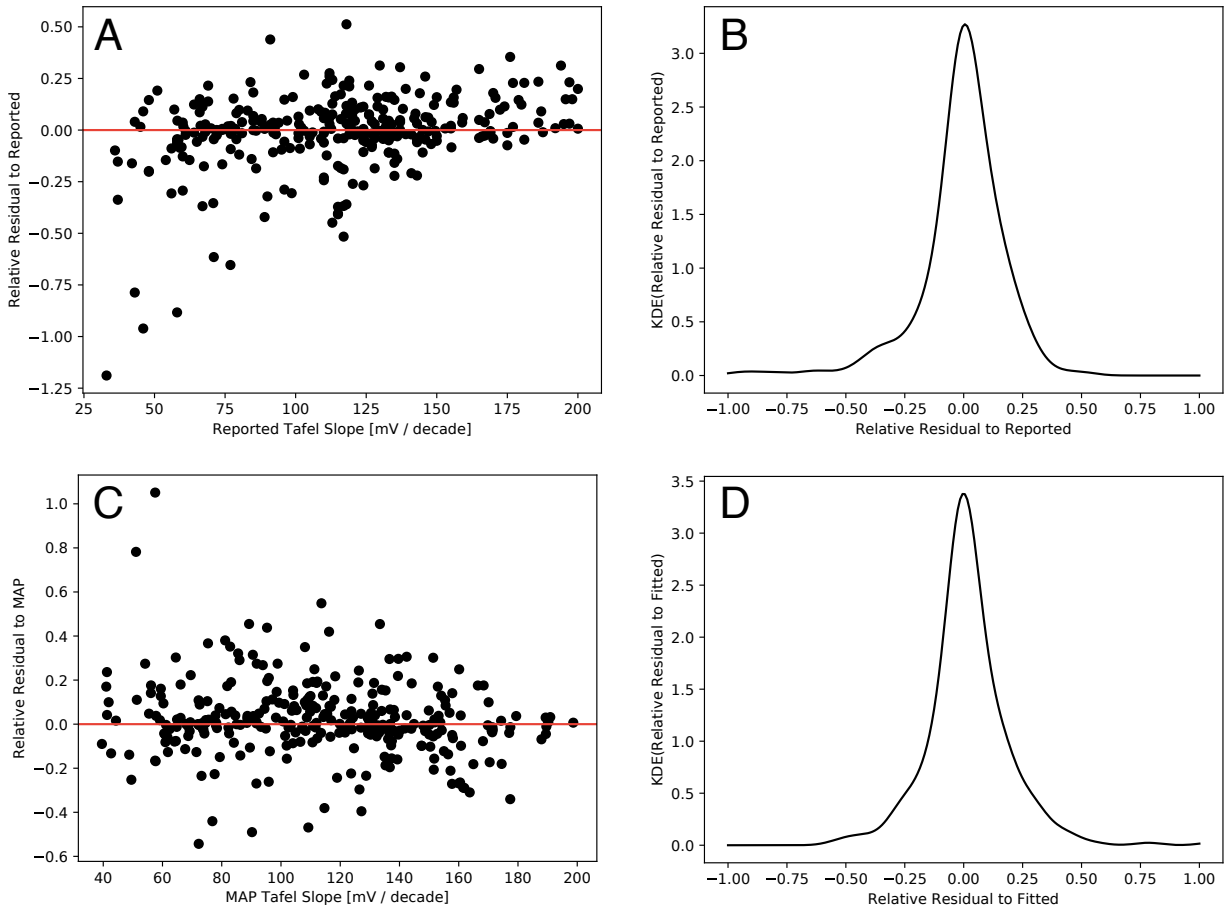

Figure 7.12: Residual Analysis. (A) Plot of the relative residual to the literature-reported Tafel slope, defined in Eq. (7.67), versus the literature-reported Tafel slope, including only reported Tafel slopes less than 200 mV/decade. (B) Kernel density estimate of the distribution over the relative residual to the literature-reported Tafel slope. (C) Plot of the relative residual to the MAP Tafel slope, defined in Eq. (7.67), versus the MAP Tafel slope, including only reported Tafel slopes less than 200 mV/decade. (D) Kernel density estimate of the distribution over the relative residual to the MAP Tafel slope.

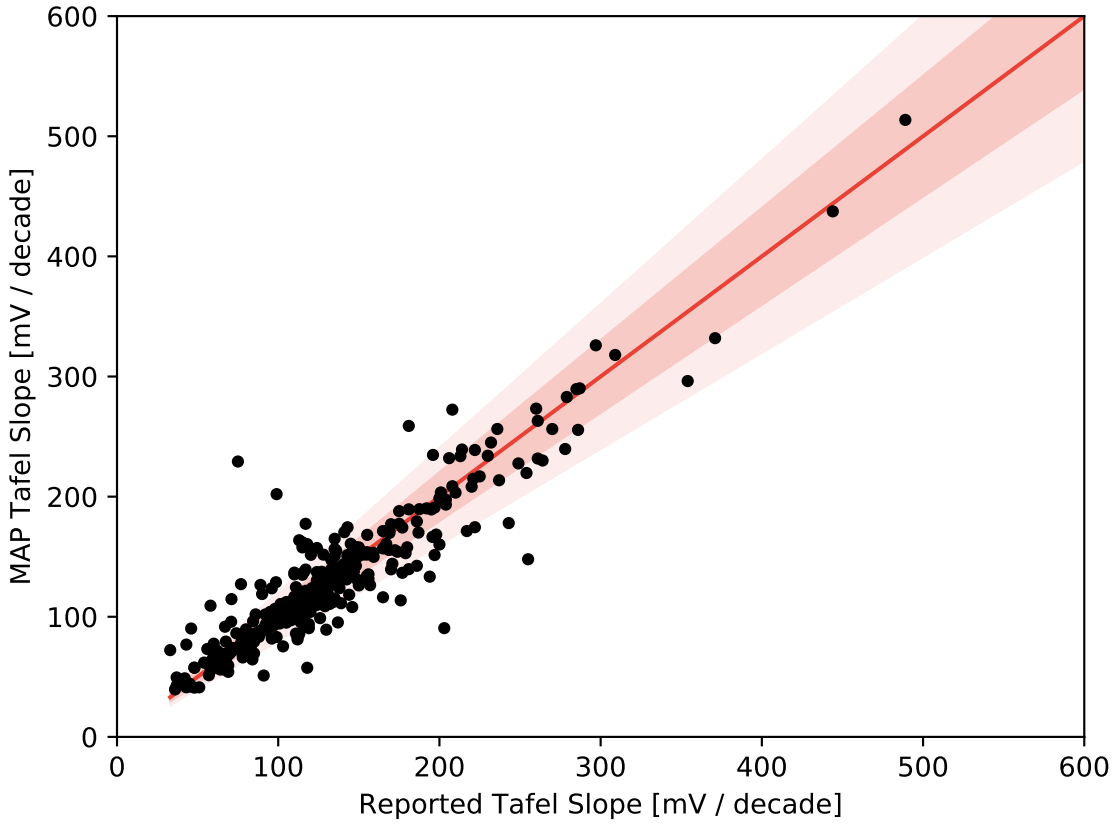

Figure 7.13: Correlation plot of reported Tafel slopes from the literature against Tafel slopes fitted by our algorithm on identical data. The solid red line represents perfect agreement, while the red filled intervals are lines representing 10% and 20% relative error.

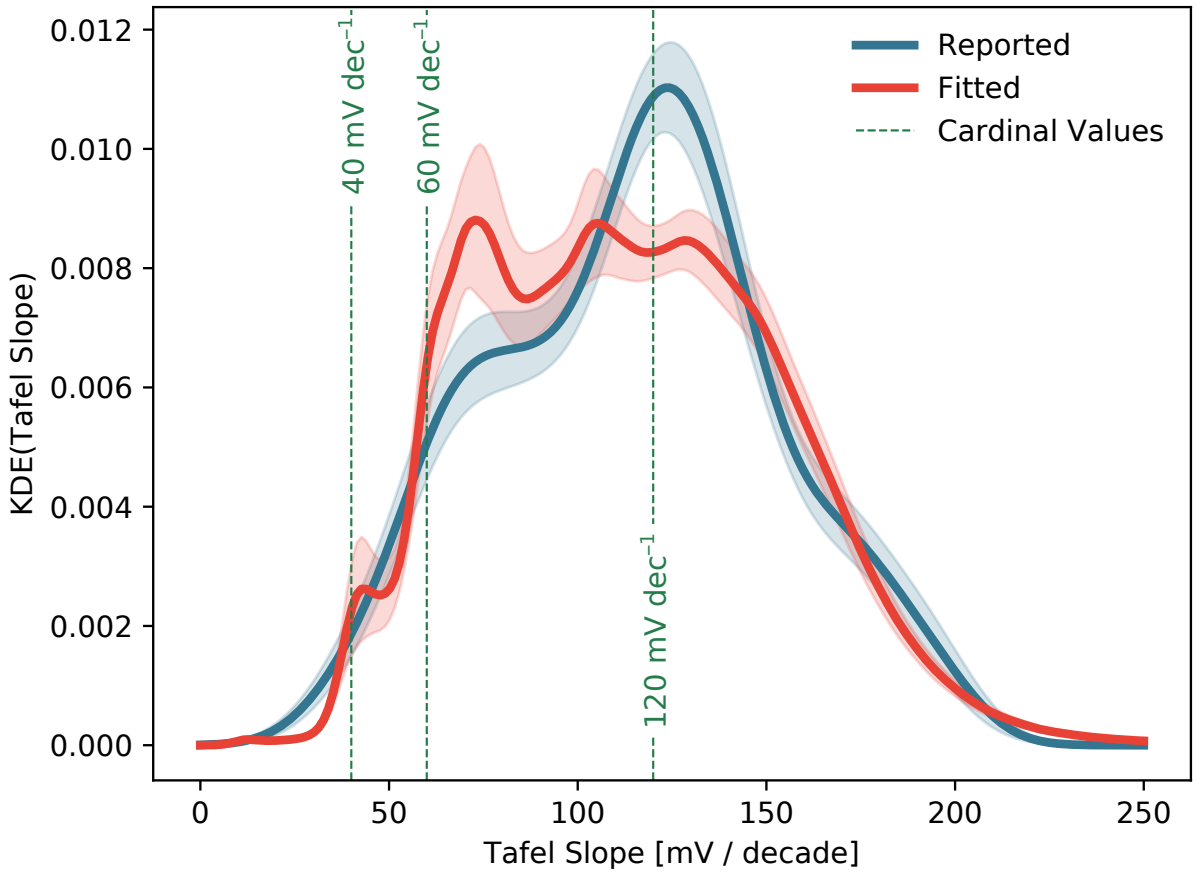

Figure 7.14: Kernel density estimates (KDE) of the empirical probability distribution function of Tafel slopes reported in literature data (blue) and those refitted by our algorithm (red). Error intervals correspond to one standard deviation of bootstrapped resamples. Green dashed lines correspond to cardinal values of the Tafel slope.

amount of total distributional mass under this peak and the high degree of sampling variability (as evinced by the bootstrap standard deviations), we do not believe it should be interpreted strongly.

Catalyst Breakout Results

As described in the main text, we split out our results on the distributions over the Tafel slope by catalyst material identity in order to confirm that our conclusion of a lack of Tafel cardinality in CO_2 reduction catalysis is not an artifact of pooling together data from several catalyst materials, each of which individually exhibit cardinality. Figures 7.15–7.20 depict these results for catalysts containing Cu, Ag, Au, Sn, and Bi. Each figure has three panels: the left-most panel plots a kernel density estimate of the distribution over Tafel slopes using all samples from the posterior distribution, akin to Fig. 7.14. The center panel plots a kernel density estimate of the distribution over the MAP Tafel slope from each dataset, akin to main text Fig. 3C. The right-most panel plots a CDF of the distributional breadth B_i

for each dataset considered. The distributional breadth is parametrized by the threshold parameter t, and is defined as,

$$B_i(t) = \mathrm{CDF}_i^{-1}(1-t) - \mathrm{CDF}_i^{-1}(t), \tag{7.69}$$

where $\mathrm{CDF}_i(m_\mathrm{T})$ represents the CDF of the Tafel slope for the i'th dataset. Intuitively, a high distributional breadth implies that the experimental data measured in the dataset does not provide information to pin down the value of the Tafel slope with high confidence. Correspondingly, if the CDF of the distributional breadth increases quickly, then most of the datasets in the catalyst material subset predict tight distributions over the Tafel slope. Conversely, if the CDF of the distributional breadth climbs slowly, then several datasets in the catalyst material subset do not determine a Tafel slope value with high confidence.

For some catalysts, the KDE constructed from all Tafel slope samples (left panel) and the KDE constructed from the MAP Tafel slope samples (center panel) show different behavior. The former plot looks more visually noisy than the latter plot; this is to be expected, since taking the mean of the posterior distribution over the parameters is a "smoothing" operation. The two ways of visualizing the data convey slightly distinct information, since the KDE constructed from all samples preserves the uncertainty information retained in a single fit, while the KDE constructed from the MAP Tafel slopes is the most direct comparison to the distribution of literature values (which do not carry an associated uncertainty, in most cases). In certain cases (Ag, Sn), the KDE comprising all samples appears to have more defined peaks than the KDE comprising MAP samples. First, we note that in these cases, the bootstrap standard errors for these peaks are much greater than in other areas of the distribution, suggesting that this peaking behavior is controlled by a small number of samples, and hence more variable with respect to a change in the specific datasets re-analyzed in this study. Second, peaking behavior in the KDE comprising all samples that does not appear in the KDE comprising MAP samples is a sign of some underlying data insufficiency issues highlighted by Fig. 2 in the main text; these peaks can easily disappear or be shifted upon measuring additional data. To declare confidently that a certain dataset espouses a cardinal Tafel slope preference, we contend that *both* ways of visualizing the distribution of Tafel slopes for a certain catalyst should show peaking around a cardinal value. This standard, while stringent, enforces that the available experimental data confidently determines a cardinal value of the Tafel slope, free of latent data insufficiency issues. While we observe this for the Bi breakout results in Fig. 7.20, the remainder of the catalyst breakout datasets do not meet this standard. Hence, though we do not foreclose the possibility that additional future data collection on these catalysts may reveal a cardinal Tafel slope preference, we argue that broadly, when considering the data extant in the literature, the typical CO_2 reduction catalyst does not exhibit a strong preference for cardinal values of the Tafel slope.

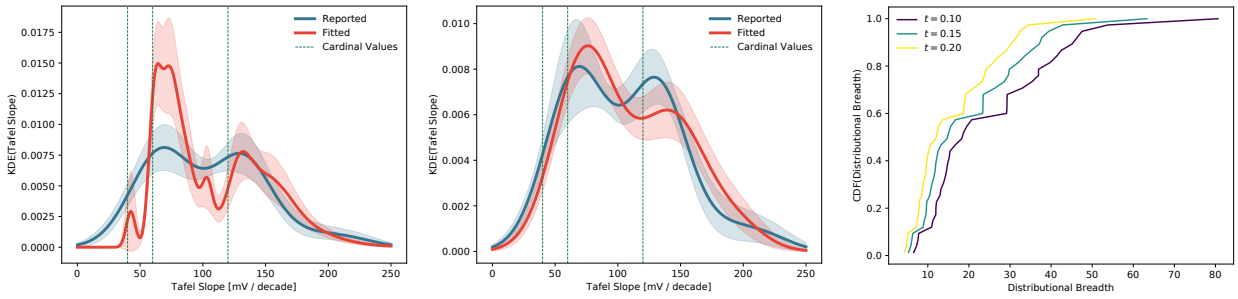

Figure 7.15: Tafel Slope statistics for catalysts containing Ag ($N_{\text{datasets}} = 38$). (Left) Kernel density estimates (KDE) of the empirical probability distribution function of Tafel slopes reported in literature data (blue) and those refitted by our algorithm (red). Error intervals correspond to one standard deviation of bootstrapped resamples. Green dashed lines correspond to cardinal values of the Tafel slope. (Center) Same as (Left), but KDEs are computed using only the MAP Tafel Slope values for each dataset. (Right) CDF of the distributional breadth, as defined by Eq. (7.69).

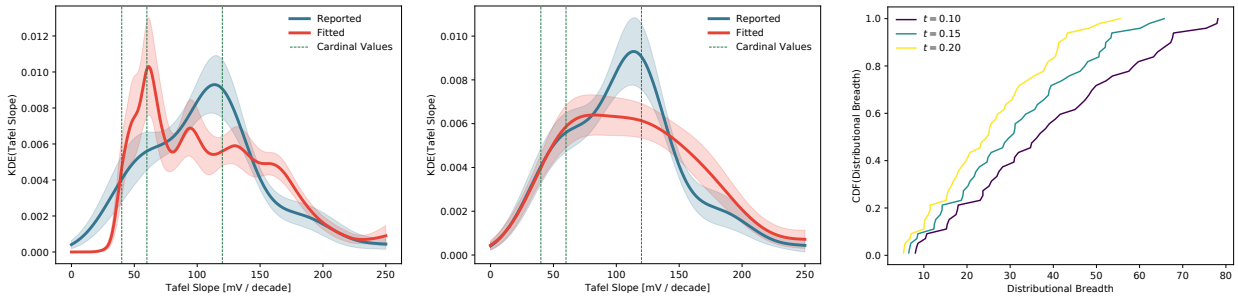

Figure 7.16: Tafel Slope statistics for catalysts containing Au ($N_{\text{datasets}} = 50$). (Left) Kernel density estimates (KDE) of the empirical probability distribution function of Tafel slopes reported in literature data (blue) and those refitted by our algorithm (red). Error intervals correspond to one standard deviation of bootstrapped resamples. Green dashed lines correspond to cardinal values of the Tafel slope. (Center) Same as (Left), but KDEs are computed using only the MAP Tafel Slope values for each dataset. (Right) CDF of the distributional breadth, as defined by Eq. (7.69).

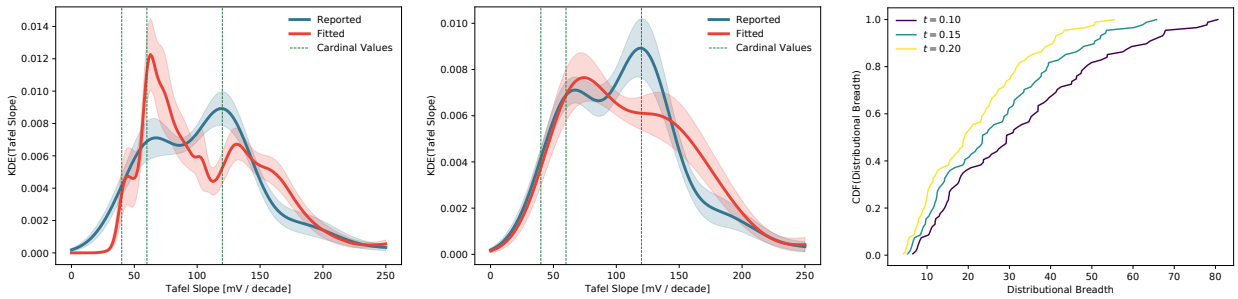

Figure 7.17: Tafel Slope statistics for catalysts containing Ag or Au ($N_{\text{datasets}} = 88$). (Left) Kernel density estimates (KDE) of the empirical probability distribution function of Tafel slopes reported in literature data (blue) and those refitted by our algorithm (red). Error intervals correspond to one standard deviation of bootstrapped resamples. Green dashed lines correspond to cardinal values of the Tafel slope. (Center) Same as (Left), but KDEs are computed using only the MAP Tafel Slope values for each dataset. (Right) CDF of the distributional breadth, as defined by Eq. (7.69).

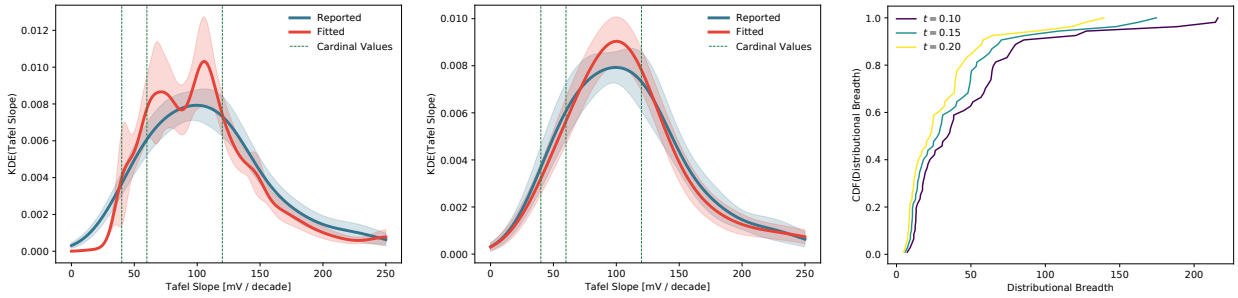

Figure 7.18: Tafel Slope statistics for catalysts containing Cu ($N_{\text{datasets}} = 54$). (Left) Kernel density estimates (KDE) of the empirical probability distribution function of Tafel slopes reported in literature data (blue) and those refitted by our algorithm (red). Error intervals correspond to one standard deviation of bootstrapped resamples. Green dashed lines correspond to cardinal values of the Tafel slope. (Center) Same as (Left), but KDEs are computed using only the MAP Tafel Slope values for each dataset. (Right) CDF of the distributional breadth, as defined by Eq. (7.69).

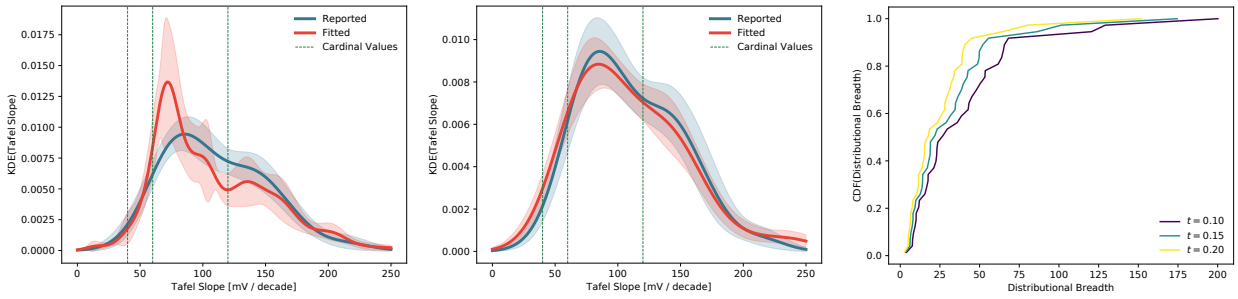

Figure 7.19: Tafel Slope statistics for catalysts containing Sn ($N_{\text{datasets}} = 37$). (Left) Kernel density estimates (KDE) of the empirical probability distribution function of Tafel slopes reported in literature data (blue) and those refitted by our algorithm (red). Error intervals correspond to one standard deviation of bootstrapped resamples. Green dashed lines correspond to cardinal values of the Tafel slope. (Center) Same as (Left), but KDEs are computed using only the MAP Tafel Slope values for each dataset. (Right) CDF of the distributional breadth, as defined by Eq. (7.69).

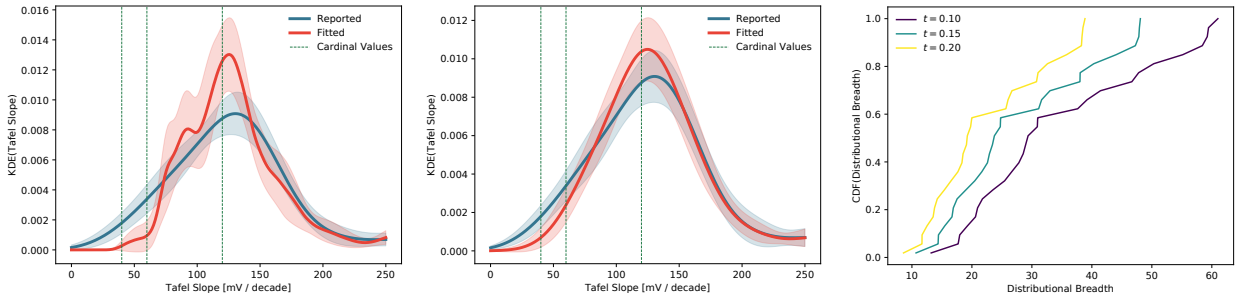

Figure 7.20: Tafel Slope statistics for catalysts containing Bi ($N_{\text{datasets}} = 27$). (Left) Kernel density estimates (KDE) of the empirical probability distribution function of Tafel slopes reported in literature data (blue) and those refitted by our algorithm (red). Error intervals correspond to one standard deviation of bootstrapped resamples. Green dashed lines correspond to cardinal values of the Tafel slope. (Center) Same as (Left), but KDEs are computed using only the MAP Tafel Slope values for each dataset. (Right) CDF of the distributional breadth, as defined by Eq. (7.69).

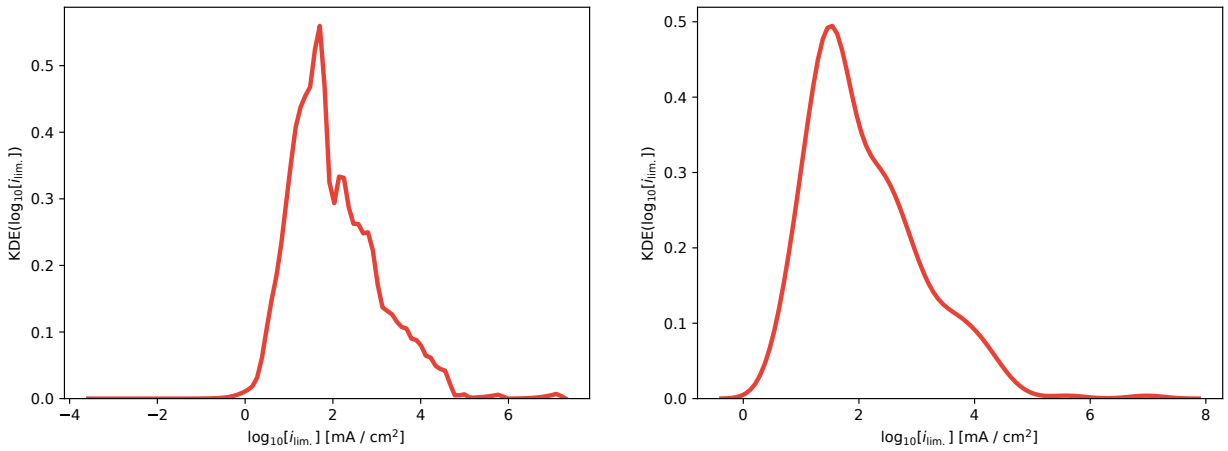

Figure 7.21: Limiting current statistics for all datasets analyzed in the study. (Left) Kernel density estimates (KDE) of the empirical probability distribution of the limiting current, i_{lim} fitted when interpreting the data through the model in main text Eq. (2). (Right) Same as (Left), but KDEs are computed using only the MAP limiting current values for each dataset.

Limiting Current Statistics

Figure 7.21 depicts kernel density estimates of the distribution of fitted limiting currents i_{lim} from a re-analysis of literature data. Roughly, the distribution appears to be in agreement with the value of the transport-limited current density for CO_2 reduction at an aqueous flooded electrode.[1]

7.4.2 Bayesian Fitting

Mathematical Detail

As quoted in the main text, Bayes' rule reads,

$$p(\theta|\mathbf{y}) = \frac{p(\mathbf{y}|\theta) \times p(\theta)}{p(\mathbf{y})}. \tag{7.70}$$

In the context of this work, $\mathbf{y}$ represents the measured current data at a set of voltage points. We will use the subscript notation $\mathbf{y}_k$ to denote a single current data point, where the index $k = 1, \ldots, N_{\text{pts}}$. The parameters of a model for interpreting current-voltage data are denoted by θ; in the context of this work, the relevant parameters for the limiting current model are i_{lim}, the limiting current density, i_0, the exchange current density, and m_{T}^{-1}, the inverse Tafel slope. We will denote the model's predictions at each voltage point by the subscript notation $\mathcal{M}_k(\theta)$.

To successfully apply Bayes' rule to glean $p(\theta|\mathbf{y})$, the posterior distribution over the model parameters given measured data, we need to identify mathematical forms for the prior distribution $p(\theta)$ and the likelihood function $p(\mathbf{y}|\theta)$. In all fits conducted in this study, we employ a uniform prior distribution (also known as an "uninformative" prior distribution) over a certain parameter range. Since the prior is uniform in the selected parameter range, as

long as the range includes the values of the parameters for which $p(\theta|\mathbf{y})$ has high probability mass, the choice of prior is unimportant (see further on for a numerical confirmation of this fact). Given this fact, the choice for the range of our uniform prior is determined by first using a standard nonlinear least-squares optimization algorithm (TRF) to determine a point estimate of the optimal set of parameters, θ^*. Formally,

$$\theta^* = \arg\min_{\theta} \left\{ \sum_{k=1}^{N_{\text{pts}}} \left[\mathbf{y}_k - \mathcal{M}_k(\theta) \right]^2 \right\}. \tag{7.71}$$

With the optimal parameters θ^* in hand, we select a uniform prior $p(\theta)$ that is supported in the range $[0, a \times \theta_i^*]$ for each parameter $i = 1, \ldots, N_{\text{params}}$. We choose the *very* conservative value $a = 10$ to ensure that the prior distribution has support over a very broad range around the optimal parameters. In principle, this choice of a results in a wide parameter space, which may affect the computational efficiency of a posterior sampling algorithm. In practice, we find very little computational disadvantage for choosing $a = 10$ as compared to $a = 2$ when using the No-U-Turn Sampler implemented in PyMC3.

The likelihood function for the data given the parameters, $p(\mathbf{y}|\theta)$, is determined by assuming that the experimental measurement represents a ground truth measurement described by the model, polluted by unavoidable experimental error,

$$\mathbf{y}_k = \mathcal{M}_k(\theta) + \epsilon_k. \tag{7.72}$$

We assume that errors at different data points are uncorrelated, and further assume that the error ϵ_i at any single data point is drawn from a Gaussian distribution with zero mean and variance σ^2,

$$p(\epsilon_k) = \frac{1}{\sqrt{2\pi}\sigma} \exp\left[-\frac{\epsilon_k^2}{2\sigma^2} \right]. \tag{7.73}$$

Because the errors at each point are uncorrelated, the likelihood now factorizes over all the data points,

$$p(\mathbf{y}|\theta) = \prod_{k=1}^{N_{\text{pts}}} \frac{1}{\sqrt{2\pi}\sigma} \exp\left[-\frac{\left(\mathbf{y}_k - \mathcal{M}_k(\theta)\right)^2}{2\sigma^2} \right]. \tag{7.74}$$

With a likelihood function $p(\mathbf{y}|\theta)$ and a prior distribution $p(\theta)$ in hand, we can plug this information into a Monte Carlo sampler of our choice to draw samples from the posterior distribution $p(\theta|\mathbf{y})$. Equation (7.74) also makes apparent how one can generalize the Bayesian posterior sampling approach to more general models $\mathcal{M}(\theta)$. After we write down a suitable model, we simply evaluate the model predictions with different parameters whenever we need to compute the likelihood function for a given set of parameters during the sampling procedure.

Gaussian Error Estimates from Nonlinear Optimization

The Bayesian posterior sampling approach advanced in this work provides a way to glean distributional uncertainty information about the estimated values of model parameters given observed data. A similar set of information can also be obtained by analyzing the Hessian

matrix determined by a nonlinear optimization algorithm seeking an optimal point estimate of the model parameters. Specifically, if the optimizer seeks to minimize a loss function,

$$\mathcal{L}(\theta) = \frac{1}{2\sigma^2} \sum_{k=1}^{N_{\text{pts}}} \left[\mathbf{y}_k - \mathcal{M}_k(\theta)\right]^2, \tag{7.75}$$

then it often also produces an estimate of the Hessian,

$$\mathbf{H}_{ij} = \left.\frac{\partial \mathcal{L}}{\partial \theta_i \partial \theta_j}\right|_{\theta^*}, \tag{7.76}$$

evaluated at the optimal value of the parameters θ^*. If we assume that the experimental data is generated by the random process described by Eq. (7.72), and further assume that the errors at different data points are uncorrelated and drawn from Gaussian distributions with mean zero and variance σ^2, then we can form a Gaussian approximation to the posterior distribution around θ^*,

$$p(\theta|\mathbf{y}) \approx \frac{1}{(2\pi)^{d/2} \left(\det \mathbf{H}\right)^{1/2}} \exp\left[-\frac{1}{2} \left(\theta - \theta^*\right)^{\mathrm{T}} \mathbf{H} \left(\theta - \theta^*\right)\right], \tag{7.77}$$

where d is the number of parameters being estimated, and $\mathbf{H}$ is guaranteed to be positive definite by virtue of being evaluated at the optimal point θ^*.

We stress that the expression provided by Eq. (7.77) is an *approximation* to the true posterior distribution; due to its Gaussian form, this expression can never accurately represent bimodality in the posterior distribution. In this sense, the Bayesian sampling approach is superior, although it comes at significant additional computational expense as d increases. In this work, $d = 3$, and this additional expense is essentially negligible given the computational power available on a typical laptop or desktop computer. Hence, we suggest that posterior distributions over the Tafel slope fitted using the model in Eq. (2) of the main text should always be computed using the Bayesian posterior sampling algorithm described in the previous section. We have simply included mention of the Gaussian approximation for the sake of completeness, and to guide possible future work that attempts to fit models with significantly more parameters.

Sensitivity to Error Distribution Width

One important parameter of the Bayesian fitting approach is the width of the normal distribution governing the probability of deviations from the model, which arises when evaluating the quantity $p(\mathbf{y}|\theta)$ in Bayes' rule. Figure 7.22 studies the sensitivity of the posterior distribution over the Tafel slope to the parameter σ, the standard deviation of the normal distribution governing the statistics of the model error. As expected, lowering the value of σ causes the algorithm to become more confident in its estimate. At $\sigma = 0.01$ logarithmic units, the model essentially nails the true Tafel slope of 80 mV/decade. For larger values of σ, a clear distributional drift to lower values of the Tafel slope is observed. This occurs because most of the data in Fig. 7.22A lies in the plateau region, and the model faces less penalty for down-weighting these points as the value of σ is increasing. Hence, the model drifts to

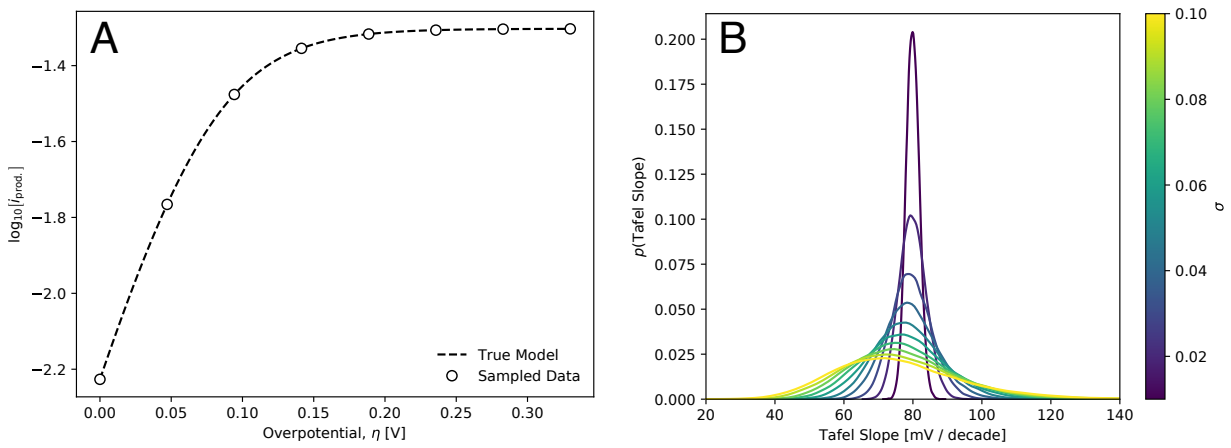

Figure 7.22: Sensitivity to the width of the error distribution at each point for a simple fit to synthetic data. (A) Synthetic data sampled from a model with an underlying Tafel slope of 80 mV/decade. (B) Several traces of the posterior distribution computed using different values of σ, the standard deviation of the normal error distribution at each point.

larger slopes on the Fig. 7.22A plot, which corresponds to lower values of the Tafel slope. Note that the distributional widening is significantly greater than the drift in the mean, suggesting that we should not put much stock into the mean drift. The upshot: for high values of the σ parameter, this particular set of data does not contain enough information to pin down the value of the Tafel slope accurately.

Sensitivity to Prior Distribution

As explained in the main text, our Bayesian approach requires specification of a prior distribution $p(\theta)$ over the parameters. Since we know very little about the true distribution of the Tafel slope at the outset, we choose an uninformative uniform box prior over the interval $[0, a \times \theta_i^*]$ for each parameter θ_i, where θ_i^* is the optimal value of the parameter gleaned from the TRF algorithm described in the Methods section. Here, we conduct a sensitivity analysis on the a parameter. Given that we are using an uninformative prior, we should expect that the prior width should not influence the posterior distribution as long as the data expresses some opinion about the ideal value of the parameters. Figure 7.23 depicts the results of the sensitivity analysis on a set of synthetic data. Indeed, as expected, the posterior distributions are insensitive to the choice of prior. Note that in all fits considered in the main text, we use a value of $a = 10$, as mentioned in the Methods section.

7.4.3 Derivations

Cardinal Tafel Slopes Equation

We will work with a generic reaction scheme, assuming that we begin with a starting species $A^{(n+q)+}$ which undergoes n electron transfers prior to the rate-determining step, and then q electron transfers at the RDS. In practice n will be an integer, and q will be either zero

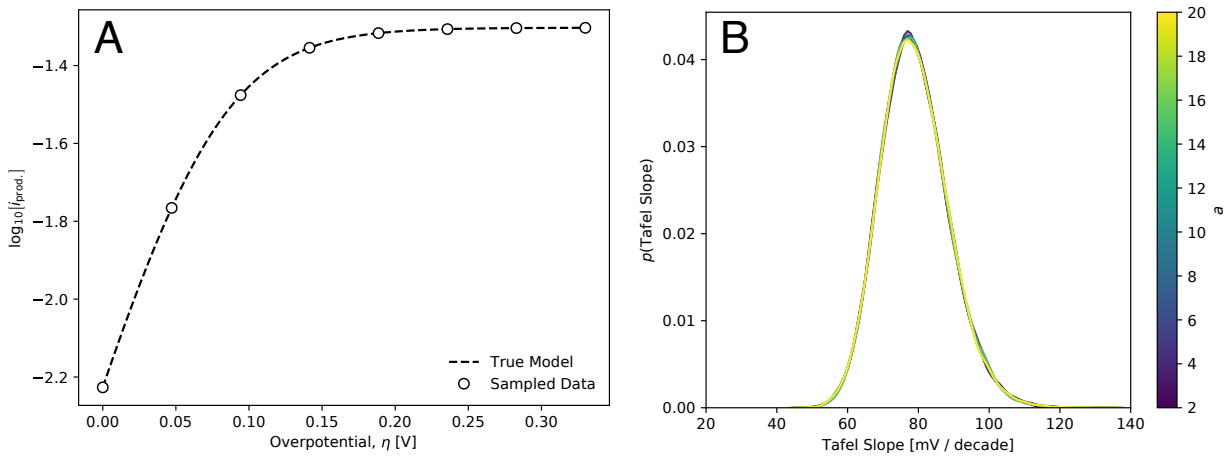

Figure 7.23: Sensitivity to the width of the uniform prior distribution bounds. (A) Synthetic data sampled from a model with an underlying Tafel slope of 80 mV/decade. (B) Several traces of the posterior distribution computed using different values of a, a parameter influencing the width of the prior distribution fed to the Bayesian posterior sampling algorithm. All posterior distributions are computed with $\sigma = 0.05$.

or one. Here we assume the reaction taking place is reductive; however, the derivation is entirely analogous for an equivalent oxidation reaction. Schematically, the reactions read,

$$\begin{aligned} \mathrm{A}^{(\mathrm{n+q})+} + \mathrm{e}^- &\rightleftarrows \mathrm{A}^{(\mathrm{n+q-1})+} \\ &\vdots \\ \mathrm{A}^{(\mathrm{q+1})+} + \mathrm{e}^- &\rightleftarrows \mathrm{A}^{\mathrm{q}+} \\ \mathrm{A}^{\mathrm{q}+} + \mathrm{qe}^- &\longrightarrow \mathrm{A}. \end{aligned}$$

The overall current is determined by the rate of the RDS. Assuming Butler-Volmer kinetics for the forward rate constant of the RDS, we have,

$$\text{rate} = k_0 \left\{ a_{\mathrm{A}^{\mathrm{q}+}} \exp\left[-\beta q e (1-\alpha) \cdot (\phi - \phi_{\text{eq.}})\right] - a_{\mathrm{A}} \exp\left[+\beta q e \alpha \cdot (\phi - \phi_{\text{eq.}})\right] \right\}, \tag{7.78}$$

where k_0 is the rate prefactor (sometimes called the Arrhenius prefactor), a_i is the activity of species i, $\beta \equiv (k_{\mathrm{B}} T)^{-1}$ is the inverse thermodynamic temperature, e is the fundamental charge, α is the symmetry coefficient, ϕ is the applied potential, and $\phi_{\text{eq.}}$ is the equilibrium potential for the RDS. At sufficiently high reductive overpotentials $\phi - \phi_{\text{eq.}} \ll 0$, only the first term survives,

$$\text{rate} \approx k_0 a_{\mathrm{A}^{\mathrm{q}+}} \exp\left[-\beta q e (1-\alpha) \cdot (\phi - \phi_{\text{eq.}})\right]. \tag{7.79}$$

To make further progress, we have to solve for the activity of the intermediate species $\mathrm{A}^{\mathrm{q}+}$ in terms of the activity of the reactant species for the overall reaction, $\mathrm{A}^{(\mathrm{n+q})+}$. If we assume that all steps prior to the RDS are fast and equilibriated, we can extract this activity by analyzing the thermodynamics of the steps prior to the RDS. The free energy change associated with the r'th reaction reads,

$$\Delta F_r = -\beta^{-1} \log a_{\mathrm{A}^{(\mathrm{n+q-(r+1)})+}} + \beta^{-1} \log a_{\mathrm{A}^{(\mathrm{n+q-r})+}} + e\phi. \tag{7.80}$$

Then, the equilibrium constant for reaction r goes as,

$$K_r \equiv \exp\left[-\beta \Delta F_r\right] \tag{7.81}$$

$$K_r = \frac{a_{\mathrm{A}^{(\mathrm{n+q-(r+1)})+}}}{a_{\mathrm{A}^{(\mathrm{n+q-r})+}}} \times \exp\left[-\beta e \phi\right] \tag{7.82}$$

$$K_r = \tilde{K}_r \times \exp\left[-\beta e \phi\right], \tag{7.83}$$

where $\tilde{K}_r$ is defined by Eq. (7.83), and is independent of potential. Since Eq. (7.83) holds for *all* reactions r before the RDS, we can easily solve for the activity of the intermediate,

$$a_{\mathrm{A}^{\mathrm{q+}}} = \left[\prod_{r=1}^{n} \tilde{K}_r\right] \exp\left[-n\beta e \phi\right] \times a_{\mathrm{A}^{(\mathrm{n+q})+}} \tag{7.84}$$

$$a_{\mathrm{A}^{\mathrm{q+}}} = \left[\prod_{r=1}^{n} \tilde{K}_r\right] \exp\left[-n\beta e \left(\phi - \phi_{\mathrm{eq.}}\right)\right] \exp\left[-n\beta e \phi_{\mathrm{eq.}}\right] \times a_{\mathrm{A}^{(\mathrm{n+q})+}}. \tag{7.85}$$

Plugging back into Eq. (7.79),

$$\text{rate} \approx k_0 \left(\left[\prod_{r=1}^{n} \tilde{K}_r\right] \exp\left[-n\beta e \left(\phi - \phi_{\mathrm{eq.}}\right)\right] \exp\left[-n\beta e \phi_{\mathrm{eq.}}\right] \times a_{\mathrm{A}^{(\mathrm{n+q})+}} \right) \exp\left[-\beta q e (1-\alpha) \cdot \left(\phi - \phi_{\mathrm{eq.}}\right)\right] \tag{7.86}$$

$$\text{rate} = k_0 \left(\left[\prod_{r=1}^{n} \tilde{K}_r\right] \exp\left[-n\beta e \phi_{\mathrm{eq.}}\right] \times a_{\mathrm{A}^{(\mathrm{n+q})+}} \right) \exp\left[-\beta e \left(\phi - \phi_{\mathrm{eq.}}\right) \left(n + q \cdot (1-\alpha)\right)\right]. \tag{7.87}$$

This is a mess, but we only care about the potential-dependent terms when extracting the Tafel slope, which means we only have to consider the last factor on the RHS. Taking the logarithm yields,

$$\log\left[\text{rate}\right] = -\beta e \left(\phi - \phi_{\mathrm{eq.}}\right) \left(n + q \cdot (1-\alpha)\right) + C, \tag{7.88}$$

where C is a constant independent of potential. For a reduction reaction, the Tafel slope is defined as,

$$\text{Tafel Slope} = \left[\frac{\partial \log_{10}\left[\text{rate}\right]}{\partial\left[-\left(\phi - \phi_{\mathrm{eq.}}\right)\right]}\right]^{-1}. \tag{7.89}$$

Hence, we have,

$$\text{Tafel Slope} = \left[\log_{10}\left(\exp(1)\right) \cdot \beta e\right]^{-1} \cdot \frac{1}{n + q \cdot (1-\alpha)}. \tag{7.90}$$

Appropriate unit scalings yield,

$$\text{Tafel Slope} = \frac{60 \text{ mV/decade}}{n + q \cdot (1-\alpha)}, \tag{7.91}$$

which reduces to the equation quoted in the main text when $\alpha = 1/2$.

7.4.4 Physical Non-Idealities

Tafel Slopes with Physical Non-Idealities

Eq. (7.91) already accounts for the non-ideality effects introduced by $\alpha \neq 1/2$. If we assume that the CO_2 adsorption step has partial charge transfer character quantified by γ, then despite the fact that the adsorption step is purely chemical, we assume that its equilibrium constant carries a non-integer order dependence on the applied potential. This can also be motivated by considering the formation of a permanent dipole on the surface species, which can access additional thermodynamic stabilization due to a dipole Stark shift from electric fields present at theinterface. The manner in which surface dipole formation augments the Tafel slope depends on whether or not the CO_2 adsorption step is the rate determining step. For the case $(n, q) = (0, 1)$, the adsorption step is the RDS. The Frumkin correction attenuates the applied potential for the rate-determining step by a factor f, which simply multiplies the latter term in the denominator of Eq. (7.91). Hence, the Tafel slope for $(n, q) = (0, 1)$ is,

$$\text{Tafel Slope} = \frac{60 \text{ mV/decade}}{\gamma \cdot f \cdot (1 - \alpha)}. \tag{7.92}$$

For the case $(n, q) = (1, 0)$, the adsorption step is the RDS, and rather than contributing $n = 1$ to the order, it instead contributes according to the γ parameter,

$$\text{Tafel Slope} = \frac{60 \text{ mV/decade}}{\gamma}. \tag{7.93}$$

Finally, for the case $(n, q) = (1, 1)$, the adsorption step occurs before the RDS, and the Tafel slope reads,

$$\text{Tafel Slope} = \frac{60 \text{ mV/decade}}{\gamma + f \cdot (1 - \alpha)}. \tag{7.94}$$

Sensitivities to Parameter Bounds

Figures 7.24 and 7.25 study the sensitivity of the distributional results presented in Fig. 4 of the main text to the bounds of the uniform distributions over non-ideality parameters. Broadly, our claim is supported by the sensitivity analysis; within reasonable parameter bounds, we still see that we can get essentially arbitrary distributional shapes depending on the nonidealities included in the model.

7.4.5 Multiple Kinetic Regimes

Here, we examine the consequences of fitting current-voltage data from a system exhibiting multiple kinetic regimes to a model that only allows a single Tafel slope (as in Eq. (2) in the main text) by analyzing synthetic data. The synthetic data is generated from the model,

$$\frac{1}{i(E)} = \frac{1}{i_{\text{lim}}} + \frac{1 + \exp\left(-e\left[k_{\text{B}}T\right]^{-1} \times \left[E - E_{\text{eq},1}\right]\right)}{\exp\left(e\left[k_{\text{B}}T\right]^{-1} \times \alpha\left[E - E_{\text{eq},2}\right]\right)}, \tag{7.95}$$

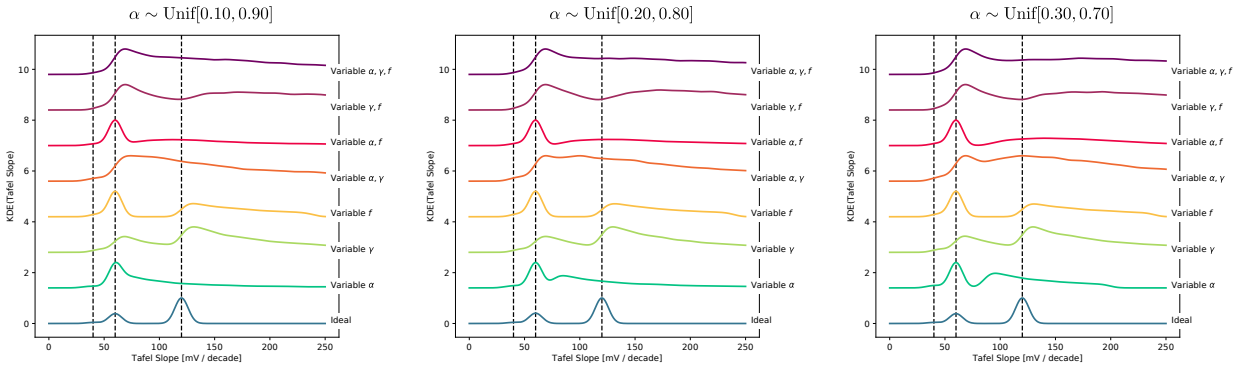

Figure 7.24: Several synthetic kernel density estimates of the probability distributions over the Tafel slope generated from including random values of different parameters governing physical non-idealities. Different panels use different uniform distributions over the symmetry coefficient parameter, α.

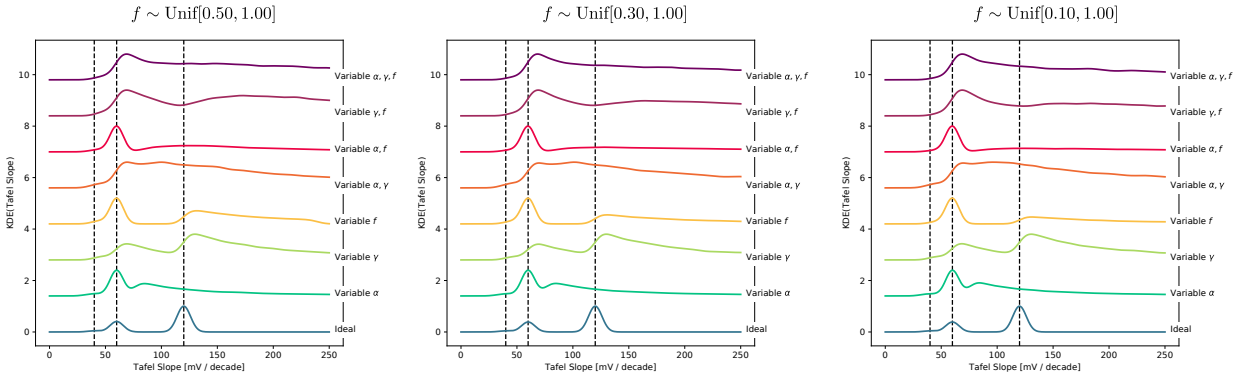

Figure 7.25: Several synthetic kernel density estimates of the probability distributions over the Tafel slope generated from including random values of different parameters governing physical non-idealities. Different panels use different uniform distributions over the Frumkin correction parameter, f.

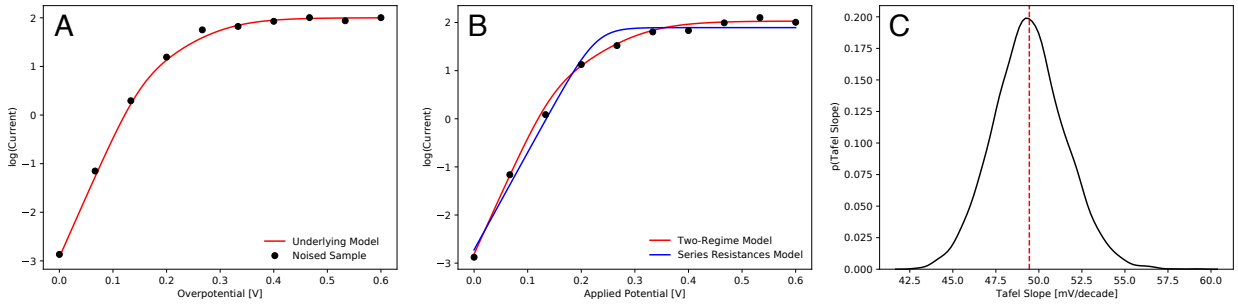

Figure 7.26: (A) Current-voltage trace generated from Eq. (7.95) using the parameters $\alpha = 1/2$, $i_{\text{lim}} = 100$ mA cm^{-2}, $E_{\text{eq},1} = 0.05$ V, and $E_{\text{eq},2} = 0.15$ V (red trace), along with artificially noised data sampled from the model (black points). (B) Current-voltage traces evaluated from the MAP fit parameters for Eq. (2) in the main text and Eq. (7.95), along with the noised data used for the fits (black points). (C) Posterior distribution over the Tafel slope for the model described by Eq. (2) in the main text.

where E is the applied potential, and the model has free fitting parameters α, i_{lim}, $E_{\text{eq},1}$, and $E_{\text{eq},2}$. This model can be shown to arise when a reaction proceeds through a rate-limiting surface reaction involving a surface intermediate generated through a one-electron transfer, and present at non-negligible surface coverages. The specifics of how this model arises are less relevant to this analysis than the fact that the model exhibits two different Tafel regimes. When $\alpha = 1/2$, the first regime has Tafel slope $m_{\text{T}} = 40$ mV decade^{-1} for $E_{\text{eq},1} < E < E_{\text{eq},2}$, and the second regime has a Tafel slope $m_{\text{T}} = 120$ mV decade^{-1} for $E > E_{\text{eq},2}$, before topping out at the limiting current i_{lim}.

Figure 7.26A shows a trace of the current-voltage behavior predicted by Eq. (7.95), with parameters $\alpha = 1/2$, $i_{\text{lim}} = 100$ mA cm^{-2}, $E_{\text{eq},1} = 0.05$ V, and $E_{\text{eq},2} = 0.15$ V, as well as artificially noised data sampled from this model at a sparsely sampled set of voltage points. Figure 7.26B shows current-voltage traces from both Eq. (7.95) (red) and Eq. (2) from the main text (blue), each evaluated under the MAP parameters determined from their respective Bayesian fits. Finally, Fig. 7.26C shows the Bayes posterior distribution for the Tafel slope fitted using Eq. (2) from the main text. As expected, when using the single Tafel regime model to fit data generated from multiple Tafel regimes, the MAP value of the Tafel slope does not coincide with the Tafel slope from *either* kinetic regime in Eq. (7.95). However, as illustrated in Fig. 7.27, when the original data is fit to Eq. (7.95), the posterior distributions are peaked around the true values of the parameters.

This analysis yields two important takeaways. First, it lends credence to the idea that fitting a single Tafel slope to data collected under multiple Tafel regimes, each individually exhibiting a cardinal Tafel slope, can produce an off-cardinal value of the Tafel slope, providing an alternative possible explanation for the lack of observed cardinality in the literature analysis in the main text. Second, and perhaps more importantly, it shows that the Bayesian framework presented here can successfully estimate the parameters of more complicated physical models that incorporate the effects of multiple different Tafel regimes, or some of the physical nonidealities discussed in the main text. Practically, we furnish the following recommendation: if one knows in advance that multiple kinetic regimes are at play

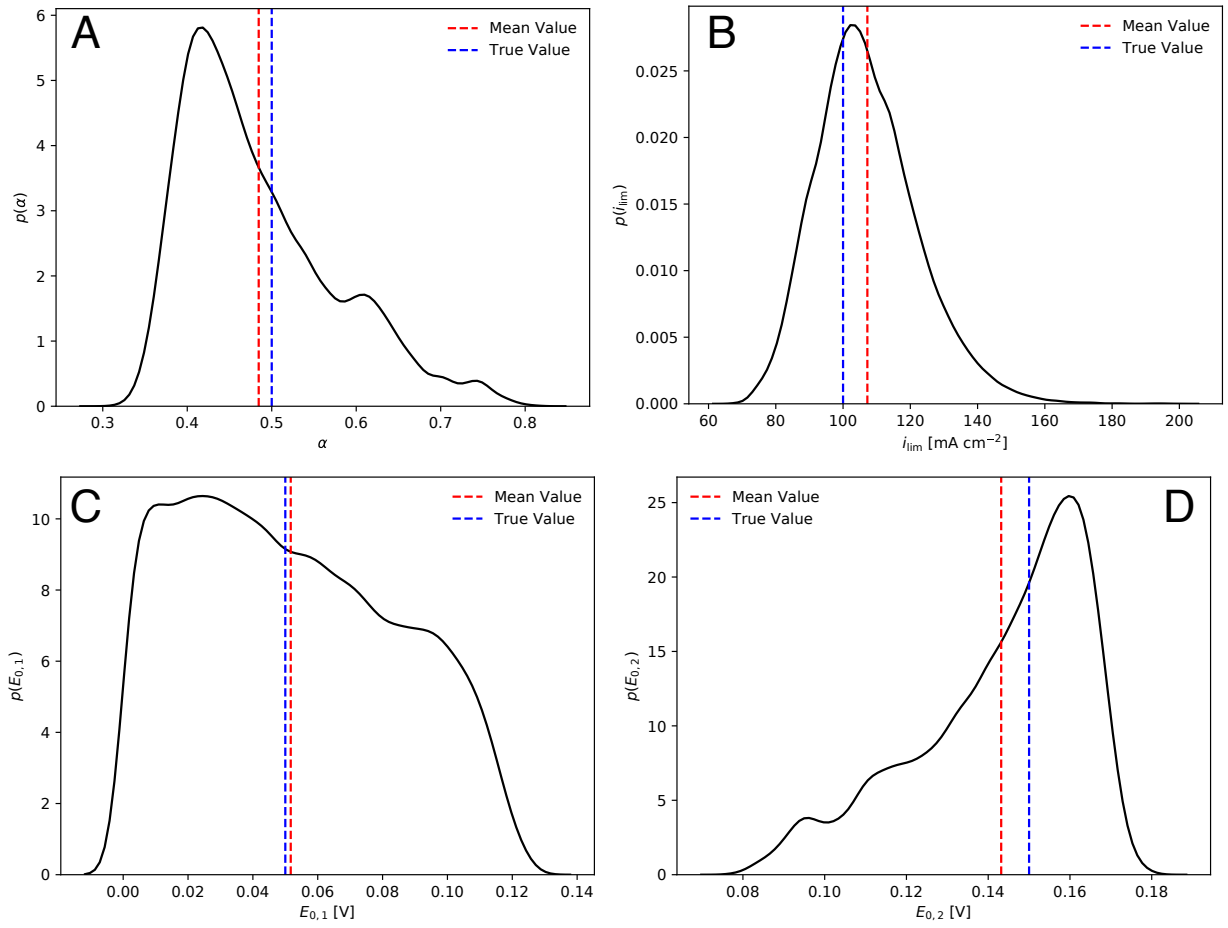

Figure 7.27: Posterior distributions for α, i_{lim}, $E_{\text{eq},1}$, and $E_{\text{eq},2}$ (A, B, C, D, respectively) gleaned from Bayesian posterior sampling on the artificially noised data in Fig. 7.26A.

in a set of current-voltage data, and the nature of these regimes can be encoded into a kinetic model like Eq. (7.95), then one should carry out Bayesian fitting to such a model. In the absence of sufficient independent evidence to pin down a kinetic model that resolves multiple kinetic regimes, Eq. (2) from the main text is a viable alternative, but one should be very cautious about over-interpreting the mechanistic implications of a Tafel slope determined in this manner.

7.4.6 References

[1] Kindle Williams, Nathan Corbin, Joy Zeng, Nikifar Lazouski, Deng-Tao Yang, and Karthish Manthiram. Protecting effect of mass transport during electrochemical reduction of oxygenated carbon dioxide feedstocks. *Sustain. Energy Fuels*, 3(5):1225–1232, 2019.

7.5 Additional Information: Electrochemical Characterization Using Analysis of Weakly Nonlinear Response to Small Amplitude Oscillating Voltage Signals

7.5.1 Reversible Reaction, Quiescent Solution

Problem Setup

Consider the two-species diffusion problem specified schematically in Figure 7.28. We will

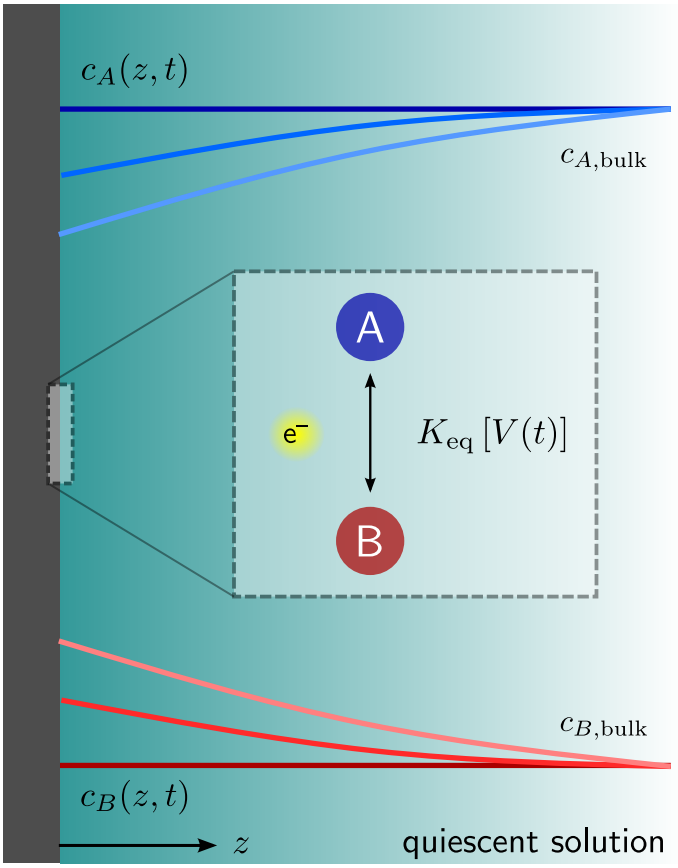

Figure 7.28: Schematic drawing of a two-species diffusion problem in a semi-infinite domain, with a reversible (Nernstian) reaction occurring at the left boundary.

track the concentration fields of two species, c_A and c_B, as explicit functions of a spatial coordinate z and a temporal coordinate t. Let $z = 0$ denote the position of the electrode; here (and only here), the two species undergo a single electron transfer reaction, which we assume occurs at a rate far greater than any other temporal scale in the problem. In other words, the electrochemical reaction is *reversible* (other treatments may refer to such a process as a

Nernstian electron transfer, this document will use the two terms interchangeably).

We take the electrolyte solution here to be quiescent (unstirred), and so as $z \to \infty$, we approach a bulk region, where the concentrations of both species are held fixed at their bulk concentrations, $c_{A,\text{bulk}}$ and $c_{B,\text{bulk}}$. Conservation of mass considering purely diffusive transport of species implies the following pair of governing equations,

$$\partial_t c_A = \mathcal{D}_A \, \partial_z^2 c_A, \tag{7.96}$$

$$\partial_t c_B = \mathcal{D}_B \, \partial_z^2 c_B, \tag{7.97}$$

where $\mathcal{D}_A$ and $\mathcal{D}_B$ are the Fickian diffusion coefficients of the two species. Henceforth in this subsection, we will assume that $\mathcal{D}_A = \mathcal{D}_B = \mathcal{D}$, corresponding to symmetric diffusion.

The physical setting of the problem supplies four boundary conditions,

$$\frac{c_A(z=0,t)}{c_B(z=0,t)} = \exp\left[+\beta e \left(E(t) - E_{\text{eq}}\right)\right], \tag{7.98}$$

$$\left.\frac{\partial c_A}{\partial z}\right|_{z=0} = -\left.\frac{\partial c_B}{\partial z}\right|_{z=0}, \tag{7.99}$$

$$c_A(z \to \infty, t) = c_{A,\text{bulk}}, \tag{7.100}$$

$$c_B(z \to \infty, t) = c_{B,\text{bulk}}, \tag{7.101}$$

where Eq. (7.98) enforces that the concentrations at the electrode are in the ratio specified by the appropriate Nernstian equilibrium for an instantaneous applied potential $E(t)$, reaction equilibrium potential E_{eq}, and inverse temperature $\beta \equiv (k_{\text{B}}T)^{-1}$. Equation (7.99) enforces mass conservation at the interface, while Eqns. (7.100) and (7.101) enforce that the concentration fields reach the bulk concentrations as $z \to \infty$.

The problem is fully specified upon setting initial conditions for the concentration fields,

$$c_A(z, t=0) = c_{A,\text{bulk}}, c_B(z, t=0) = c_{B,\text{bulk}}, \tag{7.102}$$

which corresponds to a solution beginning at open-circuit conditions, with the species concentration fields held constant at their bulk values.

We can consider the time-dependent voltage signal $E(t)$ as the "input" to this dynamical system. We are free to decompose the input signal $E(t)$ as,

$$E(t) = E_{\text{hold}} + \epsilon V(t), \tag{7.103}$$

where E_{hold} is a constant hold potential that is turned on at $t = 0$, ϵ is a small dimensionless number, and $V(t)$ is a voltage signal that admits a Laplace decomposition. The corresponding output is the passed current density $J(t)$, which can be extracted from the flux of one of the species at the electrode surface, $z = 0$,

$$J(t) = -e\mathcal{D} \left.\frac{\partial c_A}{\partial z}\right|_{z=0}. \tag{7.104}$$

Ultimately, solving the problem stated here will require developing a relationship between the input signal $E(t)$ and the output current density $J(t)$. Specifically, we will develop this relationship as a perturbative series, organized in ascending powers of ϵ, relating the Laplace space representations of the input and output signals.

Non-Dimensionalization

We introduce the following non-dimensionalization scheme,

$$\tilde{c}_A \equiv \frac{c_A}{c_{A,\text{bulk}}}, \tag{7.105}$$

$$\tilde{c}_B \equiv \frac{c_B}{c_{A,\text{bulk}}}, \tag{7.106}$$

$$\tilde{E} \equiv \beta e E, \tag{7.107}$$

$$\tilde{J} \equiv \frac{J}{e\mathcal{D}^{1/2}\omega^{*1/2}c_{A,\text{bulk}}}, \tag{7.108}$$

$$\tilde{t} \equiv t \cdot \omega^*, \tag{7.109}$$

$$\tilde{z} \equiv z \cdot \left[\frac{\omega^*}{\mathcal{D}}\right]^{1/2}, \tag{7.110}$$

where $\beta \equiv (k_\text{B}T)^{-1}$ is the inverse temperature, e is the fundamental charge, and ω^* is an arbitrary fundamental frequency.

Under this non-dimensionalization scheme, the governing equations in Eqns. (7.96) and (7.97) transform into,

$$\partial_{\tilde{t}}\tilde{c}_A = \partial^2_{\tilde{z}}\tilde{c}_A, \tag{7.111}$$

$$\partial_{\tilde{t}}\tilde{c}_B = \partial^2_{\tilde{z}}\tilde{c}_B. \tag{7.112}$$

The boundary conditions transform into,

$$\frac{\tilde{c}_A(\tilde{z}=0,\tilde{t})}{\tilde{c}_B(\tilde{z}=0,\tilde{t})} = \gamma \cdot \exp\left[\tilde{E}(t) - \tilde{E}_\text{eq}\right], \tag{7.113}$$

$$\left.\frac{\partial\tilde{c}_A}{\partial\tilde{z}}\right|_{\tilde{z}=0} = -\gamma \left.\frac{\partial\tilde{c}_B}{\partial\tilde{z}}\right|_{\tilde{z}=0}, \tag{7.114}$$

$$\tilde{c}_A(\tilde{z}\to\infty,\tilde{t}) = 1, \tag{7.115}$$

$$\tilde{c}_B(\tilde{z}\to\infty,\tilde{t}) = 1, \tag{7.116}$$

where $\gamma \equiv c_{B,\text{bulk}}/c_{A,\text{bulk}}$, and $\tilde{E}_\text{eq}$ is made nondimensional in the manner prescribed by Eq. (7.107). Finally, the initial conditions transform into,

$$\tilde{c}_A(\tilde{z},\tilde{t}=0) = 1, \tag{7.117}$$

$$\tilde{c}_B(\tilde{z},\tilde{t}=0) = 1. \tag{7.118}$$

$$\tag{7.119}$$

Now that the non-dimensionalized problem is fully specified, we will drop all tildes in subsequent expressions.

Kernel Expressions

Kernel at $\mathcal{O}(\epsilon^0)$ At $\mathcal{O}(\epsilon^0)$, we can ignore the second term in Eq. (7.103), yielding $E(t) = E_{\text{hold}}$. The first step is to take the governing equations in Eqns. (7.111) and (7.112) into Laplace space, at this order. Applying the initial conditions in Eqns. (7.117) and (7.118) yields,

$$s\hat{c}_A^{(0)}(z,s) - 1 = \partial_z^2 \hat{c}_A^{(0)}(z,s), \tag{7.120}$$

$$s\hat{c}_B^{(0)}(z,s) - 1 = \partial_z^2 \hat{c}_B^{(0)}(z,s), \tag{7.121}$$

subject to the Laplace space boundary conditions,

$$\frac{\hat{c}_A^{(0)}(z=0,s)}{\hat{c}_B^{(0)}(z=0,s)} = \gamma \cdot \exp\left[E_{\text{hold}} - E_{\text{eq}}\right], \tag{7.122}$$

$$\left.\frac{\partial \hat{c}_A^{(0)}}{\partial z}\right|_{z=0} = -\gamma \left.\frac{\partial \hat{c}_B^{(0)}}{\partial z}\right|_{z=0}, \tag{7.123}$$

$$\hat{c}_A^{(0)}(z\to\infty,s) = 1/s, \tag{7.124}$$

$$\hat{c}_B^{(0)}(z\to\infty,s) = 1/s. \tag{7.125}$$

At $\mathcal{O}(\epsilon^0)$, the current density expression reads,

$$\hat{J}^{(0)}(s) = \frac{1}{\sqrt{s}} \cdot \frac{\gamma e^{\bar{E}_{\text{hold}}} - 1}{e^{\bar{E}_{\text{hold}}} + 1}, \tag{7.126}$$

where $\bar{E}_{\text{hold}} \equiv E_{\text{hold}} - E_{\text{eq}}$. Unlike the expressions at higher order, the current density at this order can be readily transformed back into the time domain,

$$J^{(0)}(t) = \frac{1}{\sqrt{\pi t}} \cdot \frac{\gamma e^{\bar{E}_{\text{hold}}} - 1}{e^{\bar{E}_{\text{hold}}} + 1}. \tag{7.127}$$

Kernel at $\mathcal{O}(\epsilon^1)$ At $\mathcal{O}(\epsilon^1)$, we must include the second term in Eq. (7.103). Again, we take the governing equations (7.111) and (7.112) at this order into Laplace space. Note that we do not need to apply the initial conditions in Eqns. (7.117) and (7.118), since they have already been handled at $\mathcal{O}(\epsilon^0)$. Hence, we have,

$$s\hat{c}_A^{(1)}(z,s) = \partial_z^2 \hat{c}_A^{(1)}(z,s), s\hat{c}_B^{(1)}(z,s) \qquad = \partial_z^2 \hat{c}_B^{(1)}(z,s), \tag{7.128}$$

subject to the Laplace space boundary conditions,

$$\hat{c}_A^{(1)}(0,s) = \gamma \cdot e^{\bar{E}_{\text{hold}}} \cdot \left\{ \hat{c}_B^{(0)}(0,0) \cdot \hat{V}(s) + \hat{c}_B^{(1)}(0,s) \right\}, \tag{7.129}$$

$$\left.\frac{\partial \hat{c}_A^{(1)}}{\partial z}\right|_{z=0} = -\gamma \left.\frac{\partial \hat{c}_B^{(1)}}{\partial z}\right|_{z=0}, \tag{7.130}$$

$$\hat{c}_A^{(1)}(z\to\infty,s) = 0, \tag{7.131}$$

$$\hat{c}_B^{(1)}(z\to\infty,s) = 0. \tag{7.132}$$

At $\mathcal{O}(\epsilon^1)$, the current density expression reads,

$$\hat{J}^{(1)}(s) = \frac{e^{\bar{E}_{\text{hold}}}(1+\gamma)}{\left(1+e^{\bar{E}_{\text{hold}}}\right)^2} \cdot \sqrt{s} \ \cdot \hat{V}(s). \tag{7.133}$$

Kernel at $\mathcal{O}(\epsilon^2)$ Again, we take the governing equations (7.111) and (7.112) at this order into Laplace space. Again, we do not need to apply the initial conditions in Eqns. (7.117) and (7.118), since they have already been handled at $\mathcal{O}(\epsilon^0)$. Hence, we have,

$$s\hat{c}_A^{(2)}(z,s) = \partial_z^2 \hat{c}_A^{(2)}(z,s), \tag{7.134}$$

$$s\hat{c}_B^{(2)}(z,s) = \partial_z^2 \hat{c}_B^{(2)}(z,s), \tag{7.135}$$

subject to the Laplace space boundary conditions,

$$\hat{c}_A^{(2)}(0,s) = \gamma \cdot e^{\bar{E}_{\text{hold}}} \cdot \left\{ \frac{1}{2} \cdot \hat{c}_B^{(0)}(0,0) \cdot \int d\eta \, \hat{V}(\eta)\hat{V}(s-\eta) + \int d\eta \, \hat{c}_B^{(1)}(0,\eta)\hat{V}(s-\eta) + \hat{c}_B^{(2)}(0,s) \right\}, \tag{7.136}$$

$$\left.\frac{\partial \hat{c}_A^{(2)}}{\partial z}\right|_{z=0} = -\gamma \left.\frac{\partial \hat{c}_B^{(2)}}{\partial z}\right|_{z=0}, \tag{7.137}$$

$$\hat{c}_A^{(2)}(z \to \infty, s) = 0, \tag{7.138}$$

$$\hat{c}_B^{(2)}(z \to \infty, s) = 0. \tag{7.139}$$

At $\mathcal{O}(\epsilon^2)$, the current density expression reads,

$$\hat{J}^{(2)}(s) = -\frac{e^{\bar{E}_{\text{hold}}}\left(e^{\bar{E}_{\text{hold}}}-1\right)(1+\gamma)}{2\left(1+e^{\bar{E}_{\text{hold}}}\right)^3} \cdot \sqrt{s} \ \cdot \int d\eta \hat{V}(\eta)\hat{V}(s-\eta). \tag{7.140}$$

Kernel at $\mathcal{O}(\epsilon^3)$ Again, we take the governing equations (7.111) and (7.112) at this order into Laplace space. The initial conditions in Eqns. (7.117) and (7.117) have already been handled at $\mathcal{O}(\epsilon^0)$. Hence, we have,

$$s\hat{c}_A^{(3)}(z,s) = \partial_z^2 \hat{c}_A^{(3)}(z,s), \tag{7.141}$$

$$s\hat{c}_B^{(3)}(z,s) = \partial_z^2 \hat{c}_B^{(3)}(z,s), \tag{7.142}$$

subject to the Laplace space boundary conditions,

$$\hat{c}_A^{(3)}(0,s) = \gamma \cdot e^{\bar{E}_{\text{hold}}} \cdot \left\{ \frac{1}{6} \cdot \hat{c}_B^{(0)}(0,0) \cdot \int d\eta_1 d\eta_2 \, \hat{V}(\eta_1)\hat{V}(\eta_2)\hat{V}(s-\eta_1-\eta_2) + \frac{1}{2}\int d\eta_1 d\eta_2 \, \hat{V}(\eta_1)\hat{V}(\eta_2)\hat{c}_B^{(1} \right. \tag{7.143}$$

$$\left.\frac{\partial \hat{c}_A^{(3)}}{\partial z}\right|_{z=0} = -\gamma \left.\frac{\partial \hat{c}_B^{(3)}}{\partial z}\right|_{z=0}, \tag{7.144}$$

$$\hat{c}_A^{(3)}(z \to \infty, s) = 0, \tag{7.145}$$

$$\hat{c}_B^{(3)}(z \to \infty, s) = 0. \tag{7.146}$$

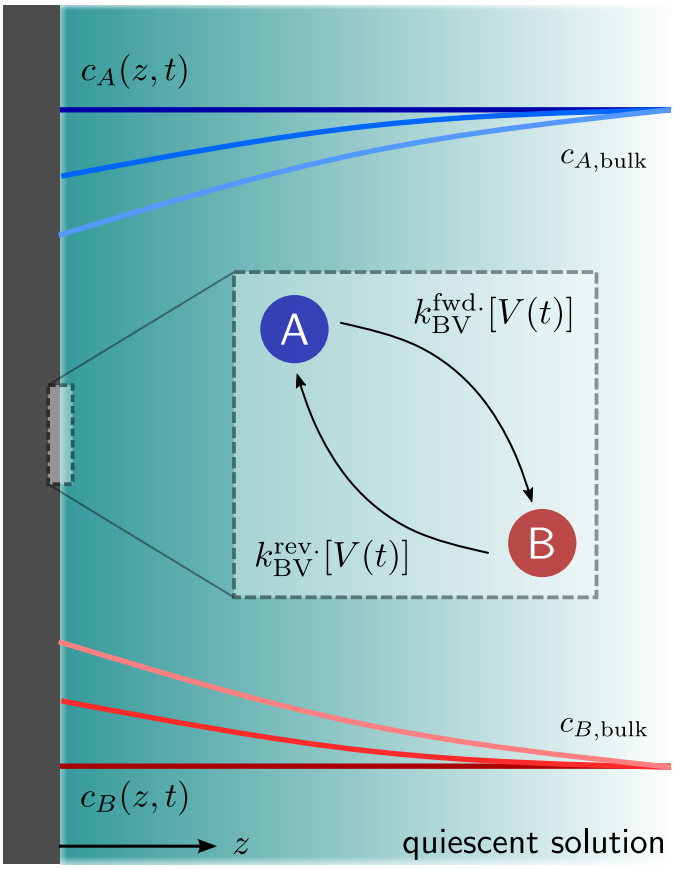

Figure 7.29: Schematic drawing of a two-species diffusion problem in a semi-infinite domain, with a quasireversible (Butler–Volmer) reaction occurring at the left boundary.

At $\mathcal{O}(\epsilon^3)$, the current density expression reads,

$$\hat{J}^{(3)}(s) = -\frac{e^{\bar{E}_{\text{hold}}}\left(4e^{\bar{E}_{\text{hold}}} - e^{2\bar{E}_{\text{hold}}} - 1\right)(1+\gamma)}{6\left(1+e^{\bar{E}_{\text{hold}}}\right)^4} \cdot \sqrt{s} \cdot \int d\eta_1 d\eta_2 \hat{V}(\eta_1)\hat{V}(\eta_2)\hat{V}(s-\eta_1-\eta_2). \tag{7.147}$$

7.5.2 Quasireversible Reaction, Quiescent Solution

Problem Setup

Consider the two-species diffusion problem specified schematically in Figure 7.29. We will track the concentration fields of two species, c_A and c_B, as explicit functions of a spatial coordinate z and a temporal coordinate t. Let $z = 0$ denote the position of the electrode; here (and only here), the two species undergo a single electron transfer reaction, the rate of which we assume to be described by the phenomenological Butler-Volmer relationship between current and potential.

We take the electrolyte solution here to be quiescent (unstirred), and so as $z \to \infty$, we

approach a bulk region, where the concentrations of both species are held fixed at their bulk concentrations, $c_{A,\text{bulk}}$ and $c_{B,\text{bulk}}$. Conservation of mass considering purely diffusive transport of species implies the following pair of governing equations,

$$\partial_t c_A = \mathcal{D}_A \, \partial_z^2 c_A, \tag{7.148}$$
$$\partial_t c_B = \mathcal{D}_B \, \partial_z^2 c_B, \tag{7.149}$$

where $\mathcal{D}_A$ and $\mathcal{D}_B$ are the Fickian diffusion coefficients of the two species. Henceforth in this subsection, we will assume that $\mathcal{D}_A = \mathcal{D}_B = \mathcal{D}$, corresponding to symmetric diffusion.

The physical setting of the problem supplies four boundary conditions,

$$\left.\frac{\partial c_A}{\partial z}\right|_{z=0} = k_0 \left\{ c_A(0,t) \cdot \exp\left[-\beta\alpha e \left(E(t) - E_{\text{eq}}\right)\right] - c_B(0,t) \cdot \exp\left[+\beta(1-\alpha) e \left(E(t) - E_{\text{eq}}\right)\right] \right\}, \tag{7.150}$$

$$\left.\frac{\partial c_A}{\partial z}\right|_{z=0} = - \left.\frac{\partial c_B}{\partial z}\right|_{z=0}, \tag{7.151}$$

$$c_A(z \to \infty, t) = c_{A,\text{bulk}}, \tag{7.152}$$
$$c_B(z \to \infty, t) = c_{B,\text{bulk}}, \tag{7.153}$$

where Eq. (7.150) enforces that the flux of species A at the boundary matches the rate of consumption of species A as prescribed by Butler-Volmer kinetics for an instantaneous applied potential $E(t)$, reaction equilibrium potential E_{eq}, and inverse temperature $\beta \equiv (k_{\text{B}} T)^{-1}$. Equation (7.151) enforces mass conservation at the interface, while Eqns. (7.152) and (7.153) enforce that the concentration fields reach the bulk concentrations as $z \to \infty$.

The problem is fully specified upon setting initial conditions for the concentration fields,

$$c_A(z, t = 0) = c_{A,\text{bulk}}, \tag{7.154}$$
$$c_B(z, t = 0) = c_{B,\text{bulk}}, \tag{7.155}$$

which corresponds to a solution beginning at open-circuit conditions, with the species concentration fields held constant at their bulk values.

The input voltage signal $E(t)$ is decomposed in the manner prescribed by Eq. (7.103), and the current is extracted from the concentration profiles in the manner described by Eq. (7.104).

Non-Dimensionalization We introduce the following non-dimensionalization scheme,

$$\tilde{c}_A \equiv \frac{c_A}{c_{A,\text{bulk}}}, \tag{7.156}$$

$$\tilde{c}_B \equiv \frac{c_B}{c_{A,\text{bulk}}}, \tag{7.157}$$

$$\tilde{E} \equiv \beta e E, \tag{7.158}$$

$$\tilde{J} \equiv \frac{J}{e\mathcal{D}^{1/2}\omega^{*1/2}c_{A,\text{bulk}}}, \tag{7.159}$$

$$\tilde{t} \equiv t \cdot \omega^*, \tag{7.160}$$

$$\tilde{z} \equiv z \cdot \left[\frac{\omega^*}{\mathcal{D}}\right]^{1/2}, \tag{7.161}$$

where $\beta \equiv (k_\text{B}T)^{-1}$ is the inverse temperature, e is the fundamental charge, and ω^* is an arbitrary fundamental frequency.

Under this non-dimensionalization scheme, the governing equations in Eqns. (7.148) and (7.149) transform into,

$$\partial_{\tilde{t}}\tilde{c}_A = \partial^2_{\tilde{z}}\tilde{c}_A, \tag{7.162}$$

$$\partial_{\tilde{t}}\tilde{c}_B = \partial^2_{\tilde{z}}\tilde{c}_B. \tag{7.163}$$

The boundary conditions transform into,

$$\left.\frac{\partial\tilde{c}_A}{\partial z}\right|_{z=0} = \zeta \cdot \left\{\tilde{c}_A(0,t) \cdot \exp\left[-\alpha\left(\tilde{E}(t) - \tilde{E}_\text{eq}\right)\right] - \gamma \cdot \tilde{c}_B(0,t) \cdot \exp\left[+(1-\alpha)\left(\tilde{E}(t) - \tilde{E}_\text{eq}\right)\right]\right\}, \tag{7.164}$$

$$\left.\frac{\partial\tilde{c}_A}{\partial\tilde{z}}\right|_{\tilde{z}=0} = -\gamma \left.\frac{\partial\tilde{c}_B}{\partial\tilde{z}}\right|_{\tilde{z}=0}, \tag{7.165}$$

$$\tilde{c}_A(\tilde{z}\to\infty,\tilde{t}) = 1, \tag{7.166}$$

$$\tilde{c}_B(\tilde{z}\to\infty,\tilde{t}) = 1, \tag{7.167}$$

where $\gamma \equiv c_{B,\text{bulk}}/c_{A,\text{bulk}}$, and $\tilde{E}_\text{eq}$ is made nondimensional in the manner prescribed by Eq. (7.107). The dimensionless group in Eq. (7.164),

$$\zeta \equiv \frac{k_0}{(\mathcal{D}\omega^*)^{1/2}}, \tag{7.168}$$

emerges naturally from non-dimensionalizing Eq. (7.150), and relates the rate of the surface reaction to the rate of diffusive transport. Finally, the initial conditions transform into,

$$\tilde{c}_A(\tilde{z},\tilde{t}=0) = 1, \tag{7.169}$$

$$\tilde{c}_B(\tilde{z},\tilde{t}=0) = 1. \tag{7.170}$$

Now that the non-dimensionalized problem is fully specified, we will drop all tildes in subsequent expressions.

Kernel at $\mathcal{O}(\epsilon^0)$ At $\mathcal{O}(\epsilon^0)$, we can ignore the second term in Eq. (7.103), yielding $E(t) = E_{\text{hold}}$. The first step is to take the governing equations in Eqns. (7.162) and (7.112) into Laplace space, at this order. Applying the initial conditions in Eqns. (7.169) and (7.170) yields,

$$s\hat{c}_A^{(0)}(z,s) - 1 = \partial_z^2 \hat{c}_A^{(0)}(z,s), \tag{7.171}$$

$$s\hat{c}_B^{(0)}(z,s) - 1 = \partial_z^2 \hat{c}_B^{(0)}(z,s), \tag{7.172}$$

subject to the Laplace space boundary conditions,

$$\left.\frac{\partial \hat{c}_A^{(0)}(z,s)}{\partial z}\right|_{z=0} = \zeta\left\{\hat{c}_A^{(0)}(0,s)\exp\left[-\alpha\left(E_{\text{hold}} - E_{\text{eq}}\right)\right] - \gamma\cdot\hat{c}_B^{(0)}(0,s)\exp\left[(1-\alpha)\left(E_{\text{hold}} - E_{\text{eq}}\right)\right]\right\}, \tag{7.173}$$

$$\left.\frac{\partial \hat{c}_A^{(0)}}{\partial z}\right|_{z=0} = -\gamma\left.\frac{\partial \hat{c}_B^{(0)}}{\partial z}\right|_{z=0}, \tag{7.174}$$

$$\hat{c}_A^{(0)}(z\to\infty,s) = 1/s, \tag{7.175}$$

$$\hat{c}_B^{(0)}(z\to\infty,s) = 1/s. \tag{7.176}$$

At $\mathcal{O}(\epsilon^0)$, the current density expression reads,

$$\hat{J}^{(0)}(s) = \frac{1}{\sqrt{s}}\cdot\frac{\zeta\cdot\left(\gamma e^{\bar{E}_{\text{hold}}} - 1\right)}{e^{\alpha\bar{E}_{\text{hold}}}\sqrt{s} + \zeta(1+e^{\bar{E}_{\text{hold}}})}, \tag{7.177}$$

where $\bar{E}_{\text{hold}} \equiv E_{\text{hold}} - E_{\text{eq}}$.

Kernel at $\mathcal{O}(\epsilon^1)$ At $\mathcal{O}(\epsilon^1)$, we must include the second term in Eq. (7.103). Again, we take the governing equations (7.162) and (7.163) at this order into Laplace space. Note that we do not need to apply the initial conditions in Eqns. (7.169) and (7.170), since they have already been handled at $\mathcal{O}(\epsilon^0)$. Hence, we have,

$$s\hat{c}_A^{(1)}(z,s) = \partial_z^2\hat{c}_A^{(1)}(z,s), s\hat{c}_B^{(1)}(z,s) \qquad = \partial_z^2\hat{c}_B^{(1)}(z,s), \tag{7.178}$$

subject to the Laplace space boundary conditions,

$$\left.\frac{\partial \hat{c}_A^{(1)}(z,s)}{\partial z}\right|_{z=0} = \zeta\left\{e^{-\alpha\bar{E}_{\text{hold}}}\left[\hat{c}_A^{(1)}(0,s) - \alpha\hat{V}(s)\hat{c}_A^{(0)}(0,0)\right] - \gamma e^{(1-\alpha)\bar{E}_{\text{hold}}}\left[\hat{c}_B^{(1)}(0,s) + (1-\alpha)\hat{V}(s)\hat{c}_B^{(0)}(0,0)\right]\right\} \tag{7.179}$$

$$\left.\frac{\partial \hat{c}_A^{(1)}}{\partial z}\right|_{z=0} = -\gamma\left.\frac{\partial \hat{c}_B^{(1)}}{\partial z}\right|_{z=0}, \tag{7.180}$$

$$\hat{c}_A^{(1)}(z\to\infty,s) = 0, \tag{7.181}$$

$$\hat{c}_B^{(1)}(z\to\infty,s) = 0. \tag{7.182}$$

At $\mathcal{O}(\epsilon^1)$, the current density expression reads,

$$\hat{J}^{(1)}(s) = \frac{\zeta(1+\gamma)e^{\bar{E}_{\text{hold}}}}{(1+e^{\bar{E}_{\text{hold}}})\left[\zeta(1+e^{\bar{E}_{\text{hold}}}) + e^{\alpha\bar{E}_{\text{hold}}}\sqrt{s}\right]}\ \sqrt{s}\cdot\hat{V}(s). \tag{7.183}$$

Kernel at $\mathcal{O}(\epsilon^2)$ Again, we take the governing equations (7.162) and (7.163) at this order into Laplace space. Again, we do not need to apply the initial conditions in Eqns. (7.169) and (7.170), since they have already been handled at $\mathcal{O}(\epsilon^0)$. Hence, we have,

$$s\hat{c}_A^{(2)}(z,s) = \partial_z^2 \hat{c}_A^{(2)}(z,s), \tag{7.184}$$

$$s\hat{c}_B^{(2)}(z,s) = \partial_z^2 \hat{c}_B^{(2)}(z,s), \tag{7.185}$$

subject to the Laplace space boundary conditions,

$$\left.\frac{\partial \hat{c}_A^{(2)}(z,s)}{\partial z}\right|_{z=0} = \zeta \left\{ e^{-\alpha \bar{E}_{\text{hold}}} \left[\hat{c}_A^{(2)}(0,s) - \alpha \int d\eta_1 \hat{V}(\eta_1) \hat{c}_A^{(1)}(0, s-\eta_1) + \frac{\alpha^2}{2} \hat{c}_A^{(0)}(0,0) \int d\eta_1 \hat{V}(\eta_1) \hat{V}(s-\eta_1) \right] - \right. \tag{7.186}$$

$$\left.\frac{\partial \hat{c}_A^{(2)}}{\partial z}\right|_{z=0} = -\gamma \left.\frac{\partial \hat{c}_B^{(2)}}{\partial z}\right|_{z=0}, \tag{7.187}$$

$$\hat{c}_A^{(2)}(z \to \infty, s) = 0, \tag{7.188}$$

$$\hat{c}_B^{(2)}(z \to \infty, s) = 0. \tag{7.189}$$

At $\mathcal{O}(\epsilon^2)$, the current density expression reads,

$$\hat{J}^{(2)}(s) = \frac{\zeta e^{\bar{E}_{\text{hold}}}(1+\gamma)\sqrt{s}}{2(1+e^{\bar{E}_{\text{hold}}})\left(e^{\alpha \bar{E}_{\text{hold}}}\sqrt{s} + \zeta(1+e^{\bar{E}_{\text{hold}}})\right)} \int d\eta_1 \left[(1-2\alpha) + \frac{2\zeta\left(e^{\bar{E}_{\text{hold}}}(\alpha-1)+\alpha\right)}{\zeta(1+e^{\bar{E}_{\text{hold}}}) + e^{\alpha \bar{E}_{\text{hold}}}\sqrt{\eta_1}} \right] \hat{V}(\eta_1)\hat{V}(s- \tag{7.190}$$

Kernel at $\mathcal{O}(\epsilon^3)$ Again, we take the governing equations (7.162) and (7.163) at this order into Laplace space. Again, we do not need to apply the initial conditions in Eqns. (7.169) and (7.170), since they have already been handled at $\mathcal{O}(\epsilon^0)$. Hence, we have,

$$s\hat{c}_A^{(3)}(z,s) = \partial_z^2 \hat{c}_A^{(3)}(z,s), \tag{7.191}$$

$$s\hat{c}_B^{(3)}(z,s) = \partial_z^2 \hat{c}_B^{(3)}(z,s), \tag{7.192}$$

subject to the Laplace space boundary conditions,

$$\left.\frac{\partial \hat{c}_A^{(3)}(z,s)}{\partial z}\right|_{z=0} = \zeta \left\{ e^{-\alpha \bar{E}_{\text{hold}}} \left[\hat{c}_A^{(3)}(0,s) - \alpha \int d\eta_2 \hat{V}(\eta_2) \hat{c}_A^{(2)}(0, s-\eta_2) + \frac{\alpha^2}{2} \int d\eta_1 d\eta_2 \hat{c}_A^{(1)}(0, s-\eta_2) \hat{V}(\eta_1) \hat{V}(\eta \right. \right. \tag{7.193}$$

$$\left.\frac{\partial \hat{c}_A^{(3)}}{\partial z}\right|_{z=0} = -\gamma \left.\frac{\partial \hat{c}_B^{(3)}}{\partial z}\right|_{z=0}, \tag{7.194}$$

$$\hat{c}_A^{(3)}(z \to \infty, s) = 0, \tag{7.195}$$

$$\hat{c}_B^{(3)}(z \to \infty, s) = 0. \tag{7.196}$$

We will define some convenience quantities for ease of understanding the expression for the current at third order. First, define the convolution kernel,

$$K(s) = \frac{1}{\zeta(1 + e^{\bar{E}_{\text{hold}}}) + e^{\alpha \bar{E}_{\text{hold}}}\sqrt{s}}. \tag{7.197}$$

Now, define two convolution operators,

$$\mathcal{C}_K[\hat{f}, \hat{g}] \equiv \int d\eta K(\eta)\hat{f}(\eta)\hat{g}(s-\eta) \tag{7.198}$$

$$\mathcal{C}[\hat{f}, \hat{g}] \equiv \int d\eta \hat{f}(\eta)\hat{g}(s-\eta) \tag{7.199}$$

At $\mathcal{O}(\epsilon^3)$, the current density expression reads,

$$\hat{J}^{(3)}(s) = \frac{-\zeta(1+\gamma)e^{\bar{E}_{\text{hold}}}\sqrt{s}}{6(1+e^{\bar{E}_{\text{hold}}})\left(\zeta(1+e^{\bar{E}_{\text{hold}}}) + e^{\alpha\bar{E}_{\text{hold}}}\sqrt{s}\right)} \left\{3\zeta\left(\alpha^2 + e^{\bar{E}_{\text{hold}}}(1-\alpha)^2\right)\mathcal{C}[\hat{V}, \mathcal{C}_K[\hat{V}, \hat{V}]] + \left(-1 + 3\alpha - 3\right.\right. \tag{7.200}$$

7.5.3 Reversible Reaction, Stirred Solution

Problem Setup

Consider the two-species diffusion problem specified schematically in Figure 7.30. We will track the concentration fields of two species, c_A and c_B, as explicit functions of a spatial coordinate z and a temporal coordinate t. Let $z = 0$ denote the position of the electrode; here (and only here), the two species undergo a single electron transfer reaction, which we assume occurs at a rate far greater than any other temporal scale in the problem. In other words, the electrochemical reaction is *reversible* (or Nernstian).

We assume that the electrolyte solution is stirred, resulting in the formation of a concentration boundary layer of length L within the vicinity of the electrode. For $z < L$, species transport is described by the diffusion equation, whereas for $z > L$, convective transport dominates, and the species concentrations as $z \to L$ can be taken to be fixed at their bulk concentrations, $c_{A,\text{bulk}}$ and $c_{B,\text{bulk}}$. Conservation of mass considering purely diffusive transport of species inside the concentration boundary layer implies the following pair of governing equations,

$$\partial_t c_A = \mathcal{D}_A \, \partial_z^2 c_A, \tag{7.201}$$

$$\partial_t c_B = \mathcal{D}_B \, \partial_z^2 c_B, \tag{7.202}$$

where $\mathcal{D}_A$ and $\mathcal{D}_B$ are the Fickian diffusion coefficients of the two species. Henceforth in this subsection, we will assume that $\mathcal{D}_A = \mathcal{D}_B = \mathcal{D}$, corresponding to symmetric diffusion.

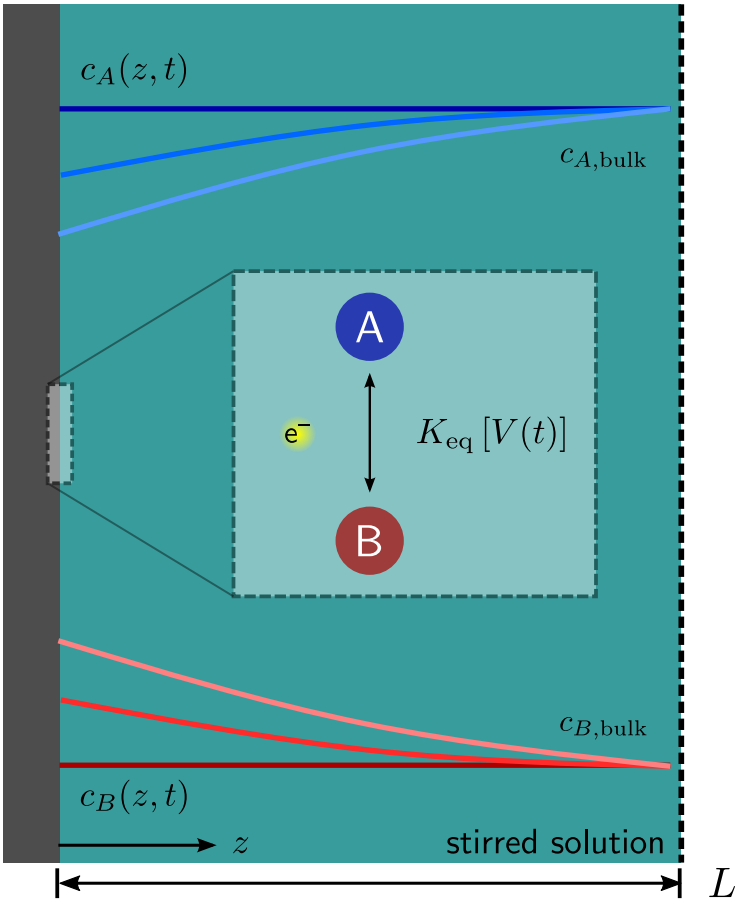

Figure 7.30: Schematic drawing of a two-species diffusion problem bounded domain, with a reversible (Nernstian) reaction occurring at the left boundary.

The physical setting of the problem supplies four boundary conditions,

$$\frac{c_A(z=0,t)}{c_B(z=0,t)} = \exp\left[+\beta e\left(E(t) - E_{\text{eq}}\right)\right], \tag{7.203}$$

$$\left.\frac{\partial c_A}{\partial z}\right|_{z=0} = -\left.\frac{\partial c_B}{\partial z}\right|_{z=0}, \tag{7.204}$$

$$c_A(z=L,t) = c_{A,\text{bulk}}, \tag{7.205}$$

$$c_B(z=L,t) = c_{B,\text{bulk}}, \tag{7.206}$$

where Eq. (7.203) enforces that the concentrations at the electrode are in the ratio specified by the appropriate Nernstian equilibrium for an instantaneous applied potential $E(t)$, reaction equilibrium potential E_{eq}, and inverse temperature β. Equation (7.204) enforces mass conservation at the interface, while Eqns. (7.205) and (7.206) enforce that the concentration fields reach the bulk concentrations as $z \to L$.

The problem is fully specified upon setting initial conditions for the concentration fields,

$$c_A(z,t=0) = c_{A,\text{bulk}}, \tag{7.207}$$

$$c_B(z,t=0) = c_{B,\text{bulk}}, \tag{7.208}$$

which corresponds to a solution beginning at open-circuit conditions, with the species concentration fields held constant at their bulk values.

The input voltage signal $E(t)$ is decomposed in the manner prescribed by Eq. (7.103), and the current is extracted from the concentration profiles in the manner described by Eq. (7.104).

We introduce the following non-dimensionalization scheme,

$$\tilde{c}_A \equiv \frac{c_A}{c_{A,\text{bulk}}}, \tag{7.209}$$

$$\tilde{c}_B \equiv \frac{c_B}{c_{A,\text{bulk}}}, \tag{7.210}$$

$$\tilde{E} \equiv \beta e E, \tag{7.211}$$

$$\tilde{z} \equiv \frac{z}{L}, \tag{7.212}$$

$$\tilde{t} \equiv t \cdot \omega^*, \tag{7.213}$$

$$\tilde{J} \equiv \frac{J}{e\mathcal{D}^{1/2}\omega^{*1/2}c_{A,\text{bulk}}}, \tag{7.214}$$

where $\beta \equiv (k_{\text{B}}T)^{-1}$ is the inverse temperature, e is the fundamental charge, and ω^* is an arbitrary fundamental frequency.

Under this non-dimensionalization scheme, the governing equations in Eqns. (7.201) and

(7.202) transform into,

$$\partial_{\tilde{t}}\tilde{c}_A = \lambda \partial_{\tilde{z}}^2 \tilde{c}_A, \tag{7.215}$$

$$\partial_{\tilde{t}}\tilde{c}_B = \lambda \partial_{\tilde{z}}^2 \tilde{c}_B, \tag{7.216}$$

where the dimensionless group

$$\lambda \equiv \frac{\mathcal{D}}{L^2 \omega^*}, \tag{7.217}$$

emerges naturally from the non-dimensionalization procedure, and physically represents the ratio of the characteristic timescale of the voltage waveform ($1/\omega^*$) and the characteristic timescale of diffusive transport ($L^2/\mathcal{D}$).
The boundary conditions transform into,

$$\frac{\tilde{c}_A(\tilde{z}=0,\tilde{t})}{\tilde{c}_B(\tilde{z}=0,\tilde{t})} = \gamma \cdot \exp\left[\tilde{E}(t) - \tilde{E}_{\text{eq}}\right], \tag{7.218}$$

$$\left.\frac{\partial \tilde{c}_A}{\partial \tilde{z}}\right|_{\tilde{z}=0} = -\gamma \left.\frac{\partial \tilde{c}_B}{\partial \tilde{z}}\right|_{\tilde{z}=0}, \tag{7.219}$$

$$\tilde{c}_A(\tilde{z}=1,\tilde{t}) = 1, \tag{7.220}$$

$$\tilde{c}_B(\tilde{z}=1,\tilde{t}) = 1, \tag{7.221}$$

where $\gamma \equiv c_{B,\text{bulk}}/c_{A,\text{bulk}}$, and $\tilde{E}_{\text{eq}}$ is made nondimensional in the manner prescribed by Eq. (7.107). Finally, the initial conditions transform into,

$$\tilde{c}_A(\tilde{z},\tilde{t}=0) = 1, \tag{7.222}$$

$$\tilde{c}_B(\tilde{z},\tilde{t}=0) = 1. \tag{7.223}$$

Under this non-dimensionalization scheme, Eq. (7.104) transforms to,

$$\tilde{J} = -\sqrt{\lambda} \cdot \left.\frac{\partial \tilde{c}_A}{\partial \tilde{z}}\right|_{\tilde{z}=0} \tag{7.224}$$

Now that the non-dimensionalized problem is fully specified, we will drop all tildes in subsequent expressions.

Kernel Expressions

Kernel at $\mathcal{O}(\epsilon^0)$ At $\mathcal{O}(\epsilon^0)$, we can ignore the second term in Eq. (7.103), yielding $E(t) = E_{\text{hold}}$. The first step is to take the governing equations in Eqns. (7.111) and (7.112) into Laplace space, at this order. Applying the initial conditions in Eqns. (7.117) and (7.118) yields,

$$s\hat{c}_A^{(0)}(z,s) - 1 = \lambda \cdot \partial_z^2 \hat{c}_A^{(0)}(z,s), \tag{7.225}$$

$$s\hat{c}_B^{(0)}(z,s) - 1 = \lambda \cdot \partial_z^2 \hat{c}_B^{(0)}(z,s), \tag{7.226}$$

subject to the Laplace space boundary conditions,

$$\frac{\hat{c}_A^{(0)}(z=0,s)}{\hat{c}_B^{(0)}(z=0,s)} = \gamma \cdot \exp\left[E_{\text{hold}} - E_{\text{eq}}\right], \tag{7.227}$$

$$\left.\frac{\partial \hat{c}_A^{(0)}}{\partial z}\right|_{z=0} = -\gamma \left.\frac{\partial \hat{c}_B^{(0)}}{\partial z}\right|_{z=0}, \tag{7.228}$$

$$\hat{c}_A^{(0)}(z\to\infty,s) = 1/s, \tag{7.229}$$

$$\hat{c}_B^{(0)}(z\to\infty,s) = 1/s. \tag{7.230}$$

At $\mathcal{O}(\epsilon^0)$, the current density expression reads,

$$\hat{J}^{(0)}(s) = \frac{1}{\sqrt{s}} \cdot \frac{\left(e^{2\sqrt{s/\lambda}}+1\right)\left(\gamma e^{\bar{E}_{\text{hold}}}-1\right)}{\left(e^{2\sqrt{s/\lambda}}-1\right)\left(e^{\bar{E}_{\text{hold}}}+1\right)}, \tag{7.231}$$

where $\bar{E}_{\text{hold}} \equiv E_{\text{hold}} - E_{\text{eq}}$.

At long times, the boundary concentrations $c_k^{(0)}(z=0,t\to\infty)$ (correspondingly, $s\cdot\hat{c}_k^{(0)}(z=0,s\to 0)$) for $k\in(A,B)$ can be shown (by taking appropriate limits) to settle into their steady-state values,

$$c_A^{(0)}(z=0,t\to\infty) = \frac{e^{\bar{E}_{\text{hold}}}(1+\gamma)}{1+e^{\bar{E}_{\text{hold}}}}, \tag{7.232}$$

$$c_B^{(0)}(z=0,t\to\infty) = \frac{1+\gamma}{\gamma\left(1+e^{\bar{E}_{\text{hold}}}\right)}. \tag{7.233}$$

Kernel at $\mathcal{O}(\epsilon^1)$ At $\mathcal{O}(\epsilon^1)$, we must include the second term in Eq. (7.103). Again, we take the governing equations (7.215) and (7.216) at this order into Laplace space. Note that we do not need to apply the initial conditions in Eqns. (7.222) and (7.223), since they have already been handled at $\mathcal{O}(\epsilon^0)$. Hence, we have,

$$s\hat{c}_A^{(1)}(z,s) = \lambda\cdot\partial_z^2\hat{c}_A^{(1)}(z,s), \tag{7.234}$$

$$s\hat{c}_B^{(1)}(z,s) = \lambda\cdot\partial_z^2\hat{c}_B^{(1)}(z,s), \tag{7.235}$$

subject to the Laplace space boundary conditions,

$$\hat{c}_A^{(1)}(z=0,s) = \gamma\cdot e^{\bar{E}_{\text{hold}}}\cdot\left\{\hat{c}_B^{(0)}(z=0,t\to\infty)\cdot\hat{V}(s) + \hat{c}_B^{(1)}(z=0,s)\right\}, \tag{7.236}$$

$$\left.\frac{\partial \hat{c}_A^{(1)}}{\partial z}\right|_{z=0} = -\gamma\left.\frac{\partial \hat{c}_B^{(1)}}{\partial z}\right|_{z=0}, \tag{7.237}$$

$$\hat{c}_A^{(1)}(z=1,s) = 0, \tag{7.238}$$

$$\hat{c}_B^{(1)}(z=1,s) = 0. \tag{7.239}$$

At $\mathcal{O}(\epsilon^1)$, the current density expression reads,

$$\hat{J}^{(1)}(s) = \frac{e^{\bar{E}_{\text{hold}}}(1+\gamma)}{\left(1+e^{\bar{E}_{\text{hold}}}\right)^2}\cdot\sqrt{s}\ \cdot\hat{V}(s). \tag{7.240}$$